A STUDY OF ACTIVE EXPERIMENTAL TECHNIQUES FOR NEUTRON DOSIMETRY IN POSITIVE ION ACCELERATOR

By

VITISHA SUMAN DAGRE

(**PHYS01201304038**)

Bhabha Atomic Research Centre, Mumbai

A thesis submitted to the
Board of Studies in Physical Sciences
In partial fulfillment of requirements
for the Degree of

DOCTOR OF PHILOSOPHY

of

HOMI BHABHA NATIONAL INSTITUTE

July, 2019

Annexure 1

CERTIFICATION ON ACADEMIC INTEGRITY

1. I **Ms. VITISHA SUMAN DAGRE** HBNI, Enrollment No. **PHYS01201304038**, hereby undertake that the Thesis titled **A Study of Active Experimental Techniques for Neutron Dosimetry in Positive Ion Accelerator**, is prepared by me and that the documents reports the original work carried out by me and is free of plagiarism.

2. I am aware and undertake that if plagiarism is detected in my thesis at any stage in future, suitable penalty will be imposed as per the applicable guidelines of the institute/UGC.

Vitisha Suman 15/10/2020

Signature of the student

Endorsed by PhD Supervisor

Ajit Kumar Mohanty
15-10-2020

Signature (with date)

Name: Prof. A. K. Mohanty
Designation: Director, BARC
Department/Centre: Bhabha Atomic Research Center
Name of the CI/OCC: Bhabha Atomic Research Center

Government of India
Bhabha Atomic Research Centre

Ref: HBNI/BARC/Ph.D./ PHYS01201304038 Date: 15/10/2020

Sub: Certification regarding incorporation of corrections suggested by the examiners for the Ph.D. Thesis of Ms. Vitisha Suman Dagre, in Physical Sciences, HBNI.

This is to certify that for the PhD thesis of Ms. Vitisha Suman Dagre, HBNI student (**PHYS01201304038**), there were no specific enquiries and suggestions made by the reviewers. The reviewers have given positive remarks and have recommended to accept the thesis in the present form.

Ajit Kumar Mohanty
15-10-20

Prof. A. K. Mohanty
Ph.D. Guide

Dean
HBNI

CONTENTS

Homi Bhabha National Institute

Ph. D. PROGRAMME

Name of Candidate:	**Ms. Vitisha Suman Dagre**
Name of the Constituent Institution:	Bhabha Atomic Research centre, Mumbai
Enrollment Number:	**PHYS01201304038**
Title of the Thesis:	**A Study of Active Experimental Techniques for Neutron Dosimetry in Positive Ion Accelerator**

1. For neutron energy spectrometry in accelerator environment in absence of direct techniques like time of flight, there is a need to utilize other indirect methods like active proton recoil or the activation technique. A Genetic Algorithm based Monte Carlo deconvolution code (GAMCD) [10] for energy spectrum determination of neutrons from indirect methods has been developed. An activation foil measurement for $^{1}H + ^{9}Be$ at 20 MeV [11] and a proton recoil measurement for $^{12}C + ^{nat}Ag$ system at 144 MeV [12, 13], were unfolded to obtain the underlying neutron energy distributions. This method overcomes the requirement of any guess spectra, in absence of which few available codes like MAXED [14] and GRAVEL [15] fail to work satisfactorily. The GAMCD code also overcomes the difficulty of generation of unphysical negative solutions, which is sometimes an issue with code like FERDOR [16]. In addition, the code GAMCD has been tested to work well on under-determined and over-determined problems. Furthermore, knowledge of the neutron response function of the detector is critical for unfolding. The response matrix for one of the liquid scintillator detector has been prepared from experimentally measured pulse height of mono-energetic neutron sources DD and DT. The pulse height response function is simulated using GEANT-4 [17] simulation tool and light output coefficients are obtained. Response function

for various incident energies has been simulated using the fitted parameters and smearing has been added to match the detector resolution.

2. The neutron yield data from heavy ion reaction on thin and thick targets is very scarcely available for radiation protection practices in the low energy range ~10 MeV/A of accelerators in operation. These thick target yield data represents the source term for shielding estimations of the facility and it is thus important to measure the double differential neutron yield experimentally. A measurement of thin target neutron yield and its angular distribution using time of flight method for thin $^{12}C + ^{12}C$ system at various projectile energies 44 MeV – 110 MeV have been carried out. The measured neutron energy distributions are compared with predictions of statistical code PACE [18]. The neutron yields from the intermediate projectile energies were interpolated over energy bin size of 1.0 MeV using a linear relation. The yield from all projectile energy was later integrated and compared with the thick target neutron yield.
3. The measurement of thick target neutron yield in addition to being source term for shielding is also useful in dose calculation due to secondary neutrons in the heavy or light ion therapy. Measurement of double differential cross section and neutron energy spectrum by time of flight method for the thick targets $^{12}C + ^{27}Al$ at 115.0 MeV [13] and $^{12}C + ^{12}C$ at 116.0 MeV are also carried out at Pelletron-Linac facility [19]. The neutron time of flight is extracted from the two-dimensional plot of time of flight and pulse shape discrimination and is converted to energy distribution. The angular distribution too has been measured to see how the yield varies from forward to lateral direction, which is essential for shielding optimizations. The measured yields were compared with the Fluka [20] and modified PACE2 [21] estimations. In the modified PACE2, a thick target has been assumed to be built from many thin layers and the yield can be estimated by integrating yield from each

layer produced by a projectile with degrading energy as it passes through each layer before completely stopping within.

4. There is a mixed field of neutrons and gammas in an accelerator environment, but neutron dose is of primary concern. The neutron dosimetry in accelerator environment is done using conventional rem-meters. However, measurements are complex due to the dynamic field and energy ranges involved. In rem-meters the fast neutrons are moderated in the high density poly-ethylene ball and are then counted by the neutron detector placed at the center of the instrument. In the process of moderation, the information on energy distribution of the neutron field is completely lost. Neutron ambient dose measurement were carried out for ^{12}C + thick ^{12}C system at 116.0 MeV using commercial dosimeters which were then compared to the doses estimated from spectral distribution obtained from time of flight measurements and reaction codes using ICRP 74 fluence to dose conversion coefficient. Also, the commercially available rem-meters have usability only till 14 MeV [22] unless modified with some converter, whereas using spectral distribution techniques a wide range of neutron energy can be covered.

Summary

One of the major research goals on radiation safety in the accelerator facilities is to accurately measure the radiation sources and understand its radiological characteristics. The positive ion accelerator environment consists of mixed radiation field including neutrons, which are of main concern. Accurate estimation of neutron dose to occupational workers is important from the radiological safety point of view. Neutron dosimetry is a complex field and fluence to dose conversion factor is normally used for estimating the neutron ambient dose. The measurement of neutron fluence and dose is also a complicated task due to highly anisotropic nature of the emission, wide range of energy and fluence and in some cases pulsed nature of the emissions. The neutron yields are usually reported in terms of energy and angular distributions and is a function of nuclear reaction parameters like, target - projectile configuration, incident projectile energy and charge state.

Double differential neutron yield, with respect to neutron energy and angular distributions, will provide the source term which is a critical input for the shielding calculation of the facility. Moreover, it is the input for estimations of air and structural activations in the high energy and high current accelerators. Also, the data generated from measurements of neutron energy distribution and neutron ambient dose will help in benchmarking the reaction codes for predictive estimations in absence of measurements. This brings out the need for carrying out the neutron spectrometry and dosimetry study using various active techniques in positive ion accelerators.

The work presented in this thesis has been divided into three parts. The first part focusses on development of a genetic algorithm based neutron spectrum unfolding code (GAMCD). This code can be applied when direct techniques like time of flight cannot be used for neutron energy spectrum measurements. Using the GAMCD code an activation foil measurement for $^{1}H + ^{9}Be$ at 20 MeV and a proton recoil measurement for $^{12}C + ^{nat}Ag$ system at 144 MeV, were

unfolded to obtain the underlying neutron energy distributions. This method overcomes the requirement of any guess spectra, in absence of which few available codes like MAXED and GRAVEL fail to work satisfactorily. In addition to the code, the neutron response function of the organic liquid scintillator detector that goes as input in unfolding is prepared. For one of the liquid scintillator detector used in this study the pulse height of mono-energetic neutron sources DD and DT are measured experimentally. Pulse height distribution for various incident energies has been simulated using GEANT-4 and the fitted parameters and smearing has been added to match the detector resolution.

In the second part of the work, measurement of double differential neutron yield and angular distribution by time of flight method for the thick targets $^{12}C + ^{27}Al$ at 115.0 MeV and $^{12}C + ^{12}C$ at 116.0 MeV has been carried out. The measured yields were compared with the reaction codes Fluka and modified PACE2 estimations. A measurement of neutron yield and its angular distribution using time of flight method for thin target $^{12}C + ^{12}C$ system at various projectile energies 44 MeV – 110 MeV have also been carried out. The measured neutron energy distributions are compared with predictions of statistical code PACE2.

In the final part neutron ambient dose is estimated from neutron energy distribution obtained from time of flight measurements and the reaction codes, using ICRP 74 fluence to dose conversion coefficients. The estimated doses are compared to the experimentally measured neutron ambient doses and its angular distribution, using commercial dosimeters for thick target $^{12}C + ^{12}C$ system at 116.0 MeV.

The present study brings out the importance of neutron ambient dose estimation from measured and estimated neutron energy distributions compared to experimental rem meter measurements. The theoretical estimations and experimental measurements compare reasonably well except there is a noticeable under estimation by the dosimeters and the empirical formulation.

The present study further emphasizes that the dose measurements carried out with commercial rem meters should be periodically compared with the neutron ambient doses estimated using neutron energy distribution data, either obtained experimentally from time of flight technique or neutron spectrum unfolding and obtained from nuclear reaction codes. The present study will also help in understanding radiation environment both qualitatively and quantitatively in low energy positive ion accelerator facilities and plan for radiation protection activities. The measured data will also help to benchmark the reaction codes for neutron yield and dose predictions when experimental data are not available for quick references.

APPENDIX – A

Modified PACE2 - Thin to thick target neutron yield conversion

The incident particle inside a thick target undergoes energy degradation as it traverses the thickness and finally, on losing complete energy stops within the target. The emitted secondary particles, which are mostly neutrons, correspond to each interaction of the degraded projectile energy at different layers of the target. The final distribution of the emitted neutrons as seen by the detector can be approximated as superposition of neutron distribution from various thin targets incident with gradually decreasing projectile energies, starting from the maximum projectile energy and going down till the Coulomb barrier of the system. The estimations from the statistical model codes have been carried out in the lab frame of reference for estimating the evaporation contribution. For the ease of calculation, the thick target is taken as to be made up of number of thin slabs with an assumption that the projectile loses a fixed energy ΔE in each slab. The thickness of the slabs is not equal but is a function of the stopping power $(-dE/dx)$ of the projectile. The slowing down as a result is considered to be in discrete steps. Within a slab for mathematical simplification the projectile is assumed to interact with the target nuclei with an average energy. Here, slowing down of the projectile due to multiple scattering and straggling in between the interactions within the slab thicknesses is ignored. Also, the scattering of the emitted neutron within the target is not considered. The emitted neutron spectra from all the slabs when added give the total neutron spectra from the thick target.

During the process of superimposition of thin target neutron spectra the estimation from PACE2 was done for various incident energies starting from the lab frame projectile energy going down till Coulomb barrier around which the reaction cross-section becomes very small, with a step of reduction in incident energy by ΔE. For the each incident energy the respective

fusion cross-section was considered. The kinetic energy E_P^i when incident on the i^{th} slab and the average energy in the i^{th} slab $E_{P,avg}^i$ for the projectile energy E_P^0 incident on the thick target is mathematically represented as

$$E_P^i = E_P^0 - (i-1)\Delta E \tag{A.1}$$

$$E_P^i = (E_P^i + E_P^{i+1})/2 \tag{A.2}$$

The slab thickness x_i is

$$x_i = \int_{E_P^i}^{E_P^{i+1}} \frac{dE}{-dE/dx} \tag{A.3}$$

where, dE/dx is the stopping power of the projectile in the target material.

The neutron yield $Y(\epsilon,\theta)d\epsilon d\theta$ at energy ϵ and the direction θ with respect to the initial projectile direction is given by

$$Y(\epsilon,\theta)d\epsilon d\theta = \sum_{i=1}^{n} \sigma\left(E_{P,avg}^i, \epsilon, \theta\right) d\epsilon d\theta N_T\, x_i \times exp\left[-N_T\left\{\sum_{k=1}^{i-1} \sigma_{fus}\left(E_{P,avg}^k\right) x_k\right\}\right] \tag{A.4}$$

where, N_T is the number of target atoms per unit volume, the running index *n* represents the number of thin slices depending upon the discrete energy decrement,

$$n = (E_P^0 - E_P^{th})/\Delta E \tag{A.5}$$

where, E_P^{th} is the projectile threshold energy for neutron production, $\sigma\left(E_{P,avg}^i, \epsilon, \theta\right)$ is the emission cross-section of the neutron of energy ϵ at an angle θ when a projectile of energy E_P is incident on the target nucleus, and σ_{fus} is the fusion cross-section of the projectile with the target.

CHAPTER 1

Introduction

Particle accelerators have found wide applications and have become an essential device in the field of scientific research, medicine, industries and agriculture [1 – 12]. Although, the work on particle accelerator started more than 100 years ago, the major advancements in this field took place mostly in the past sixty years. These accelerators are based on the principle of interaction of the electric charge with static and dynamic electromagnetic fields in the frequency range from 50 Hz to radio frequency fields in GHz in the present-day accelerators. Over the years, with the advancement in technologies, the simple acceleration machines developed by Cockcroft and Walton [13, 14] have become more complex in terms of size, beam energies, type of accelerated particles, target compositions and large beam currents. The particle accelerators can be broadly classified as linear and circular. The linear accelerator uses many accelerating cavities through which the particle beam passes only once, whereas circular accelerators have small number of radio frequency accelerating cavities through which the particles are made to pass repeatedly. The drift tube and waveguide linacs fall under the class of linear accelerators while the cyclotrons and synchrotrons fall under the circular accelerators. These facilities differ widely over the operating parameters and generate a complex radiation environment around the accelerators, thus giving rise to new radiation protection challenges as well as neutron dosimetric problems. Except for accelerated electrons, other charged particles

even when sufficiently accelerated do not produce secondary particles (under desired vacuum conditions) unless the primary beam interacts with either the target or any structural material. The primary beam constitutes the directly accelerated charged particles or the one influenced under electromagnetic fields within the accelerators. The primary beam when incident upon a target or beam dump or if it accidentally hits any structural material of the beam line will produce ionizing radiations like neutrons and gammas. The radiation field due to emitted neutrons and gammas are crucial parameters in radiation protection. In positive ion accelerator environment, neutron is the major source contributing to the dose [15, 16], due to its higher penetration, relative biological effectiveness (RBE) and radiation weighting factor (W_R) and is thus of foremost concern in the field of radiation protection. The neutron yield depends primarily on the type and thickness of target materials besides the charge state and incident energy of the projectiles and are reported in terms of energy and angular distributions. Nevertheless, the neutron dose estimation in particle accelerators is particularly difficult due to the wide range of energy and fluence, pulsed nature of the emitted radiation and highly anisotropic emissions. There is ample worldwide scientific research and ongoing efforts to develop new techniques as well as to improve the existing methodologies for the detection and measurement of neutron spectral yield and the associated dose values in the complex radiation environment around the particle accelerators.

1.1 Importance of energy distribution measurements in neutron dosimetric studies and the difficulties associated with these measurements

Neutron yield and energy distribution are important parameters for radiological safety aspects involving the protection of personnel, equipment and environment. Moreover, all the nuclear and accelerator facilities are meant to meet the guidelines for radiation safety set by regulatory bodies ensuring the compliances in dose limits by the facility operators and users. For this purpose, the measurement of energy distribution of the neutrons emitted from nuclear

reactions is required for understanding the origin, intensity and angular distribution of the radiation environment in any facility. As mentioned earlier, neutrons are the particles of primary concern for radiation protection in such facilities and differs from photon (despite both being neutral) in the process of depositing its kinetic energy in human tissues and matter. Consequently, the radiation-weighting factor and fluence to dose conversion factors for neutrons are different from that of photons and has typical energy dependence unlike photons [17-19]. Furthermore, the discrimination of neutrons from the invariably presence of photons is also essential to properly quantify the dose values.

In addition, the upcoming accelerator facilities such as medical cyclotrons [20], neutron spallation sources [21], radioactive ion beam (RIB) facility [22] and accelerator driven sub-critical system (ADSS) [23], are characterized by high beam current (few hundred μA or more), which manifests the importance of knowledge and understanding of emitted neutron spectra. Owing to the higher currents and beam energies, these facilities can also lead to air activation and/or induced activity in the structural components or the concrete walls. Unless the detailed yield and angular distribution of emitted neutron spectra are known, it will be difficult for accurate dose estimations and activation calculations. The thick target neutron yield and its angular distribution are critical inputs for radiation protection and shielding calculation for any accelerator facility [24, 25]. The radiation survey in such facilities is commonly carried out using active detector based rem-meters for neutron dose or dose rate measurements which are designed to measure neutron energy up to about 14 MeV unless modified with some converters. The conventional rem-meters are designed to follow the ambient neutron response curve proposed by International Commission of Radiation Protection (ICRP) [26, 27]. These rem-meters do not record any energy distribution while the dose coefficient factors (DCFs) are highly energy dependent as reported in ICRP-74 [28] and is shown in Fig 1.1. Based on different biological and multiple epidemiological studies, the ICRP has already introduced

changes in the DCFs in few occasions in past [29] and in near future similar set of up gradations might be expected with further improvements in the knowledge of radiation effects. The plausible future improved recommendations [30] may result in conventional dosimeters to be corrected for the amendments.

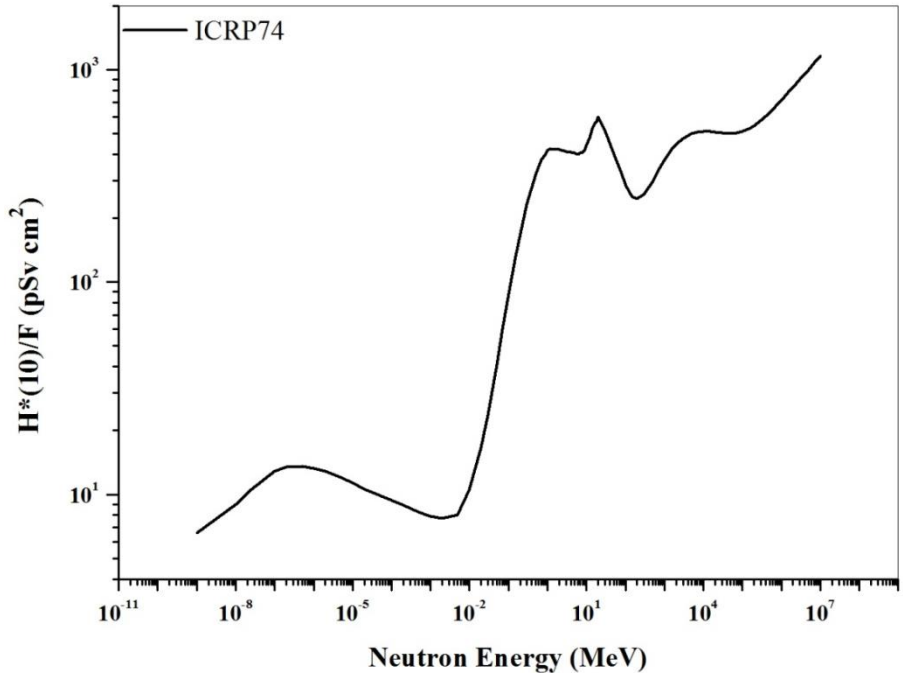

Fig. 1.1 Curve representing the ambient dose-equivalent per unit fluence, H*(10)/ϕ for mono-energetic neutrons incident on ICRU sphere (Image courtesy: ICRP74).

On the other hand, the neutron yield distributions being basic quantities are not affected by any changes in the DCFs. Hence, measuring the double differential yield of neutrons by any active or passive technique becomes an important task for the dosimetric practices and radiation protection purposes. The spectral yield can then be folded with the recommended DCFs to estimate the ambient neutron dose. In case of any changes in DCFs, the yield distribution can be folded with the new set of DCFs to obtain more realistic doses compared to that from a rem-meter. The difficulties associated with neutron measurements are mainly due to the presence of other interfering radiations (such as gamma) with the detector. Also, the accelerator environment has dynamic, pulsed and directional sources which further complicate the

measurement procedure. No single detector or detection procedure covers the entire range of neutron energies encountered in these high energy facilities. Time of flight technique being the most opted procedure for neutron spectrometry has limitations for high-energy (≥ 50 MeV) neutrons due to requirement of longer flight paths. Moreover, this technique cannot be used to measure the neutron energy distribution outside the facility shield. The proton recoil measurements followed by unfolding techniques, have limitations to be used in high intensity neutron field due to detector saturation setbacks. Unfolding and obtaining the neutron spectra from activation foil measurement also have setbacks in the situations of low intense neutron field. The conventional rem-meters that are commonly used in surveys, have neutron response till ~ 14 MeV unless covered with a high Z shell to increase its energy response till ~1 GeV utilizing the (n, 2n) reactions. To add further, these rem-meters fail to register any energy information of the measured filed, which as explained above, is a requirement for precise dosimetry.

1.2 Lack of the spectrometric data for the accelerators operating in the domain of intermediate energy

There are many accelerator facilities which operate in the energy range of ~ 10 MeV/A. As can be found in the literatures, vast amount of data is available for neutron yield in the energy range (100 MeV/A – few GeV/A) and in low energy range (≤ 100 MeV/A) for lighter projectile induced reactions (p, n), (d, n) and (α, n) [31 – 38]. Nevertheless, the data for neutron yield in the projectile energy range of ~ 10 MeV/A is scarce particularly for emissions from heavy ion interacting with thick targets [39 – 42]. The data in this energy domain would help to standardize and improve the existing reaction codes for yield and dose estimation. It is important to mention that, these codes come handy for neutron yield and dose estimation (and predictions) as it is not always possible to carry out experiments with different target projectile combinations covering all energy ranges. Therefore, these codes need to be carefully

benchmarked for neutron yields with different projectile and target combinations over a wide energy range to have reliable predictions.

In absence of time of flight measurements, the indirect techniques like proton recoil measurement or activation foil measurements are used, which are two step processes involving measurement followed by unfolding of the data. The available unfolding codes have limitations like requirement of *'a priori'* knowledge to start with. In addition, most of the unfolding codes fail in solving under-determined and over-determined problems. Besides, a few codes are also seen to generate negative flux values, which are not physical solutions. Thus a code, which can overcome all these shortcomings, is required along with a methodology to generate response function [43] of the detection system.

1.3 Mechanism of neutron production in particle accelerators

Particle accelerators based on the nature of primary beam can be categorized as of two types: electron accelerators and ion accelerators. The neutron production mechanism is different in both these types of accelerators. In electron accelerators of energy 15 MeV and above, photons with energies above the typical binding energy of nucleons (> 5 – 15 MeV) lead to photo-nuclear interaction and emission of photo-neutrons as well as photo protons. Photo-nuclear interaction is mainly the outcome of three explicit processes: giant nuclear dipole resonance, quasi-deuteron production and photo-pion production followed by its decay and intra-nuclear cascade generation. In case of ion accelerators, it can be further classified as low, medium and high energy accelerators based on the range of acceleration energy. The work discussed here deals in range of low energy heavy ion accelerators with typical beam energy of ~ 10 MeV/A. The neutron production mechanism in this range of heavy ion accelerators is completely different from those of high energy heavy ion and the electron accelerators. Heavy ions by definition are projectiles with A > 4 in the nuclear reactions. The different routes in

which heavy ion reaction can proceed as a function of impact parameter are shown schematically in Fig. 1.2. The impact parameter plays an important role to decide which mode of interaction will take place [44].

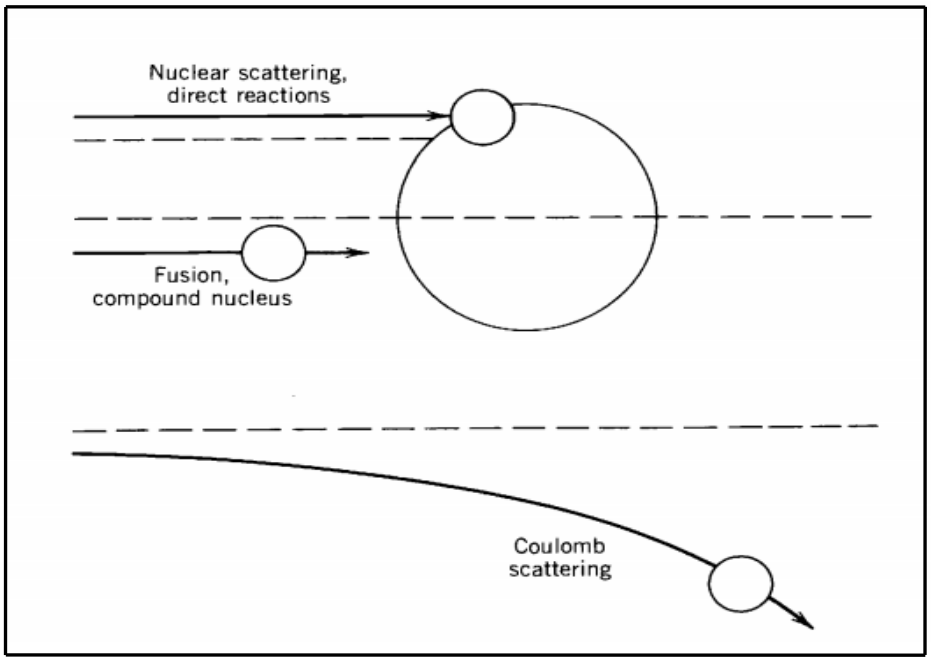

Fig. 1.2 Various modes of nuclear interactions as a function of impact parameter (Image courtesy: Kennethe Krane, 1987).

With large impact parameter, as the projectile grazes far away from nucleus, Coulomb scattering dominates. In Coulomb scattering the projectile nucleus does not change the nature of the target nucleus. There is also a probability of Rutherford scattering and Coulomb excitation. The other nuclear reaction possibilities open up when impact parameter becomes small enough to result in overlap of the projectile and target nuclei ensuing complete fusion of the two nuclei. The fused nuclei called compound nucleus have high excitation energy that may result in emission of variety of particles. Emission of charged and heavier particles is prohibited by a Coulomb barrier and requires very high excitation energy; however neutrons being neutral particles are the most likely to come out.

Nuclear reactions may proceed through many possible distinct mechanisms as a function of bombarding energy; where particle emission is categorized mainly as direct reactions, compound and pre-equilibrium nuclear reactions [35, 45 – 48], as shown in Fig. 1.3. Different regions in the figure show different modes of nuclear reactions as marked. The associated angular distribution of the three modes is also shown, which for low emission energies shows an isotropy (extreme left). These reactions are also differentiated based on time scale or number of intra nuclear collisions they undergo before emission. It has been observed that each mechanism preferentially excites specific part of the nuclear level spectrum and is characterized by different type of angular distributions.

In direct reactions, the projectile and the target interact on shortest time scale of order 10^{-22} sec, with a possible exchange of energy or particle. Here, the projectile interacts only with a limited portion of target nuclei and the ejectile carries most of the incident energy with it. It usually has a characteristic peak corresponding to some discrete state and the emission angular distribution is strongly peaked in forward direction. The compound nuclear reactions involve longer interaction times ~ 10^{-18} sec and are predominant over lower bombarding energies $\leq$ 10 MeV/A.

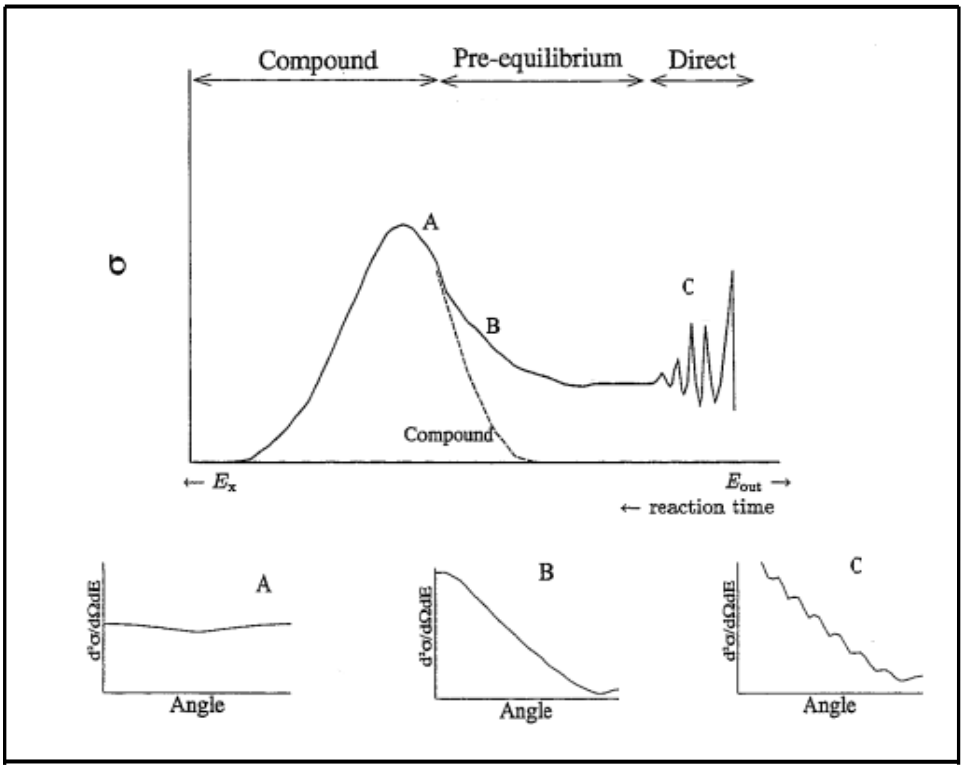

Fig. 1.3 A typical neutron emission spectra of a reaction A(a,b)B, with a projectile energy of several tens of MeV. Different regions marked show different modes of nuclear reactions and associated angular distribution of the three modes, which for low emission energies shows an isotropy (Image courtesy: A. J. Koning, ICTP Workshop, 1998).

Compound nuclear reaction mechanism proceeds through multiple intra nuclear collisions. The projectile fuses with the target nucleus to form a highly excited compound nucleus. Subsequently, the incident energy is shared among the other nucleon and after sufficient energy is accumulated on one nucleon or a cluster of nucleons to escape. The compound nuclear emissions are uncorrelated and are generally linked with memory loss as manifested from the isotropic angular distribution of the particle emissions in center of mass system. As compared to the other two emission processes, energy available per particle is small and the emission spectra are very often called evaporation spectra. The energy distribution of the emitted particles follows a Maxwell-Boltzmann distribution.

Apparently, as an intermediate between the two extreme cases on the reaction time scale, there is a reaction type that retains both direct and compound like features. These reactions are

referred to as pre-equilibrium or pre-compound emissions. Pre-equilibrium emissions take place after the first stage of direct reaction within time ~10^{-20} sec, but long before statistical equilibrium is reached. Pre-equilibrium processes dominate mostly above 10 MeV/A. The typical neutron energy spectra, which are measured in the present work and its contributions from different nuclear reaction processes, will be discussed in the following chapters.

1.4 Present work – Determination of neutron spectrum and Improvement in dosimetric studies

For neutron spectrometry in accelerator environment in situations when techniques like time of flight cannot be carried out there is a need to utilize other methods like active proton recoil or the activation technique. Several unfolding codes [49 - 55] have been developed over the years but have some or the other limitation, like suitable energy range, requirement of *a priori* information etc. The present work deals with development of a neutron spectrum unfolding code, which could be used to obtain the neutron energy distribution from proton recoil and activation foil measurements. A Genetic Algorithm based Monte Carlo de-convolution code (GAMCD) [56, 57] for energy spectrum determination of neutrons from indirect measurements has been developed. The code has been validated by unfolding a proton recoil measurement for C + ^{nat}Ag at 144.0 MeV system [57, 58] and neutron energy spectrum for activation foil measurement of ^{1}H + ^{9}Be at 20.0 MeV system [59]. This method overcomes the requirement of any guess spectra, in absence of which few available codes like GRAVEL [49] and MAXED [50] fail to work satisfactorily. The GAMCD code also overcomes the difficulty of generation of non-physical negative solutions, which is sometimes an issue with code like FERDOR [60]. In addition, the code GAMCD is found to work well on under-determined and over-determined problems.

Furthermore, knowledge of response function of the detector is very important since it goes as input in unfolding to extract the original neutron distribution. The response matrix for one of the liquid scintillator detector was prepared from experimentally measured pulse height spectrum of mono-energetic neutron sources DD and DT. The pulse height response function is simulated using GEANT-4 [61] simulation tool and light output coefficients have been obtained. Response function for various incident energies have been simulated using the fitted parameters and smearing is added to match the detector resolution.

The neutron yield data from heavy ion reaction on thin and more importantly on thick targets is sparsely available for energy ~10 MeV/A for accelerators in operation. These thick target yield data represents the source term for shielding estimations of the facility and it is thus important to measure the double differential neutron yield experimentally. Measurement of double differential neutron yield using time of flight method for the nuclear system, thick targets $^{12}C + ^{27}Al$ at 115.0 MeV [42] and $^{12}C + ^{12}C$ at 116.0 MeV have been carried out at Pelletron-Linac facility. The neutron time distribution is extracted from the two-dimensional plot of time of flight and pulse shape discrimination and is then converted into the neutron energy distribution. The angular distribution also have been measured to study the variation in neutron yield from forward to lateral direction, which is essential for shielding optimizations. The measured yields compared well with the modified PACE2 [62] and Fluka [63] estimations.

A measurement of thin target neutron yield and its angular distribution using time of flight method for thin $^{12}C + ^{12}C$ system over a range of projectile energies 44.0 MeV – 110.0 MeV have been also carried out. The measured neutron energy distributions are compared with yield estimated from reaction code PACE2 [64]. The neutron yields from the intermediate projectile energies are interpolated over energy bin size of 1.0 MeV using a linear relation. The yield from all projectile energies are later integrated and compared with the thick target neutron

yield for the above system. The thick target yield is seen to be slightly higher compared to the thin target integrated yield.

For the radiation protection and dosimetric requirements, the ambient neutron doses from the thick ^{12}C + ^{12}C system at 116.0 MeV have been measured using the conventional rem meters. In rem-meters, the fast neutrons are moderated in the high-density polyethylene shell thus losing all the energy distribution information. Ambient neutron dose is also estimated from time of flight measurement for the thick ^{12}C + ^{12}C system at 116.0 MeV, by folding the measured neutron energy distribution with the fluence to dose conversion coefficients. In addition, the ambient dose is estimated from the PACE2 and Fluka spectral results for the above system and all the results are compared. The ambient dose measured using rem-meter is seen to be under-estimation when compared to the doses estimated from spectra obtained from time of flight technique, PACE and Fluka.

The radiation protection for any facility is very critical and becomes more complex with the complexity in the radiation field of the facility. The accuracy in dose received by users in the facility will let proper analysis of the situation and take required corrective measures. The under-estimation or over-estimation will lead to under-utilization of the resources and the manpower. Frequently, complimenting one method with other provides confidence in correctness of the data generated. The improvements in neutron dosimetry have been demonstrated in this work based on the results obtained. The neutron ambient doses obtained from the measured neutron yields using time of flight techniques when convoluted with the fluence to dose conversion coefficients gives improved dose values. The doses so obtained, can be easily modified if required in future due to any change or modification in the dose conversion coefficients (DCF), as has been done in the past.

1.5 Organization of the thesis

Chapter 2 deals with the basics of neutron measurement techniques and neutron detection in accelerator environment. The interaction of neutron with matter has been described to understand the detection technique. The passive and active methodologies to carry out neutron spectrometry have also been presented. This chapter also gives details of theoretical nuclear reaction models such as PACE2 and Fluka used in the present study for the neutron yield estimations.

Chapter 3, describes development of genetic algorithm based unfolding algorithm GAMCD with improved features. Details of the steps involved in the code to carry out unfolding are discussed in detail. The chapter further contains the details of proton recoil unfolding method and the results of unfolding using GAMCD. The unfolding was carried out on a proton recoil measurement from thick target C + ^{nat}Ag (~ 2 mm) system at 144 MeV. In addition, details of the neutron spectrometry from activation foil measurements followed by unfolding are discussed. The neutron spectrum from 20 MeV protons on thick ^{9}Be (~2mm) target was measured using multiple foils (Ta, In, Au, Al etc.) and was unfolded using GAMCD. The unfolded results from GAMCD was compared with standard codes like MAXED and GRAVEL. Study of different smoothing techniques for handling fluctuations in the unfolded solutions is also presented.

Chapter 4, illustrates importance of detector response function in accuracy of the unfolded spectrum. Details of experimental measurements with two mono-energetic neutron sources DT and DD, using a liquid organic neutron scintillator of size 5″×2″ is given. The results of GEANT-4 simulation used to estimate the pulse height for the DD and DT mono-energetic sources is given. The procedure of fitting the generated pulse heights using light output equations [65] to the experimental data are given. The detail of smearing effect has been explained to match with the experimental resolution. The actual neutron spectra of DD and DT obtained from unfolding the simulated response function and proton recoil spectra is presented.

Chapter 5, gives details of the Time of flight technique used for measurement of kinetic energy distribution of emitted neutrons in a nuclear reaction. The experimental setup along with the electronics used for thin and thick target measurements are explained.

Details of experimental measurements and data analysis of energy and angular distribution of neutrons from thick targets, for the $^{12}C + ^{27}Al$ (~ 3 mm) at 115 MeV and $^{12}C + ^{12}C$ (~ 3.2 mm) at 116 MeV systems have been presented. The comparison of thick target yield measured using time of flight and estimated from reaction codes modified PACE2 and Fluka is given. The modifications carried out in PACE2 code for implementing thick target data analysis is also described in this chapter.

The experimentally measured thin target neutron yield and its angular distribution for $^{12}C + ^{12}C$ system in the energy range 44.0 MeV to 110.0 MeV in steps of 11.0 MeV have been discussed. The comparison between integrated thin target neutron yield and the thick target neutron yield from $^{12}C + ^{12}C$ reaction is presented.

Chapter 6, the procedure for dosimetry in accelerator facilities has been described in this chapter. The experimental details of dose measurement from the thick target $^{12}C + ^{12}C$ system at 116.0 MeV using rem meter and Microspec BTI have been provided. In addition, the procedure of neutron ambient dose estimation from the neutron yield distribution obtained by time of flight technique and reaction codes has been explained. Additionally, an empirical formulation used by Guo et. al. [39] is given for dose estimation.

Chapter 7, gives summary, conclusions and future scope for the present work. A neutron spectrum unfolding code GAMCD has been developed for proton recoil and activation method measurements. The code eliminates need of any guess spectra; it has been tested on proton recoil and an activation foil measurement to obtain the un-convoluted neutron energy distribution. The pulse height spectra measurement of the two mono-energetic sources DD and DT has been carried out using liquid scintillator detector. Batchelor's [65] light output

equations were used to simulate the pulse height spectra using GEANT-4 tool and were compared with the measured data. The response function for a 5″×2″ liquid organic scintillator detector was prepared and used for unfolding the actual DD and DT neutron spectra. The double differential neutron yields have been measured using the time of flight technique for thin target $^{12}C + ^{12}C$ reaction in the energy range 44.0 MeV – 110.0 MeV in a step of 11.0 MeV and thick target in $^{12}C + ^{12}C$ at 116.0 MeV and $^{12}C + ^{27}Al$ at 115.0 MeV. The angular distributions were also measured using five EJ301 detectors simultaneously. The double differential neutron yields estimated from nuclear reaction codes PACE2 and Fluka have been compared with the measured data. The neutron spectral distributions obtained from time of flight have also been folded with the fluence to dose conversion factors given in ICRP 74 to obtain the ambient neutron dose. This has been compared with the theoretical estimations from the reaction codes and the dose measurements using conventional dosimeters rem meter and Microspec BTI.

In conclusion, the present study suggests use of neutron energy spectrum in addition to any conventional dosimeters to obtain the ambient neutron doses. Performances of the conventional rem-meters should be tested regularly by obtaining the detailed energy distribution and estimating the ambient dose.

CHAPTER 2

Basics of Neutron Detection, Spectroscopy and Dosimetry

The process of neutron [66] detection begins with neutron interacting with nuclei in the matter, which initiates release of one or more charged particles in single step (p, α, etc.) or two step process (first emitting γ which in turn results in emission of electrons). The charged particles or photons are emitted in various ways in neutron-induced nuclear reactions, e.g. recoil nuclei from elastic or inelastic scattering $^{A}X(n, n)^{A}X$ and $^{A}X(n, n'\gamma)^{A}X$, photons from radiative capture $^{A}X(n, \gamma)^{A+1}X$, radioactive nuclei produced in $^{A}X(n, 2n)^{A-1}Y$ reactions or fission fragments from neutron-induced fission. These charged particles traversing through the medium dissipate the gained energy from the interaction, across its traced path producing free electrons, which are then collected in the form of electrical signals in detection system. The neutron interaction can be broadly categorized in two types. First, the scattering, by which neutron can transfer part of its kinetic energy to the interacting nucleus. During the interaction if sufficient energy is transferred, the recoiling nucleus ionizes the surrounding material around the point of interaction. The scattering is most efficient for detection material with low Z elements as the energy transfer during scattering is inversely proportional to Z of the interacting material. The second mode of neutron interaction with material is when it undergoes a nuclear reaction. The product from these reactions, such as protons, alphas, gammas and heavier fission

fragments initiate the detection procedure. Some of these nuclear reactions require some minimum neutron energy (threshold) to initiate, but most of them begin with thermal neutrons.

The energy information obtained in neutron detection system is usually poor because of the limitation of available neutron induced reactions. The recoil type of detection systems measures the first interaction event. The full energy of the neutron is usually not deposited in the detection material. In contrast, the reaction based counters take advantage of high reaction probability at low neutron energies by moderating the incoming neutrons. As is in the case of thermal, epithermal and slow neutrons with energies below10 keV, reactions with large positive Q-values are required to produce secondary charged particles of sufficient energy for detection. Due to the high Q-value, the energy of the secondary particles is almost independent of the incident energy of the neutron. Thus, it is associated with the disadvantage that the initial energy information before moderation of the neutron is completely lost. The energy recorded by the detector is the reaction energy plus the remaining neutron energy. Thus, moderation based neutron detectors provide information only on the neutron flux i.e. number of neutrons detected and not their energy distribution. The energy distribution from the moderation-based detectors can be obtained indirectly, using the detailed knowledge of the response of the moderating systems using mathematical procedures like spectrum unfolding.

In contrast, the detectors employed for measuring the fast neutrons are generally used as neutron spectrometers, i.e. the energy of the recoiling particle depends on the neutron energy and inversion procedures can be applied to infer the incident neutron energy. The elastic scattering $^{A}X(n, n)^{A}X$ mode of interaction plays an important role here. The recoil energy E_r is related to the E_n energy of the incident neutron by following relation [67]

$$E_r = E_n \frac{4A}{(A+1)} cos^2(\varphi_r^{lab}) \tag{2.1}$$

where, φ_r^{lab} is the emission angle of the recoil nucleus in the lab frame.

2.1 Neutron interaction with matter

Neutrons are highly penetrating particles and can travel several centimeters in material without interacting [68]. The probability that a neutron will undergo particular nuclear interaction depends on the neutron energy and the target identity. The type of interaction that neutrons undergo are categorized based on its energy and is presented in the Table 2.1.

Table 2.1 Types of neutron interaction over different energy ranges

	Energy	**Type of Interaction**
Cold	< 0.025 eV	Diffraction
Thermal	<0.5 eV	Elastic Scattering (n, n)
Epithermal	0.5 eV- 50 keV	Nuclear Reaction
Fast	>50 keV	Radiative Capture (n, γ)
Medium Energy	>1 MeV	Other Captures (n, p) or (n,α)
High Energy	>10 MeV	Inelastic Scattering (n, x) Nuclear Fission (n, f)

The different modes of interaction of neutrons with matter are described briefly in the following section.

2.1.1 Elastic scattering $^{A}X(n, n)^{A}X$

A neutron undergoes elastic scattering when the total kinetic energy of the colliding systems remain conserved. The speed and direction of the interacting neutron changes but the nucleus remains same with unchanged number of neutrons and protons. A pictorial representation is shown in Fig. 2.1(a). The collision between neutron and the nucleus can be approximated to the billiard ball collision. The neutron transfers part of its energy in the collision to the target nucleus. The target nucleus gains this parted energy and moves away at

an increased speed. The intensity or how hard the hit was determines the amount of energy transferred. If the target nucleus is of low atomic number and neutron is of low energy, the neutron effectively slows down by losing all its energy. Elastic scattering is not effective in slowing down neutrons with very high energy.

2.1.2 Inelastic scattering $^{A}X(n, n'\gamma)^{A}X$

For neutron energies above several MeV when neutron-nucleus scattering takes place, a new interaction channel opens up where neutron can excite the target nucleus to higher nuclear state. In inelastic scattering, the total kinetic energy of the colliding particles is not conserved and a part of the incident kinetic energy of the neutron is used up in exciting the nucleus. Other possibilities when a neutron strikes a target nucleus a compound nucleus is formed, which is unstable and within no time ($t \sim 10^{-22}$ s) comes to ground state by emitting a secondary radiation, which is either a neutron or a gamma. The schematic representation of inelastic scattering is shown in Fig.2.1 (b). The neutrons that undergo inelastic scattering typically loses a larger fraction of their kinetic energy in single interaction. This is the most effective interaction by which the fast neutrons lose their energy in the interacting medium.

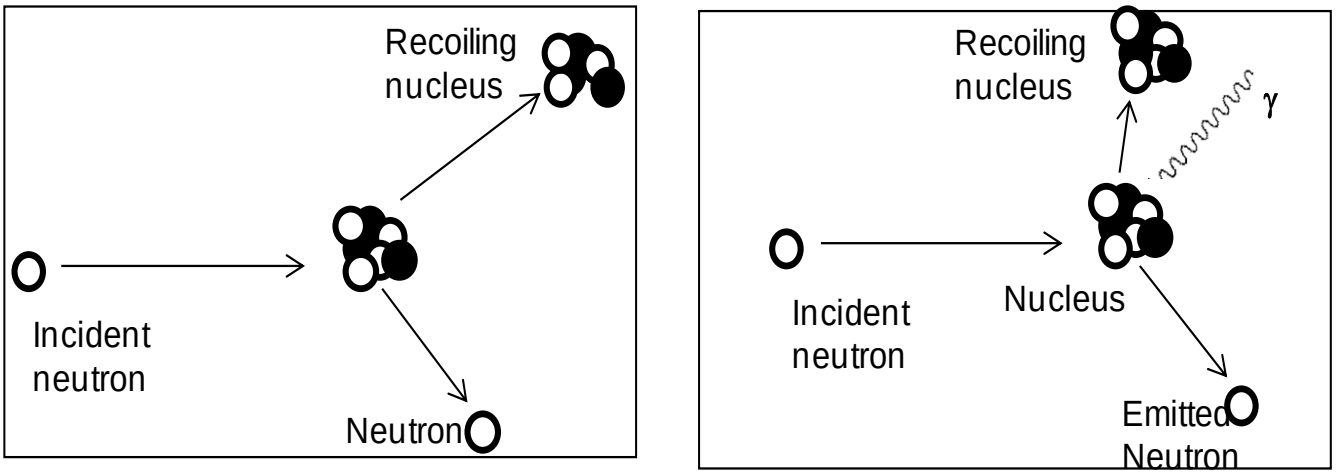

Fig.2.1 Schematic representation for (a) elastic and (b) inelastic scattering.

2.1.3 Capture reaction

Another neutron interaction, important for radiation protection is the radiative capture reaction that involves absorption of a neutrons followed by emission of gamma rays. In radiation protection and reactor physics radiative capture is very important due to very large capture cross sections (resonances) at low energies. Thus, neutron shielding usually includes a material to slow down neutrons followed by a material with high absorption cross section to absorb the slowed neutrons.

2.2 Neutron detection system

The neutrons based on their kinetic energy can be divided into three broad categories as presented in Table 2.1.

- Cold and Thermal neutrons $E_n \leq 0.025\ eV$
- Epithermal neutrons $0.025\ eV \leq E_n \leq 1\ MeV$
- Fast neutrons $E_n > 1 MeV$

Due to low energy of thermal neutrons, only reactions with high Q-values can be employed to detect them. To use the inherent signal amplification inside the detector, the proportional counters are filled with ^{3}He and BF_3 gases [67 - 69]. The higher neutron interaction cross-section is associated with the high Q-value which makes detection easy.

$$^{3}He(n,p)T \qquad (Q = 0.764\ MeV)$$

$$^{10}B(n,\alpha)^{7}Li \qquad (Q = 2.792\ MeV)$$

$$^{10}B(n,\alpha\ \gamma)^{7}Li \qquad (Q = 2.310\ MeV)$$

The total energy of charged particle is determined by the Q-value of the reaction products. The pulse height spectra of the counters are almost independent of the incident neutron energy. The advantage of proportional counters is the ease of the construction in various shapes and sizes. The pressure of the gas can also be varied as required, thus making the sensitivity of the detector to be more easily tailored as required by the measurement problem. The counters are also sensitive to photons, but due to the large range of the secondary electrons in the counting gases, photon induced events can usually be discriminated easily using a pulse-height threshold method. There is also fission ionization detectors used for measuring thermal neutrons using fission reactions

$$^{235}U(n,f) \qquad (Q \approx 200\ MeV)$$

2.2.1 Moderation based neutron detectors

The interaction cross sections of neutrons vary inversely with energy. Thus, the fast neutrons are slowed down by making them to pass through some moderating material usually hydrogenous material like high-density polyethylene (HDPE) to increase the detection probability. Consequently, the detectors used for measuring thermal neutrons, ^{3}He or BF_3 are covered by thick moderator materials which brings down the energy of the incident fast neutrons by multiple scattering with hydrogen in the moderator. The moderator is usually divided in two annular parts outer and inner separated by a cadmium layer. One such commercially available neutron rem meter [26, 27] is shown in Fig.2.2.

Fig. 2.2 Commercially available moderation based rem meter.

2.2.2 Liquid and plastic organic scintillator based detectors

Organic scintillators consist of low Z hydrocarbon compounds. The scintillation light is emitted from the transition of the free valence electrons of the molecules. The organic scintillator detectors work on the principle of dE/dx converted to visible light detected using photomultiplier tubes. Scintillator detectors have good sensitivity to energy, very fast response time (~ ns) and advantage of pulse shape discrimination. Pulse shape discrimination becomes important for its application in accelerators, which always has mixed fields. For the various available materials the desired properties to have are as follows

- High efficiency for conversion of excitation energy to fluorescent radiation
- Transparency to its fluorescent radiation to allow transmission of light
- Emission of light in a spectral range detectable for photo sensors
- Short decay time to allow fast response

The organic scintillator materials have two light components namely slow and fast. Fast corresponds to the prompt scintillation whereas; the slow component corresponds to the

delayed fluorescence. The composite yield curve is sum of both the exponential curves. The fraction of light that appears in the slow component often depends on the nature of the exciting particle. This property of pulse shape discrimination is used to differentiate between different particles. The slow component of the scintillation primarily depends on the rate of energy loss dE/dx of the exciting particle and would be large for the highly ionizing particle. A few commercially available scintillator detectors [70] are shown in Fig. 2.3 of various shapes and size.

Fig. 2.3 Commercially available organic a) liquid and b) plastic scintillator detectors in different size and shape. (Image courtesy: Eljen technology)

To separate different radiation components having different ionizations in mixed field environments, one such example is measurement of neutrons mixed with gammas in an accelerator facility. The time dependence of the scintillation pulses for different ionizing radiations alpha, gamma and neutrons in Stilbene crystal [67] is show in Fig. 2.4. There is a clear separation in the decay times for the marked three particles. The decay time is longer for the highly ionizing particle and shorter for the low ionizing particle. Using the available advanced timing electronics this important feature can be used

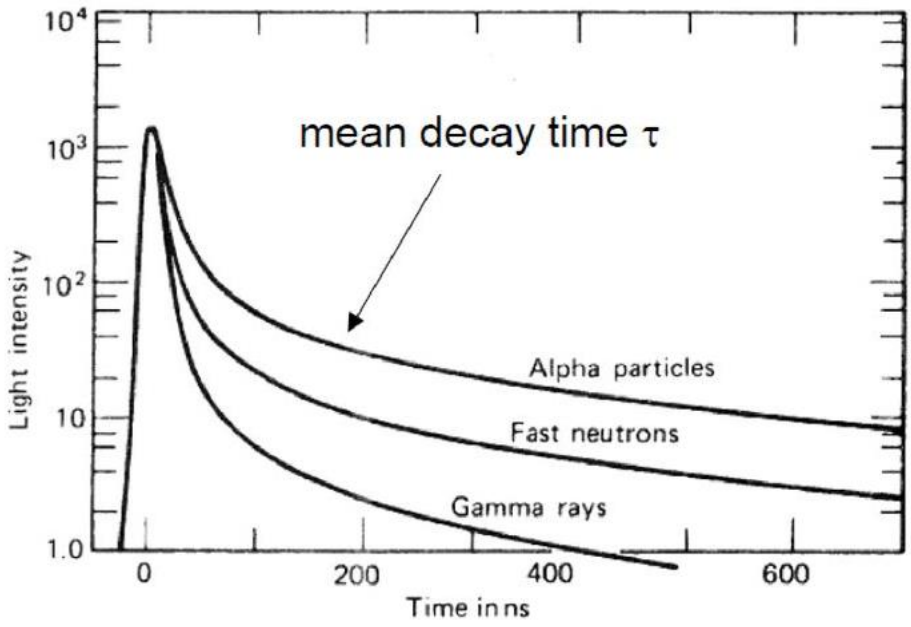

Fig. 2.4 The time dependence of scintillation pulses in Stilbene when excited by radiation of different types [67].

2.3 Neutron spectrometry techniques

Neutron spectrometry [60, 71 - 73] challenges began with the discovery of neutron itself. The discovery of neutron was based on indirectly measuring neutron energy by scattering it on hydrogen or other lighter nuclides, and measuring kinetic energy of the recoiling nuclei. Neutron spectrometry over the years has become an important tool in nuclear technology, radiotherapy, radiation protection and many more. The neutron spectral distribution in radiation protection provides the source term required to carry out the shielding calculations. The methodologies for neutron spectrometry can be broadly divided into two categories, viz. passive and active techniques, based on the mode of data extraction offline or online. Both the techniques have their own advantages and inadequacies. Depending on the type of field and energy ranges several available methods which are categorized under these two broad sections are utilized for the neutron spectrometric purposes.

2.3.1 Passive techniques

Passive neutron detectors are being used in accelerator facilities for a very long time. Passive detectors are normally used in personal dosimetry. Passive detectors record the radiation or dose information either by an excited electron getting trapped at a defect site in crystalline structure, induced activity or a track formed along the path of the radiation causing damage while traversing that medium to mention a few. Post processing like annealing, counting the decay photons or chemical etching is required for extracting the spectrum and/or dose information. The information about the actual distribution of the radiation field to which the detector was exposed can be extracted using mathematical procedures. The passive detectors in general have the advantage of being of low cost, small in size, easy to use, insensitive to photons in mixed fields. But all these passive detectors have time consuming post-processing associated with it. Post processing of the extracted information further requires some mathematical techniques like unfolding to extract the actual neutron energy distribution in the real radiation field. Another issue associated with these detectors is that, it cannot be used for on-line measurements or real time data acquisition as required during surveys.

2.3.2 Active techniques

Active detectors used for neutron measurements are based on either scintillator plus photomultipliers or gas filled counters operated in the proportional or Geiger-Muller mode. Their main advantage is real time data acquisition and at times, good gamma ray discrimination. They are used to monitor fields and set-off alarms for radiation protection requirements. Data are collected and displayed automatically. Time of flight and proton recoil based measurement methods are few among the active techniques. The gas filled detectors, semiconductors and scintillator detectors form the basis for active detection. The gas filled detectors use either BF_3 or ^3He. In case of BF_3, the gas used is enriched for ^{10}B. The reactions used for mostly thermal neutrons in these gas filled detectors are

$$^{3}He + n \rightarrow {}^{3}H + {}^{3}H + 765\ KeV \qquad \sigma = 5330\ b$$

$$^{10}B + n \rightarrow {}^{7}Li* + {}^{4}He + 2310\ KeV \qquad \sigma = 3840\ b$$

$$^{7}Li* \rightarrow {}^{7}Li + 480\ KeV \qquad \sigma = 940\ b$$

These reactions being exothermic, releases energetic charged particles which while traversing the detection material loses energy to produce ionization, which under the influence of applied potential difference is collected and appears as readable electric pulse. For measuring fast neutrons these detectors are placed inside some moderating materials. The fast neutrons when pass through these moderating material, they lose energy as they undergo scattering and thermalize. The cross section of the above mentioned reactions is very high for thermal neutrons.

Semiconductor neutron detectors are devices coated with a neutron reactive material or being partly composed of neutron reactive material. An example would be a common planar Si diode coated with either ^{10}B or ^{6}LiF. The neutron detection principle works as follows: a neutron is absorbed in the reactive film and spontaneously emits energetic reaction products. A reaction product may reach the semiconductor surface, and upon entering the semiconductor produces electron-hole pairs. Under a reverse bias voltage, these electrons and holes are drifted through the diode to produce an induced current, usually integrated in pulse mode to form a voltage output. The semiconductor devices coated with either ^{10}B or ^{6}LiF are preferred mainly because of high Q-value of the reaction and thus the energetic charged particle reaction products are much easier to discriminate from the background radiations.

The most frequent and easiest way for carrying out fast neutron measurement is by using proton recoils in hydrogen containing scintillator [72]. Fast neutron incident on the scintillator material gives rise to recoil protons whose energy distribution should be approximately a rectangular distribution, ranging from zero to maximum energy of the neutron. The hydrogen

rich organic materials like stilbene and anthracene crystals are dissolved in hydrogenous solvent to prepare organic liquid scintillator detectors. When incorporated in bulk matrix of polymerized hydrocarbons plastic scintillator detectors are made. Both organic liquid and plastic scintillators have been widely and successfully used for neutron detection and measurement. Though, the inorganic crystal anthracene has high light output and stilbene has better gamma-ray rejection, due to high cost, difficulty to obtain desired size and shapes and directional variation in light output; the organic liquid and plastic detectors are more preferred. Liquid scintillators are still preferred over the plastic scintillators because of their better pulse shape discrimination capabilities, to suppress gamma-ray response in the mixed field which is always the case in any accelerator facility. These organic liquid scintillator detectors find their usage in neutron detection by measuring the proton recoil followed by spectrum unfolding method using the response function of the detector. In addition these detectors are also widely used to measure fast neutrons using the time of flight techniques, where no mathematical deconvolution is required. Time of flight techniques are popular for measuring the kinetic energy distribution of the emitted neutrons by measuring the time taken by the neutron to travel a known distance between the point of generation to the position of detection in the detector.

In addition to experimental techniques for measuring the neutron energy and angular distributions empirical formulations and nuclear reaction codes like PACE2 [62], Fluka [74], EMPIRE [75] are used by the radiation protection experts. These reaction codes come handy to predict the neutron kinematics and the double differential yields when there is limitation on experimental measurements and need is for some referral estimations. In this study, the reaction code outputs have been compared and parameterized with experimental observations from various projectile target combinations. A few reaction codes will be discussed briefly in the next section.

2.4 Nuclear reaction codes

The nuclear reactions for relatively lower projectile energies, proceed via an unstable intermediate state known as compound nuclear state. In this case, the incident particle loses enough energy that it cannot escape the struck nucleus. According to liquid drop model, nucleus can be considered as a conglomeration of particles held together by attractive forces acting between them. An energetic nucleon approaching this nucleus enters into the target nucleus under an attractive potential and probably collides with one of the nucleons, and the energy is shared between both of them. Each nucleon again has the probability of colliding with other nucleons and thereby sharing the energy and ultimately the initial transferred energy is shared between many nucleons. In this situation, it is called a compound nucleus. There are few statistical model codes available to address compound nuclear formation and its decay, as discussed below.

2.4.1 Statistical model code PACE2

When a heavy ion is bombarded with an energetic projectile, a compound system is formed and a large number of different excited state configurations become possible. The density of quantum mechanical state increases with the added excitation energy. In addition, a large number of residual states are possible due to likely emissions of the particles from the compound nucleus. Since, each state cannot be studied individually; nuclear reactions codes based on statistical methods are commonly used to study the nuclear reaction mechanism.

The statistical model code PACE2 is an updated version of code PACE (Projection Angular- momentum Coupled Evaporation) developed by Gavron [62] for heavy ion interaction at intermediate energies, which are used to calculate the reaction cross-section of highly excited compound nucleus having higher angular momentum. It uses the Monte Carlo simulation techniques, as it is based on the statistical model approach, for estimating the de-

excitation of compound nucleus. PACE2 carries out only the statistical equilibrium called the evaporation calculations and does not consider the pre-equilibrium emissions. The angular distribution of the emitted particles or residues in the laboratory frame can be estimated from this code. The parameter like the Q-value of the reaction, level density, fusion cross-sections, optical model parameters required for the calculation is in-built. A multi-step procedure to determine the sequence of successive emission of the particles from compound nucleus is used by the statistical model code PACE2. But only the strong emission channels like proton, neutron, alpha, fission and subsequently γ-decay widths are calculated. Starting from a compound nucleus with well-defined excitation energy, angular momentum combination, random number selection algorithm allows the final state to be selected based on the partial decay widths for each process. For processing the information about each emitted particle is stored, the code allows calculating the laboratory energy spectra and angular distributions of the emitted particles or residual nuclei for each final nucleus produced in the reaction. Fission also is considered as a decay mode, while the incomplete fusion is not taken into account. In this code the most of the required input parameters can be used as default except the charge and mass of the projectile and target nucleus. The modified version of the code PACE2 takes into account the excitation energy dependence of level density parameter $'a'$ using the recommendations of Kataria, Ramamurthy and Kapoor (KRK) [76]. In the other version of the code Gilbert and Cameron (GC) formulism [77] for level density parameter $'a'$ is also available. The value of level density parameter $'a'$ can be calculated from the expression $a = A/K\ MeV^{-1}$, where A is the mass number of the compound system and K is a free parameter, which may be varied to match the experimental data. Fission probability is calculated using the Bohr-Wheeler's saddle point formalism [78] and the fission barriers used are those of Sierk [79]. For any bombarding energy the partial cross-section for compound nucleus formation at angular momentum $\boldsymbol{\ell}$ is given as,

$$\boldsymbol{\sigma_{\ell}} = \boldsymbol{\pi}\lambda\!\!\!^{-2}(2\boldsymbol{\ell} + \mathbf{1})\mathrm{T}_{\boldsymbol{\ell}} \tag{2.2}$$

Where, ƛ is the reduced wavelength, and $\mathrm{T}_{\boldsymbol{\ell}}$ is given as

$$\mathrm{T}_{\boldsymbol{\ell}} = \left[1 + \exp\left(\left(\boldsymbol{\ell} - \boldsymbol{\ell_{max}}(\boldsymbol{i})\right)\right)/\Delta\right]^{-1} \tag{2.3}$$

where, Δ is the diffuseness parameter and $\boldsymbol{\ell_{max}}$ is determined by the total fusion cross-section $\boldsymbol{\sigma_{Fus}}$

$$\boldsymbol{\sigma_{Fus}} = \sum_{\boldsymbol{\ell=0}}^{\infty} \boldsymbol{\sigma_{\ell,fus}} \tag{2.4}$$

The transmission coefficient for lighter particles *n*, *p* and α emission were determined using optical model potential of Perey and Perey [80], which is made available in code as default. The fusion cross-section is calculated using Bass formula [81]. The theoretical estimations obtained from the code have been compared with the results obtained from experimental measurements in the following chapters.

2.4.2 Fluka Monte Carlo code

Fluka is a general purpose simulation tool for calculation of particle transport and interaction with the matter. It has a wide application varying from calculation of proton and electron accelerator shielding, activation calculations, dosimetric calculations, detector design, cosmic rays, neutrino physics and radiotherapy. Fluka can simulate with high accuracy, propagation of 60 different particles in matter of interaction, from 100 eV to thousands of TeV. Fluka can handle even very complex geometries, using improved version of the well-known combinatorial geometry package. It hugely simplifies preparing the required physical structures or the detectors and its size and positioning. Multiple options are available to choose projectile particles light as well as heavy ions and to set their initial kinematics either in term of kinetic energy or momentum. The source distribution can be set as isotropic or different

from the available options. The source distribution can be set as isotropic or different from the available options. Fluka is intrinsically an analogue code, but can be run in biased mode for a variety of deep penetration problems. It covers a wide range of studies that can be carried out like particle accelerator shielding, activation, dosimetry, accelerator driven system, detector design, radiotherapy etc. The presence of a graphic interface further simplifies the visualization of the prepared geometries. Many standard materials are already provided in the material assignment list to choose from but an option to add a new material if its constituents, suppose are known in atomic fractional or any other convertible way. There are options available for different scorings like fluence, dose estimation, energy deposition to name a few. The output generated is saved into two formats of .tab and .lis with ASCII compatibility.

2.5 Neutron dose estimation

At particle accelerators, radiation dosimetry is performed mostly for the following reasons

- investigation of radiation accident
- routine radiological-protection survey
- individual (personal) monitoring
- environmental monitoring
- beam-intensity measurement
- radiation-field quantification

the first four points are mainly concerned with radiological protection, while the last two points are related to the general application. Measurements are made solely for the purpose of radiological protection to demonstrate compliance with the protection limits.

The report ICRP 74 [28] summarizes the work of joint task group on dose related quantities for radiological protection against external radiation. The three principal protection quantities recommended by the ICRP to be used in radiological protection are

a) Mean absorbed dose in an organ or tissue, D_T
b) Equivalent dose in the organ or tissue, H_T
c) Effective dose, E

The protection quantities are not directly measured, but may be related by calculations to the radiation field in which exposure occurs. To fill in this gap ICRU has developed operational quantities for measurement of exposures to external radiations. The operational dose-equivalent quantities defined by the ICRU for physical measurement are

a) The ambient dose equivalent, $H^*(d)$
b) The directional dose equivalent, $H'(d, \Omega)$ and
c) The personal dose equivalent, $H_p(d)$

The ICRP74 briefly defines the quantities used in radiological protection. It also provides a brief discussion on how these quantities are calculated. In addition it also provides the dose conversion coefficients that either relates the air kerma free-in-air or the frequently used particle fluence to the protection and operational quantities. The dose conversion factors are given for organ absorbed dose, effective dose, ambient dose equivalent, directional dose equivalent and personal dose equivalent as suitable. The data available is for mono-energetic photons, neutrons and electrons over a range of energy and several irradiation geometries.

The neutron yield energy distribution can be estimated either by direct method like time of flight measurement or obtained indirectly by unfolding the experimentally measured activities in activation foils or the proton recoil pulse height spectrum in scintillator detector measurements. The estimated neutron energy distribution, when folded back with the dose

conversion coefficients given in the ICRP 74 and integrated over the energy gives the total neutron ambient equivalent dose.

$$H*(d) = \sum \varphi(E) DCF(E) \tag{2.5}$$

where, $\varphi(E)$ is the energy distribution of the emitted neutrons, and $DCF(E)$ is the energy dependent fluence to dose conversion coefficients.

The following chapters discuss the estimation of neutron energy distribution obtained from different approaches like time of flight technique; proton recoil measurement and activation foil measurements followed by unfolding. The spectral distribution of neutrons obtained from the time of flight measurement was used to estimate the ambient neutron dose using the ICRP74 neutron fluence to dose conversion coefficients. The doses so obtained were compared with the rem meter measurements and are discussed in chapter 7. The following chapter deals with development of a genetic algorithm based neutron spectrum unfolding code GAMCD.

CHAPTER 3

Development of Neutron Spectrum Unfolding technique GAMCD (Genetic Algorithm based Monte Carlo De-convolution technique)

The spectrum unfolding technique has been extensively in use to characterize neutron energy distributions from detector pulse height spectrum measurements. A number of neutron detection systems and spectrometers such as proton recoil scintillators [82], bonner sphere systems [83], and foil activation detectors [84] have been employed in general to detect neutrons and measure their energy distributions. Most, if not all, of them deal with the inverse problem of unfolding when used to characterize neutron fields. Many studies [51, 85 - 92] have been done and methodologies have been developed and some with very high mathematical rigor to obtain a meaningful, physically acceptable solution using this indirect method. The reason for the need of so many different approaches, [48 - 49, 52 – 54, 91] is because of the energy range of spectra encountered and the limitation of any single method to work properly over the entire energy range. Although most of these approaches are promising, sometimes when compared they yield quite different solutions for the same problem and they crucially depend on the initial guess spectrum particularly for under-determined problems. An unfolding

method based on simple genetic algorithm has been reported in the past [52], but it is not freely available for general user. However, quantifying the confidence of the unfolding methodology remains a complex task.

One of the aims of the present work is to develop a general purpose unfolding technique based on the genetic algorithm and the Monte Carlo technique for both over-determined and under-determined problems considering the uncertainties in the measurement as well as in the response matrix. With this motivation, an unfolding code GAMCD (Genetic Algorithm and Monte Carlo based spectrum De-convolution method) has been developed where an attempt has been made to address the above mentioned problems. To evaluate the performance of the present code GAMCD, the results obtained using this code have been compared with a few existing standard unfolding codes like the FERDOR [60], MAXED [50] and GRAVEL [49] using data from actual experimental measurements.

In the following sections a brief description of the physics and the mathematical methodology behind the spectrum unfolding is given. This follows by the validation of the GAMCD code by unfolding simulated and experimentally measured data.

3.1 Physics of spectrum unfolding

In neutron spectrometry using proton recoil detectors one actually measures the proton recoil scintillation pulse height distributions or the saturation activity distribution for different neutron induced reactions in the case of activation foil measurements. The count rate in the detector, $C(dN/dE)$, or the activity in case of activation foils, and the neutron spectrum, $\varphi(E)$ to be unfolded from the measured detector response are related through the detector response matrix $R(E^{'},E)$. The response matrix represents the probability that a neutron of energy E deposits energy between $E^{'}$ and $(E^{'}+\Delta E)$ in the detector. All the three quantities and the error in the measurement are related through the Fredholm integral equation as

$$C + \varepsilon = \int_{E_{min}}^{E_{max}} R(E', E)\varphi(E)dE \quad (3.1)$$

here, C is the experimental measurement and $\boldsymbol{\varepsilon}$ is the inherent error in the measurement. The above equation has many solutions which are non-unique. Also in the unfolding process the difficulty is that the solutions may contain severe oscillations. These oscillations are inherent in the numerical solution to the Fredholm equation. The above integral equation (3.1) is written in the matrix form as

$$C + \varepsilon = R\varphi \quad (3.2)$$

where, C, $\varepsilon$and φ are column vectors and R is the response matrix. Physical interpretation of the above equation is that for every measurement vector C there is an associated physical vector φ that along with the response function of the detection system satisfies this mathematical relation. Obtaining an exact mathematical solution of this problem is possible but the solution thus obtained may not always have a physical significance as in many cases it might contain unwanted oscillations or negative values.

Further the equation (3.2) can be discretized using the quadrature approximation as follows

$$C_j \pm \varepsilon_j = \sum_{i=1}^{n} R_{j,i}\varphi_i \qquad for \qquad j = 1, 2, \ldots m \quad (3.3)$$

where, C_j is the recorded counts in the j-th channel, $R_{j,i}$ is the response matrix element, coupling the j-th measurement channel with the i-th incident energy channel, and φ_i is the total neutron fluence in the i-th energy interval. The group of equations resulting from the above equation generally may not have a unique solution, even when the experimental errors ε_j are neglected. Physically this is caused by the fact that part of the information contained in the response matrix is lost due the finite resolution of the measuring devices and also because the response matrix may be an ill-conditioned one.

In the unfolding problem, instead of an exact mathematical solution it is of interest to obtain an appropriate solution that represents a physically meaningful solution. The appropriate solution is any solution which satisfies the above equations to within the error ε, and has to be accepted as a physically meaningful solution. The appropriate solutions in addition to satisfying equation (3.2) must satisfy following physical requirements:

(i) the input vector $\boldsymbol{\varphi}$ contains non-negative or at most vanishing components,

(ii) the output vector $\boldsymbol{C}$ can either be vanishing or non-negative,

(iii) the response matrix $\boldsymbol{R}$ should have non-negative values and should be non-singular.

With the above requirements imposed on the feasible solutions an appropriate solution is sought which will have the highest resemblance to the actual distribution of interest.

The available experimental data can further be categorized as the multi-channel measurements leading to over-determined problem or the few-channel measurements corresponding to under-determined problems. For any unfolding problem in a mathematical form like equation (3.3), one gets $\boldsymbol{C}$ as a column vector with dimension, say, $(m \times 1)$ and the response matrix $\boldsymbol{R}$ with dimension $(m \times n)$, and $\boldsymbol{\varphi}$ the solution sought for has a dimension $(n \times 1)$. The problem is called over-determined if$(m > n)$. In over-determined problems the number of measurements is more than the number of energy bins over which the solution is required. If the condition is reversed i.e. $(m < n)$, then it is called an under-determined problem which in few methods require additional *a priori* information to carry out unfolding. Existing methods requires a good initial guess spectrum to solve the under-determined problems. In the present study genetic algorithm method has been adopted for neutron energy spectrum unfolding.

3.2 Genetic algorithm –Brief introduction

The genetic algorithm method is inspired from the natural genetics and science of natural selection; it mimics the Darwinian theory of Survival of the fittest. The basic principle of Genetic algorithm [93 - 95] deals with improving the result over some certain closed loop operations by successively incorporating the transitional results aiming to achieve a better solution. Genetic algorithm is a stochastic process and is suitable for searching a single optimized solution – global optima or minima in a complex and multi-dimensional search space, where multiple solutions are possible. The genetic algorithm search mechanism is probabilistic and is initiated through the creation of a large number of prospective solutions. The potential solutions are referred to as individuals and when encoded in binary strings or real values are called '*chromosomes*' for the name sake. All genetic algorithms contain four basic operations: *initial population generation (reproduction), selection, crossover (mating) and mutation*, where all are analogous to their namesakes in genetics. The worth of each individual within a population is numerically calculated and the parameter is referred to as 'fitness'.

To start with, a large but fixed size of population is generated randomly. The fitness of each prospective solution is calculated which is represented by the parameter fitness. Under selection, parent solutions with good fitness values are randomly selected, the parent with better fitness values stand the chance to be selected more than once therefore chances of duplicacy is there, the solutions with low fitness values are removed from the new population. For crossover, two pairs of the parents from the population are selected randomly and are crossed over (mated) at a randomly selected gene location to produce two new offspring i.e. two new solutions. Individuals with higher fitness values are preferentially selected to mate to pass on the strong genetic material compared to rest in the population.

The crossover results in exchange of high performing genetic information between two good solutions in hope to produce a pair of superior solutions. The solutions with lower fitness values also mate but they do so with a low frequency and with the passing generations due to

evolutionary weightage, they are not able to survive and are in the process killed off. In the meanwhile, the solutions with better fitness and the information carried by them is carried forward to prospective generation to result in a solution with the best match with the requirement. The flowchart for genetic algorithm process is as shown in Fig. 3.1. Genetic algorithm also mimics the process of genetic mutation by randomly modifying the solution structure. Randomly a solution is selected from the population and a randomly selected gene is modified, introducing a new gene material into the population. The mutation helps the solution to reach the global minima and not to get stuck in any local minima. All the steps can be compiled in an algorithm

```
Simple Genetic Algorithm ( )    {
Initialize Population ( );
Evaluate Population ( );
While termination criteria is not reached       {
        Select solution for next population;
        Perform crossover ( );
        Perform mutation ( );
        Evaluate population ( );
        Pass solution to next generation ( );    }    }
```

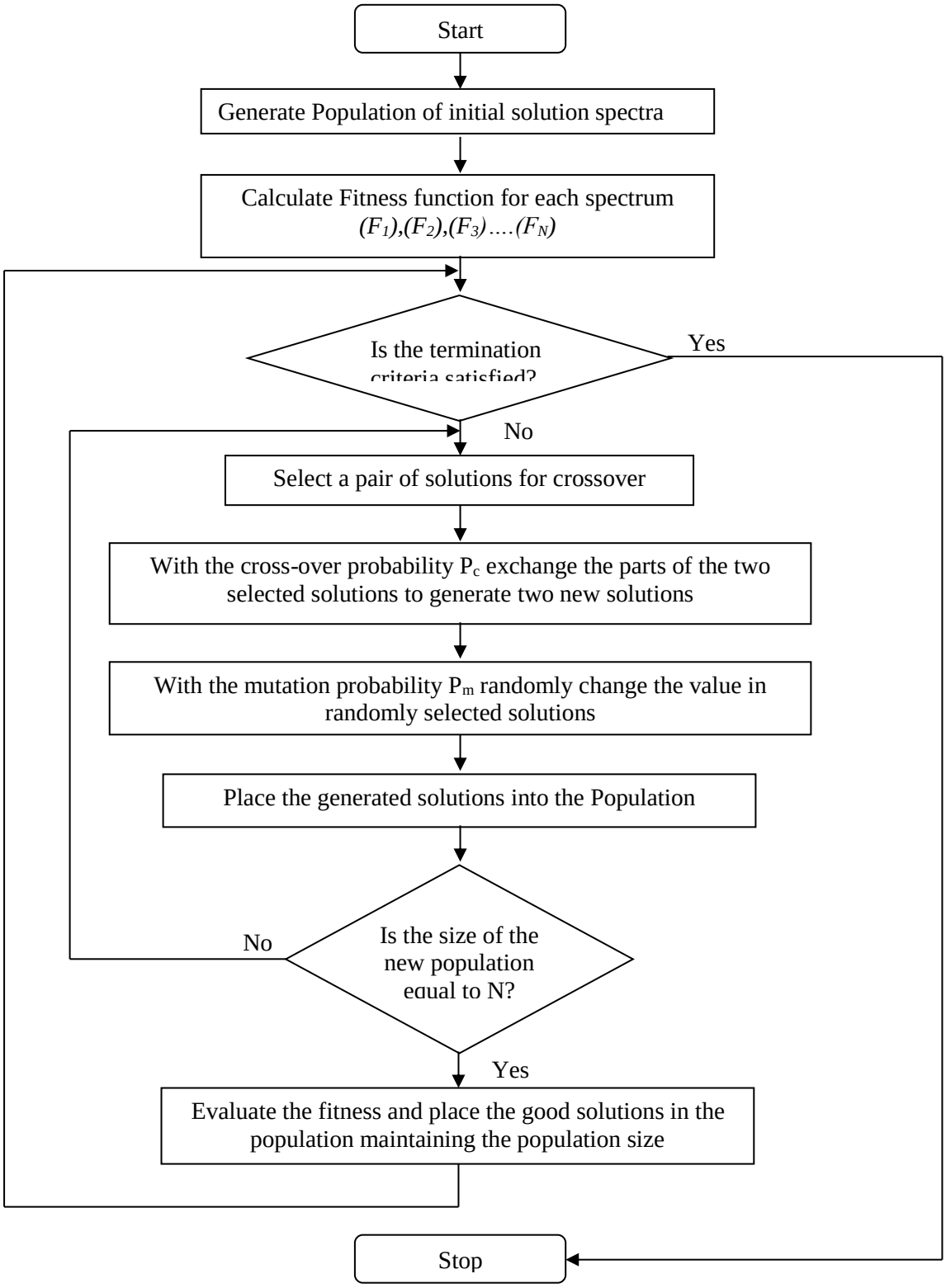

Fig. 3.1 Flowchart for genetic algorithm

All the processes when repeated through successive generations collectively lead to solution evolution. As solution evolves, better and better solutions with improved fitness values

are produced. Once the stopping criterion is achieved either in the form of fixed number of generations, desired fitness values or fixed passage of time; the iteration is stopped. The solution in the final generation is then further processed for averaging out or smoothing before passing it out as result. Genetic algorithm very efficiently and effectively explores through very large solution search spaces with very good timing. It also has the ability to avoid convergence of any solution in the local minima or maxima, instead the method searches for global minima or maxima.

3.3 Methodology for unfolding – present technique

In the present method, the unfolding problem is solved within the framework of a Monte Carlo simulation [55 – 57, 96]. Each Monte Carlo history uses the genetic algorithm to search the solution space and arrive at an appropriate solution close to the measured data (C) when folded with the detector response. As an input each history takes a set of measured data (C) and a set of the response matrix both perturbed randomly to within the specified errors associated with each data set. Here, each spectrum can be considered as a point in the n-dimensional solution space and transition of all such points towards the appropriate solution are accomplished by using the genetic algorithm till the desired results are achieved or a specified number of transitions are completed. To start with the initial guess spectrum may be denoted as x_i (i=1,2, … n) which at the end of the entire unfolding procedure is presumed to tend to φ_i.

Standard codes like FERDOR, MAXED and GRAVEL are used to compare the unfolded spectrum obtained from GAMCD. FERDOR code is based on iterative least square constrained minimization. It uses a smoothing window defined by detector resolution. MAXED is a code based on maximum entropy principle for unfolding the multi-sphere neutron spectrometer data and can also unfold multi-channel measurements. GRAVEL is a modification of the SAND–II

algorithm [92] which is based on an iterative method. Both these codes MAXED and GRAVEL require good guess spectrum to start with, whereas in GAMCD (present method) an attempt is made[96] to eliminate this requirement of supplying a guess spectra as input. To apply and evaluate the present method of spectrum unfolding, one proton recoil measurement and an activation foil measurement done in accelerator environment have been tested. Following sections discusses briefly the different steps involved in getting the final unfolded spectra.

3.3.1 Preparation of the solution set

The present method (GAMCD) starts with a uniformly distributed initial guess spectrum $x_i(i = 1,2 \dots n)$ by default and generates S prospective solutions around it randomly between some specified lower values x_i^L and some specified higher values x_i^H to generate the initial population set as

$$x_i^l = x_i^L + (x_i^H - x_i^L) * \rho_i^l \qquad for \qquad i = 1,2 \dots n \; and \; l = 1,2 \dots S \qquad (3.4)$$

where, ρ_i^j is a uniformly distributed random number in (0, 1). Here, *n* represents the number of discrete points in the spectrum and *S* represents the number of initial spectra to start with. Usually *S* is kept either 100 or a higher value, the higher value of *S* represents the vast solution space that the problem will start its search in. The present technique gets rid of the necessary requirement of supplying a "good" guess spectrum as *a priori* to start with. The method has the option to provide any guess spectrum if available; which will then lead the search to become somewhat localized and thus fast. Accordingly, the set of initial spectra are points in an *n*-dimensional space contained within an ellipsoid of revolution, the length of the axes of the parallelepiped is given by$(x_i^H - x_i^L)$. These prospective solutions are then ch ecked for their fitness. Fitness parameter is what judges how good the solution is in terms of reproducing back the detector measurements.

3.3.2 Selection

In the literature [93, 94] many ways of selection technique to be used in genetic algorithm codes is available. In the present algorithm tournament selection approach has been used. In this selection procedure two solutions are selected randomly from the population, are compared and the one with higher fitness value is retained. This results in the next level population to have solutions with better fitness values by removing the ones with lesser fitness values.

3.3.3 Crossover

The evolution of the solution through successive iterations is carried out through biological namesake procedure of mating or crossover. Two solutions from the new population, obtained after carrying out selection, are picked randomly and a point for crossing over is selected randomly. Crossover results in two new solutions for every crossover carried out which in turn increases the search points. The number of crossovers to be carried out is controlled by a parameter P_c, which is a pre-assigned probability for crossover and is usually kept between 0.5 - 0.8. The value assigned to the control parameter P_c depends on the objective function. Lower P_c value will result in slow convergence and very high value will result in unwanted distortions in the solution.

3.3.4 Iterative-mutation

In the most general way of carrying out mutation, a spectrum is selected randomly from the solution set and at a random location in the selected spectrum a small perturbation is introduced. This perturbation can be introduced at a single point, multiple points or for the entire spectrum. In the present work a method of iterative mutation is introduced where a few spectra from the solution set is picked randomly and are improved by the following iteration method

$$\varphi_j^k \left[\sum \frac{C_j^{obs} D_{ij}}{\sum_j R_{ij} \varphi_j^k} \right] \Big/ \sum D_{ij} \tag{3.5}$$

$$D_{ij} = \frac{R_{ij}}{C_i^{obs}} \cdot \frac{1}{\rho_i^2} \tag{3.6}$$

where, $\varphi_j^0 = x_j$ and the iterative solution [97] φ_j^{k+1} is obtained from the previous solution φ_j^k. Here, ρ_i is the standard deviation associated with the measurement C_i^{obs}. The number of spectra picked up is, decided by the mutation probability given by number P_m. This solution is then added to other prospective solutions. The mutation by iterative method highly speeds up the search for better solutions, and reduces the computation time.

3.3.5 Transferring population to the next generation

Subsequently carrying out crossover and mutation, the resultant solutions are checked for their fitness and are ranked accordingly. There are number of approaches to set a fitness factor. In our method the fitness of the prospective spectra is calculated as the chi square per degree of freedom between the folded data and the measured (perturbed) data. Higher difference leads to lower fitness value of the spectra. The unfit spectra are removed from the solution set to keep the population size constant. The solution set is then checked for the stopping criterion, if the stopping criterion is achieved the run is terminated, otherwise the solution set is passed on to the next generation and this is repeated till either the stopping criteria are satisfied or the process has gone through the stipulated maximum number of generations.

3.3.6 Smoothing the unfolded spectra

As mentioned earlier the fluctuation in the solution of Fredholm equation is inherent and is independent of the approach for solving it. While solving smaller sets of measurements [96]

(smaller *n*), no unwanted fluctuations in the solutions were observed. But as the number of measurements becomes large and so is the size of response matrix, the solution starts suffering from undesired fluctuations. Although the solutions when folded back gave a very good match with the measurements, these fluctuations give a false impression of very good resolution of the detector when it is not the case. Since, there is no physical reason for these fluctuations and since one is looking for an appropriate solution rather than an exact one, it is required to introduce some smoothing to the obtained solution. In the present study, different approaches for smoothing were carried out and the details are presented as following

(i) Second difference smoothing

(ii) Monte Carlo (MC) based smoothing

(iii) Second difference smoothing and Monte Carlo smoothing taken together

(iv) Gaussian smoothing

The second difference smoothing was carried out by using a smoothing function expressed by the square sum of the second differences, minimization of which introduces the smoothing condition [91]. By minimizing,

$$f = \sum_{j=2}^{n-1}\left(\varphi_{j-1} - 2\,\varphi_j + \varphi_{j+1}\right)^2 \tag{3.7}$$

where, 'f' is the square sum of the second difference, 'φ' represents the prospective spectra, 'n' is the number of energy bins of interest, we get an approximated spectra. In addition to the square sum second difference term we also introduced an entropy term to see its effect on smoothing, the two parameters were checked in different weightage combinations. Also, the first difference minimization was checked for smoothing. It was observed that the first difference and entropy terms did not contribute much to smoothing. The second difference term did result in smoothing and the unfolded spectra closely matched the standard output but still there was some small unwanted oscillations and deviations compared to the unfolded spectrum from the standard FERDOR code.

Moreover, a technique based on Monte Carlo sampling was considered, where 5000 runs were taken and the averaging over it introduces the smoothing effect. Here, the code was run to get the unfolded spectra, after each complete run the output set was stored as one solution set and this was repeated for required number of runs. A huge effort was made to minimize the run time for larger history sizes; the code was optimized accordingly. As a result the run time was largely reduced from several hours to few minutes. Using the MC based study we also calculated the variance in the obtained solution. A third study for smoothing was done where both the second difference smoothing and the Monte Carlo smoothing was carried out.

In all the three approaches studied above although the unfolded spectrum very closely matched with the FERDOR code output, it still had some oscillations and deviations. Therefore, Gaussian smoothing was carried out on the averaged output from the MC run. The deviations and the oscillations were highly reduced after the Gaussian smoothing where the values at adjacent channels of the solution vector are folded with a Gaussian function. The obtained spectra when folded back if looked carefully although the difference seems to be very small but the one from reported method shows a better match with the measurements compared to the folded spectra from the FERDOR output. The results of the above mentioned smoothing techniques are presented in the section 3.5.1.

3.4 Unfolded neutron spectra from simulated and experimental measurements

The present technique was employed to unfold one artificially constructed (simulated) data using hypothetical spectra folded with the response matrix of a proton recoil scintillation detector, presented in the following section. Subsequently, the method was applied on two sets of experimentally measured data in an accelerator environment with mixed radiation fields. The first measurement [58] was proton recoil data of emitted neutrons from 144 MeV carbon ions interacting with a natural thick Ag target, presented in section 3.4.2. The second

experimental measurement [57] was with activation foil sets and the measured activities of the respective foils were unfolded to obtain the neutron yield distribution from 20 MeV proton on thick ^{9}Be target, discussed in section 3.4.3.

3.4.1 Unfolding simulated neutron spectra - A Maxwellian distribution

An artificial Maxwellian spectrum [96] was simulated to be tested on the code. The spectrum closely represents the type of neutron spectra generally prevalent in the accelerator environment and is shown in Fig. 3.2 (black boxes). The spectrum has a high rise at the lower energy side and a continuous falling trend resembling a Maxwellian distribution. This was folded with the proton recoil response matrix to obtain the simulated measurement data, which was then used as input along with the response matrix for the spectrum unfolding. The unfolded spectra using GAMCD, FERDOR, MAXED and GRAVEL are shown in Fig. 3.2. Except the first point on the lower energy side, the GAMCD almost overlaps with the actual spectrum whereas for the results from FERDOR, MAXED and GRAVEL there are significant mismatches. For the FERDOR result, the peak is shifted and also the hump appearing at the higher energy side suggesting a very hard spectra, which is misleading as to be an additional peak when actually it is not there. The results from GRAVEL show a closer match particularly in the high energy region. The results from MAXED under predict in the energy region till 20 MeV also shows some fluctuations in the low energy region while reproducing well over the high energy part. It was observed that the results from MAXED and GRAVEL can be significantly improved if the initial guess spectrum was made close to the original spectrum. All these unfolded spectra were folded back with the response matrix to find out how well the unfolded spectra can reproduce the input data used for unfolding. The folded back spectra from respective methods are presented in Fig. 3.3. The matching of the folded data from GAMCD with the simulated data is clearly evident. It should be noted that the present GA based

unfolding method works efficiently for the simulated spectra; even when the initial solutions are generated from a uniform distribution.

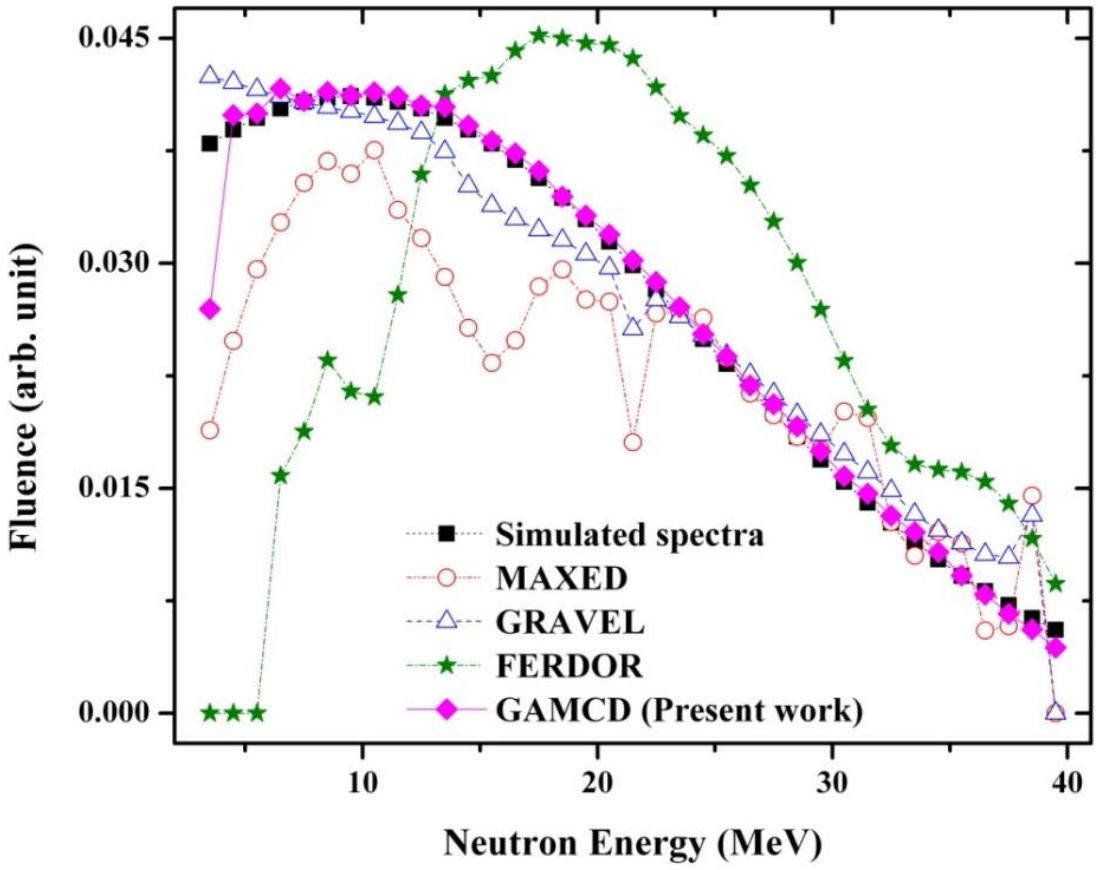

Fig. 3.2 Unfolded spectra from GAMCD (present work), MAXED, GRAVEL and FERDOR compared with the simulated actual spectrum (solid squares) shaped as Maxwellian.

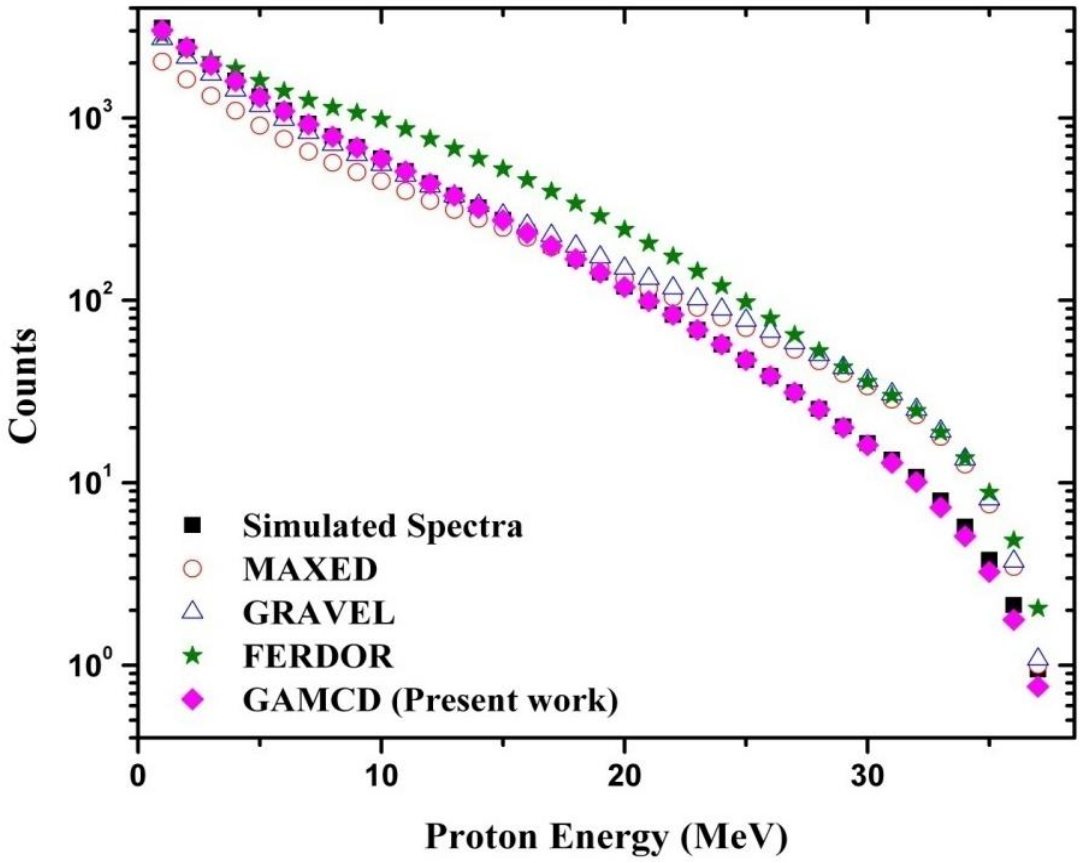

Fig. 3.3 Folded back data using the response matrix (proton recoil) and the unfolded spectra (as shown in Fig. 3.2) obtained from MAXED, GRAVEL, FERDOR and GAMCD.

Though the performance of the standard codes MAXED and GRAVEL depend on the shape of the guess spectrum provided. This is because for the present GA based method the initial starting points are many different spectra (100 for each history for 40 histories) generated with high random fluctuations around a uniform distribution. The present method, in fact, uses the advantage of a multi-start global optimization technique. The code was further tested with actual proton recoil measurements carried out using organic liquid scintillator detectors and activation measurements using set of activation foils presented in the next section.

3.4.2 Determination of neutron energy spectrum by unfolding Proton Recoil for $^{12}C^{5+}$ + ^{nat}Ag nuclear reaction

Detection of fast neutrons in scintillation detectors [98, 99] is when the incident neutron on the detector undergoes scattering imparts part of its energy and gives rise to a recoil proton. The energy distribution of the recoil proton is approximately rectangular ranging from zero to full neutron energy that can be transferred during the scattering. Since, the recoil protons have smaller ranges compared to the detector dimension all its energy is deposited within the scintillator material. Usually, the neutron entering scintillation detection material has some finite probability of elastic scattering single or multiple time with hydrogen or carbon there on transferring its energy partially $E_p \leq E_n$ in its p^{th} collision. The neutron may finally leave the detection material with remaining energy $E_n - \sum_p E_p$. The scintillation produced will be finally converted to a detectable pulse. This measured pulse height will also have an approximate rectangular distribution. The physical process that leads to detection of a neutron in a scintillation detector has complications added by different factors, to the coupling between the neutron energy E_n and the resulting pulse height L. To account some, the light output from most organic scintillators does not increase linearly as the deposited energy increases. This nonlinear behavior distorts the rectangular recoil proton energy distributions. Similarly, the edge effect when the detector size is small or the neutron energy is high; the range of the recoil proton will be more compared to the detector dimension which may result in escape of the protons. This will affect the response function which will shift event from high pulse height to low pulse height. In addition to this, the response function of organic scintillation detector gets distorted by multiple scattering from hydrogen and carbon.

To obtain the energy distribution from proton recoil measurements using the organic liquid scintillator detectors, the measured pulse height and the response function of the mono-energetic neutrons incident on the detector should go as input. However, the overall response function for the scintillator detectors is slightly complex and so it should be known with a good accuracy since the error contained in it will be propagated through the de-convolution, into the

unfolded neutron energy distribution. An experimentally measured proton recoil distribution is unfolded and is presented here. The energy distribution of neutrons emitted from the nuclear reaction of 144 MeV carbon ions with a thick silver target, at the extreme forward angle (about 0°) with respect to the incident beam of $^{12}C^{5+}$ ions, were measured using 5" × 5" proton recoil scintillation detector BC 501A [58]. A set of 37 measurements and a response matrix of 37 energy points (3.5 MeV- 39.5 MeV) with 1.0 MeV bin size were used for the unfolding. The unfolded spectrum from the GAMCD (present method) is shown in the Fig. 3.4 and is compared with the results from the codes FERDOR, MAXED and GRAVEL.

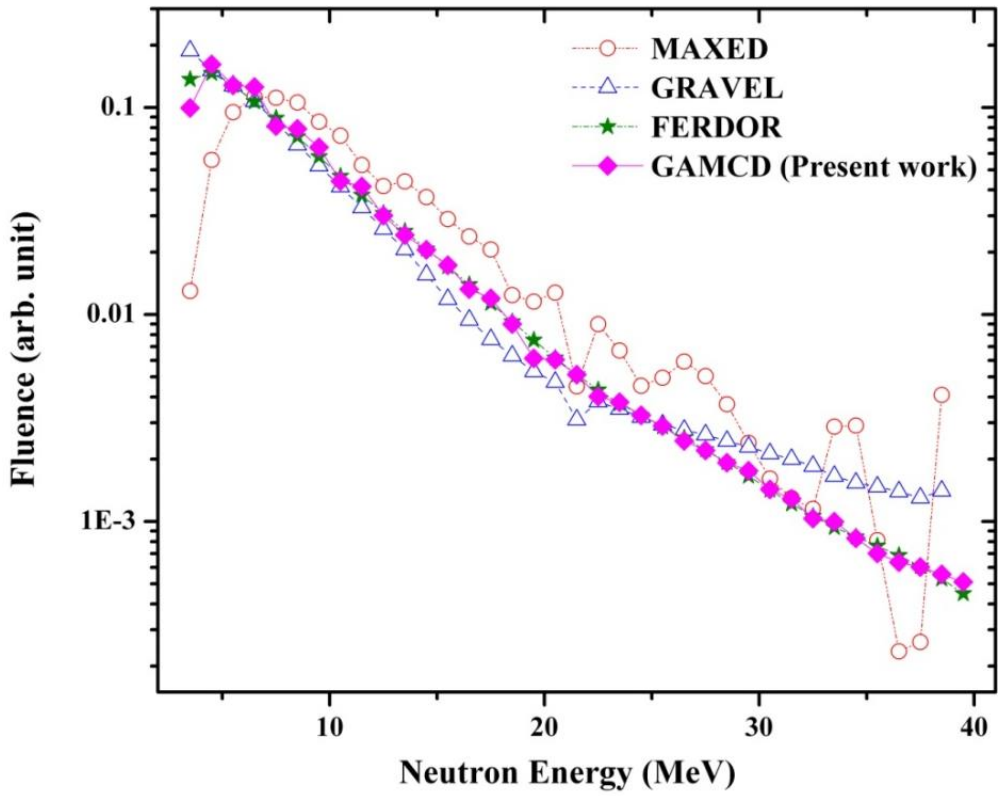

Fig. 3.4 Unfolded results from measured proton recoil data from a $^{12}C^{5+}$ + ^{nat}Ag at 144 MeV reaction using MAXED, GRAVEL, FERDOR and GAMCD (present work).

The unfolded spectra using GAMCD can be seen to match very well with the FERDOR results. The results of MAXED show some fluctuations where as for the GRAVEL results such fluctuations are absent but have an unrealistic rising trend near the high energy end. The folded back spectra with response matrix shows (Fig. 3.5) that the output from GAMCD matches better with the measurements compared to FERDOR and the other two codes.

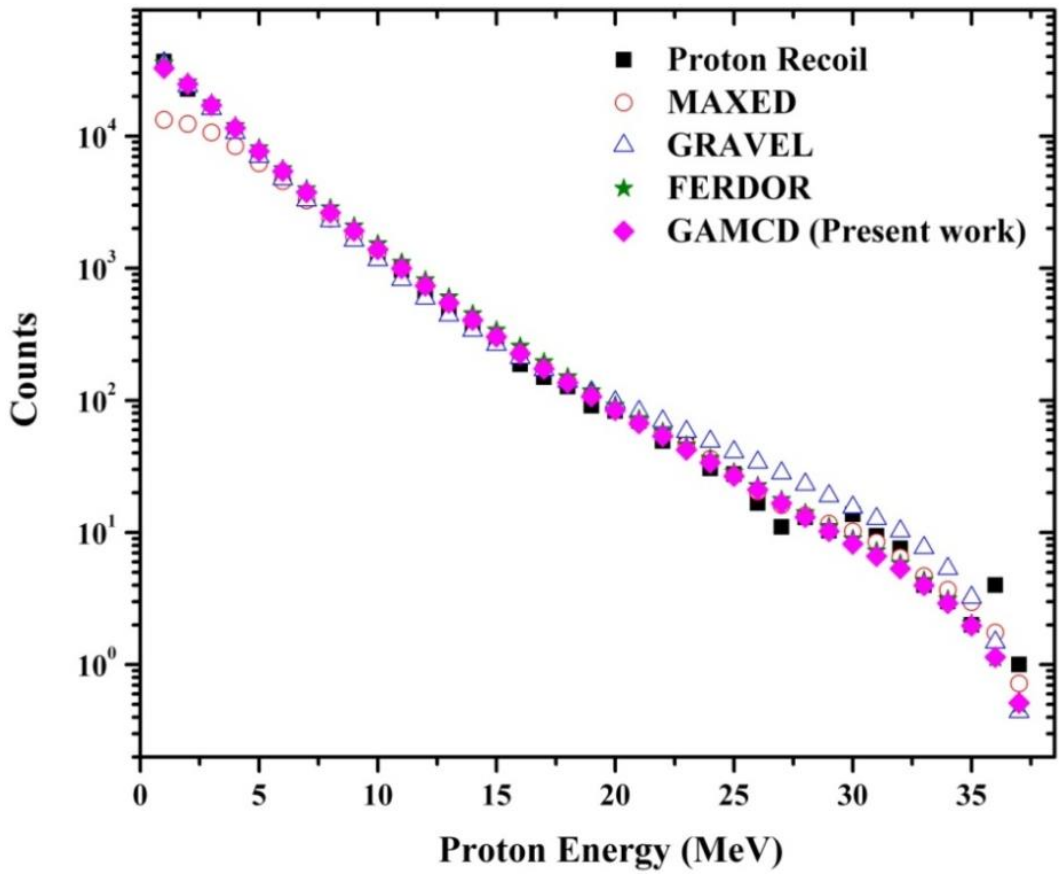

Fig. 3.5 Folded back data for $^{12}C^{5+}$ + ^{nat}Ag at 144 MeV unfolded spectra (as shown in Fig. 3.4) obtained from MAXED, GRAVEL, FERDOR and GAMCD (present work).

In order to study the convergence of the present method, the differences between the folded data and the measured data are plotted in Fig. 3.6 as chi-square per degree of freedom for each evolved best spectrum over 500 generations. It can be seen in Fig. 3.6 there is an initial, rapid and then a relatively slower decrease of the chi-square value indicating an improvement of the generated solutions over successive generations. The closeness in fit of spectrum at any stage of its evolution is an inverse function of this chi-square value. The run time for the code was of the order of a few minutes, which reduces with the reduction of the population size but then the number of generation increases to obtain the same result.

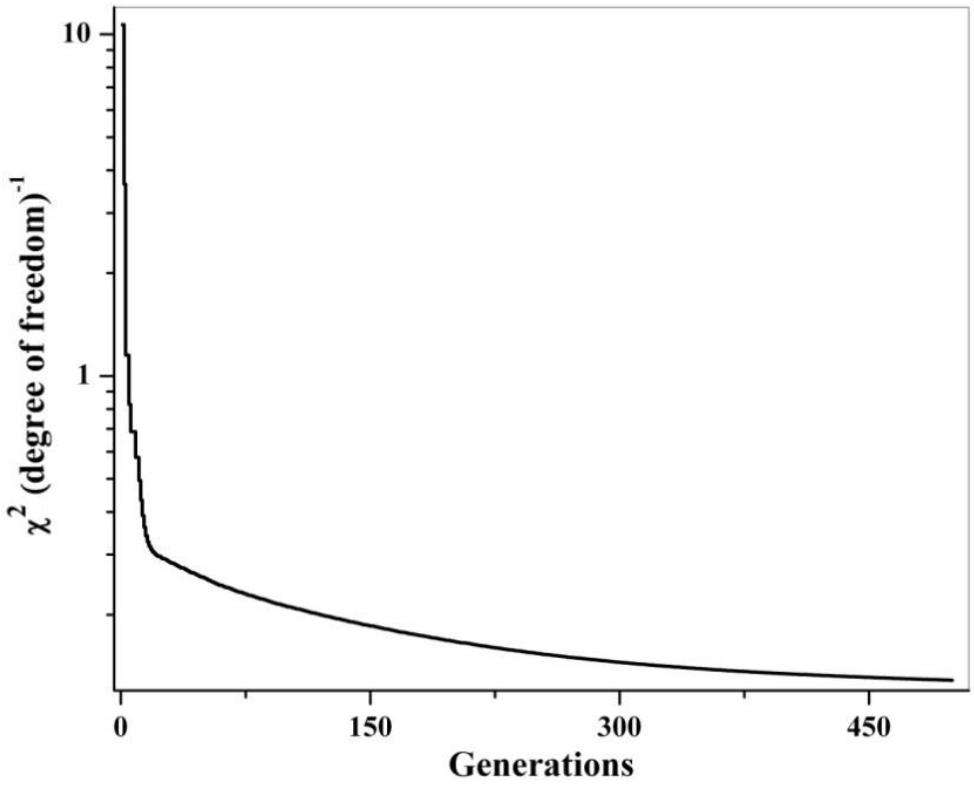

Fig. 3.6 Difference between the folded back spectrum and the measured proton recoil data in GAMCD (present work) plotted as chi square per degree of freedom over 500 generation for the spectrum shown in Fig. 3.4. Decreasing chi-square indicates higher fitness.

The unfolding problem of proton recoil data of neutrons emitted from the $^{12}C^{5+}$ + ^{nat}Ag at 144 MeV nuclear reaction was the reduced to sets of under-determined problems where the numbers of measurements were made less than the energy bin information of interest (i.e., $m<n$). This was done by randomly removing a few of the measured data and by reducing the response matrix accordingly. Unfolding an under-determined data set will be presented in the section 3.5 where the data was unfolded using the GAMCD (present method), MAXED and GRAVEL.

3.4.3 Determination of neutron energy spectrum using activation foil measurement for ^{1}H + ^{9}Be at 20 MeV

The neutron detection method discussed above produces prompt output pulses by indirect interaction in the detection material for each detected neutrons. Neutron detection and

measurement can also be done indirectly by means of radioactivity by measuring the induced activity in the detection material produced by neutron interaction. Such detector materials can be exposed in the flux of the unknown neutron fields for a known time. It can be later removed and counted for the induced radioactivity using a conventional HPGe detector. The measured radiation then can be used to extract the information about the flux and energy distribution of the original neutron field. The detection materials used are called activation detectors [57, 100, 101] and have been widely used in nuclear physics and radiation protection applications. The activation detectors have a threshold for the nuclear reaction to start thus they are also called threshold detectors. Various activation foils with different threshold energies should be used to cover over large range of energy while carrying out neutron spectrum unfolding. The dominant nuclear reactions are *(n, n'), (n, α), (n, p), (n, 2n), (n, γ)* etc. The activation foils got popularity in measurement of neutron flux distribution in nuclear reactors for their small dimensions and the ease of placing inside the core for flux measurement. Soon the advantages of its use in accelerator facilities were recognized.

Mathematically, the neutron spectrometry with activation detectors is to measure the reaction rates for suitable foils when exposed to some unknown neutron flux [67], the expression is as follows

$$A = \int \sigma(E)\varphi(E)dE \tag{3.8}$$

where, A is the reaction rate, σ the neutron cross-section and $\varphi(E)$ the neutron flux density. For an exposure time of t_0 when the foil is removed from the field, the activity A_0 build in the foil at time of removal is given as

$$A_0 = A_\infty(1 - e^{-\lambda t_0}) \tag{3.9}$$

where, A_∞ is the saturation activity and λ is the decay rate. The foils once removed from the field are counted in a counting system. Since, the activity continuously decays it should be

properly accounted for time involved in all stages, from irradiation to removal, cooling till final counting. When the counting is done for a period t_1 to t_2, the number of counts is given as

$$N_\lambda = I_\gamma \, \epsilon \frac{A_0}{\lambda} e^{\lambda t_0}\left(e^{-\lambda t_1} - e^{-\lambda t_2}\right) + B \tag{3.10}$$

where, N_λ is the counts under the full energy peak for the gamma characterizing the reaction, I_γ is the gamma yield, ϵ is the efficiency of the detector at the emitted gamma energy, B is the background counts expected in $(t_2 - t_1)$. Simplifying, the equation (3.9) and (3.10) gives following relation, from where substituting all the unknowns, saturation activity can be calculated.

$$A_\infty = \frac{\lambda(N_\lambda - B)}{\epsilon(1-e^{-\lambda t_0})e^{\lambda t_0}\left(e^{-\lambda t_1} - e^{-\lambda t_2}\right)} \tag{3.11}$$

Finally, using the relation for saturation activity from prolonged irradiation as function of flux and reaction cross-section as presented in equation (3.12), the unknown flux distribution can be deduced using some suitable unfolding code.

$$A_\infty = \varphi(E) N \theta \sigma\,(E) \tag{3.12}$$

where, N is the number of nuclei present in the threshold detector, θ is the isotopic abundance of that nuclei, $\sigma(E)$ is the reaction cross-section for the induced reaction at neutron energy E, adopted from the ENDF/B-VII.I library [102, 103]. The detail of an activation foil measurement and its unfolding is presented in chapter 4.

Since, the neutrons in medium and high-energy particle accelerators contribute a significant dose [104] and furthermore the radiation weighting factors for neutrons vary a lot with neutron energy [28], the actual energy distribution of the neutrons is of utmost importance and becomes significant for radiological safety purposes [2]. In such radiation environments where the field can often be pulsed and can have interference from radiofrequency field, passive detectors such as threshold foils [84, 101], TLDs [105, 106], solid polymeric track detectors [107, 108] etc., are found to be suitable for neutron measurements. For spectrum

measurements using passive methods, the most commonly used methods are Bonner sphere systems [109 - 111], threshold foils as activation detectors [84, 101, 112 - 113].

The proton-induced nuclear reaction cross-section data are very important [114] for the production of medical radioisotopes, radiation damage studies and study of astrophysical reaction mechanism and sustainable nuclear energy technology [115] using cyclotrons. Nuclear data evaluation is generally carried out on the basis of experimental data and theoretical model calculations. Nuclear interaction and emission cross sections are, in principle, obtained from experimental measurements, though substantially augmented by model based predictions, especially to fill up the gaps left in the sparse measurements. Neutron activation technique is also one of the widely used methods for neutron cross section measurements.

The essential motivation behind the present study is for the fact that cross section measurements, particularly energy differential, remain an active and front line area of science, technology and medical therapy mainly because of the sparseness in and spread among different measurements is still found to be unacceptably large. Also, the measured values for the chosen reaction are rare as can be verified with the EXFOR database [103].

The threshold activation foil measurements were carried out and the data was unfolded to extract the underlying neutron distribution. The experimental measurement was carried out at 6-m irradiation facility of BARC-TIFR Pelletron-Linac facility India. The experimental arrangements and other particulars are given in details elsewhere [57]. The threshold foils were irradiated with the neutrons emitted from the nuclear reaction of 20 MeV protons on thick ^{9}Be target. Two sets of sixteen threshold foils were mounted at $0°$and $90°$ with respect to the beam direction. The ^{9}Be target was irradiated with ~ 500 nA beam current for approximately 14 hours. The beam current was not constant throughout the irradiation thus the total number of projectiles seen by the target was determined from the total charge measured by the current integrator.

At the end of the irradiation the foils according to their half-lives were counted for its neutron induced gamma ray activity using a high purity germanium (HPGe) detector. The HPGe detector was well shielded to minimize the background. The detector was calibrated for energy and full photo peak efficiency using a ^{152}Eu source covering almost the entire range from 100 keV to about 1.4 MeV as plotted in Fig. 3.7. The induced activity in each foil irradiated for duration of T_{irr}, (same for all the foils) counted for a period of T_{count} (different for different foils depending on cps) after a cooling or decay of T_{decay} (different for different foils) was determined using the following expression

$$A_i = \frac{\lambda_i N_\gamma}{I_\gamma \varepsilon \left(1-e^{-\lambda T_{irr}}\right)\left(e^{-\lambda T_{decay}}\right)\left(1-e^{-\lambda T_{count}}\right)} \tag{3.13}$$

where, A_i is the induced activity, λ_i is the decay constant of the formed radionuclide, N_γ is the counts under the full energy peak for the gamma characterizing the reaction, I_γ is the gamma yield,

ε is the efficiency of the detector at the emitted gamma energy.

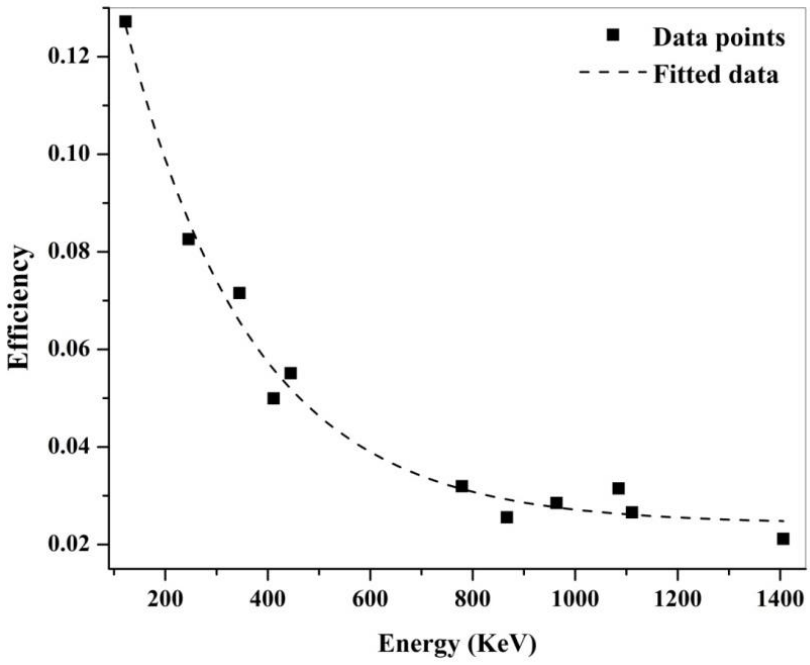

Fig. 3.7 The detector efficiency (η) measured at different energies using ^{152}Eu source. The fitted curve (dash) to the measured data (solid square) was used to determine the efficiency at intermediate energies.

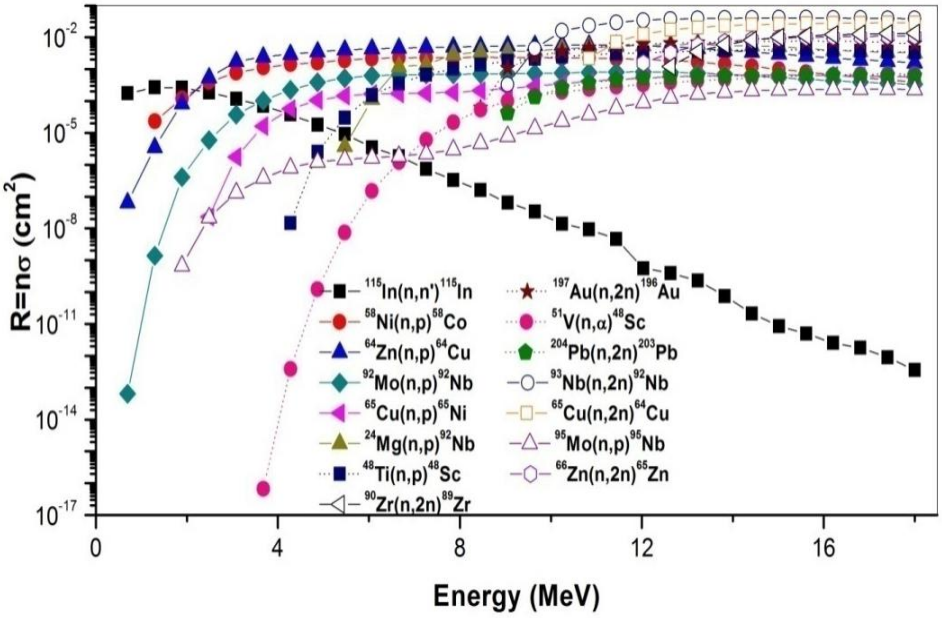

Fig. 3.8 The response matrix constructed for the 15 reactions used to generate the neutron spectra.

The response matrix was prepared by multiplying the total number of atoms in the sample (corrected for the isotopic abundance) with the cross-section values taken from the ENDF/B-VII.I library [103]. A total of 31 energy bins with constant bin-width covering the entire energy range of interest was prepared and shown in Fig. 3.8. This response matrix and the activity values served as input to the unfolding methods as explained below.

3.4.3.1 Procedure for unfolding

Generation of a discrete neutron spectrum at many energy bins from a few measurement points involves numerical solution of Fredholm integral equation of the first kind as discussed previously. The problem is essentially ill-conditioned because there can be many solutions around the exact one satisfying the equation. As discussed earlier several approaches for handling this unfolding problem have been developed by different investigators. In this work,

the unfolding method based on Genetic Algorithm and Monte Carlo approaches (GAMCD) was used to generate the neutron spectrum and the results were compared with those obtained from other commonly used codes, viz. MAXED and GRAVEL. However, the details of this code for analysing activation foil data have been reported [56, 57].

Using the experimentally measured quantityN_γ, the estimation of activity (A_i) induced in the threshold detectors to the impinging neutrons can be put into the well-known mathematical form

$$A_i = \int_{E_{th}}^{E_{max}} \theta_i n_i \sigma_i(E)\, \varphi(E)\, dE \tag{3.14}$$

where, n_i is the number of the isotope i_{th} present in the foil, $\sigma_i(E)$is the reaction cross-section for the induced reaction at neutron energy E adopted from the ENDF/B-VII.I library. $\varphi(E)$ is the neutron flux at energy E, E_{th} is the threshold energy for the reaction to occur and E_{max} is the maximum neutron energy emitted in the reaction. The above equation (3.14), is generally put in the form given below

$$A_i = \int_{E_{th}}^{E_{max}} R_i(E)\, \varphi(E)\, dE \tag{3.15}$$

where, $R_i(E) = n_i \sigma_i(E)$ is the response function for the i_{th} threshold detector. The solution to this integral to estimate $\varphi(E)$ is obtained by discretizing this equation using the quadrature method as given below.

$$A_i = \sum_{j=1}^{m} R_{ij}(E) \varphi_j(E) \tag{3.16}$$

where, i = 1, 2, 3,..., n is the number of detectors used or the number of measurements, j = 1, 2, 3,..., m and m is the number of energy groups, which is taken as 31 in the present work. Once discretised, all the parameters are in the form of matrices and the problem is reduced to solving a set of simultaneous linear equations, under-determined in nature because of n < m. In such unfolding problems one needs to select a physically acceptable solution out of infinite solutions available to the above set of equation. However, in these types of measurements, the

uncertainties are usually introduced from several sources, complicating the estimation further, and those can be grouped into three major categories:

(i) material characteristics (thickness, weight, purity),

(ii) irradiation process (neutron absorption, scattering, energy dependence of the cross section, fluctuations in fluence rate, contributions from neutrons below threshold energy), and

(iii) foil counting process (counting geometry, detection efficiency, gamma-ray self-absorption, coincidence effects, decay during irradiation up to final counting) [116].

The possible sources of error mentioned here are listed in Table 3.1, along with the estimated magnitude. Some of the parameters mentioned in Table 3.1, viz. reaction decay half-life, reaction gamma decay branching ratio and standard reaction cross sections were adopted from literature and the maximum errors mentioned on the literatures were used for the calculations to have a conservative error estimation of the activity.

Table 3.1 Possible sources of uncertainty in the activity estimation.

Source of Uncertainty	**Magnitude (%)**
Reaction decay half life	4.2
Target mass/Reaction sample mass	1.0
Standard reaction cross section	4.2
Neutron irradiation flux	1.0
Reaction Gamma decay branching ratio	0.1
Gamma ray detection efficiency	8.0

Irradiation time	0.1
Decay time	3.0
Counting time	1.0
Standard sample counting statistics	5.0
Total Uncertainty	**11.7**

Among 30 possible reactions 15 reactions covering the entire energy range and the respective response function of interest were used to carry out the unfolding. The selected reactions along with the details such as half-life, effective threshold energies, gamma energies, isotopic abundance etc. of the target nuclei is listed in Table 3.2. The induced activities for the chosen detectors at two angles of measurements, i.e. 0° and 90° are presented in Table 3.3.

Table 3.2 Important characteristics of the neutron induced nuclear reactions of the activation foils used in this study. These are the reactions selected for unfolding procedures.

Reaction	$T_{1/2}$ (h)	E_{th} (MeV)	E_γ(MeV)	I_γ(%)	ε(%)	θ (%)
$^{115}In(n,n')^{115}In$	4.49E+00	0.50	0.336	45.8	6.7	95.71
$^{58}Ni(n,p)^{58}Co$	1.70E+03	2.50	0.81	99.5	3	68.08
$^{64}Zn(n,p)^{64}Cu$	1.27E+01	2.53	0.511	35.2	4.5	48.63
$^{92}Mo(n,p)^{92}Nb$	2.44E+02	3.55	0.934	100.0	2.8	14.85
$^{65}Cu(n,p)^{65}Ni$	2.52E+00	4.50	1.115	15.4	2.5	30.83
$^{24}Mg(n,p)^{24}Na$	1.50E+01	6.50	1.368	100.0	2.5	78.99
$^{48}Ti(n,p)^{48}Sc$	4.37E+01	7.00	0.983	100.0	2.7	73.72
$^{197}Au(n,2n)^{196}Au$	1.48E+02	9.00	0.356	87.0	6.4	100.00
$^{51}V(n,\alpha)^{48}Sc$	4.37E+01	9.00	0.983	100.0	2.7	99.75
$^{204}Pb(n,2n)^{203}Pb$	1.12E+00	9.50	0.279	80.9	7.8	1.40
$^{93}Nb(n,2n)^{92}Nb$	2.44E+02	9.70	0.934	100.0	2.8	100.00
$^{65}Cu(n,2n)^{64}Cu$	1.27E+01	11.0	1.346	0.48	2.5	30.83
$^{95}Mo(n,p)^{95}Nb$	8.40E+02	11.0	0.765	99.8	3.2	15.92
$^{66}Zn(n,2n)^{65}Zn$	5.85E+02	12.0	1.115	50.0	2.6	27.90
$^{90}Zr(n,2n)^{89}Zr$	7.84E+01	12.7	0.909	99	2.8	51.54

Table 3.3 Measured activities at both the angles, i.e. 0° and 90° with respect to the beam direction.

Reaction	A_0 Saturation activity in Bq (0°)	A_0 Saturation activity in Bq (90°)
$^{115}In(n,n')^{115}In$	2.08E+04	1.90E+03
$^{58}Ni(n,p)^{58}Co$	5.68E+04	9.89E+03
$^{64}Zn(n,p)^{64}Cu$	1.23E+05	1.52E+04

$^{92}Mo(n,p)^{92}Nb$	9.00E+03	1.33E+03
$^{65}Cu(n,p)^{65}Ni$	8.91E+03	9.45E+02
$^{24}Mg(n,p)^{24}Na$	5.90E+04	5.74E+03
$^{48}Ti(n,p)^{48}Sc$	3.29E+04	4.93E+03
$^{197}Au(n,2n)^{196}Au$	5.94E+04	1.05E+04
$^{51}V(n,\alpha)^{48}Sc$	3.16E+03	4.53E+02
$^{204}Pb(n,2n)^{203}Pb$	4.74E+03	5.56E+02
$^{93}Nb(n,2n)^{92}Nb$	2.60E+05	-
$^{65}Cu(n,2n)^{64}Cu$	2.16E+05	2.98E+04
$^{95}Mo(n,p)^{95}Nb$	1.84E+03	1.94E+02
$^{66}Zn(n,2n)^{65}Zn$	9.39E+04	9.39E+03
$^{90}Zr(n,2n)^{89}Zr$	8.15E+04	6.43E+03

The measured activities and the response matrix prepared using the ENDF/B-VII.I library was fed as input to the three unfolding codes MAXED, GRAVEL and GAMCD. The shapes and peak positions of the spectra (measured at both angles) unfolded using proper guess spectra were found to be similar with the spectra unfolded without using proper guess spectra.

Use of such uniformly distributed initial guess spectrum resulted in unphysical estimation of the solution in the case of MAXED and GRAVEL. It is important to note that when the *a priori* information for a neutron energy distribution is not available, present method can be used reliably to unfold the spectrum without using any proper guess spectrum. The GAMCD code was found to be working well without any proper guess-spectrum [56, 57] as shown in Fig. 3.9. Where, the term 'no guess' indicates a guess spectrum as a uniformly distributed spectrum over the energy range of interest with no additional a priori information.

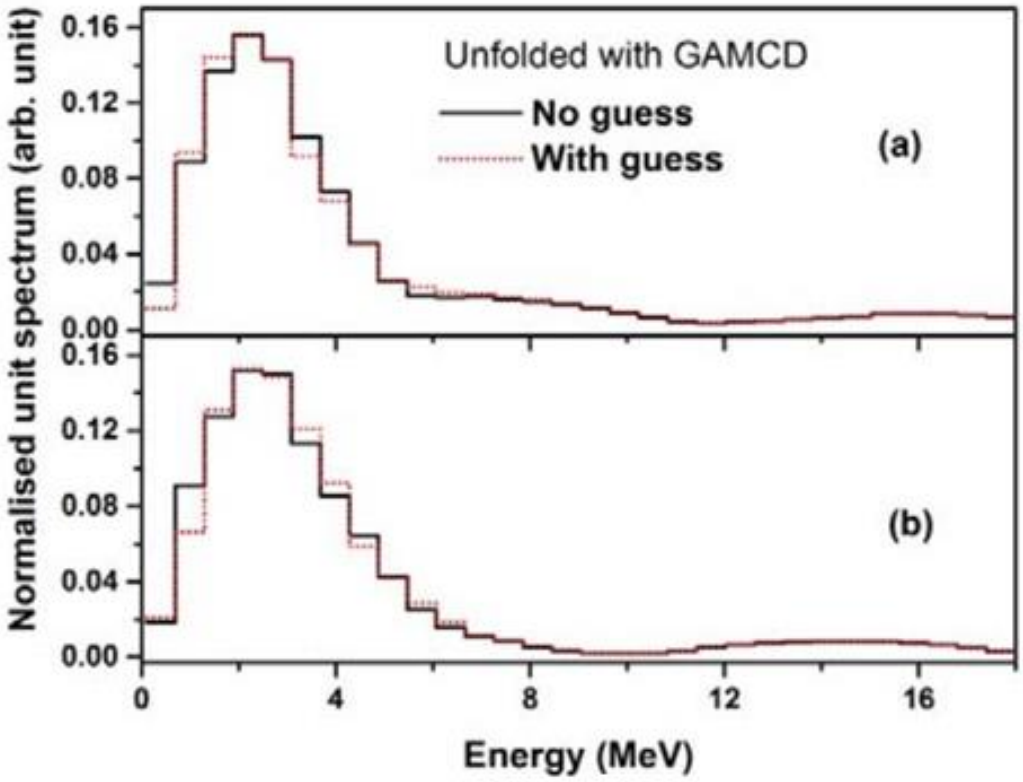

Fig. 3.9 Neutron energy distribution for measurements at (a) 0°, (b) 90° with respect to the incident beam direction, unfolded using GAMCD (with and without guess spectrum).

However, as discussed earlier a provision is made available in the code to supply any proper a priori guess spectrum, if available, which can result in guided search over all the possible solution space thereby reducing the search time as discussed earlier. The comparison of the neutron energy distributions for the reaction of 20 MeV proton with Be, measured at 0º and 90º with respect to the incident beam and unfolded using the three different codes are presented in Fig. 3.10. The unfolding with GAMCD was carried out without the use of any proper guess spectra while for MAXED and GRAVEL a Maxwellian guess spectrum approximately resembling the solution spectrum (with Temperature = 1.02 MeV and slope = −0.01) was supplied as a priori information.

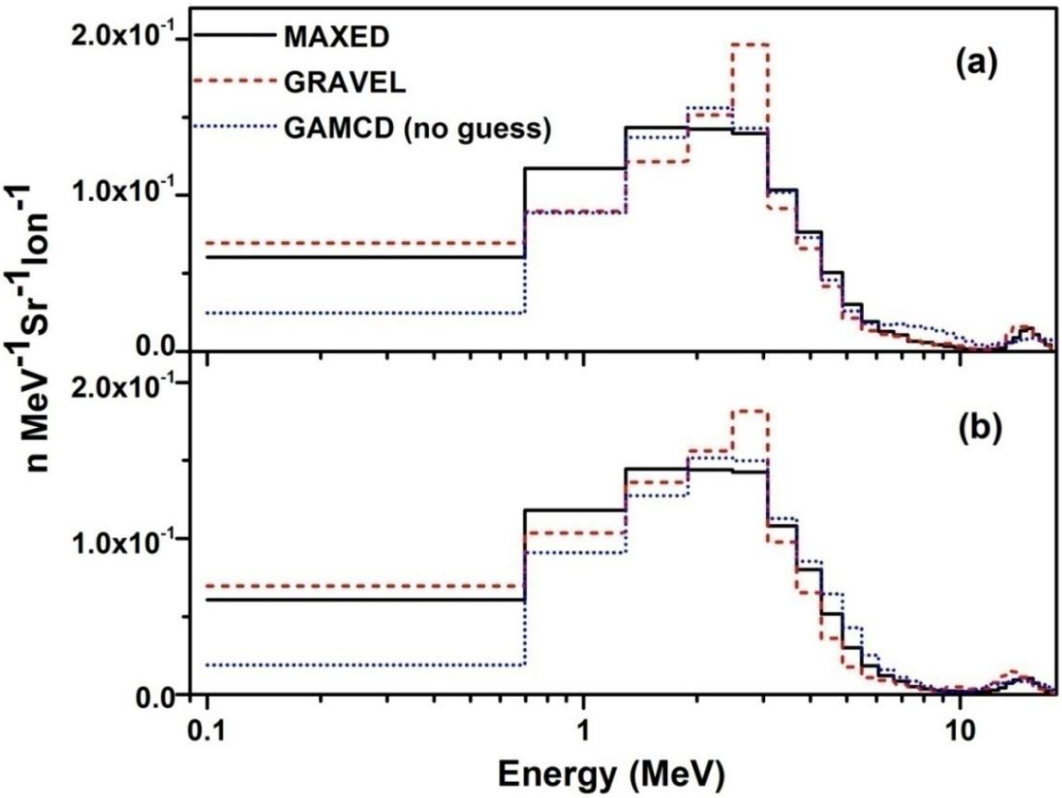

Fig. 3.10 Neutron energy distribution for the reaction of 20 MeV proton on thick Be, measured at (a) 0°, (b) 90° with respect to the incident beam. The spectra were unfolded using MAXED, GRAVEL and GAMCD codes. The unfolding with GAMCD was carried out without the use of any proper guess spectra.

The figure of merit (FOM) for each code was calculated using the equation (3.17) as given below and the values are given in Table 3.4. FOM = 1 gives the best agreement and less than 1 are increasingly worse with smaller values.

$$FOM = \frac{1}{\left(1+\sum_i \left|\left[\frac{A_i - A_i^c}{A_i}\right]\right|\right)} \tag{3.17}$$

where, A_i is the measured activity and A_i^c is the calculated activity after folding back the unfolded spectrum.

Table 3.4 Values of figure of merit (FOM) for the 3 different codes used in this study.

Location	MAXED	GRAVEL	GAMCD

0°	0.089	0.087	0.260
90°	0.097	0.093	0.303

The neutrons emitted from the interaction of 20 MeV protons with a thick Be target were found to have a peak in the energy distribution at about 2–3 MeV along with a small hump at about 15 MeV. The peak at 2–3 MeV is contributed by the three body breakup process of the nuclear reaction mechanism.

The hump at around 15 MeV might be a contribution from the ^{9}Be (p, n)^{9}B reaction to the ground state (Q = −1.85 MeV) and partially to highly excited states (2.3 MeV, 1.4 MeV). However, contribution from such reaction is anticipated to be forward peaked [117] and the fact of its presence in both 0º and 90º having almost equal magnitude makes it look like an artefact generated by the unfolding process. The results of GAMCD shows a broad hump from about 6 MeV to about 10 MeV in the forward direction (0º) while such hump is absent in the spectrum obtained at 90º suggesting a contribution from the pre-equilibrium process in the ^{9}Be (p, n)^{9}B nuclear reaction mechanism because of its presence in the forward direction only. The spectra are found to agree fairly well with each other except for some variation in the peak heights. This is probably due to different algorithms used by these unfolding codes. Fig.3.11 shows the folded back data for the unfolded distributions from the three methods and was compared with the actual detector measurements. It can be seen that the folded back activity values obtained using GAMCD code (without guess) almost overlaps with the actual measurements compared to those obtained from the MAXED and the GRAVEL codes. The slight difference in the folded back values can be attributed to the fact that a complete convergence could not be possibly attained even though a complete convergence may not lead to a physically acceptable result.

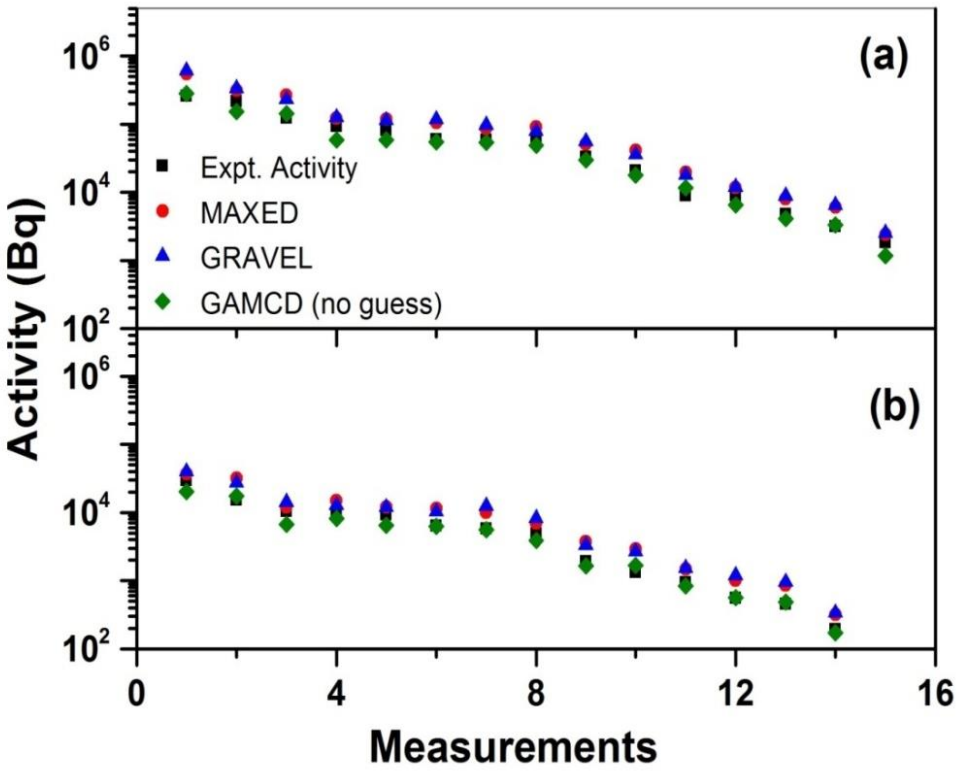

Fig. 3.11 Folded back activities obtained from the three unfolding methods and compared with the actual activity measurements for the threshold detectors irradiated at (a) 0° and (b) 90°.

Therefore the convergence criterion is required to be set carefully. Also the approximations used in the unfolding procedures might lead to the slight variation from the actual measurements.In Fig. 3.12, the measured data by Uwamino and Ohkubo [117] are compared with the present data. For the sake of comparison both sets of data were normalized to unit area under the spectra. The agreement is fairly good. The data by Uwamino and Ohkubo were only given above 3 MeV and hence comparison at lower energy was not possible. Their data show a comparatively small contribution at low energies with a larger contribution at high energies. The difference in the shapes stems from the difference in the target used. In the present case the target is much thicker (4 mm compared to 1 mm used by Uwamino and Ohkubo) leading to a comparatively higher low energy contribution and smaller high energy contribution because of the degradation in the target.

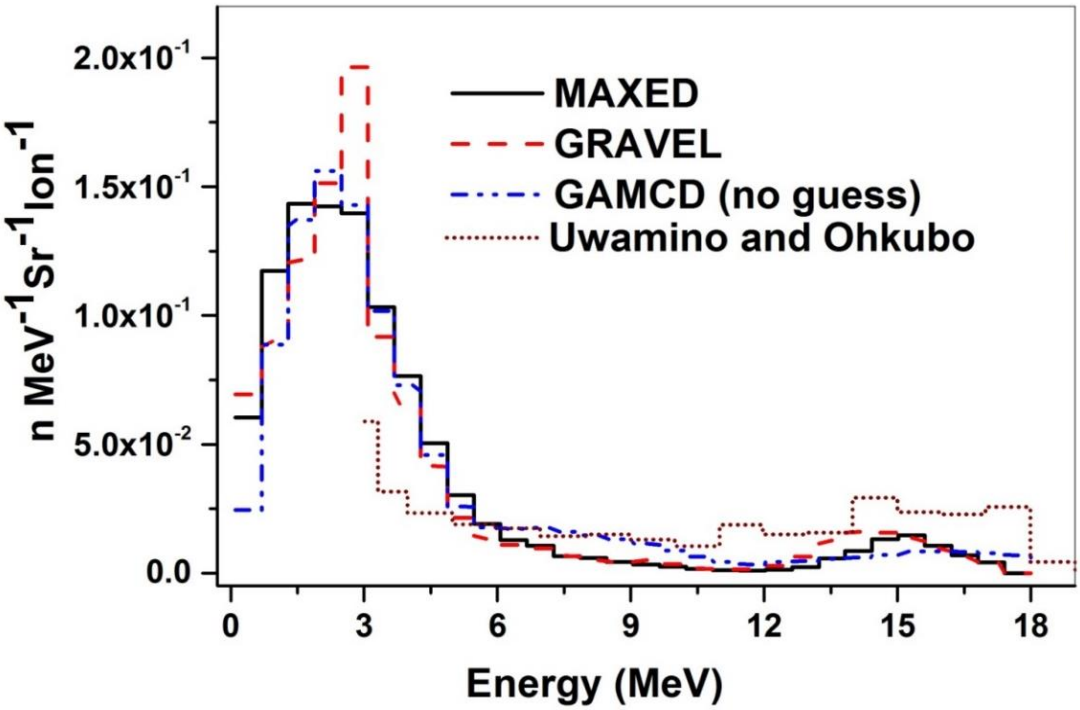

Fig. 3.12 Comparison of the neutron spectra obtained in this study with that of Uwamino and Ohkubo [117]. Both sets of data are normalized to unit area under the spectra.

The shapes and peak positions of the spectra (measured at both angles) unfolded using proper guess spectra were found to be similar with the spectra unfolded without using proper guess spectra [59]. Use of such uniformly distributed initial guess spectrum resulted in unphysical estimation of the solution in case of MAXED and GRAVEL. It is important to mention that the commonly used unfolding codes require an initial guess spectrum to start with. But in situations where the source term is unknown then assuming a guess spectrum close to the actual one would be difficult. In that case, the code GAMCD can be useful as it runs successfully without any guess spectrum, which is demonstrated in this work.

3.5 Applying neutron energy spectrum unfolding on limited measurements

In the practical scenarios, most of the time measurements are under determined with the detection systems used. An under determined problems are those where number of measurements were less than the energy bin information of interest. The proton recoil

measurement as discussed and unfolded in above section 3.4.2, was a completely determined problem. There the number of the measurements was 37 and the energy information available was also 37, with a detector response matrix of size 37x37. The same problem was reduced to sets of under-determined problems where the numbers of measurements were made less than the energy bin information of interest. The reduction was carried out with removal of few of the measured data of the fully determined set and reduction in the response matrix accordingly. Two such sets were prepared of sizes 24 and 16 measurement data, corresponding to 24×37 and 16×37 response matrix respectively, and were unfolded.

The spectrum was unfolded for the both under-determined problems using genetic algorithm based method (GAMCD) and is plotted, in Fig. 3.13, in addition to the unfolded spectra of completely determined problem and these are compared with the neutron spectrum unfolded using the FERDOR code for the completely determined problem (black circles) as FERDOR has a limitation that it cannot handle the under-determined problems. The GAMCD method reproduces the spectra even for a highly under-determined case as can be shown in the Fig. 3.13, but shows oscillations for the same reason as explained above i.e. absence of any kind of smoothing.

3.5.1 Different Smoothing techniques studied

To resolve the issue of unwanted oscillations a study was made on different smoothing methods as in section 3.5. Here, we present results for the smoothing using second difference method, Monte Carlo averaging, combining both the second difference method and the Monte Carlo averaging, and finally the Gaussian smoothing details which were discussed in section 3.3.6. The Gaussian smoothing result matches the FERDOR output most closely. The result of GAMCD, when smoothness using the second difference method is incorporated is shown in Fig. 3.14.

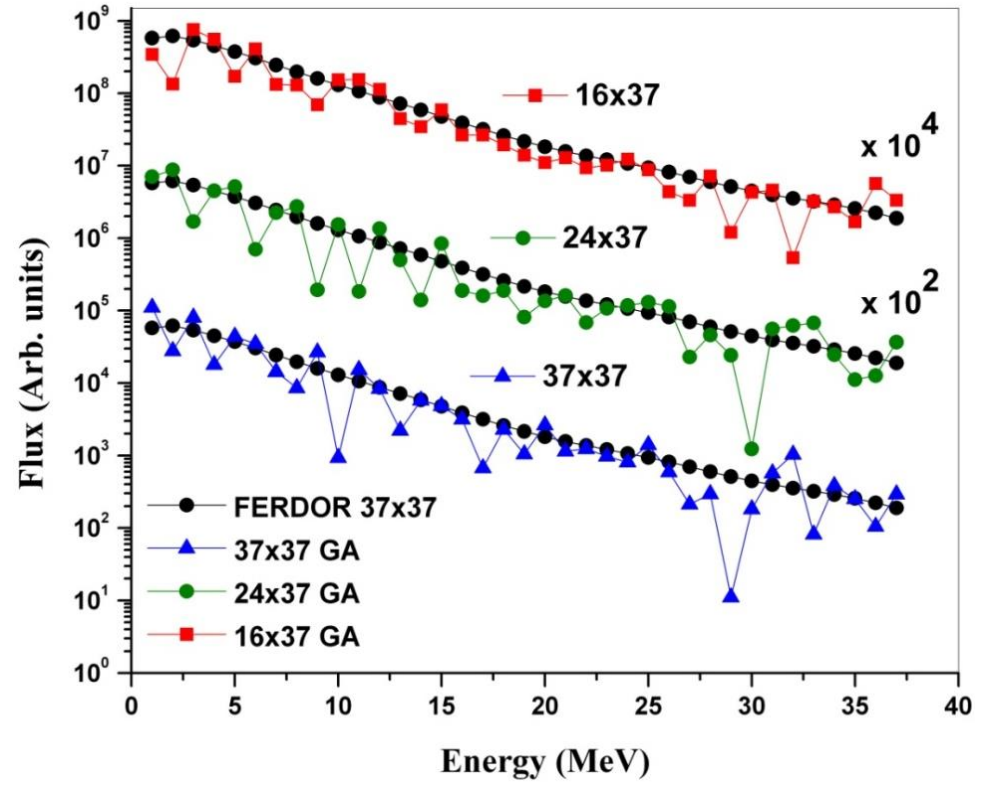

Fig. 3.13 Spectrum obtained by BC501A liquid scintillator unfolded with GAMCD for completely determined and undermined cases, black circles represent FERDOR unfolded spectra for completely determined case.

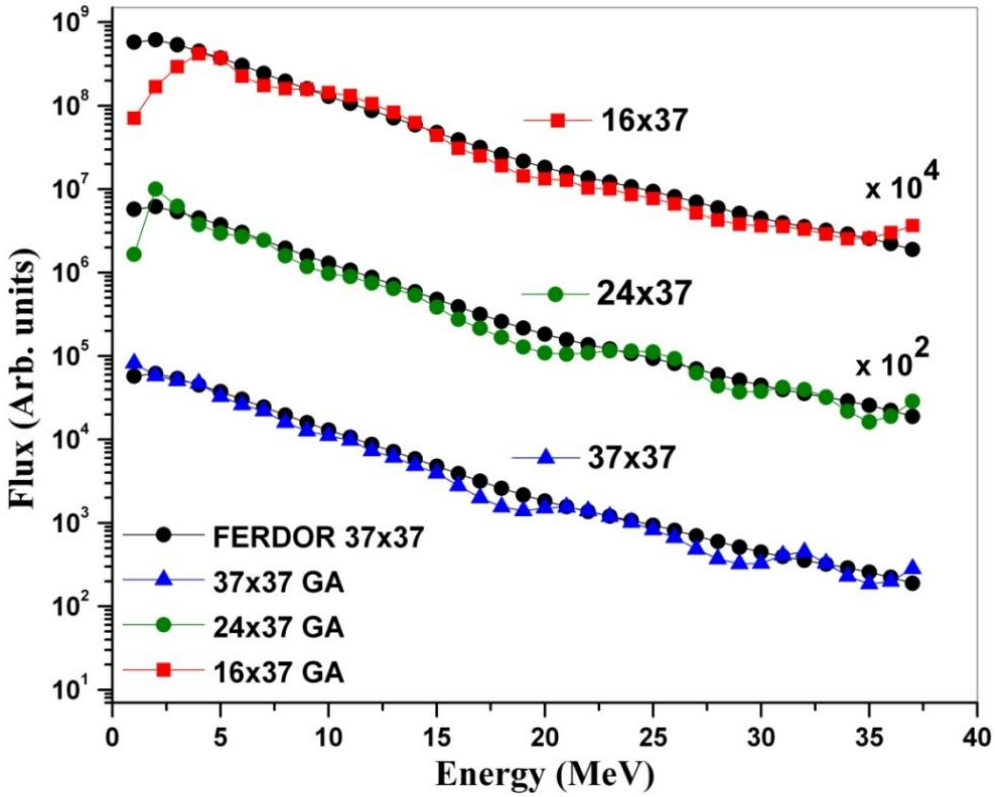

Fig. 3.14 Unfolded spectra after applying second difference smoothing.

It can be seen that the oscillations are reduced and the GA output very closely follows the FERDOR output except in the high energy region in all the three cases but there is a slight mismatch in the lower energy region for the case of 16x37 set. The spectrum were then unfolded and the smoothing applied was based on the Monte Carlo averaging scheme the output compared to FERDOR is presented in the Fig. 3.15. Here, also the unfolded spectra matches well with the FERDOR output except the slight oscillations in the higher energy region. The two smoothing techniques second difference method and the Monte Carlo averaging were then applied together as a result the oscillations were further reduced but at the lower energy the difference between the FERDOR and the smoothened GA output becomes evident as shown in Fig. 3.16.

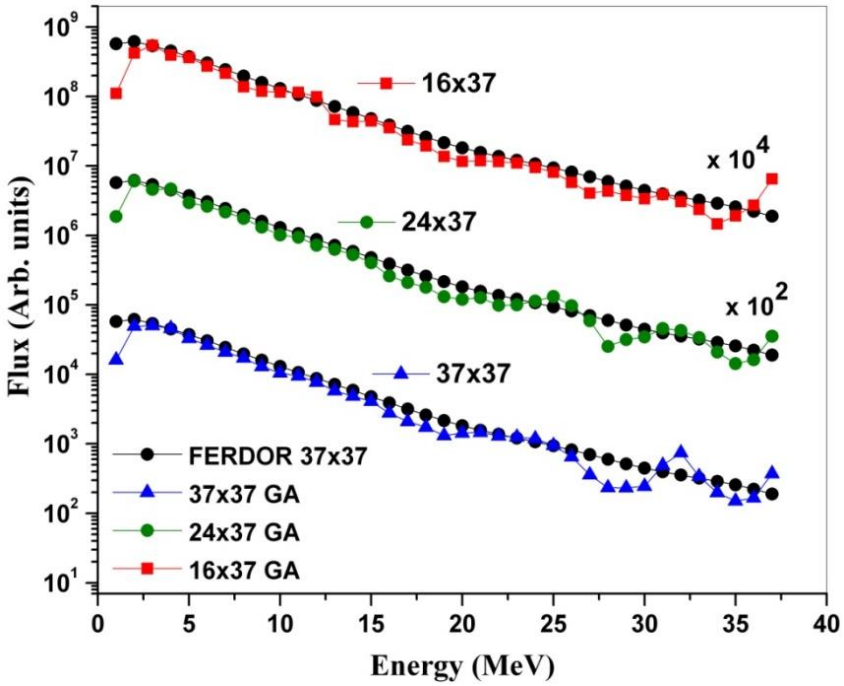

Fig. 3.15 Unfolded spectra using GA after applying Monte Carlo based smoothing.

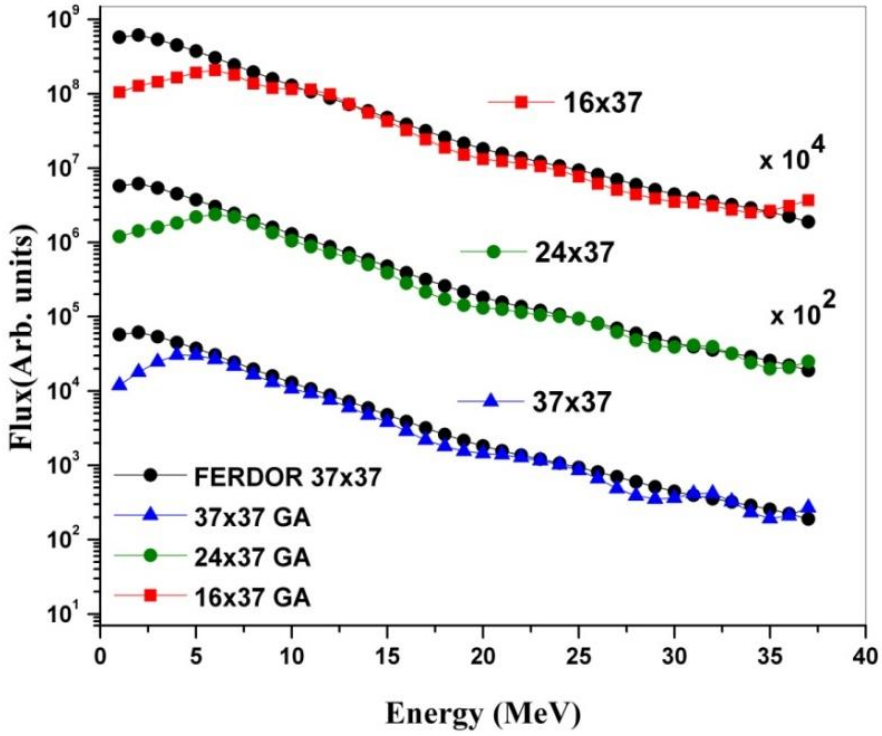

Fig. 3.16 Unfolded spectra using GA after applying second difference method in addition to Monte Carlo based smoothing.

In all the three smoothing methods discussed above the folded spectra (not presented here) showed a very good match with the actual measurements except slight mismatch. Gaussian smoothing was also studied as discussed earlier and was applied during the unfolding. The unfolded spectra after

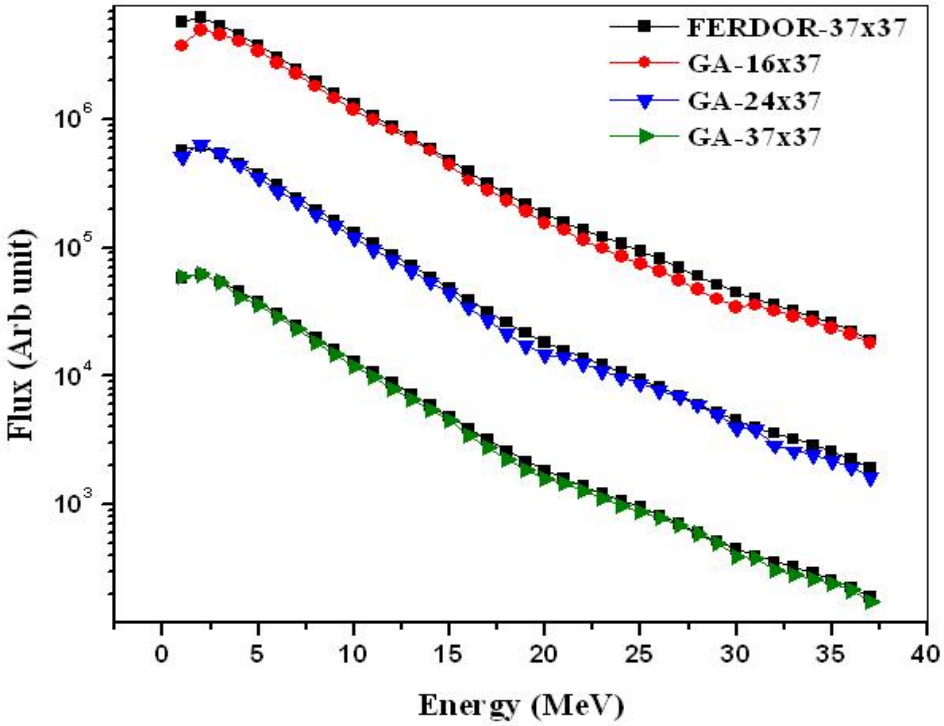

carrying out Gaussian smoothing as presented in Fig. 3.17 showed a very close match with the FERDOR output in all the three cases; the oscillatory part is completely gone as can be seen. The spectrum when folded back is shown in, Fig. 3.18. The folded back spectra are compared with the measured data and in case of the completely determined problem the folded spectra of the FERDOR output is also plotted. The folded back data shows a very good match with the measurements.

Fig. 3.17 Unfolded spectra using GA after applying Gaussian smoothing.

In case of the under-determined sets the folded back data is compared only to the actual measurements. The genetic algorithm based method appears to be a promising unfolding technique in case of under-determined problems, where the measurements are less than the energy bins information required. The GA approach overcomes the problem of inconclusive outputs generated using few methods like matrix inversion in case of under-determined

problem, as few of the calculated flux values come out to be negative, resulting in an unphysical solution.

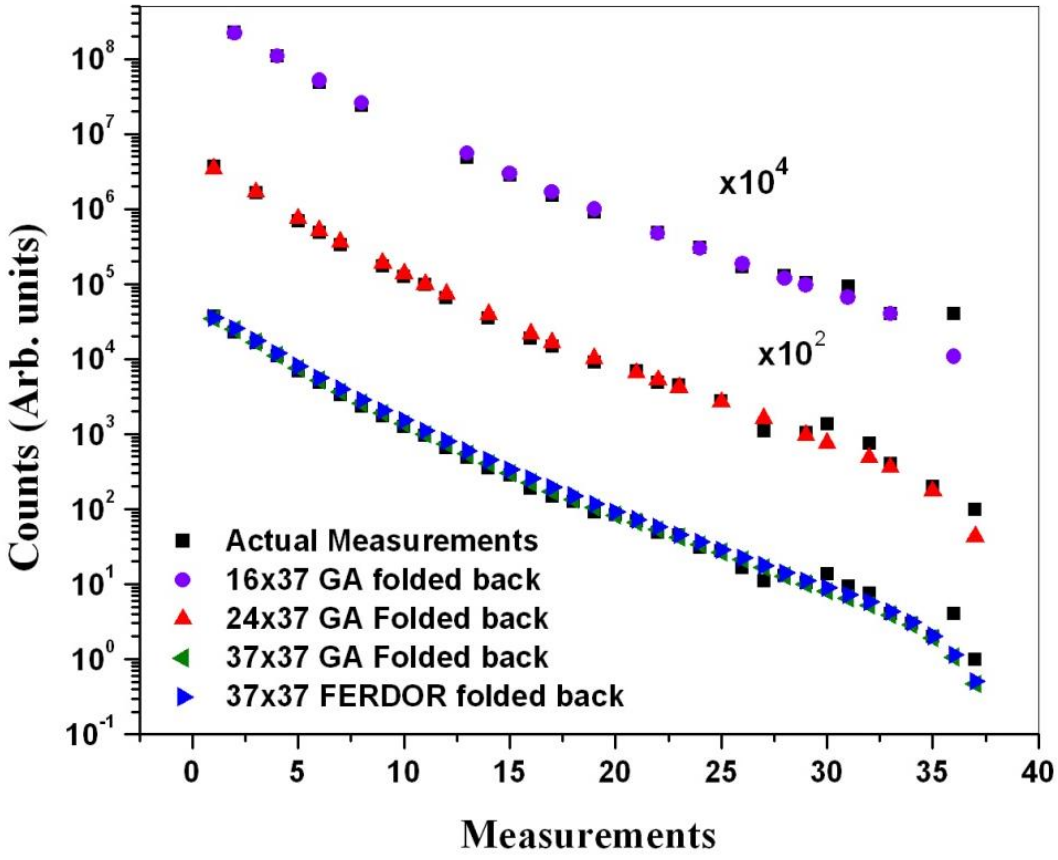

Fig. 3.18 Folded back Gaussian smoothened spectra for the under-determined cases.

3.6 Distribution of the convergence solutions in GAMCD

The solutions obtained in each Monte Carlo simulation history for the case as described above were saved for 1000 histories and the number distributions of the resulting solutions at all energy bins were analyzed. A few of the distributions are shown in Fig. 3.19. It can be seen that although the solution data points are not exactly normally distributed but they very much look similar to a normal distribution and seems to be distributed symmetrically around a most probable value.

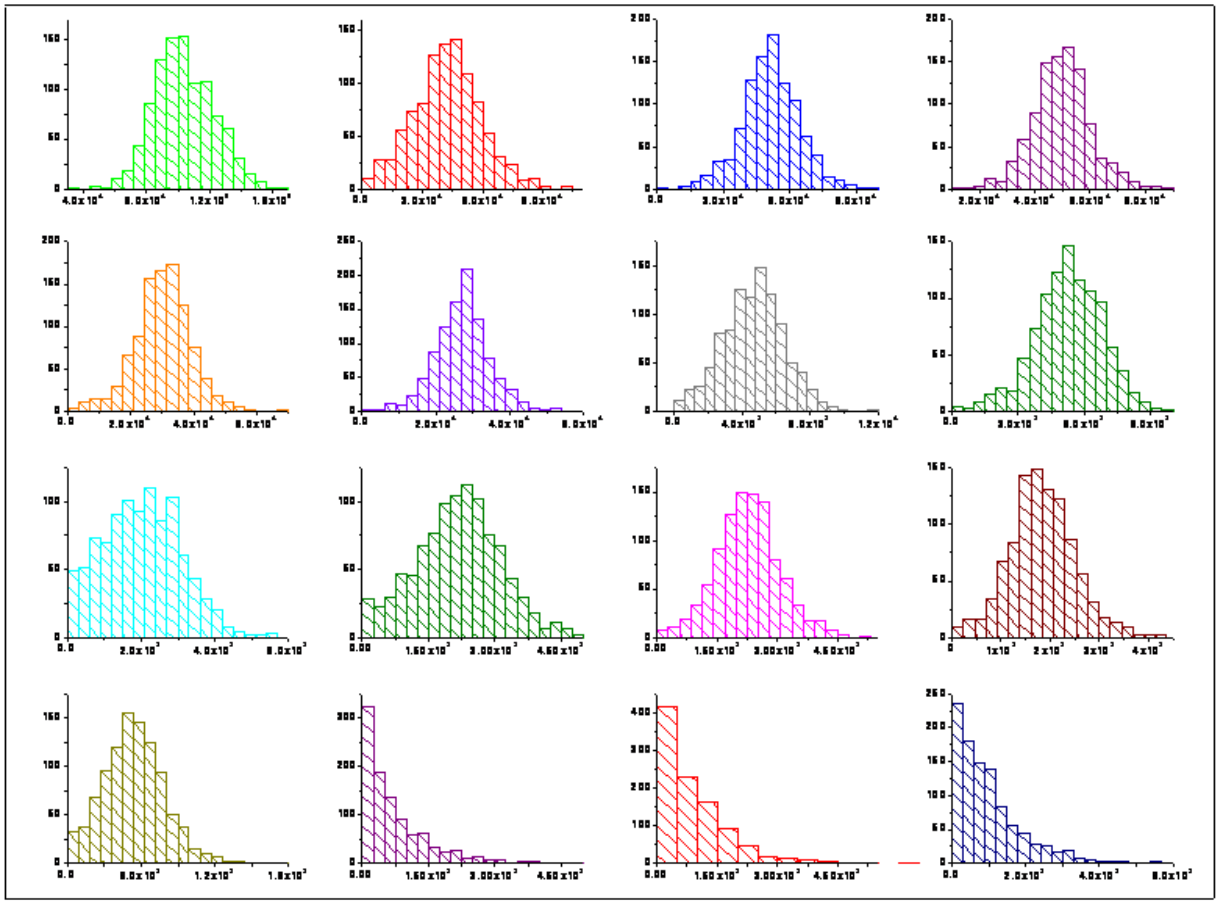

Fig. 3.19 Distribution of scores in GAMCD (present work) at different energy bins of the solution spectra (corresponding to Fig. 3.13) for 1000 Monte Carlo histories. The x-axis denotes the score (arbitrary scale) and the y-axis denotes the number of times such score is contributed in 1000 Monte Carlo histories.

Few of the distributions appear to be skewed. The shape of these distributions is so because for them the mean value is close to zero and because of the non-negativity constraint; these distributions cannot extend below zero and thus cannot be symmetric. All other distributions can be more or less approximated to a normal distribution and thus the confidence interval of the final solution can be estimated. For the results where the distribution is skewed or deviate from the normal distribution the Chebyshev's inequality as given by equation (3.18) can be used for estimating the confidence interval. The Chebyshev's inequality states that for a random variable X with finite mean μ and finite non-zero variance σ^2, and for any real number > 0 .This mathematical statement means that for any distribution with known mean μ

and variance σ^2; and for a real number $k > 1$; at least $\left(1 - {}^{1}/_{k^2}\right) \times 100$ % of data falls within $\pm k\sigma$ i.e. $\pm k$ times the standard deviation of the mean of the distribution.

$$\Pr(|X - \mu| \geq k\sigma) \leq \frac{1}{k^2} \tag{3.18}$$

3.7 Summary

In the present study a neutron spectrum unfolding procedure, based on stochastic global search method like genetic algorithm and the Monte Carlo technique (GAMCD) has been developed. It is a population-based model which, uses selection and crossover operators to generate new solution points in a search space while the initial starting points are generated randomly from a uniform distribution requiring no *a priori* information about the shape of the solution spectrum. A new mutation operator based on iterative method was adopted in addition to point wise mutation and the former was found to speed up the search. Mutation in general helps the solution to overcome the local minima. The entire process of evolution of the solution from a population of several initial solutions constitutes a single Monte Carlo history where the final score is the best solution as per a stipulated fitness criterion. Each Monte Carlo history solves the problem with randomly perturbed different sets of measurement data and the response matrix. The average of all the scores from each history is taken as the final solution.

The following points highlight the salient features of the present technique:

i. considers the uncertainties present in the measured data as well as in the response matrix.
ii. does not yield any negative values in the solution.
iii. does not require any *a priori* information about the shape of the final solution, although there is provision for accepting any *a priori* information
iv. confidence interval of the final solution after considering all uncertainties (measured data and response matrix) can be estimated easily.
v. the method is well suited for solving the under-determined problems.

The proposed method is tested by unfolding a set of simulated spectra in addition to proton recoil spectra and activation foil measurements carried out in the accelerator environment. The method is also tested with artificially constructed under-determined problem from the measured data. The results of the present method have been compared with the results from standard unfolding codes and were found consistent. The present code performs better in the absence of any guess spectra.

The successful performance of the present method though demonstrated only for neutron energy spectrum unfolding can be extended easily to other over-determined or under-determined unfolding and optimization problems. The important inputs to carry out spectrum unfolding are the measured data and the response function of the detection system used. The reaction cross-section being a function of the incident neutron energy is used to prepare the response function in case of activation measurements. In case of proton recoil measurements using liquid or plastic organic scintillators the response function of the detector is a function of the dimension of detector, quantity and the property of the detection material. This response function is thus unique for each detector system. Consequently, for accuracy in unfolding the response function for the detector system used to carry out the measurement is required to be prepared accurately. The next chapter deals with need and methodology of preparing response function of one of the organic liquid scintillator detector used in the measurements.

CHAPTER 4

Response Function for Liquid Organic Scintillator detector system

Spectrometry of fast neutrons (~ MeV range) grew very fast with development of organic liquid scintillator detectors like NE-213 and EJ-301 for its improved neutron gamma discrimination properties [72]. In addition, these detectors have high detection efficiency and comparatively good energy resolution. Recently, these detectors have found an increased usage in field of neutron spectrometry in mixed field environments mostly in accelerators, for dosimetric applications. In the present work, EJ-301 organic liquid scintillator detectors of different dimensions were extensively used in time of flight and the proton recoil measurements, to carry out fast neutron spectrometry.

Notably, the time of flight measurement technique is based on measuring the temporal distribution in travel of the neutrons between the point of production and detection. Sophisticated instruments are used for precise measurement of the time taken by the neutrons produced in the target to reach and get detected in the neutron detector. However, in the proton recoil measurements the actual neutron energy distribution is enveloped in the detector response function, which needs to be extracted to obtain the true neutron distribution. The spectrum unfolding procedures require the response function of the detector, which is specific

to the details of the detector used [42, 43]. In absence of photo peak signatures, the knowledge of organic liquid scintillators light output function becomes essential as it is related to the energy deposition by the neutrons. In addition, the response function becomes important as the uncertainties in data of response function will be transmitted in the unfolded neutron spectrum. In such situations, where very limited mono-energetic neutron sources are available, tools like GEANT-4 becomes important for simulating the response functions for different types of neutron detector systems and verifying with measurements from the available mono-energetic neutron sources. The following sections will further discuss importance and methodology for preparing the response function and its utilization to unfold a neutron spectrum.

4.1 Need of Response function

As discussed above, the accurate evaluation of the response function is indispensable to get the correct neutron energy distribution from the experimentally measured pulse height distribution of neutrons. The evaluation of light output to recoil protons of the *H(n, n')* reaction is especially important because the neutron energy is determined from this light output. The light output relation $L_{scint}(E_p)$ is between the amount of energy E_p, deposited on a single recoil nucleus in the detector medium, and the amount of resulting scintillation light L_{scint}, produced as the recoil nucleus slows down within the medium. The clear understanding will lead to accurate knowledge of the actual neutron energy distribution, which is wrapped in the response function of the detection system used, thus estimating response function becomes fundamental for carrying out unfolding. In addition, the uncertainties associated with the determination of response matrix will disseminate in the unfolded spectrum.

4.2 Methodology for estimation

The response of a liquid organic scintillator detector to energetic neutrons is to see how the incoming mono-energetic particle deposits its energy in the detection media. Using mono-energetic neutrons the characterization of energy distribution in the detector material can be done straightforwardly. However, there is limited availability of mono-energetic neutron sources like DD and DT and quasi-mono-energetic neutrons from nuclear reactions such as Li(p, n) and Be(p, n). Therefore, in addition to the available 2.5 MeV and 14.1 MeV mono-energetic energies from DD and DT reactions respectively, simulation tools along with some empirical formulations become handy to generate the response function of the neutron detectors.

4.3 Experimental Detail

The study was carried out in two parts; one was the experimental measurement of the pulse height distribution of the available mono-energetic neutrons. The two mono-energetic neutrons of energies 2.5 MeV and 14.1 MeV were measured using a liquid organic scintillator. While, in the other part the detector system was simulated using the GEANT-4 [61] simulation tool. The coefficients of the light output function were estimated to generate the pulse height distribution, to fit with the measured pulse height distribution. The following sections will discuss the measurement and the simulation studies in details.

4.3.1 Measurement of DD and DT Mono-energetic Neutrons

The experimental measurements were carried out at N&XPF, Purnima facility [118], BARC, Mumbai. The pulse height spectrum of the two mono-energetic neutrons from DD and DT neutron sources were measured using organic liquid scintillator EJ-301 (Scionix make) [119] neutron detector. The experimental setup mainly consisted of an EJ-301 neutron detector

of dimensions 12.7 cm in diameter and 5.08 cm in length. The detector was placed at 72 cm from the target at a height of 90 cm from the ground. The pulse height was measured using the multi parameter discriminator (MPD-4, Mesytec make) module. The schematic block diagram of the electronics and the data acquisition used for the measurement is shown below in Fig. 4.1. The pulse height and the pulse shape discrimination (PSD) timing data were acquired in list mode using linux advanced multi parameter system (LAMPS) [120] package, which enables one to carry out offline analysis. Two parameters, the pulse height and the pulse shape discrimination were acquired through analog to digital converter (ADC).

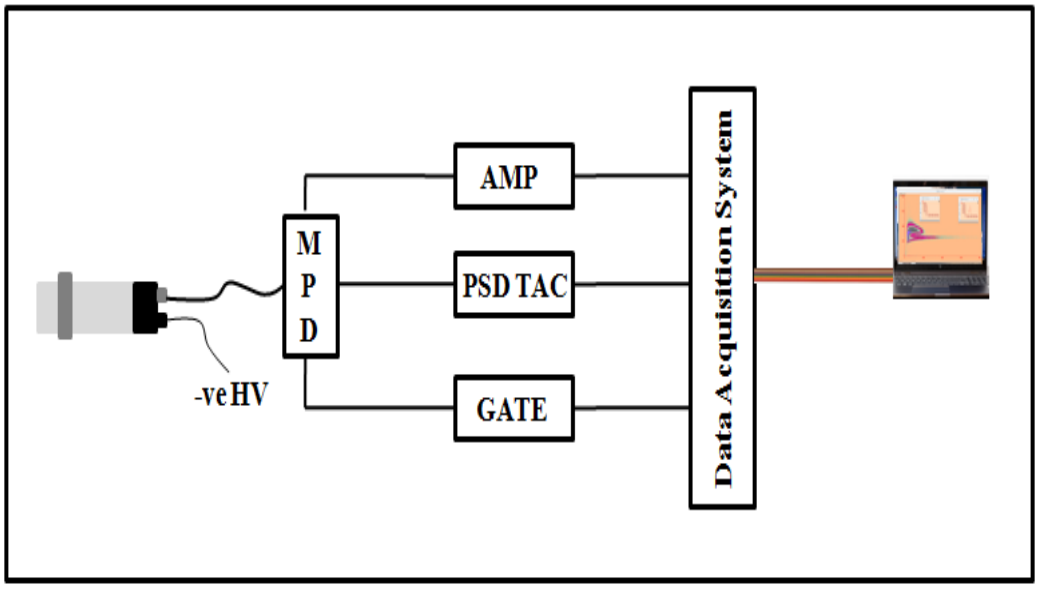

Fig. 4.1 Schematic representation of the electronic setup used in the measurement.

4.3.2 Data Analysis

The pulse height and the PSD spectrum from the DD and DT reactions from the measurements are shown in Fig. 4.2 - 4.5. A two dimensional plot was constructed by plotting pulse height spectrum versus the pulse shape discrimination data for the DD and DT reactions, as shown in Fig. 4.6 and 4.7 respectively.

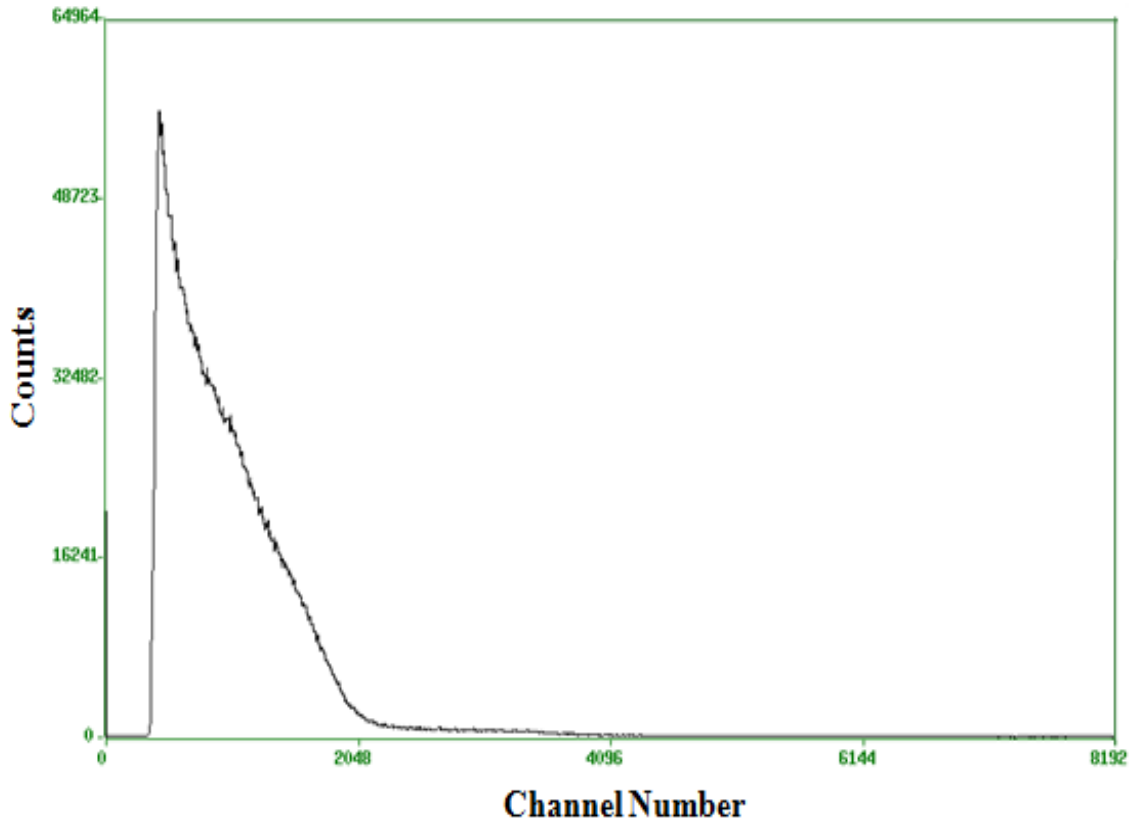

Fig. 4.2 Pulse height distribution plot from DD mono-energetic neutron measured using 5″×2″ EJ301 detector.

As can be seen there are two distinct distributions, the upper distribution corresponds to the neutrons and the lower consists the gammas as marked in the figures. Using the offline feature of LAMPS, a software gate was prepared selecting only the neutrons, as shown by the red line. The projection of this selection was taken on the pulse height axis and was converted into an ASCII file. The PSD data shows a good separation between gamma and neutrons. The energy calibration for the detector was carried out using Compton edge of standard gamma sources; Cs-137 and Na-22. The calibration curve fitted by straight line is shown in Fig. 4.8. The fitting parameters were noted and the channel was converted to electron energy equivalent. The neutron pulse height distribution so obtained is shown in Fig. 4.9, where abscissa is in units of electron equivalent energy.

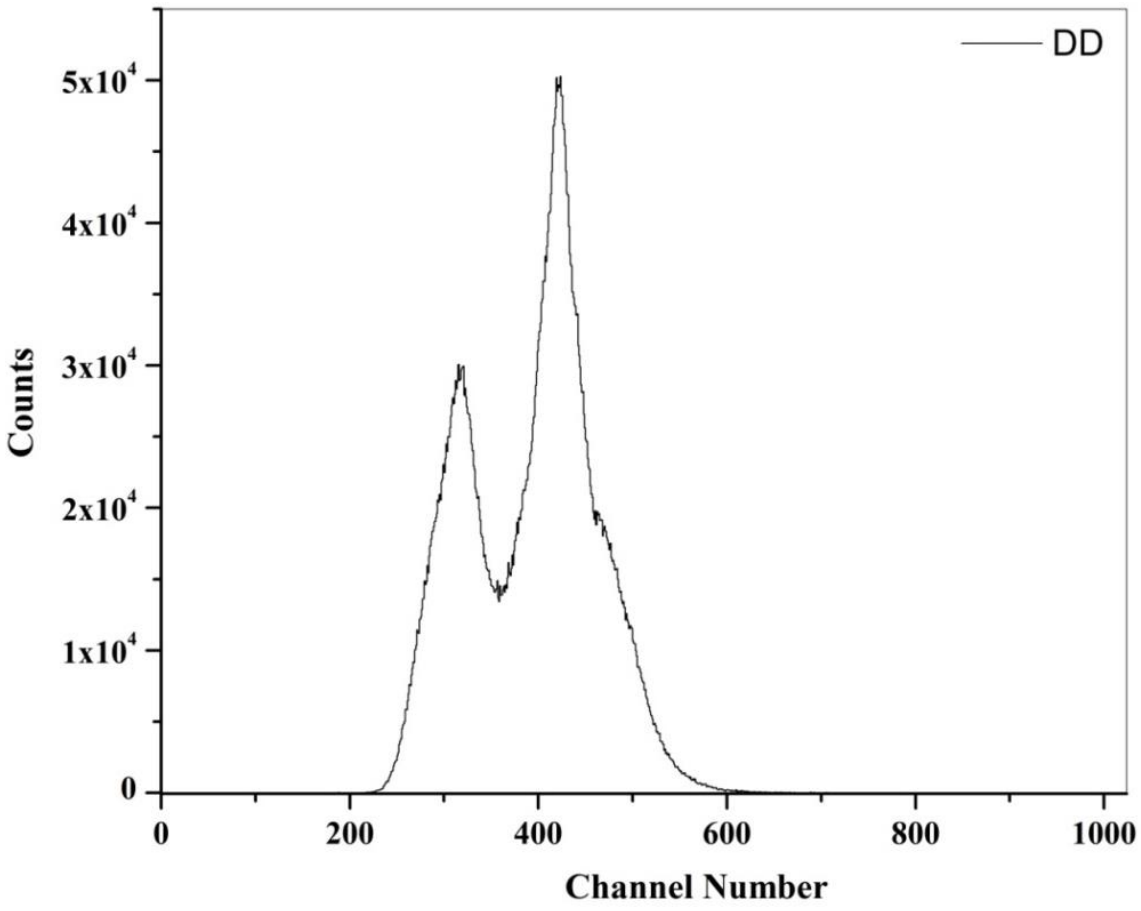

Fig. 4.3 Pulse shape discrimination plot from DD mono-energetic neutron measured using 5″×2″ EJ301 detector.

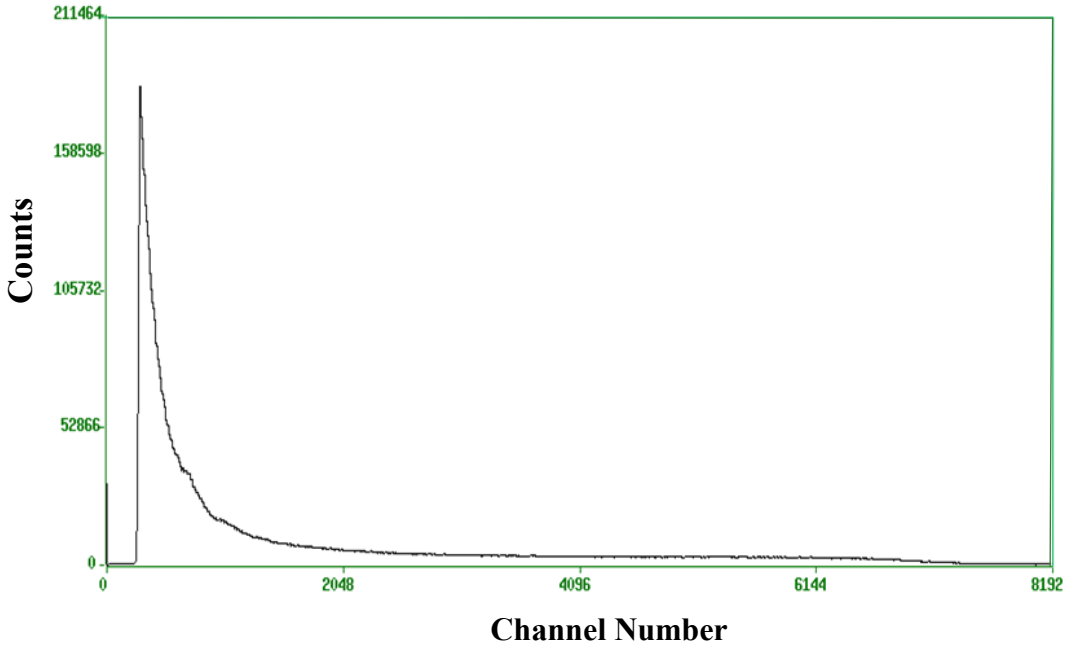

Fig. 4.4 Pulse height distribution plot from DT mono-energetic neutron measured using 5″×2″ EJ301 detector.

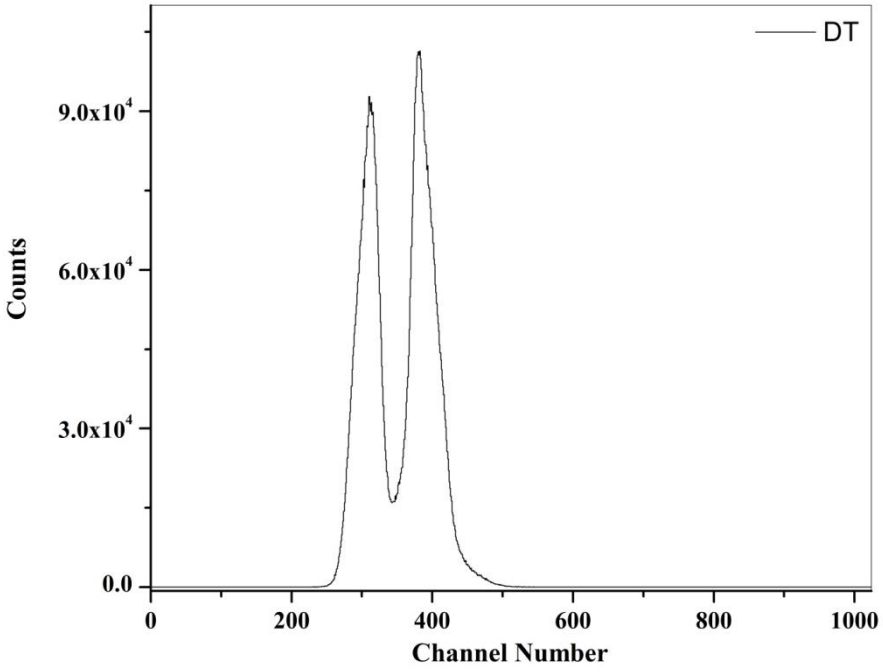

Fig. 4.5 Pulse shape discrimination plot from DT mono-energetic neutron measured using 5″×2″ EJ-301 detector.

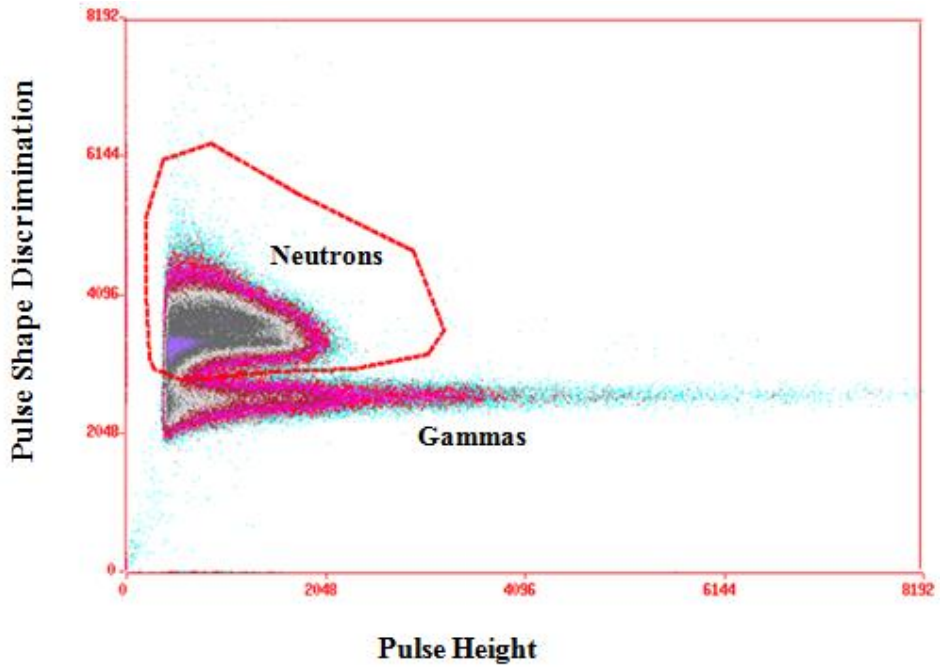

Fig. 4.6 Two dimensional plot of pulse height versus pulse shape distribution, for the DD neutron measurement using 5″×2″ EJ301 detector. The distribution circled in red is the neutrons separated from gammas as marked in the figure.

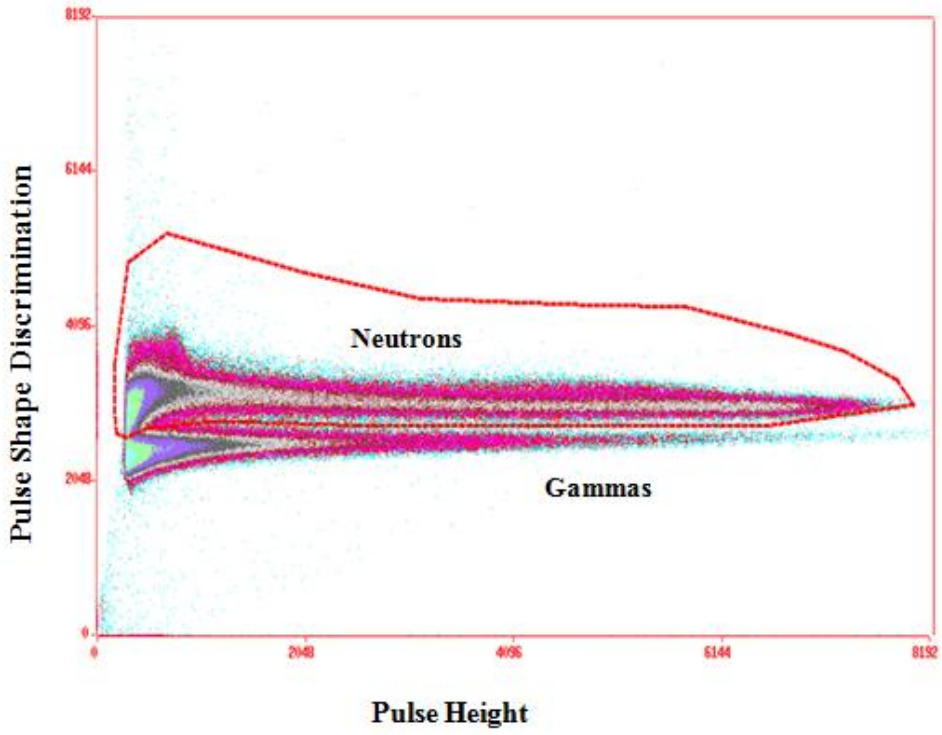

Fig. 4.7 Two dimensional plot of pulse height versus pulse shape distribution, for the DT neutron measurement using 5″×2″ EJ301 detector. The distribution circled in red is the neutrons separated from gammas present in the mixed field.

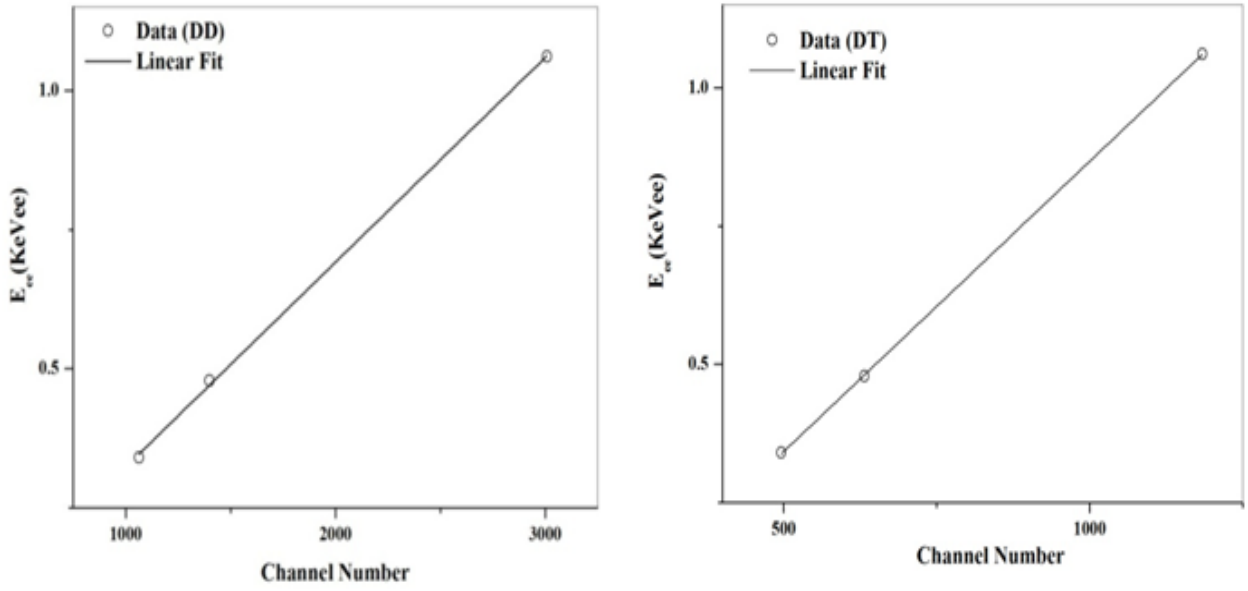

Fig. 4.8 The energy calibration curve for the two settings of DD and DT using gamma peaks of ^{137}Cs and ^{22}Na and were fitted linearly.

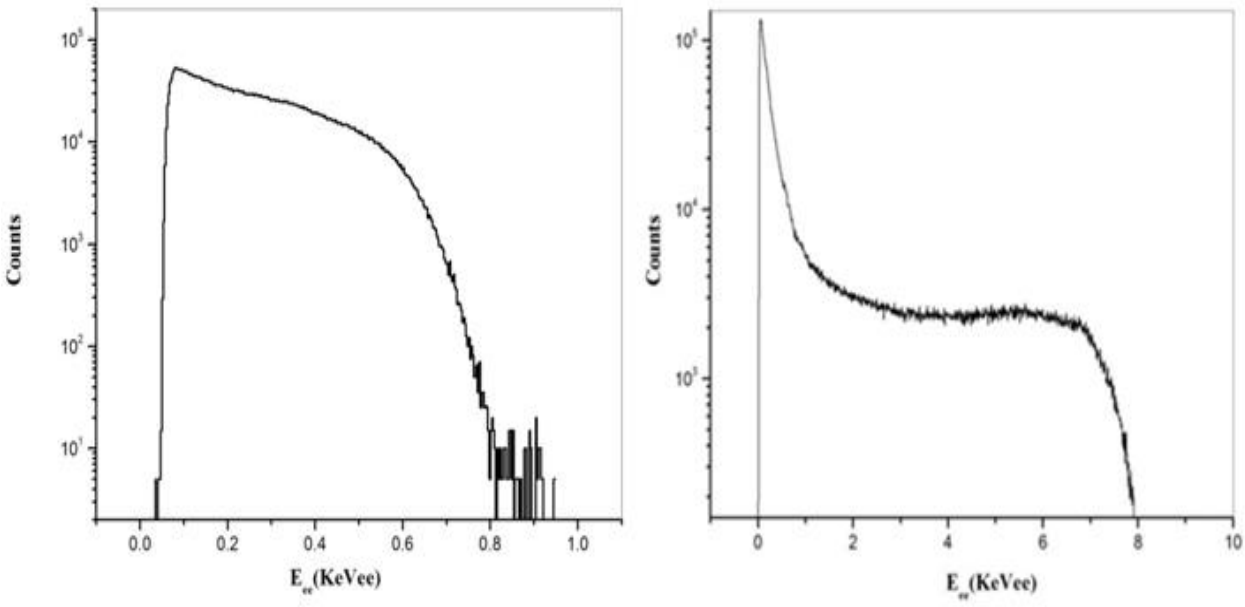

Fig. 4.9 Pulse height distribution of the extracted neutrons from the two dimensional plot for DD and DT reactions respectively.

The pulse height of the extracted neutrons is seen to have the expected rectangular shape. Instead of a sharp edge we see a shoulder due to the inherent detector resolution. The shoulder extends till ~ 0.8 KeVee and ~ 8.0 KeVee for DD and DT respectively.

4.4 Theoretical simulation using GEANT-4 Tool

Monte Carlo simulations offer an important tool in the study of design of detection system and it is therefore interesting to test its capability of such calculations by benchmarking with experimental measurements. GEANT-4 toolkit offers particle tracking in position and in time, the kinetic energy, deposited energy and many other features. The toolkit was used to determine the kinetic energy of the recoil protons from the incident mono-energetic neutrons. Each neutron history, including generation of possible charged particles like recoil protons, carbon ions and the like were considered. These secondary particles may either fully deposit their energy or participate in partial energy deposition and escape from the sensitive volume of the scintillator. The light produced from the interaction of these charged particles in the

scintillation material is related to their kinetic energy by means of an appropriate light output mathematical relation.

In this simulation a simple model of the organic scintillator detector with dimensions 12.7 cm diameter and 5.08 cm in length, encapsulated in a 0.5 mm thick aluminium casing was prepared. Material composition of the EJ-301 scintillator was taken as H and C ratio of atoms 1.212 and density of scintillator 0.874 g/cm^3 [119]. In the present study, light pipe and photo multiplier tube (PMT) were ignored and were not simulated. To model the hadronic interactions standard QGSP_BIC_HP physics list was used [61]. Which is a high precision neutron model used for neutrons below 20.0 MeV and is used for radiation protection, shielding and medical applications.

4.4.1 Light response function

When the organic scintillator material is exposed to neutron radiation, the material emits light in response [61, 121] to the ionization produced by the incident particles. The ionization can be either produced directly if charged particles are incident or by production of recoil nuclei and electrons from interaction of uncharged particles like neutrons and gamma interacting in the material. As these incident particles travel through the detection medium they lose energy and as a result produce column of excited and ionized molecules along their path. The fraction of the excitation and the ionization energy thus deposited by the incoming particle is then emitted as florescent emission. It has been studied and found that the light output is not directly proportional to the energy deposited by the ionizing particle and it has been observed to depend on the particle type and its energy [122 - 124]. Although, it has also been seen and as shown in Fig. 4.10 this is mainly true for all particles heavier than an electron. There have been many investigations over the light output responses of the several available scintillator materials.

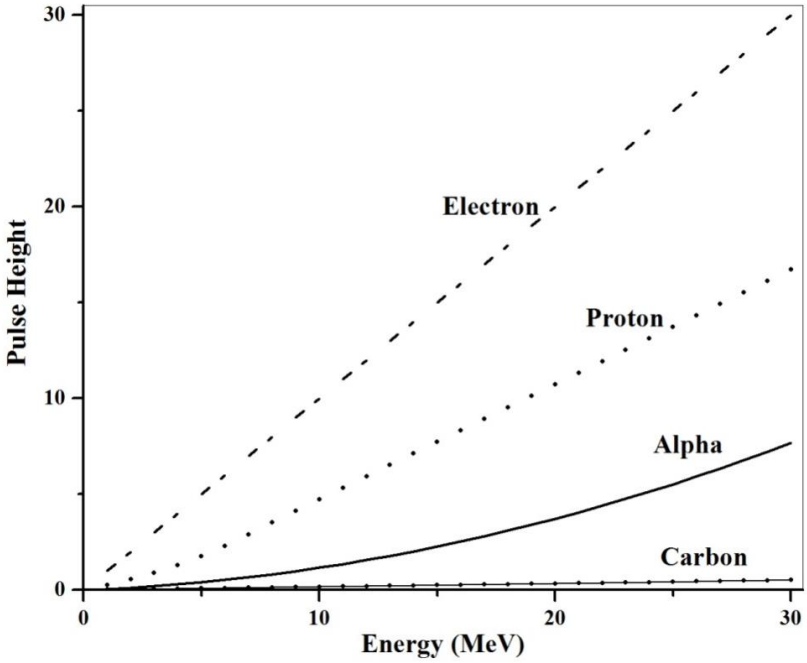

Fig. 4.10 Light output plotted as function of energy for electrons, protons, alpha particles and carbon recoils, using Monte Carlo calculations.

Birk's [123] was among the founders to have derived a relation between the differential light outputs as a function of the differential energy lost by the particle as given in equation (4.1).

$$\frac{dL}{dx} = S\frac{dE}{dx}\left[1 + kB\left(\frac{dE}{dx}\right)\right]^{-1} \tag{4.1}$$

Here, S is the scaling parameter related to the absolute scintillation efficiency, kB is related to quenching of the light output. Defining

$$\frac{dL}{dx} = Sf\left(\frac{dE}{dx}\right) \tag{4.2}$$

where,
$$f = \left[1 + kB\left(\frac{dE}{dx}\right)\right]^{-1} \tag{4.3}$$

The light output $L(E)$ can be written as

$$L(E) = S\int_0^R f\left(\frac{dE}{dx}\right)dx \tag{4.4}$$

where, R is the range over which the incident particle losses all its kinetic energy E.

4.4.2 Results and Discussion

The light output *L(E)* is expressed in terms of the equivalent electron energy L_{ee}, it is the electron energy, that when stops in the material would give same amount of light as seen for a particular particle. To get an insight, many phenomenological parameterization of above equation has been reported by authors like Cecil [125] and Batchelor [65]. We have used the simple dependence between light output (L_P) and the energy of the incident particle (E_P as used by Batchelor)

$$L_P = aE_P + bE_P^2 (0 < E_P < 6.5MeV) \tag{4.5}$$

$$L_P = cE_P - d(6.5MeV < E_P < 15MeV) \tag{4.6}$$

where, *a, b, c* and *d* are the coefficients obtained by fitting the experimental data. The fitted values for the coefficients are *a* = 0.101, *b* = 0.041, *c* = 0.6 and *d* = 1.5, as obtained from the experimental data. The pulse height estimated from GEANT-4 using the above parameters is shown in Fig. 4.11 and 4.12 in comparison with the experimental measurements, for the DD and DT reactions respectively. The filled symbols show the GEANT-4 data whereas the line plot represents the experimental measurement. For the DD reaction as seen in Fig. 4.11, the pulse height distribution has a small mismatch in the lower energy, although the match is good towards the high energy. This may be due to the use of a very simplified modeling as similar mismatch can also be seen in the Fig. 4.12 of DT reaction. In the experimental measurement the scattered component could not be subtracted and the simulated spectra do not address the scattered component. The increased pulse height in the experimental measurement could be associated with the scattered low energy neutrons contributed from the structural material in the vicinity.

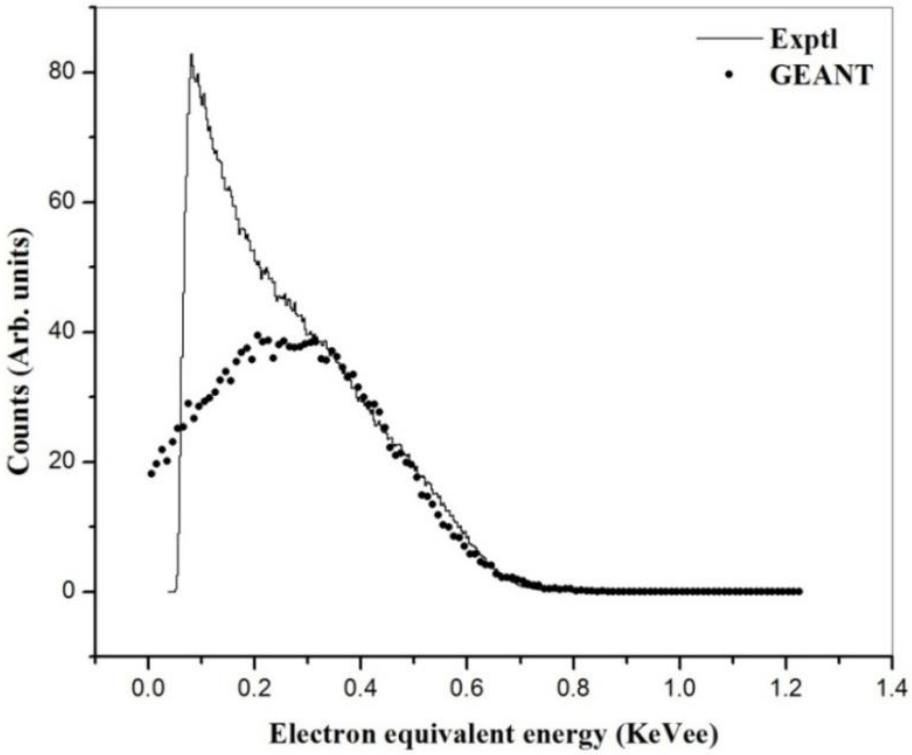

Fig. 4.11 Comparison of pulse height from measurement and GEANT-4 simulations for the DD reaction. The symbol represents the GEANT-4 simulation and the curve represents the experimental measurement.

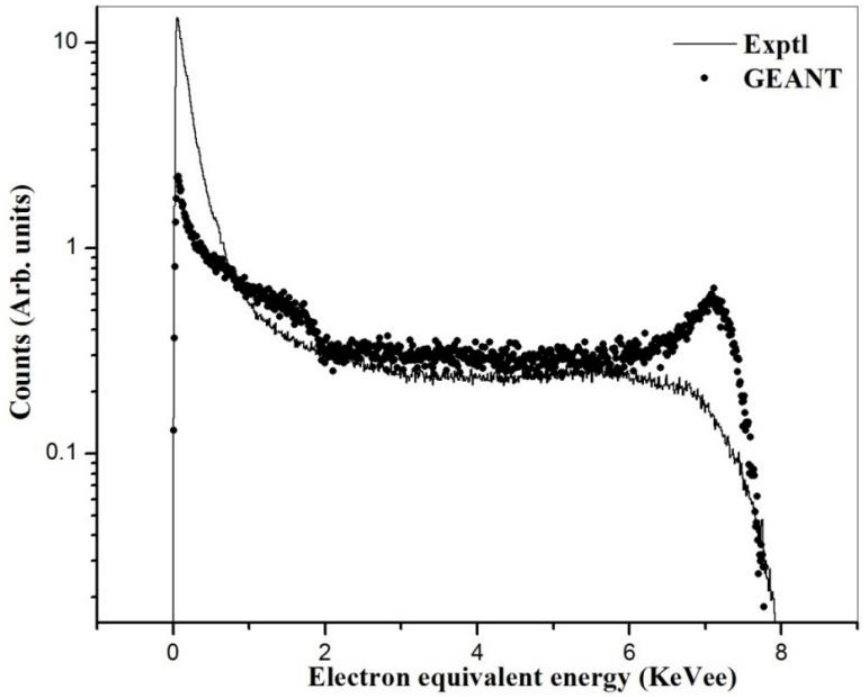

Fig. 4.12 Comparison of pulse height from measurement and GEANT-4 simulations for the DT reaction.

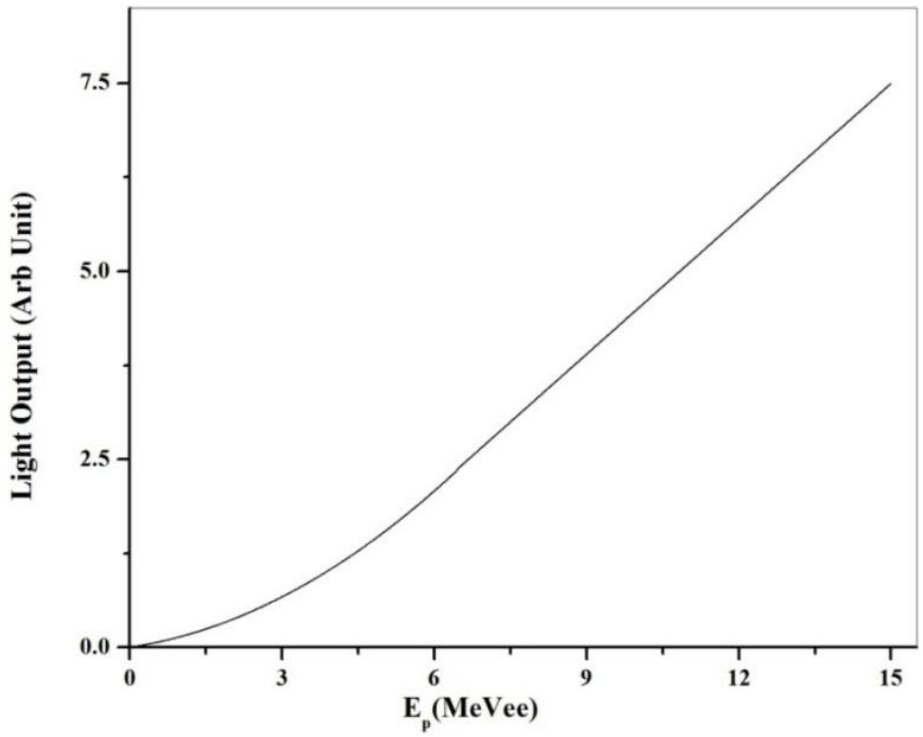

Fig. 4.13 Light output for the detectors used for the measurement using equations (4.5) and (4.6).

In addition, in case of DT the mismatch towards higher energy can be improved by further fine tuning the smearing coefficients. This will be incorporated in the future course of study. The light output calculated using the set of equations mentioned above and the coefficients determined from the fitting, for the detector set used, is plotted in Fig. 4.13. The non-linearity in low energy region is visible and almost becomes linear towards the higher energy. Using the above set of equations and the estimated coefficients the response function for the used detector set for various incident mono-energetic neutrons was determined. The simulated response function is rectangular in shape as expected. For the incident energies E_n = 5, 10 and 15 MeV, the response of the detector system is shown in Fig. 4.14.

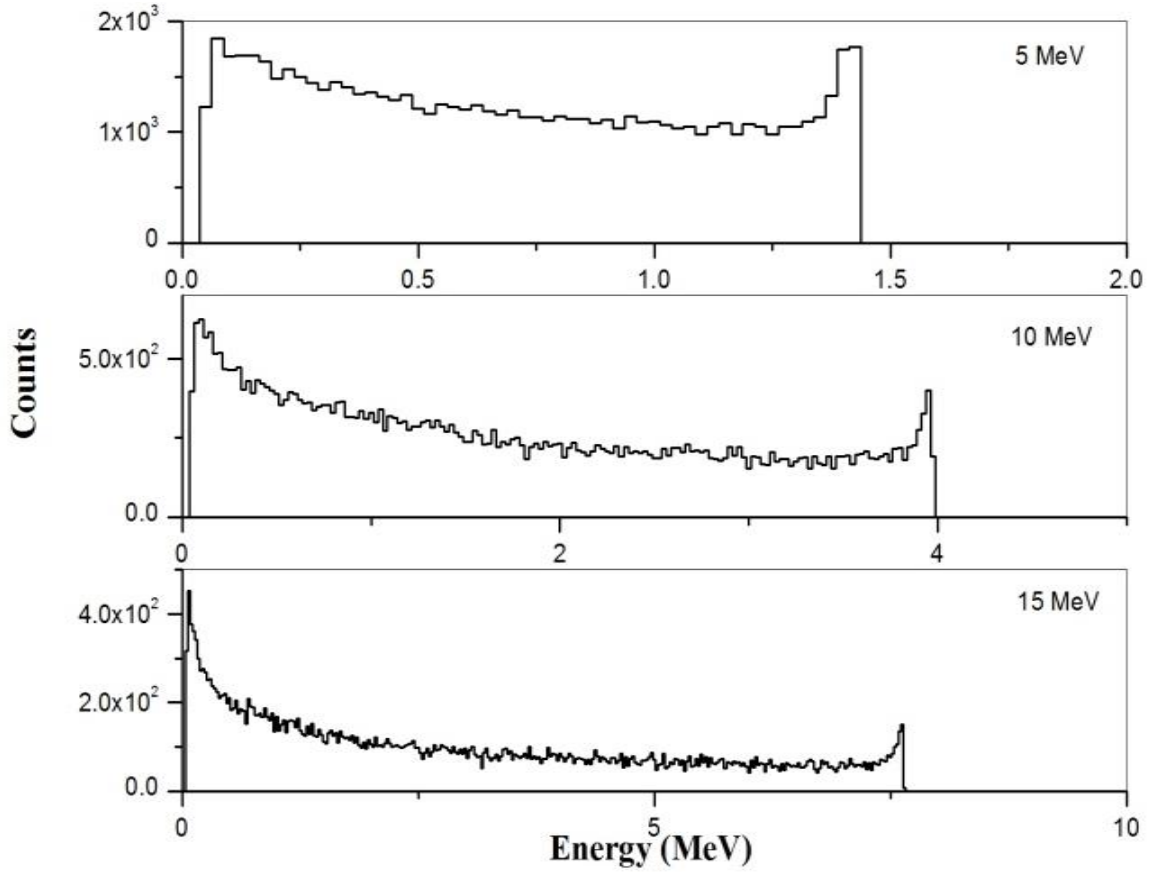

Fig. 4.14 Simulated response functions for the detector system without smearing for incident neutron energies 5, 10 and 15 MeV.

However, in practice several factors like wall effect, carbon recoil, and undesired reaction channels that open up above 8 - 10 MeV, distorts the rectangular shape. To match with the experimental resolution the light output L in the simulation was smeared using the following relation [122]

$$L_{smeared} = L + R(\sigma_1) + R(\sigma_2)\sqrt{L} \tag{4.7}$$

where, $R(\sigma)$ is a random number sampled from a normal distribution with mean zero and standard deviations, $\sigma_1 = 0.125\ MeV$ and $\sigma_2 = 0.067\ (MeV)^{0.5}$.

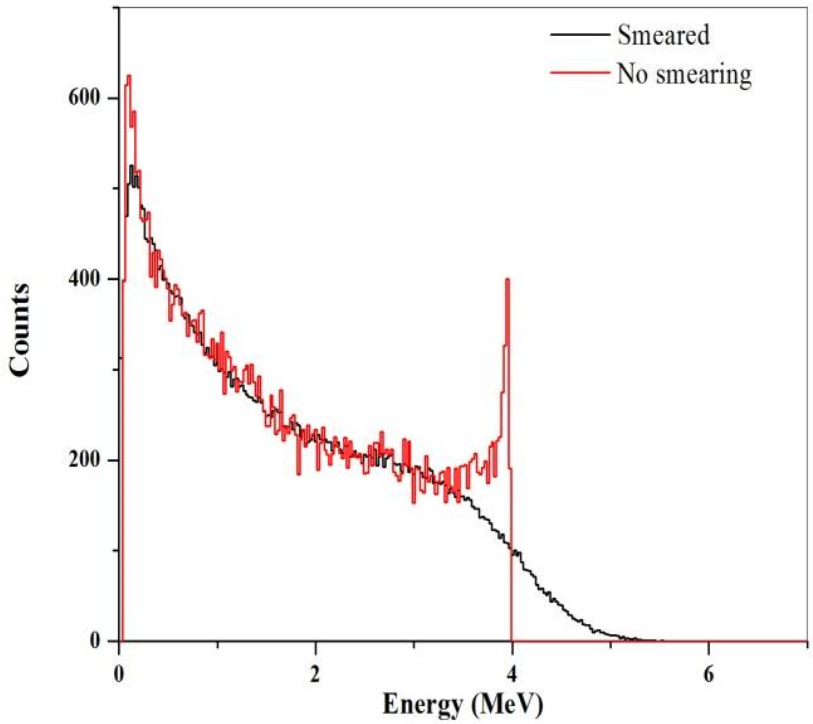

Fig. 4.15 Simulated response function compared for 10 MeV with and without smearing.

The effect of smearing on the response function corresponding to incident energy 10 MeV is shown in Fig. 4.15 the sharp fall at the end of the distribution smoothens and smears out to match with the actual resolution of the detector system. Further, the response curve for various neutron energies E_n (1, 2, 3, 5, 10 and 15 MeV) with similar smearing is plotted in Fig. 4.16.

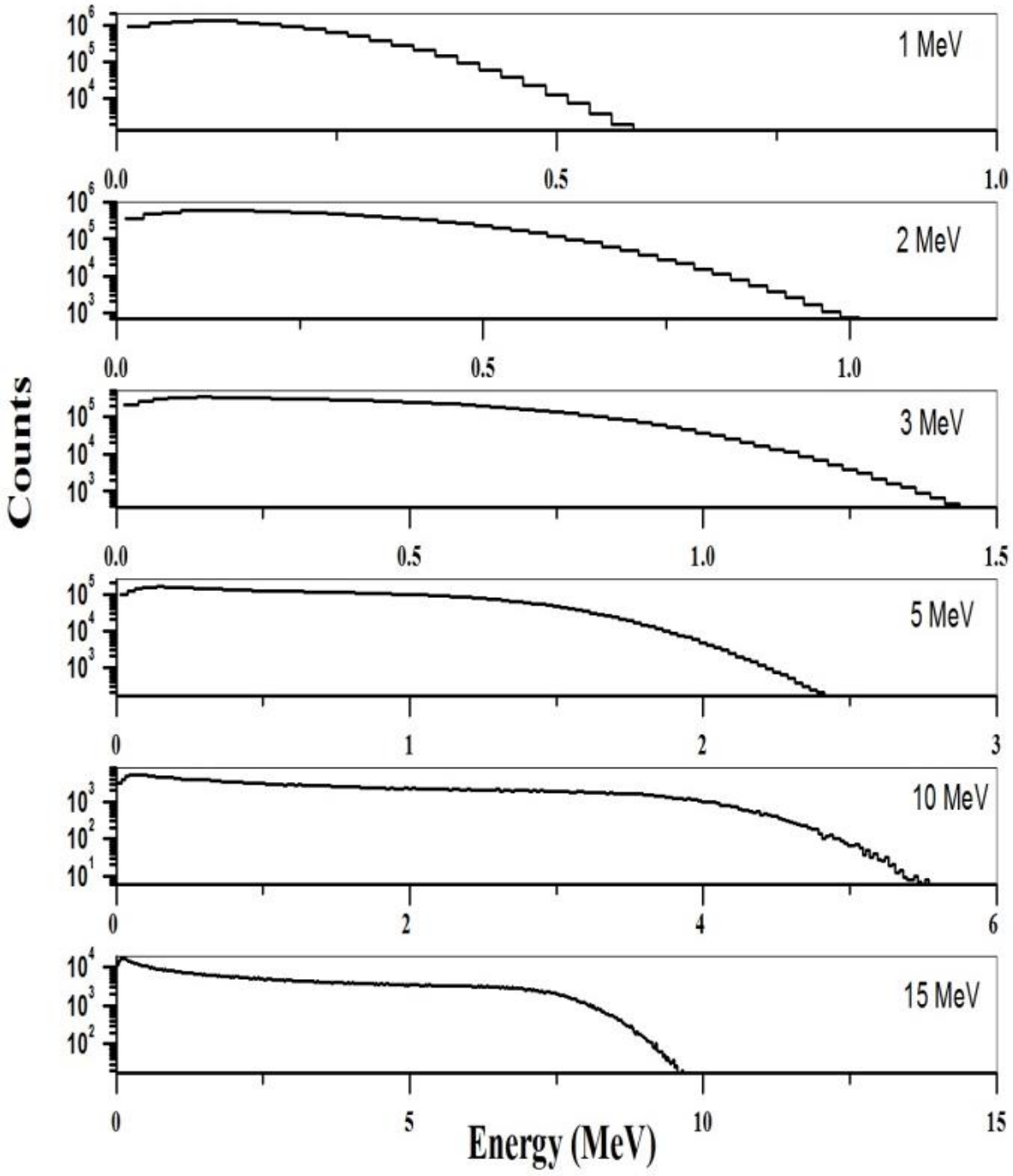

Fig. 4.16 Simulated response functions for the detector system with smearing for energies 1,2, 3, 5, 10 and 15 MeV.

The response function generated for the organic liquid scintillator EJ-301 of diameter 12.7 cm and length 5.08 cm, was subsequently used for unfolding to obtain the underlying neutron energy distribution from the measured pulse height distributions. The in house developed neutron spectrum unfolding code GAMCD [55, 56] was used for this. The unfolded

neutron energy distribution from DD and DT reactions are presented in Fig. 4.17 and Fig. 4.18. The neutron energy distribution plotted in Fig. 4.17 and 4.18 are inclusive and the scattered events were not considered. As can be seen in the Fig. 4.17, the peak of the distribution is positioned at 2.5 MeV as expected for the DD reaction. However, there is a small contribution in the lower energy side which may be attributed to the events registered due to the scattered component from the surrounding structural material.

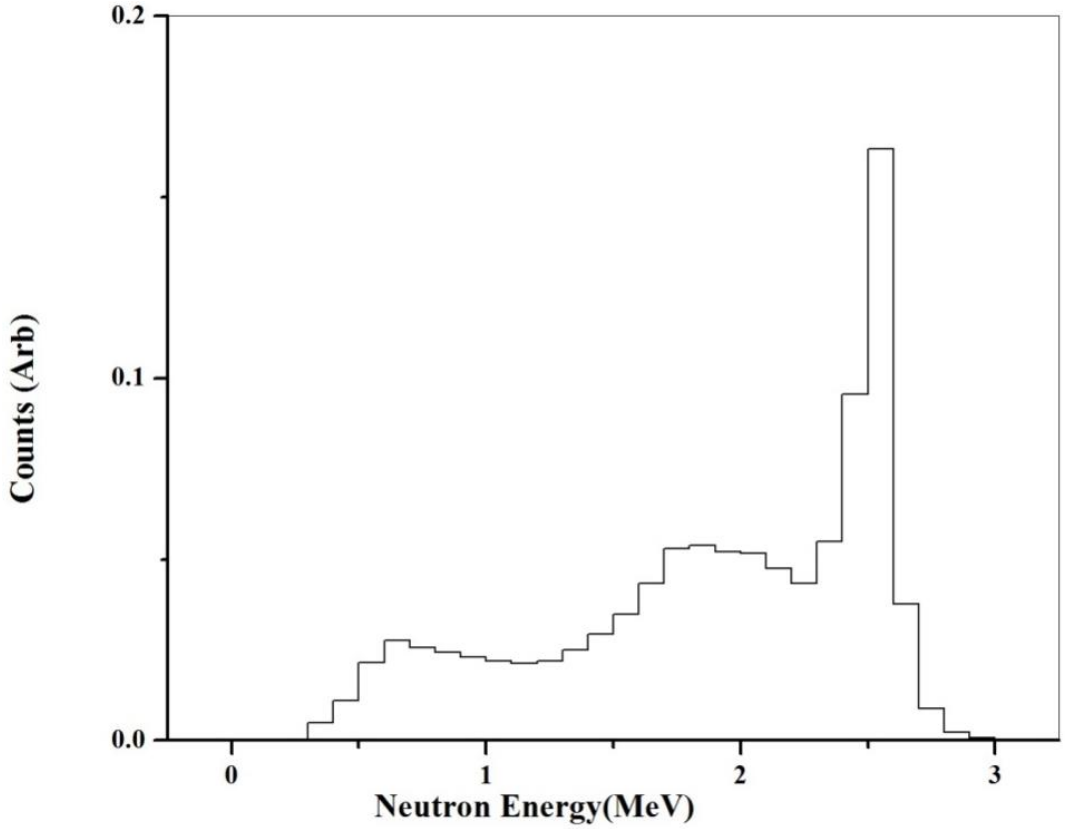

Fig. 4.17 Neutron energy distribution obtained by unfolding the pulse height spectra measurement of DD reaction using GAMCD code.

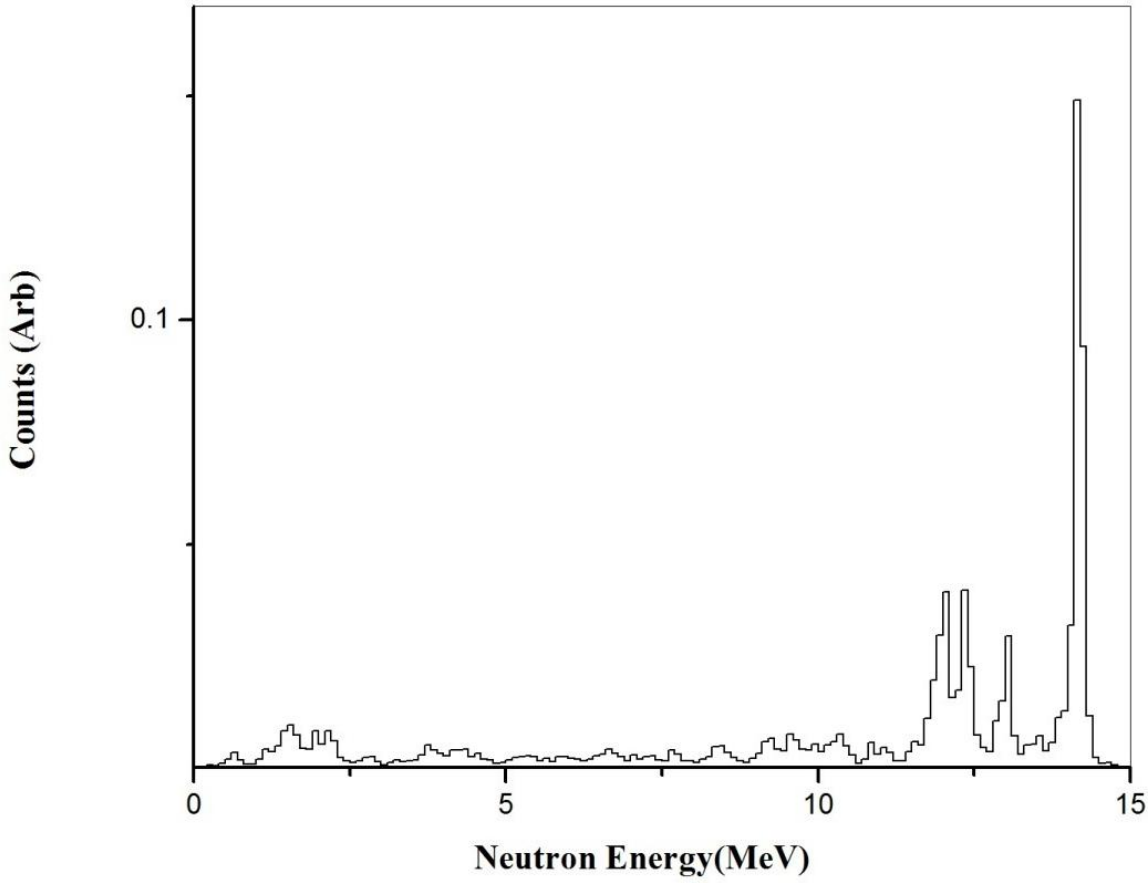

Fig. 4.18 Neutron energy distribution obtained by unfolding the pulse height spectra measurement of DT reaction using GAMCD code.

The effect of which is seen as a continuous distribution in the lower energy side and is anticipated to go away when shadow bar measurements are carried out and subtracted from the inclusive detector measurements.

From the Fig. 4.18, the 14.1 MeV peak from the DT reaction is clearly evident but along with it are seen few additional peaks around 12 MeV with a reduced intensity of 20%. The lower energy peaks are the contribution of the scattered neutrons from the surrounding walls and the beam line components. These additional peaks can be removed by carrying out the scattered component measurement and subtracting it from the direct measurements.

4.5 Summary

The response function preparation for a 5″x 2″ liquid scintillator detector has been carried out using the GEANT-4 simulation tool. The pulse height distribution of the two mono-energetic neutrons from DD and DT reactions has been measured. The light output coefficients were estimated by fitting the experimental data to the parametric equations on pulse height versus incident neutron energy. Using the fitted equations for various energies of neutrons incident on the scintillator material, the energy deposition over the energy bins have been studied. A smearing function was also used in the simulated response to match with the actual response to account for the smeared Compton edge. The response matrix for the liquid scintillator detector was prepared using the fitted relation. With the simulated response function and the measured pulse height distribution the actual neutron energy distribution from DD and DT reactions were unfolded using GAMCD. It gave satisfactory spectral distribution with clear peaks located at 2.5 MeV and 14.1 MeV for DD and DT respectively. A low energy contribution was also observed in the unfolded spectra which is expected due to scattering from the surrounding structural materials. The scattered events were not taken into consideration for this study.

The neutron spectrum estimation using unfolding methods should be supplemented and benchmarked with neutron energy distribution measured using time of flight method. In the following chapter the neutron spectrometry using time of flight technique will be discussed in details. The spectrum measured for various projectile, target and energy systems will be presented.

CHAPTER 5

Experimental Measurement and Data Analysis

Time of flight technique is mostly used in mass and energy spectroscopy of different particles. In addition to previously discussed neutron spectrum unfolding techniques, the time of flight method is a precise and commonly used technique for fast neutron spectrometry. Attaining a higher degree of precision has been possible with state of the art detectors and improved acquisition, detection systems with the associated electronics.

5.1 Time of Flight Spectroscopy - Principle

A simple time of flight neutron energy spectroscopy is illustrated in Fig. 5.1. There are four primary requirements for determination of the neutron speed. First, a precise and well defined neutron source of short duration compared with the total flight time is required. Secondly, the detection time should also be well defined. Third, requirement of a device or arrangement for measuring the flight duration between these two events. Finally, the flight length must be known with a good accuracy. The time of flight technique uses fast and precise time measurements.

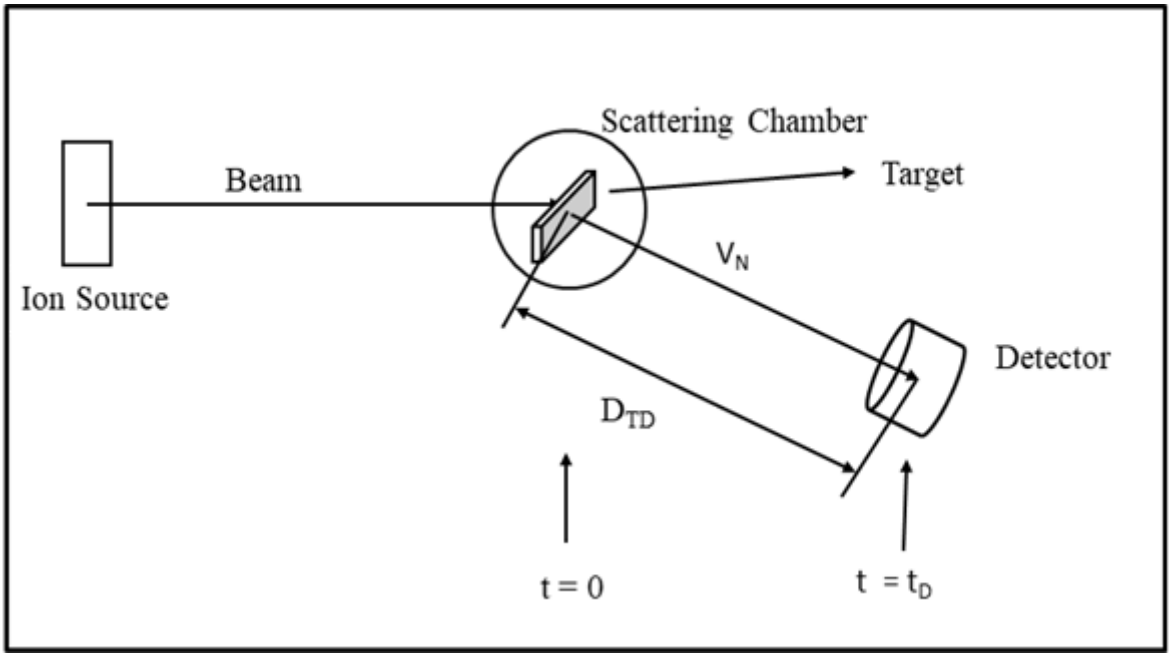

Fig. 5.1 Schematic diagram for a simple time of flight spectrometry.

The availability of advanced instruments over the years has resulted in reduction of uncertainty in the measurements. If the distance as shown in Fig. 5.1, between the target and detector, is known and the time of flight over this distance can be measured then the kinetic energy of the emitted neutrons from the target can be obtained using the basic Newtonian equation of motion as given below,

$$E = \frac{1}{2}mv^2 \tag{5.1}$$

$$E = \frac{1}{2}m\left(\frac{l}{t}\right)^2 \tag{5.2}$$

where, E (MeV) is the neutron energy, $l(cm)$ is the flight length in the present experimental setup which was kept as 150 cm, t (ns) is the flight time and $m(MeV/c^2)$ is the neutron rest mass. Substituting the neutron rest mass and flight length as 150 cm, the equation (5.2) can be simplified to

$$E = \frac{11737.5}{t^2} \tag{5.3}$$

In most of the applications, the flight length is accurately known, so the uncertainty in the velocity determination is mainly due to error in the time measurements.

5.2 Neutron yield measurement using time of flight method - Experimental set-up

A schematic of the experimental arrangement used in the measurements is shown in Fig 5.2. Five EJ-301 organic liquid scintillator detectors (Scionix make) [119] were placed at 0º, 30º, 60º, 90º and 120º for the neutron yield and its angular distribution measurement from thick target experiments. Fig 5.3, shows one typical picture of the experimental setup. The detectors were mounted horizontally facing the beamline at a height of ~ 172 cm. The center of the detector face was carefully kept in the plane with the target.

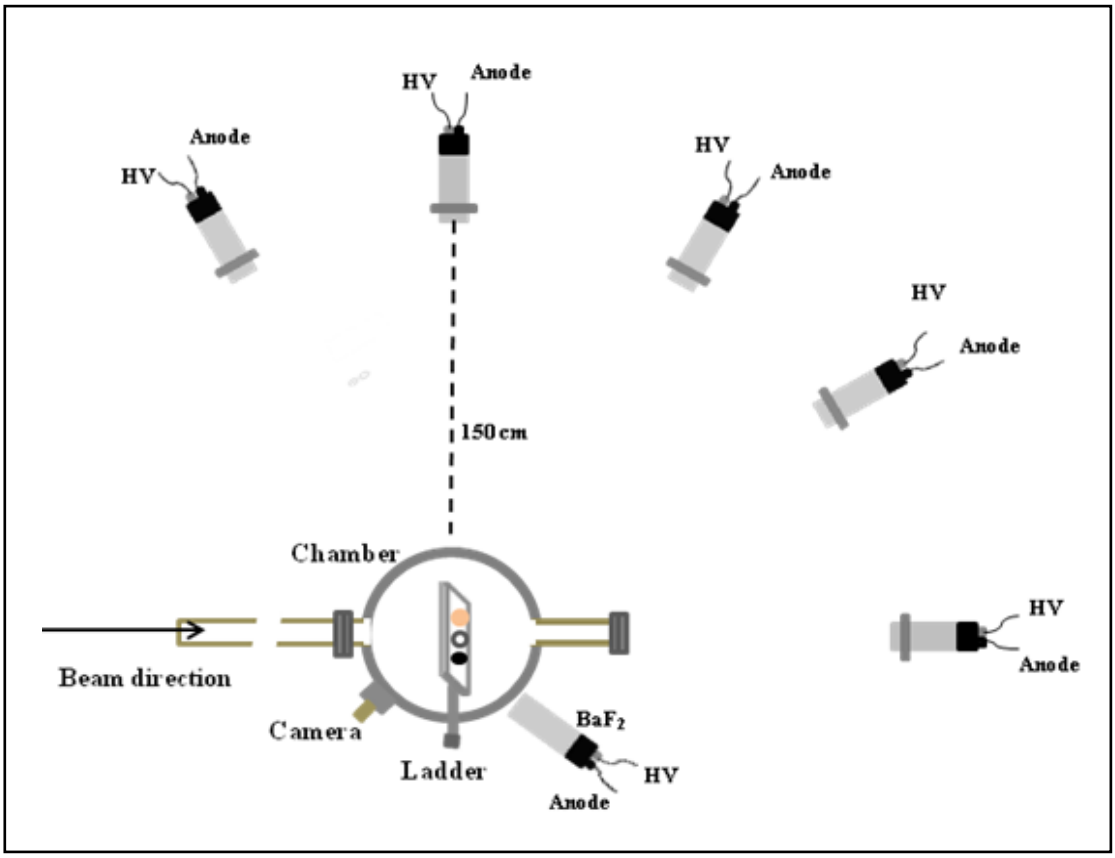

Fig. 5.2 Schematic presentation of the experimental setup.

The center of the target to the center of the detectors was kept 150 cm apart. The detector details as mentioned by the manufacturer are given in Table 5.1. The anode signal of all the five detectors were taken out from beam to the counting room for further processing. A separate BaF_2 detector was mounted very close to the target chamber to monitor the beam pulse width.

The target was mounted in an aluminium chamber of 10 cm height and 45 cm of diameter. The chamber had a bellow type mechanism for moving the ladder on which target was mounted, in and out for positioning it.

Table 5.1 Properties of Eljen technology EJ301 organic liquid scintillators

Properties	**EJ301**
Light Output (% Anthracene)	78
Scintillation Efficiency (photons/1 MeV e^-)	12000
Wavelength of Maximum emission (nm)	425
Decay time (ns) [short component]	3.2
Specific gravity	0.874
Refractive index	1.505
No. of H atoms per $cm^3(\times 10^{22})$	4.82
No. of C atoms per $cm^3(\times 10^{22})$	3.98

In the chamber along with the target, a piece of graph paper and an alumina disc were also mounted for periodically monitoring the beam location by looking on the burn mark on graph paper and illumination on the alumina disc. The wall thickness of chamber was ~2 mm such that the emerging neutrons do not undergo any significant scattering. A Fluka simulation was done to study the attenuation due to the thickness of chamber. An attenuation of < 5% for 1 MeV neutrons traversing the chamber was obtained and this further reduces as neutron energy increases. For the measurement of neutron yield from thick aluminium target, instead of using a chamber, the target was designed in a hemispherical shape and was mounted as beam dump,

as can be seen in Fig 5.3. For the thin target yield measurement, the beam line was extended by 2 m from the target chamber and a thick tantalum disc was pasted on an aluminium end flange. Since, the ions hitting the tantalum disc were still energetic and well above the neutron emission threshold energy of tantalum, it led to high emission of secondary gammas and neutrons.

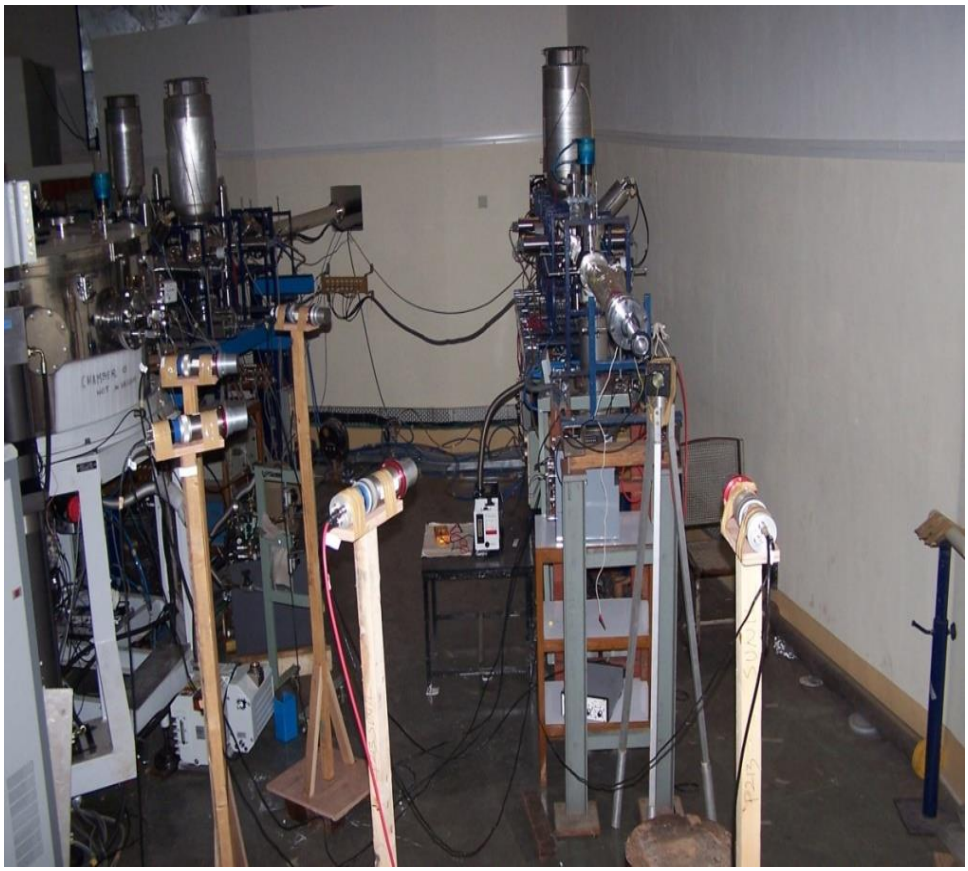

Fig. 5.3 Actual picture of one of the experimental set up.

The shielding around the end flange was constructed to cut out the gammas and neutrons coming from the dump that may reach the neutron detectors. The beam dump was completely shielded using lead bricks and high density polyethylene (HDPE) blocks as shown in Fig 5.4.

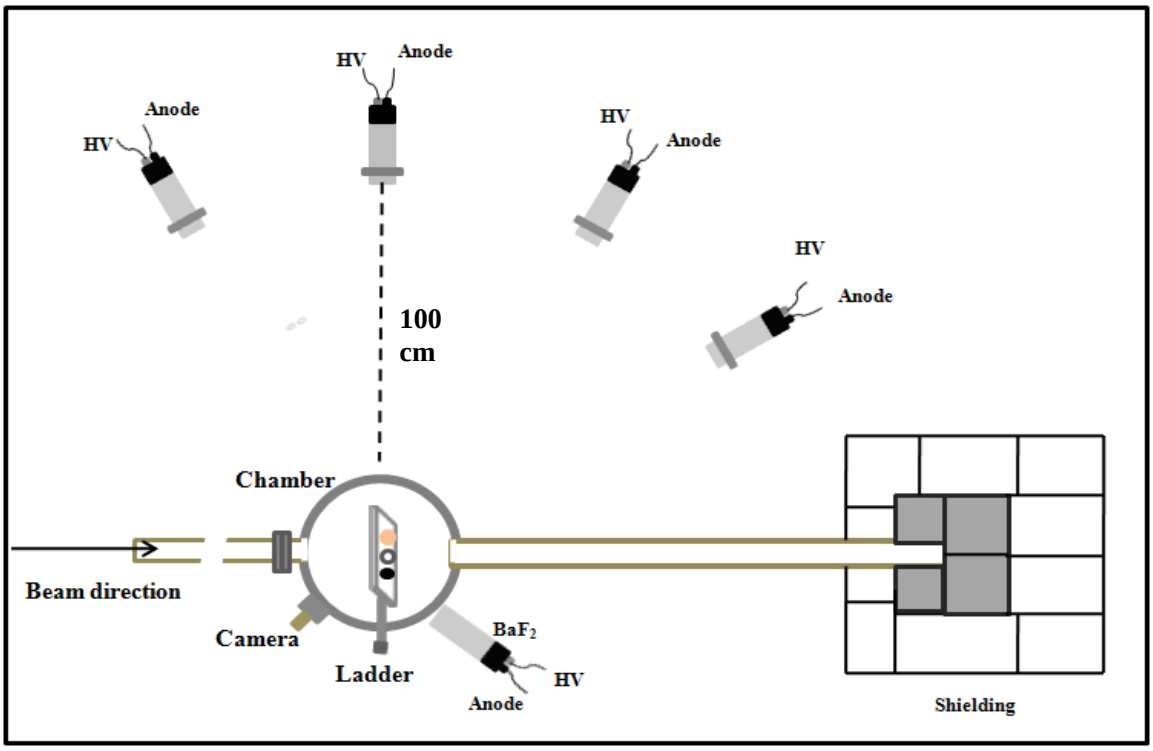

Fig.5.4 Schematic presentation of the experimental setup for the thin target measurement.

The experimental measurements were inclusive in nature, it consisted the direct neutrons as well as the scattered neutrons from the nearby walls and the structural materials. The scattered component was subtracted using shadow bar method. A HDPE bar of length 30 cm and diameter 5.08 cm, in combination to an iron rod of same dimensions were placed in between the target and the detector. The neutrons emitted from target in forward direction will undergo multiple inelastic scatterings in the iron rod and is eventually stopped in the HDPE rod. This stops the direct contribution of the neutrons from the target reaching the detector. Thereby the detector sees only the scattered component of the neutrons from the surrounding. The difference of the scattered component from the total (inclusive) measurement will give the direct neutron contribution. Only one shadow bar was employed at a time to avoid scattering from a neighboring shadow bar. The schematic of the shadow bar placement is also shown in Fig 5.5.

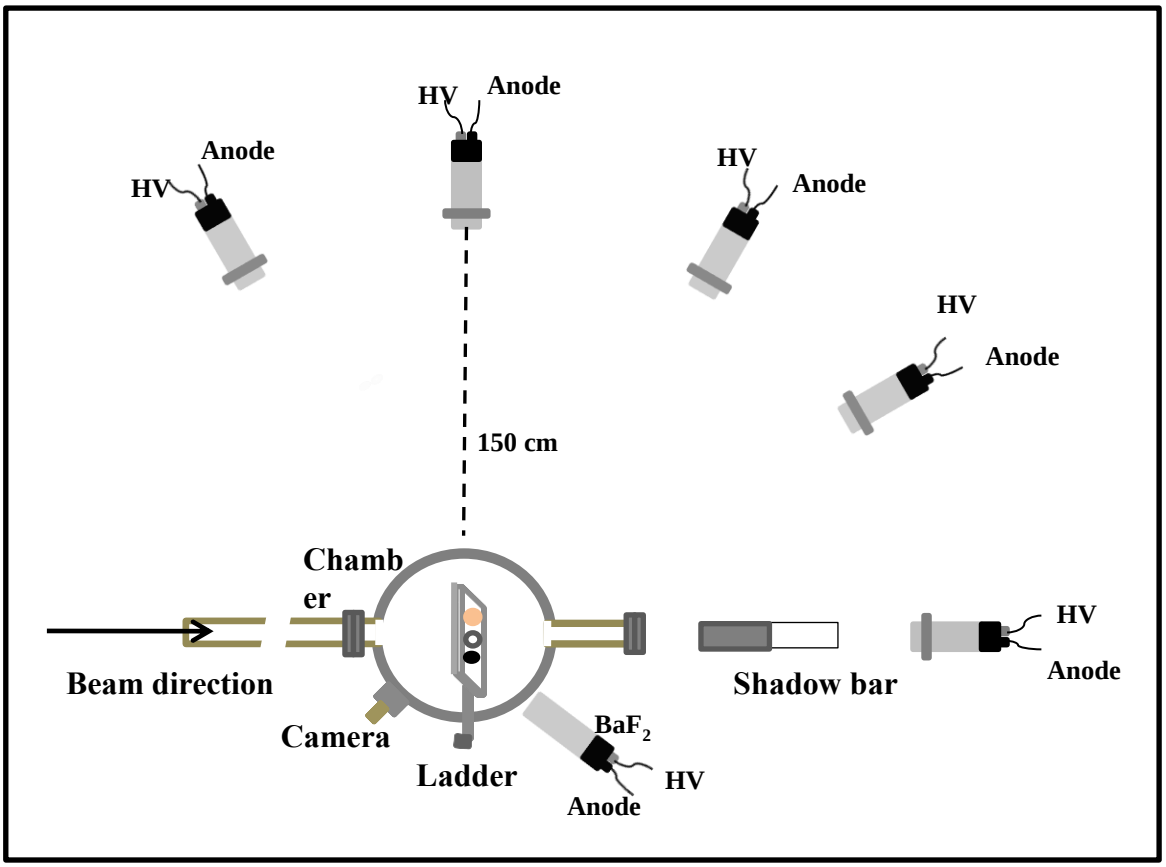

Fig. 5.5 Schematic presentation of the experimental setup with the shadow bar arrangement for the background correction for the 0º measurement.

A Fluka Monte Carlo [63] simulation was carried out to ensure that this configuration of shadow bar is adequate to stop the direct neutron contribution from the target. The target was mounted inside the chamber and its thickness was kept larger than the range of the highest energy projectile and was calculated using SRIM [126] package, which were 116.0 MeV and 115.0 MeV carbon ions in the thick targets C and Al, respectively. The block diagram for the electronic circuit used for data acquisition is shown in Fig 5.6.

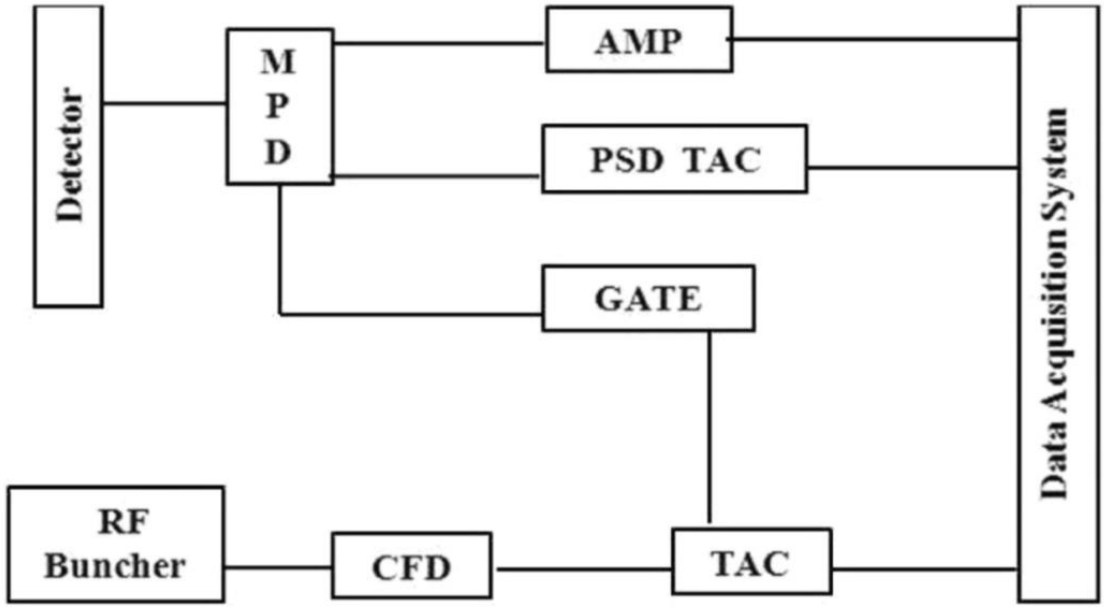

Fig. 5.6 Simplified block diagram for the electronics used for data acquisition (shown for one detector).

5.2.1 Electronic Set-up

The four-channel multi parameter discriminator (MPD-4) electronic module of make Mesytec [127] was used. MPD-4 unit has the pulse shape discriminator (PSD) and constant fraction discriminator (CFD) as its internal components. It uses the ratio of fast to slow component of the scintillator light output and converts it to a time to amplitude signal. The anode output of the detector, which is a fast signal and used for timing information was drawn from it and was given as input to the MPD-4 unit. The MPD-4 unit has pulse height, pulse shape discrimination and the timing gate information as three outputs. The first output, pulse height distribution carries the energy information of both the neutrons and the gammas. The experimentally measured 1-D pulse height distribution of neutrons and photons from one of the actual experimental measurement is presented in Fig5.7. The amplifier output is delayed and is given as input in the Analog to digital converter (ADC) through multi-channel analyzer (MCA).

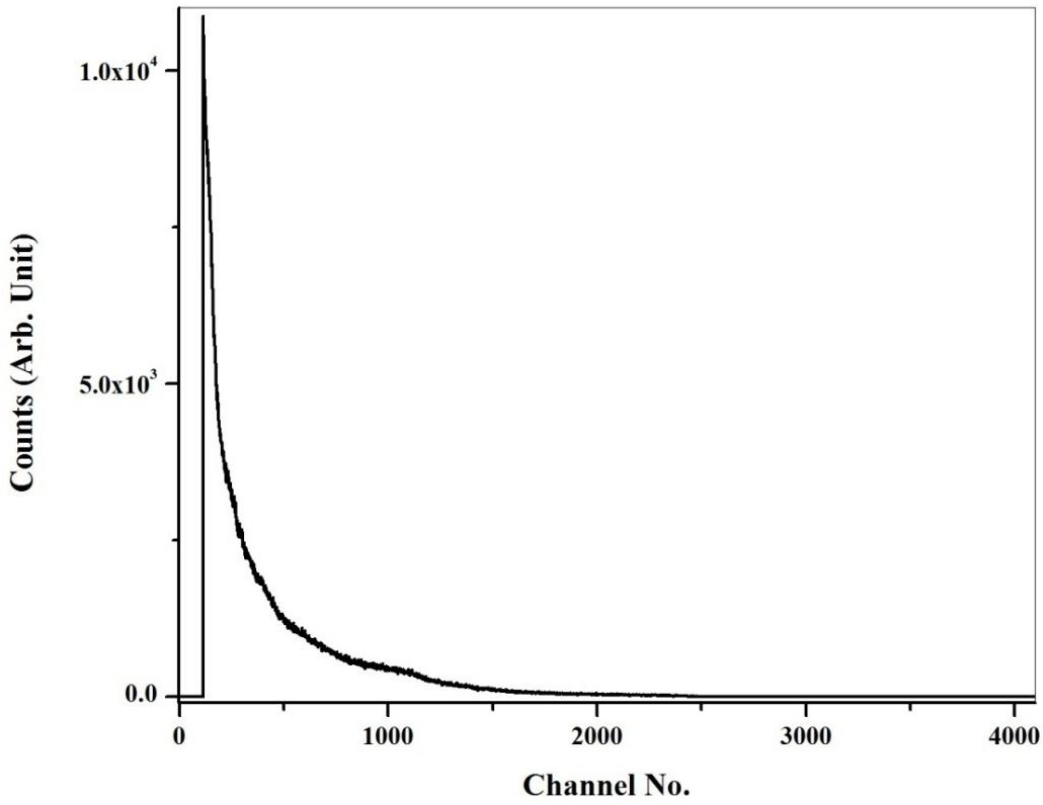

Fig. 5.7 Experimentally measured 1-D pulse height distribution of neutrons and photons.

The second output is the pulse shape discriminator output. The signal produced by the internal PSD unit is integrated and differentiated in an amplifier and added to produce a bipolar signal. The point of zero crossing of this bipolar pulse is independent of the amplitude of the input signal, but only depends on the rise time of the detector signal, as shown in Fig 5.8.The pulse generated by the electrons produced from gamma interaction in scintillator has difference in rise time compared to the rise time of pulses produced by recoil protons from neutron interaction in the same scintillator material. Thus, the time difference in the rise and decay tail of the pulse can be converted to amplitude using a time to amplitude converter (TAC).

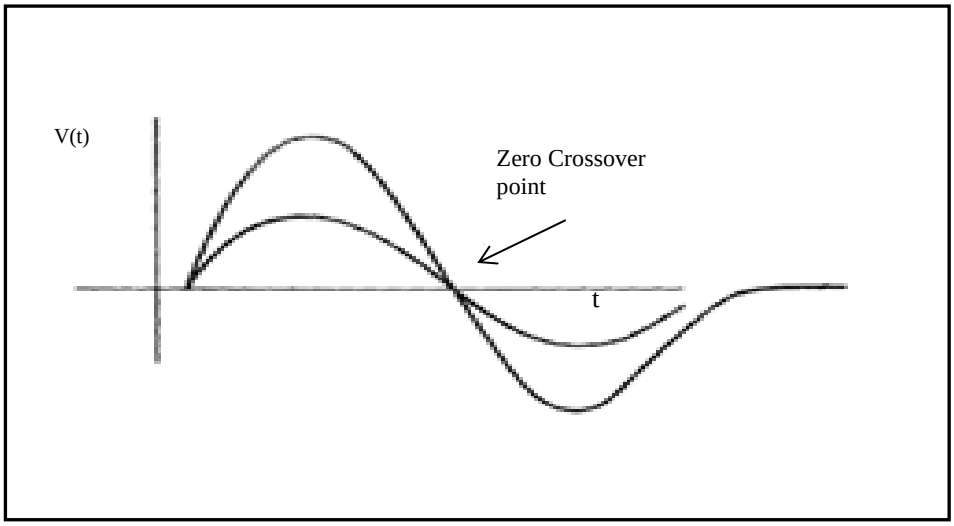

Fig.5.8 Bipolar pulses of different amplitude showing the same time of zero crossover.

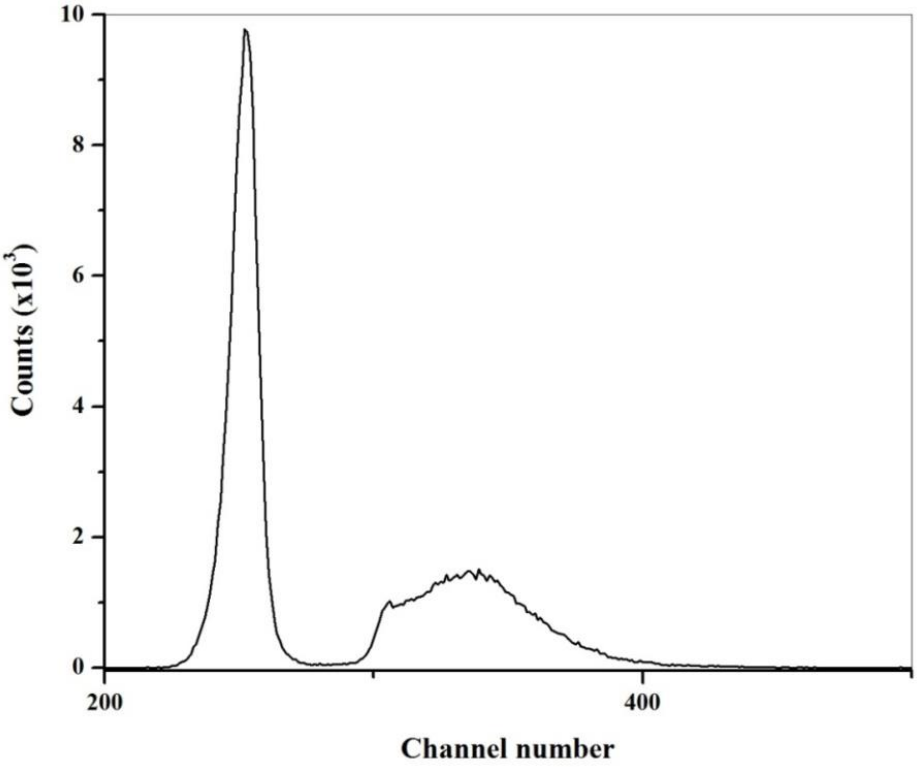

Fig. 5.9 Experimentally measured 1-D pulse shape discrimination spectrum for neutrons and photons

The neutrons by this method are separated from the mixed field of gammas; the Fig 5.9 presents the TAC output of MPD-4. When the pulse height is plotted against PSD output to obtain a 2-D plot as shown in Fig 5.10, a separation between gamma and neutrons is seen. The

lower extended band corresponds to the gamma distribution and the upper distribution corresponds to the neutron, as marked in the figure.

The pulse height distribution and the PSD distribution can be traced back by taking projections on x-axis and y-axis respectively. A careful inspection shows there is an overlap in the circled area as marked in Fig 5.10, which makes it difficult to completely separate neutrons from gammas, which is a source of uncertainty in the calculated distribution.

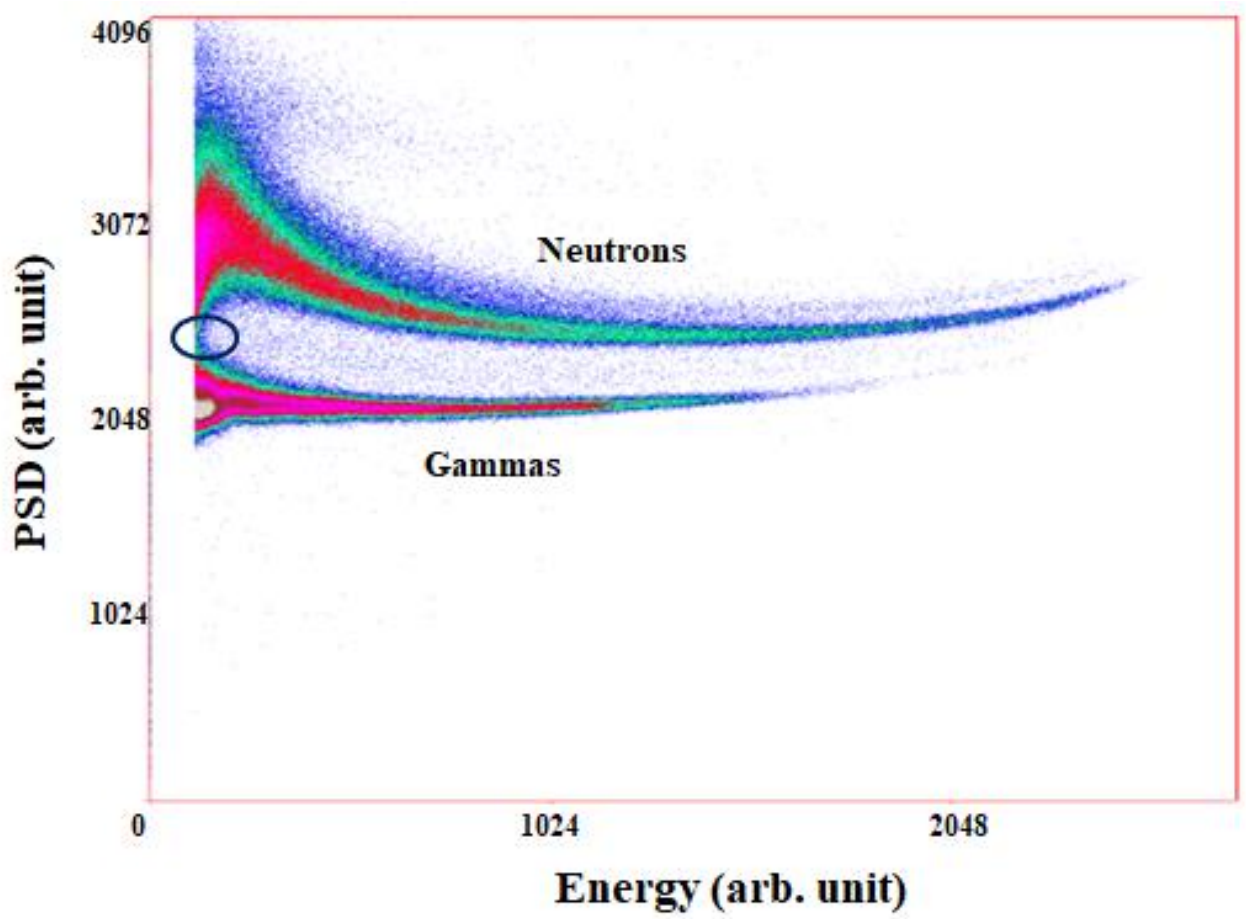

Fig. 5.10 Two dimensional plot when pulse height (x-axis) is plotted against pulse shape discrimination (y-axis), showing neutron and gamma separation as indicated.

The one dimensional time of flight spectra is shown in Fig 5.11, the two peaks corresponds to the gammas and the humps correspond to the neutrons, from the two bunches of beam projectile on the target. A 2-D plot of pulse shape discrimination versus the time of

flight TAC spectra is presented in Fig. 5.12, again the x-axis and y-axis projections retraces the two quantities back. The two chunks on the upper side as marked in the figure correspond to the two neutron clusters coming from the two bunches of the beam that fall within the TAC settings.

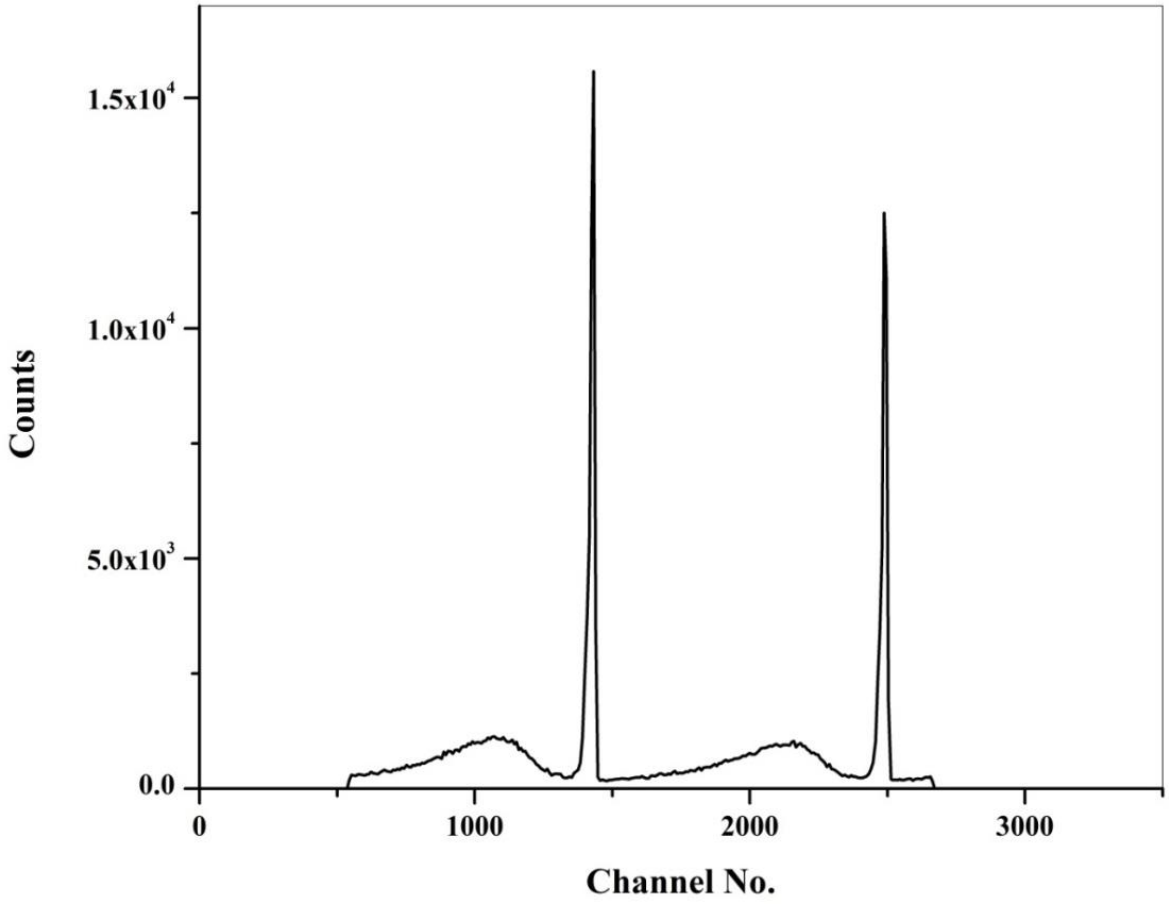

Fig. 5.11 Experimentally measured 1-D time of flight spectra showing neutrons (humps) and the gammas (peaks). Two bursts of beam are seen in the TAC range.

The separation between neutrons and gammas is comparatively better with much reduced uncertainty. The neutron distribution thus can be extracted by preparing a software gate during the offline analysis. In order to convert the data to some meaningful distribution, the flight time

information of the emitted neutrons is extracted using the TAC calibration factor in addition to the prompt gamma peak positions.

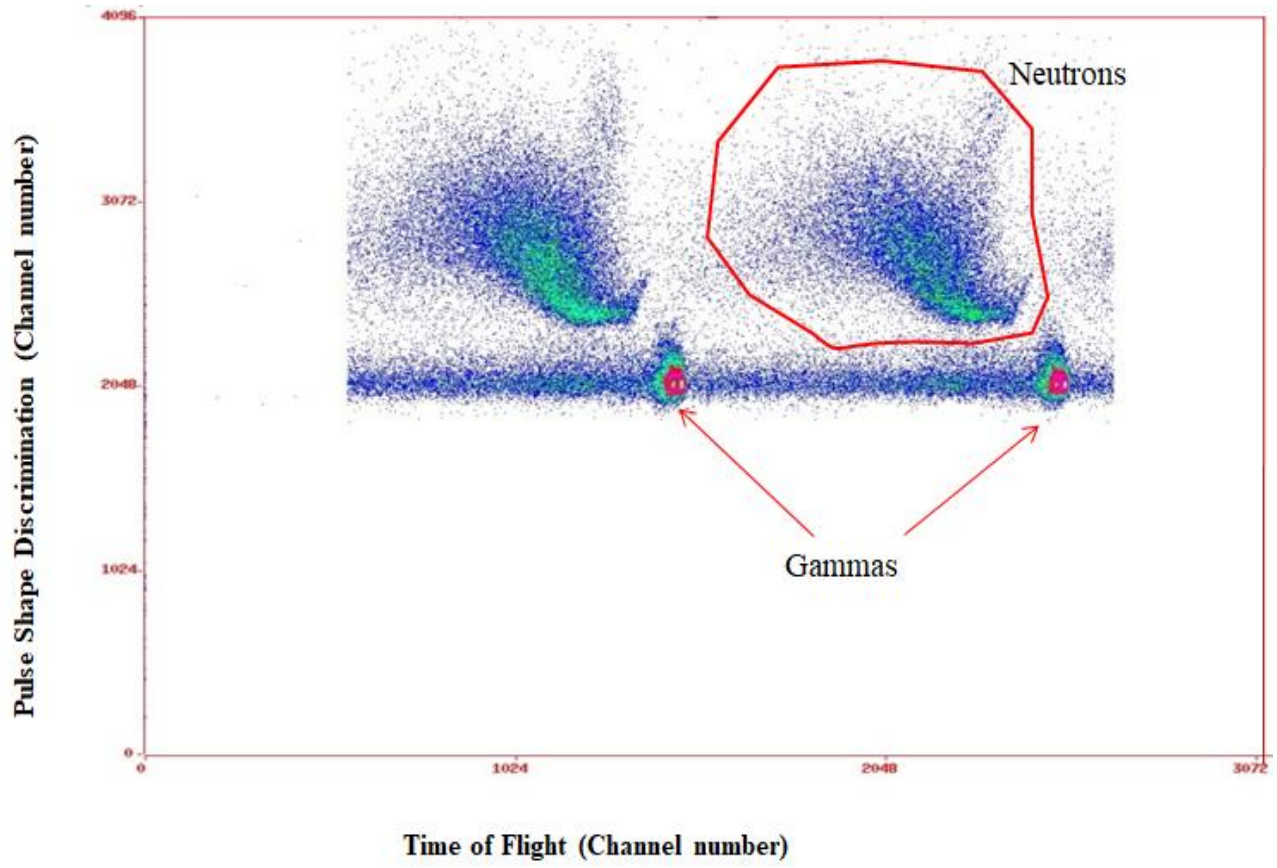

Fig. 5.12 Two dimensional plot of PSD and TOF spectra showing neutron and gamma well separated. Two bursts of beam are seen in the TAC range

The third output from the MPD-4 unit is the timing and the control logic gate which is split using a fan in fan out (FIFO) unit. One part of this logic gate, from all the detectors was ORed to construct the master gate for the pulse acquisition. The second part goes as the start input in the time to amplitude converter, Canberra make (Model 2154). The stop input in the TAC is drawn from the RF output of buncher that signals the arrival of the beam pulse at the target. This TAC unit converts the time difference between the events, beam pulse reaching the target and then the second event when the neutron emitted from the target reaches the detector after travelling a fixed length of path. The amplitude output from TAC unit is given in the ADC, which is the third parameter of the experimental measurement from one detector. The

energy information of the neutrons is embedded in the travel time for the neutrons over the fixed length thus we get a broad time spectrum for the neutrons in TOF spectra. A BaF_2 detector was placed very close to the target chamber to obtain the spread in the beam bunch. Though, a very good timing was obtained and the full width at half maxima was measured as less than 1 ns. The figure of merit for the measured spectra is defined as the ratio of the separation between the gamma and the neutron peaks to the sum of the FWHM of both the peaks as can be obtained from Fig 5.8. The peak positions can be obtained by fitting a Gaussian curve. The mathematical expression for FOM is

$$FOM = \frac{(P\gamma - Pn)}{(FWHM\gamma + FWHMn)} \tag{5.4}$$

where, $P\gamma$ and Pn are the gamma and neutron peak positions respectively. $FWHM\gamma$ and $FWHMn$ are the full width at half maxima of the gamma and the neutron peaks respectively. Figure of merit for a detector tells about how well is the neutron and gamma separation. The FOM for the detectors used was in range 1.2-1.4.

Time calibrator (Canberra make) was used for calibrating the TAC's (TOF). Time calibrators are units, which generate sharp and periodic pulses that are separated by a known time period set by the user. The difference between the channel numbers of the pulses for the chosen difference in time set in the time calibrator is the calibration factor. The smallest pulse that can pass to the data acquisition system is decided by the threshold set in the CFD of the MPD-4 unit. If the threshold is kept high the low energy neutrons will be cut off, while a very low threshold will introduce very high noise components. The threshold for the detector is measured in the pulse height spectra and is important parameter to define the efficiency of the detector. Using standard point gamma sources the energy threshold of each detector was determined. Two peaks of sodium (^{22}Na) and a peak of cesium (^{137}Cs) were used for the energy calibration of the detectors, which was carried out individually. The energy calibration curve

for one of the detectors is shown in Fig 5.13. The pulse height obtained from the detector is calibrated using gamma peaks.

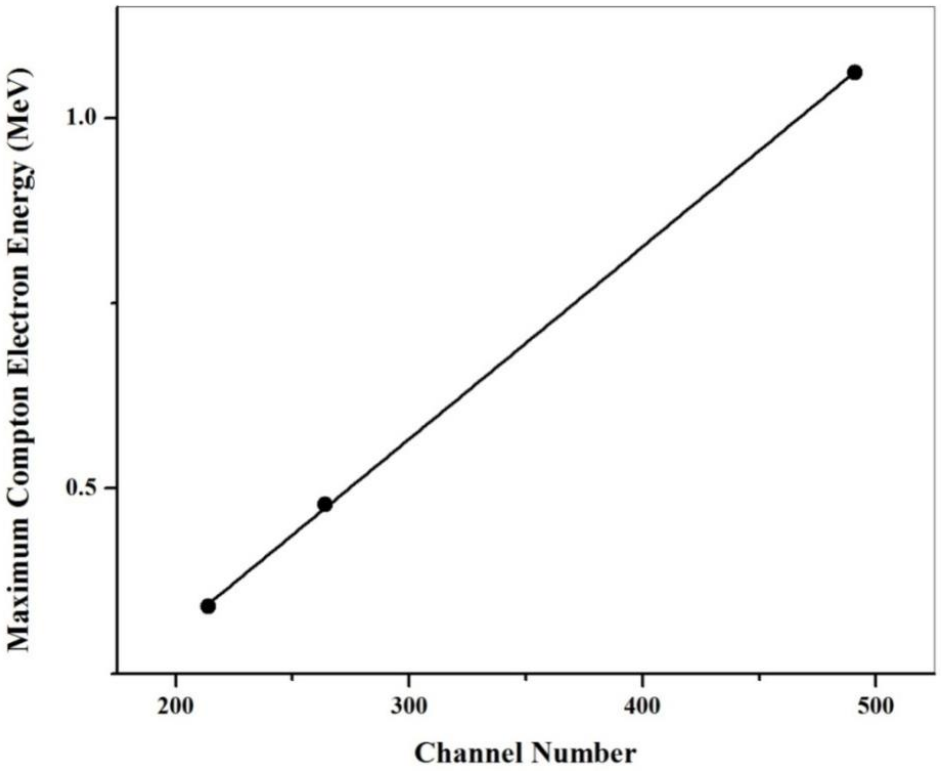

Fig. 5.13 Energy calibration curve used in experiment for one of the detector. The gamma sources were used and a linear fit is obtained.

Since the liquid organic scintillator has low Z constituents, the pulse height spectrum obtained does not have a photo peak. Consequently, the Compton edge (maximum energy transferred to electron by the photon) can be used for the calibration. Also, the pulse height is nonlinear with the proton energy but is linear to the electron energy deposited. Thus, the calibration for proton recoil energy is done in terms of equivalent electron energy.

For detectors based on proton recoil measurements if it constitutes only one elemental species like hydrogen then its intrinsic efficiency is given as,

$$\epsilon = 1 - \exp(-N\sigma_s d) \tag{5.5}$$

here, σ_s is the scattering cross section of hydrogen, N is the number density of target nuclei, and d is the path length for the incident neutrons in the detection medium.In EJ-301 used for our experimental measurements, the H/C (atomic ratio) can be calculated from the number densities of hydrogen and carbon atoms given in Table 5.1, is ~ 1.21, and hence neutron scattering from carbon nuclei also need to be considered for the counting efficiency calculations. Taking in the recoil effects from carbon nuclei also, modifies the intrinsic efficiency equation (5.5) and is given as follows

$$\epsilon = \frac{N_H \sigma_H}{N_H \sigma_H + N_C \sigma_C} [1 - exp\{-(N_H \sigma_H + N_C \sigma_C) d\}] \quad (5.6)$$

where, the subscript C and H stand for carbon and hydrogen values for the parameters defined above respectively.

The intrinsic efficiency of the detector for threshold energy E_{th} = 120 KeV was generated using Monte Carlo simulations [128, 129] and is presented in Fig 5.14. The measured neutron yield has been corrected for the detector intrinsic efficiency, solid angle and the total number of incident projectiles on the target.

Gaining experience from the $^{12}C+ ^{27}Al$ at 115.0 MeV measurements where CAMAC based acquisition system was used which has high dead times, for the next set of time of flight measurements VME based system was used which has low front-end dead time and high data throughput. The dead time losses recorded during data acquisition was found to be less than 1%, and the final results were corrected for the same. Also instead of using TAC and CAMAC ADC, VME based TDC and 32 channel multi event peak sensing ADC with scalar and other components were used.

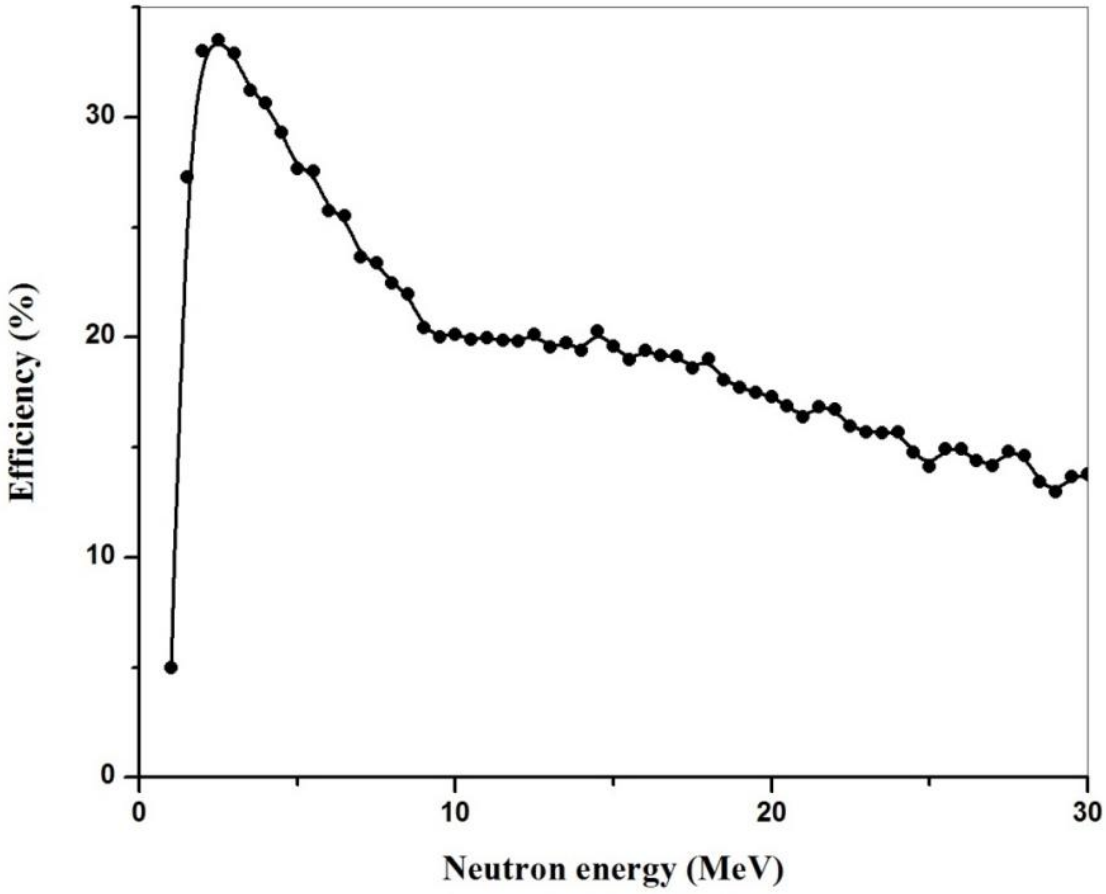

Fig. 5.14 A typical efficiency plot of one of the detectors obtained by Monte Carlo simulation (line is to guide the eyes).

5.2.2 Details of Target material

The experimental measurements were carried out in the Pelletron-Linac, BARC-TIFR [130, 131] facility. Thick targets were chosen, since the neutron yield actually represents the practical scenarios of any accidental or intentional beam hitting or loss anywhere in the structural material, beam line or beam dump. The thick target neutron yield, its energy and the angular distribution forms the basis for neutron dosimetry and shielding studies in any ion accelerator. The thickness of the targets is such that, the accelerated projectile completely stops within it after gradually losing its energy through the interactions. The neutron yield emitted from the thick target are known as the thick target neutron yield (TTNY), these are essential in the source term estimation for accelerator shield design. These data are also useful in dose

calculation to the healthy tissues in patients, due to the secondary neutron interactions during the heavy or light ion therapy. It is also worthwhile to point out that analysis of neutron angular distribution provides some insight in the mechanism of reactions populating the neutron emission channels [132]. The thick target makes it possible to make measurements in the extreme forward direction with respect to the incident ions. This measurement is important as the forward emissions carry the information about the early stages of the nuclear reaction and the compound nuclear formation. The neutron emission data from both thin and thick target are scarce, though it is very essential in reactor studies, nuclear physics, in activation studies and most importantly in medical field for isotope productions.

In the present study, the $^{12}C + ^{27}Al$ reaction at 115.0 MeV has been chosen because aluminium is often used as structural material for beam transport, besides there is limited data available on thick target measurements. The target was made from natural aluminium and was designed in hemispherical shape. The aluminium target had thickness of 3 mm and 40 mm of diameter. The target was designed such that the traversing neutrons do not undergo significant scattering and energy loss. Estimations from Fluka code for 1 MeV neutron traversing a thickness of 3 mm and 5 mm of aluminium shows an attenuation of 5% and 8 % respectively, this reduces as the neutron energy increases. The carbon ions incident on the target completely stops within the target as their range estimated from SRIM code in aluminium is 0.2 mm. For the measurement of neutron yield from 116.0 MeV carbon ions incident on thick C target, again the data available was limited and is also important from the point of dose estimation in heavy carbon ion therapy. A set of thin target measurement was also carried out for similar target and projectile combination, for energy ranging from 110.0 MeV to 44.0 MeV with a step of 11.0 MeV. This was done to see how well the assumptions made in modified PACE2 code holds when it is modified from thin to thick target yield calculation. The results for the experimental measurements carried out using time of flight technique are presented in the following sections.

5.3 Experimental Measurement and Data Analysis

In the Pelletron accelerator cesium sputter ion source produces negative ions, which are then accelerated, stripped of electrons and converted to positive ions of various charge states. The analyzing magnet is used for steering and selecting the required charge state. For the time of flight measurement bunching of the beam was done with a temporal separation of ~107.3 ns. The spread of energy over each bunch was estimated to be less than few hundred KeV.

5.3.1 Thick target neutron yield from nuclear reaction system $^{12}C^{+6}$ + ^{27}Al

The charge state of $^{12}C^{+6}$ was chosen and was made incident on the natural aluminium target designed as thick hemisphere. The target when hit by projectiles undergoes a nuclear reaction and results in formation of compound nuclei $^{39}K^{*}$. The reaction has a Coulomb barrier and center of mass energy of 17.70 MeV and 80.31 MeV respectively. The compound nucleus excitation energy is about 96.92 MeV as calculated for the projectile energy of 116.0 MeV. This energy is high enough for the nucleons to carry a part of it and eject from the system. Neutrons are simplest to come out in absence of any Coulomb barrier to overcome. For the nuclear reaction under study the fusion cross-section over different projectile energies estimated from Bass model [81] is presented in Fig 5.15. Using the time of flight technique energy distribution of the emitted neutrons was obtained by measuring the time taken to travel over the known distance and converting it to energy distribution using the time to amplitude calibration factor as presented in Fig 5.16. The experimental data and the reaction code calculations are shown in Fig 5.17. The data is scaled as marked in the Fig. 5.17 for the visibility. The statistical uncertainties in the experimental results are shown as error bars. Due to good statistics in the forward directions the error bars are of the size of the experimental symbols but in the backward direction it starts becoming visible. The experimental data are

shown as symbols, the results from the statistical code modified PACE2 [64] are shown as solid lines while the results from the Fluka [74, 133] code are shown as broken lines.

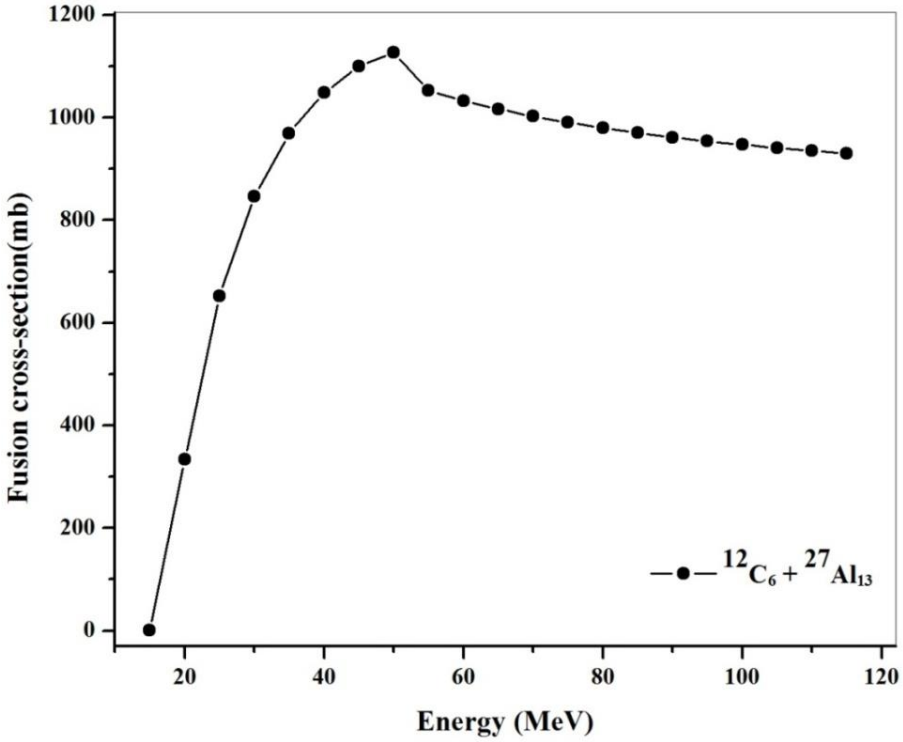

Fig. 5.15 The fusion cross section for the reaction $^{12}C_6$ + ^{27}Al at different projectile energies.

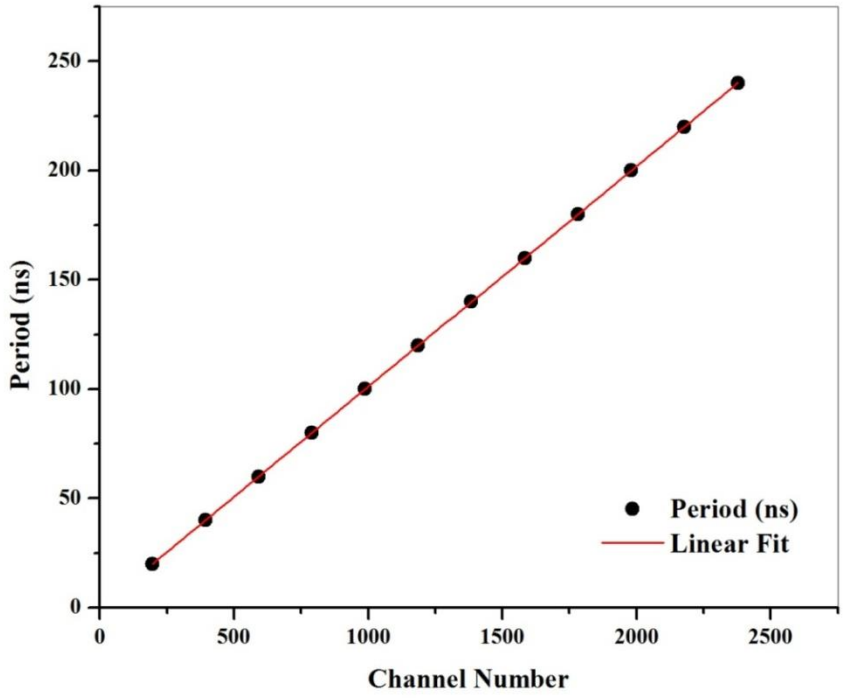

Fig. 5.16 Time to amplitude calibration plot for ^{12}C + ^{27}Al system at 115.0 MeV experimental setup. Calibration factor here is obtained from the slope.

In simulation five liquid organic scintillator detectors have been constructed and positioned similar to the actual experimental setup using Fluka simulation tool. The heavy ion card has been activated and carbon beam has been set with incident energies in MeV/u format. The detector volumes have been assigned with the prepared material as per the compositions mentioned in Table 5.1.

USRYIELD estimator has been used to score the double differential fluence distribution in all the detectors. The code has many physics models which get activated based on the energy of projectile, heavy ion interactions and the domain of reaction. In the present analysis Boltzmann Master Equation (BME) [134, 135] was activated. Whereas, in the statistical code PACE2 formation of the compound nucleus is calculated using the Bass Model [136]. The system is considered to de-excite exclusively by evaporation. Optical model potentials are used for the light particle emissions. The mode of de-excitation is calculated for the excited compound nucleus using a Monte-Carlo random sampling with all possible decay channels according to their respective probabilities. The PACE2 code gives neutron yield from thin target to obtain the double differential neutron yield from thick target the code was modified using an assumption that a thick target is made from many thin targets stacked together. The detailed calculations and assumptions used in modified PACE2 are given in Appendix A.

The experimental measurements in all the directions have a lower energy cut-off of 1 MeV due to the threshold setting and the flight time. The peak energy of the spectra obtained by experiments is about 3.5 MeV at 0º and 30º, which then reduces to 2.5 MeV at 60º and to 1 MeV at 90º and 120º.

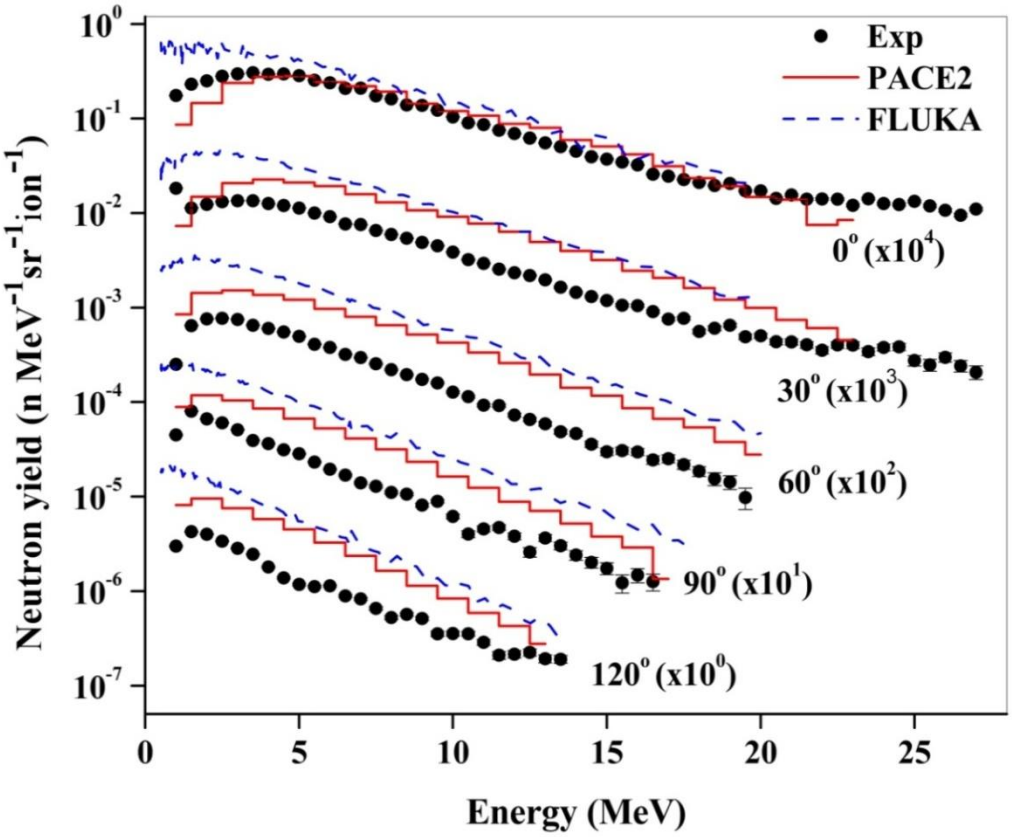

Fig. 5.17 Double differential neutron yield for thick target obtained from experimental plotted in comparison to nuclear reaction model outputs.

Results from the modified PACE2 code shows higher peak energy value at 0º (by 1.5 MeV) but appears to agree well with the experimental data at other angles. The Fluka calculations show lower values at all the emission angles. The slope of the spectra obtained from PACE2 calculations overall agree with the slopes of experimental data at all the emission angles, with minor deviations at the backward angles while the Fluka code appears to predict similar slopes at all angles. The energy differential yield obtained from the PACE2 and Fluka codes agree well with the experimental data in the forward angle but are higher by a factor of 2 to 3 at the backward angles. The comparison between the neutron yield and the scattered component measured by the shadow bar technique as discussed earlier is presented in Fig 5.18. Two representative data one for the forward direction (0º) and the other in the backward direction (90º) is presented, as can be seen in the Fig 5.18.

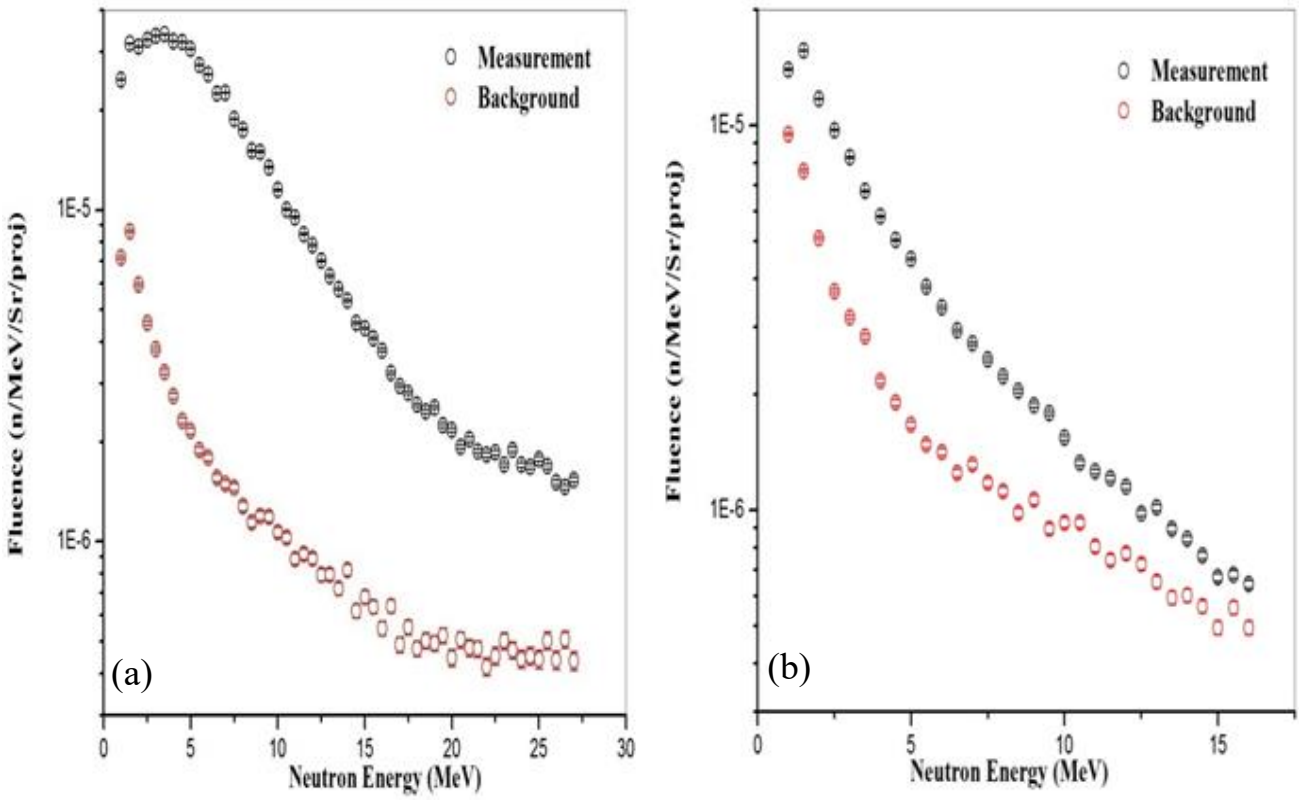

Fig. 5.18 Comparison between measured neutron yield and the background in (a) forward (0º) and (b) background (90º) for the $^{12}C^{6+}$ + ^{27}Al at 115.0 MeV

The yield in extreme forward direction (0º) for the energy less than 3 MeV the yield is almost 4-5 times higher than the background, whereas for the energies above 3 MeV and less than 15 MeV the yield is almost an order high when compared to the background yield. On the higher energy side again the measurement to background ratio is nearly 5 to 3. The yield goes down in the backward direction as is evident from Fig 5.18 (a) and (b).

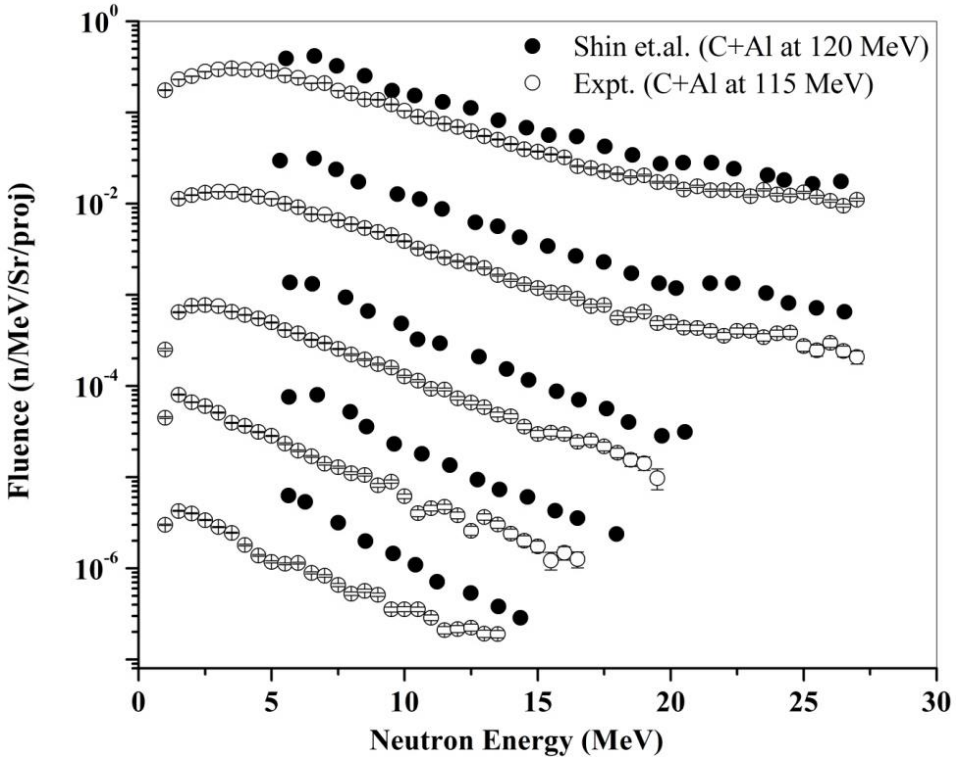

Fig. 5.19 Neutron yield for the carbon ion bombarded on thick aluminium target present study and data from Shin et. al for the mentioned projectile energies. Filled dark circles are the Shin et.al and the open circles are for the present study.

In addition, the neutron yield measurement is nearly three times the background till 10 MeV, the relative increase in the yield in higher energy is found to be less. The forward peakedness of the neutron emission in the studied reaction is evident from the comparison of Fig 5.18 (a) and (b). A comparison from the published work of author Shin et. al. [40] is shown in Fig 5.19. The projectile and target system were same though the projectile energy was different as marked in the Fig 5.19, also the thickness of the target was 2.36 gm/cm^2, almost three times higher than considered in the present study. The high yield can also be contributed to the slightly high projectile energy and the thickness of the target. However, if the slopes of the yield in all directions are compared they grossly seem to match.

5.3.1.1 Angular distribution of neutron yield from $^{12}C^{6+}$+^{27}Al system

The data from the five detectors placed and used simultaneously around the target provides the angular distribution of the emitted neutrons. This can be seen from Fig 5.20, where the energy integrated neutron yield over various angles is shown. The integrated yield for the studied system is presented in the Table 5.2. The experimental data agrees well with the PACE2 data in the extreme forward angle but is lower by a factor of 1.5 – 2.5 at all other angles. On the other hand, results obtained from the Fluka code are higher by a factor of 4.5 – 1.5 with the maximum deviation observed at 0^{o}. The statistical reaction code PACE2 is used to compute the emission from the compound nucleus. Fluka on the other hand uses the Boltzmann Master Equation (BME) [134]. The resulting difference in the yield could be due to different fusion cross section database, the level densities and the optical model parameters used in the two codes. The slope of the measured and the calculated spectra grossly agree with the experimental result. There is no indication of an appreciable change in the slope at higher energies that might have indicated the presence of pre- equilibrium emissions.

Since the emissions calculated by the codes are from the compound nucleus only, the emission from this system appears to be predominantly from the compound nucleus formation and its subsequent statistical decay through various channels.

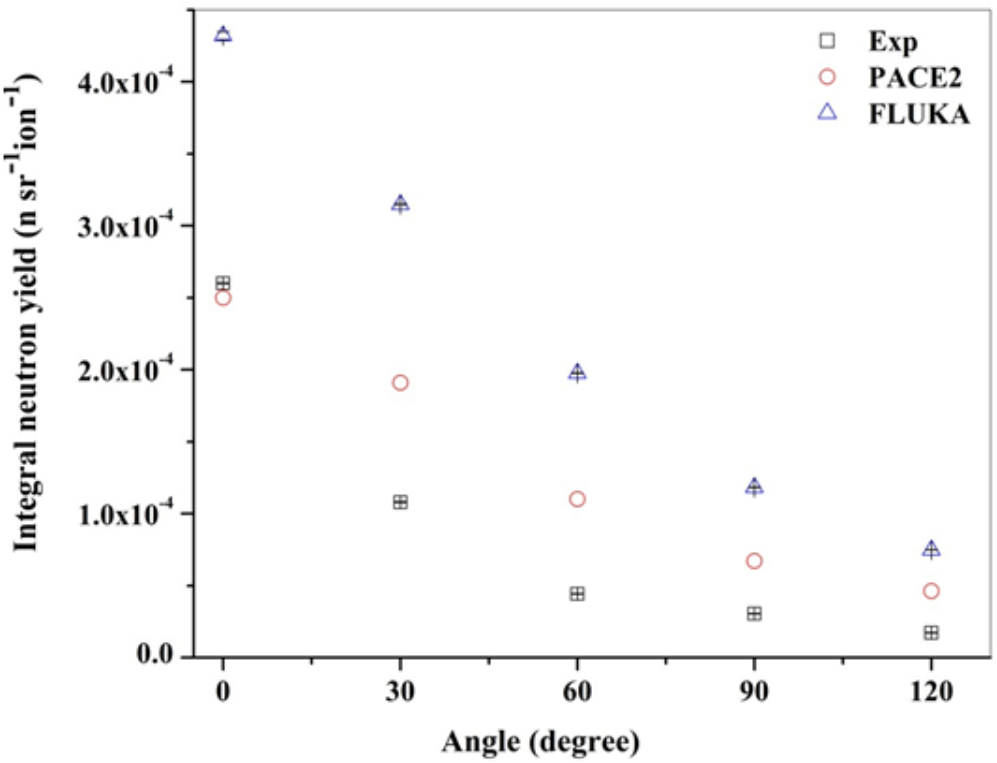

Fig. 5.20 Energy integrated neutron yield obtained from experimental measurements compared with nuclear reaction model outputs.

Table 5.2 Angular distribution of neutron yield from ^{12}C on thick natural ^{27}Al at 115.0 MeV

Angle (degree)	Neutron Yield from 115.0 MeV ^{12}C + ^{27}Al (nSr^{-1}ion^{-1})		
	ToF	PACE	Fluka
0º	2.6×10^{-4}	2.5×10^{-4}	4.3×10^{-4}
30º	1.1×10^{-4}	1.9×10^{-4}	3.2×10^{-4}
60º	4.4×10^{-5}	1.1×10^{-4}	2.0×10^{-4}
90º	3.1×10^{-5}	6.7×10^{-5}	1.2×10^{-4}
120º	1.7×10^{-5}	4.6×10^{-5}	7.5×10^{-5}

The neutron spectra reported here can be used to estimate the unshielded dose rate at unit distance at various angles, for the reaction and energy considered here. From the radiation protection point of view, the discrepancy in the results obtained by the various techniques as discussed could lead to an over estimation of the neutron ambient dose equivalent, when the double differential yield is calculated by the PACE2 and the Fluka codes.

5.3.1.2 Measurement uncertainties

The experimental uncertainties are mainly categorized as normalization uncertainty which is due to pulse pile up leading to detector dead time which was observed to be less than 5 %, the data was accordingly corrected for it. Uncertainty in solid angle due to uncertainty in neutron flight path of the neutron detected in the finite size detector and the position of neutron production in thick target was estimated to be less than 1 %. Uncertainty in beam current integrator was also within 1%. The uncertainty in detector efficiency obtained from Monte Carlo calculations is less than 2%. The other contributing factor to uncertainty is the statistical uncertainty that arises due to statistical nature of the counts in the energy bins and process of subtracting the scattered neutron component from the surrounding structural components. The statistical uncertainties in counts varies from < 1 % in lower energy region to 5 % in higher energy region for forward direction (0° and 30°) and less than 10% in backward angles (90° and 120°) due to the poor statistics; the statistical uncertainty is shown as vertical error bars in result and is anticipated to reduce with increased data acquisition time.

5.3.2 Thick target neutron yield from nuclear reaction system $^{12}C^{6+}$ + ^{12}C

In the range of projectile energy < 10 MeV/A, compound nuclear formation dominates in the nuclear reaction. The compound nucleus so formed as a result of nuclear reaction between the target and the projectile decays probabilistically through the possible available

decay channels. The level density of the compound nucleus and the energy levels of the residual nucleus together decide the emission probabilities through the decay channels. The Coulomb barrier as calculated for the compound nucleus formation is ~ 13.34 MeV. The excitation energy for the reaction $^{12}C + {}^{12}C \rightarrow {}^{24}Mg^{*}$ is ~ 72.0 MeV and the center of mass energy is 58.0 MeV, taking the lab frame projectile energy of 116.0 MeV.

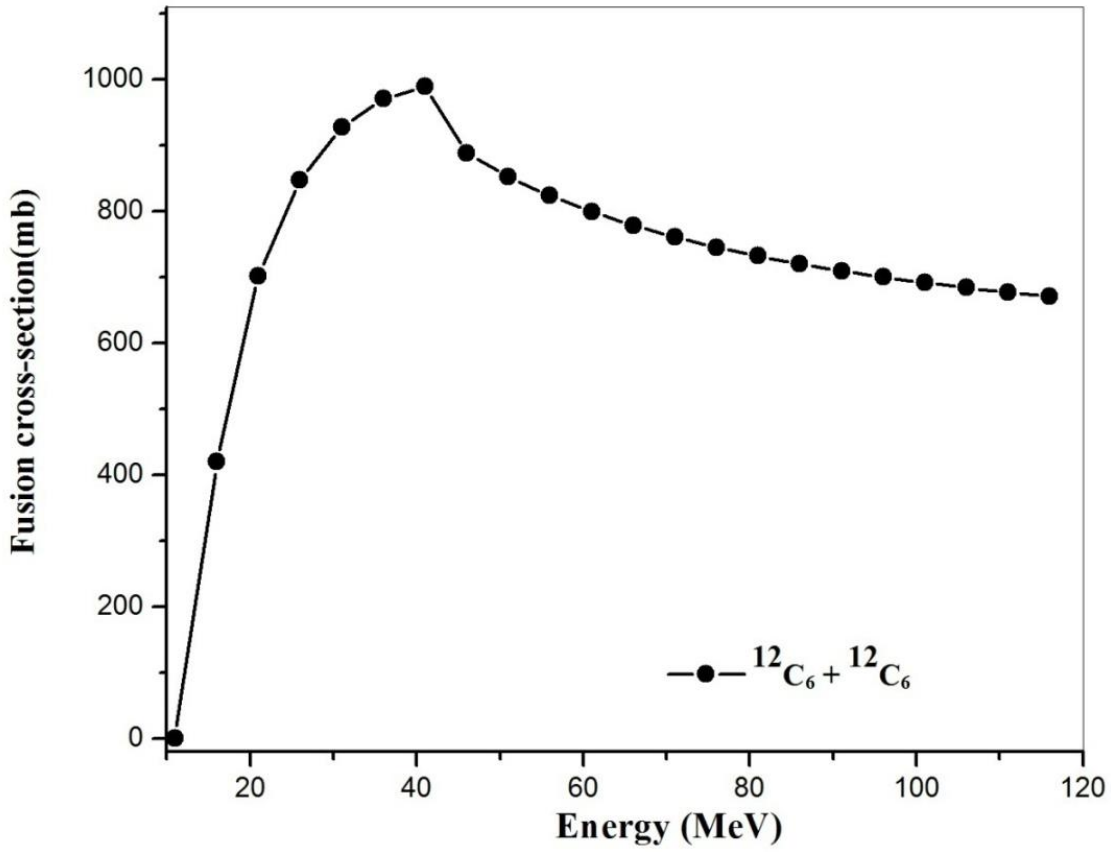

Fig. 5.21 Bass fusion cross-section for $^{12}C^{6+}$+ ^{nat}C system at different projectile energies.

Although, the Coulomb barrier is less for this system when compared to the earlier system but the corresponding center of mass energy and the excitation energy reduces almost by 25.0 MeV. One of the probable channels for the compound nuclei to de-excite is by emitting excess energy in the form of neutrons. The fusion cross-section from the Bass model is plotted in Fig 5.21, for the nuclear reaction system $^{12}C^{6+} + {}^{nat}C$ at various projectile energies. The cross

section steeply rises to a maximum at around 40.0 MeV and then starts gradually falling and decreases by ~ 42 % at 116.0 MeV incident energy.

The order of fusion cross-section is fraction of a barn. Due to decrease in cross-section for higher energy neutron emission the yield of harder neutrons reduces which leads to low statistics and thus the observed fluctuations towards the higher energy side, which are anticipated to reduce to very small with longer acquisition periods. In the low energy part of the spectrum the emitted neutrons follow the Maxwellian distribution which is explained by the evaporation model [137, 138]. The emission of low energy neutrons will leave the residual nucleus with higher excitation energy and since level density will be high the statistical model can be used, which leads to Maxwellian kind of distribution. The neutron yield obtained from time of flight method and as estimated from the codes PACE2 and Fluka are plotted in Fig 5.22.

The emitted neutrons from the compound nucleus in the center of mass frame of reference have isotropic angular distribution with no preference in the direction of emission. However, in the lab frame of reference the neutron emission is forward peaked. Kinetic energy and angular distribution of the thick target neutron yield from $^{12}C^{6+}$ + ^{12}C reaction at 116.0 MeV have been measured. The results from the experimental measurement are plotted and compared with the neutron yield obtained from nuclear reaction codes PACE2 and Fluka in Fig 5.22. The experimental data are shown with filled black circles, PACE2 calculations with open circles and Fluka with open triangles. The data are scaled up as marked in the plot.

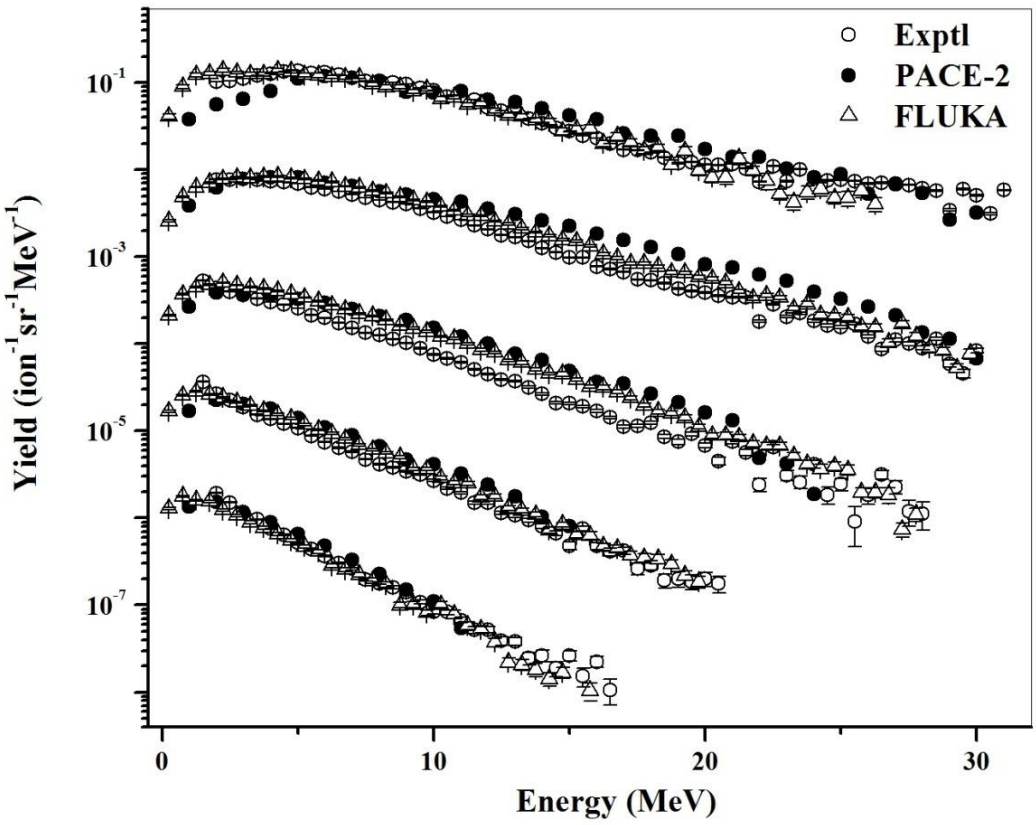

Fig. 5.22 Thick target double differential neutron yield obtained from $^{12}C^{6+}$ + ^{12}C reaction at 116.0 MeV, compared with the reaction model PACE2 and Fluka calculations.

The statistical uncertainty associated with the measurements is presented as vertical bars. At low energy part of the neutron energy spectrum, the error in measured data are small due to good statistics and the error bars are not visible. Nevertheless, at higher neutron energies the counting statistics become poor and the error bar are larger than the symbols. Neutron emission cross section decreases significantly, as one moves towards higher energy leading to low count rates. As a result, the statistics suffer and fluctuations start appearing; data presented here are until where no oscillations occur.

The peak in the energy distribution in the forward angle 0º appears at around 5.0 MeV, which becomes softer as we start moving towards backward angles. At 30º the neutron distribution peaks at 3.0 MeV. As we further move to backward angles the peak of the energy spectrum shifts to 1.5 MeV. The neutron spectrum from thick carbon target is much harder in

the forward direction and softens towards the backward angle. The peak in the experimentally measured spectra appears at lower energies when compared to those in the theoretical calculation of PACE2 and Fluka codes.

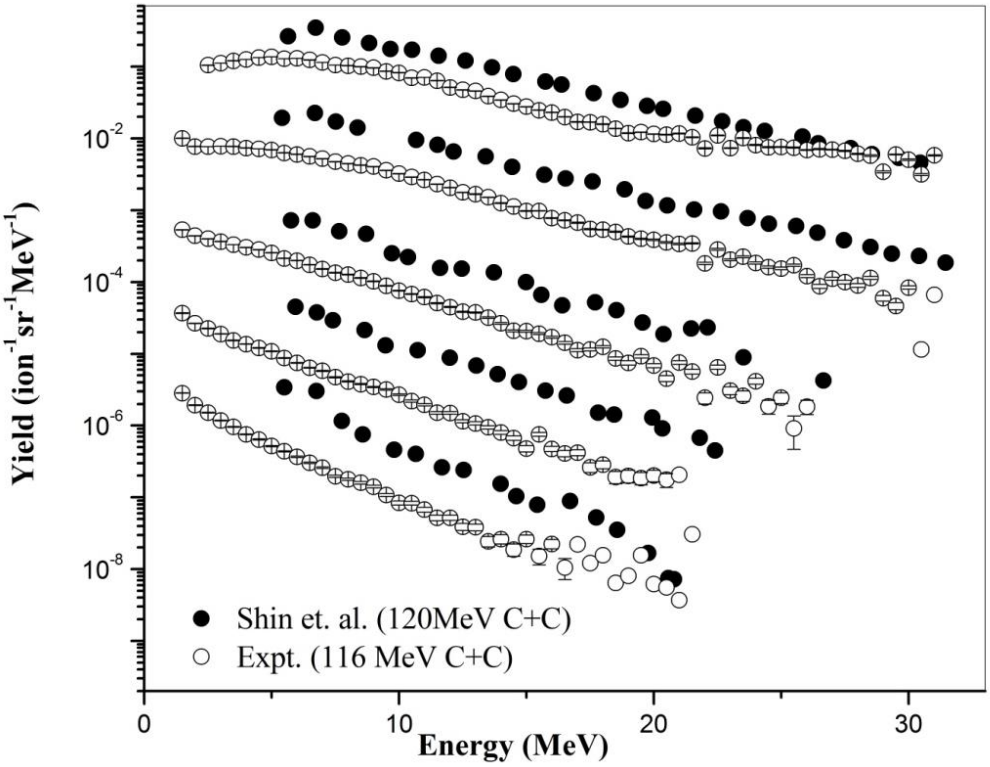

Fig. 5.23 Neutron yield for the carbon ion bombarded on thick carbon target present study and data from Shin *et al* for the mentioned projectile energies. Filled dark circles are the Shin et.al and the open circles are for the present study.

The neutron yield, as can be seen from Fig 5.22, extends up to 30.0 MeV in the forward direction and the maximum energy of the emitted neutrons decreases in the backward angles. It is evident from Fig 5.22, the slope of the experimental measurements match closely with the PACE2 and Fluka calculations in the backward angle, while there is slight deviation in the forward angles. The Fluka calculations agree better with the measured thick target yield compared to that for thin target that can be attributed to the fact that Fluka is a transport code developed to estimate particle production and transport through materials (which simulates thick target). A comparison in the neutron yield from same reaction system from the work of Shin *et al* [40] is also presented in Fig 5.23. The Shin data is higher when compared to the

present study, this can be attributed to the higher projectile energy and the thickness of the target used in Shin measurements is almost three times as ours. However, the slope of the two measurements generally match.

5.3.2.1 Angular distribution of neutron yield from $^{12}C^{6+}+^{12}C$

The double differential neutron yield distribution obtained above was integrated over the energy to obtain the energy integrated angular distribution. The energy integrated angular distribution of the neutron yield is given in Fig 5.24. As can be seen clearly from the figure, the angular distribution has stronger forwardness. There is a reduction of integrated yield by an order from forward to backward direction with respect to the incident beam.

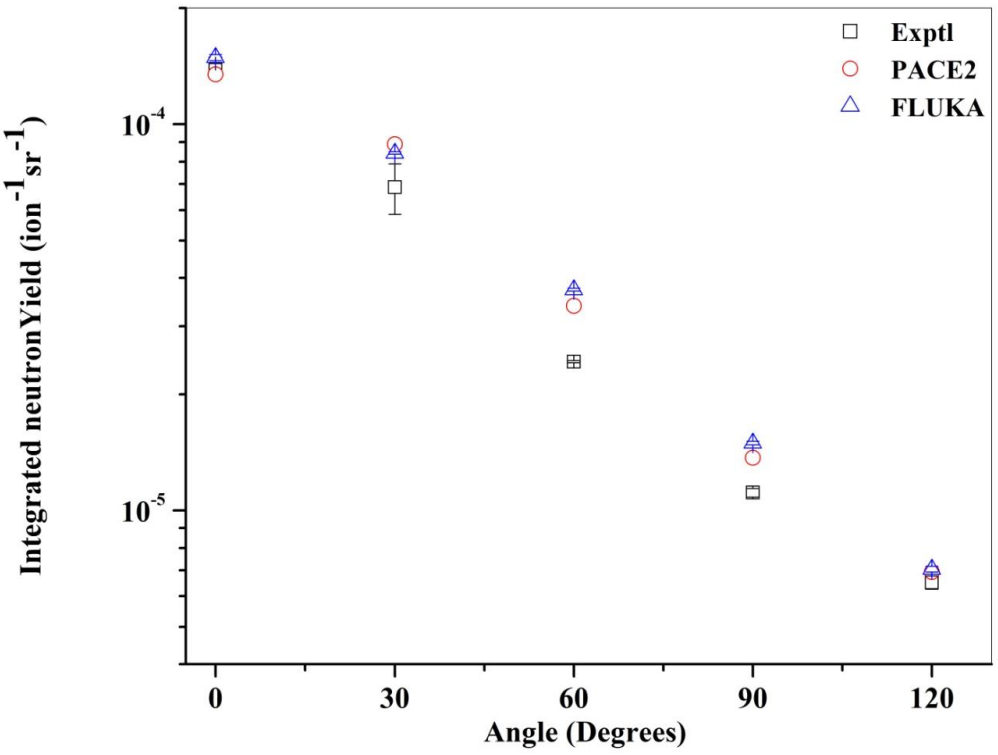

Fig. 5.24 Angular distribution of energy integrated neutron yield as obtained from this experiment and is compared with reaction model calculations.

Moreover, it can be seen that in extreme forward direction the experimental data is falling in between the values of the two reaction codes. In the intermediate directions, both the

reaction codes over-estimate the yield by 40 – 55 %. In the extreme backward direction, the match is comparatively better. The yield values over different angles from the measurement and the two reaction codes are presented in the Table 5.3.

Table 5.3 Angular distribution of neutron yield from ^{12}C on thick natural ^{12}C at 116.0 MeV

Angle (degree)	Neutron Yield from 116.0 MeV ^{12}C + ^{12}C ($nSr^{-1}ion^{-1}$)			Ratio	
	ToF	PACE	Fluka	PACE/ToF	Fluka/ ToF
0º	1.44×10^{-4}	1.35×10^{-4}	1.49×10^{-4}	0.94	1.04
30º	6.87×10^{-5}	8.88×10^{-5}	8.43×10^{-4}	1.29	1.23
60º	2.43×10^{-5}	3.39×10^{-5}	3.73×10^{-4}	1.40	1.54
90º	1.11×10^{-5}	1.37×10^{-5}	1.50×10^{-4}	1.23	1.34
120º	6.51×10^{-6}	6.93×10^{-5}	7.05×10^{-5}	1.06	1.08

5.3.3 Comparison of the neutron yields from $^{12}C^{6+}$+^{27}Al and $^{12}C^{6+}$+^{12}C reactions

In Fig 5.25, the present results are compared with the earlier discussed thick target energy integrated neutron yield obtained from $^{12}C^{6+}$+^{27}Al reaction at 115.0 MeV [42]. The systems have same projectile $^{12}C^{6+}$ and nearly equal incident energies ~ 10.0 MeV/u. The yield from $^{12}C^{6+}$ + ^{27}Al at 115.0 MeV is approximately 1.5 – 2 times in forward direction 0º - 60º, but this factor increases to 2.5 – 4 in the backward angles 90º and 120º. The yield from the two reactions is tabulated in Table 5.4 the ratio between the two is also given.

In the forward directions, the heavier target yields more neutrons almost twice the lighter one while in backward angles the yield is higher by nearly three factors. In the same projectile

and nearly same projectile energy in case of heavier target since the excitation, energy available to the compound nucleus is high by almost 25.0 MeV, the probability of emission of neutrons increases.

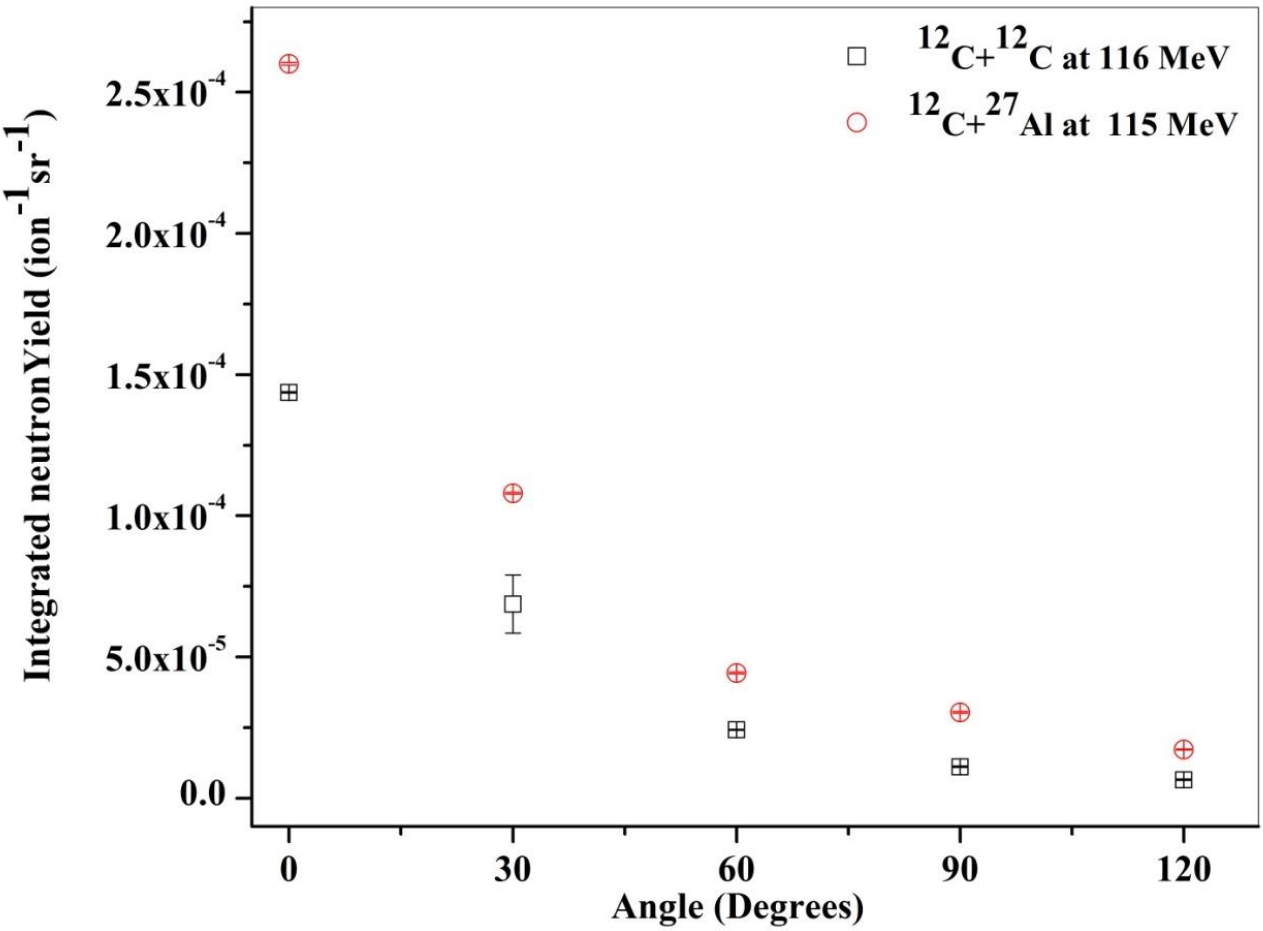

Fig. 5.25 Comparison of the energy integrated neutron yield from $^{12}C^{6+}$ + ^{12}C at 116.0 MeV and $^{12}C^{6+}$ + ^{27}Al at 115.0 MeV.

Table 5.4 Angular distribution of neutron yield from $^{12}C^{6+}$ on thick ^{27}Al at 115.0 MeV vs $^{12}C^{6+}$ on thick ^{12}C at 116.0 MeV

Angle (degree)	Neutron Yield (nSr^{-1}ion^{-1})		Ratio
	$^{12}C^{6+}$ + ^{27}Al at 115.0 MeV	$^{12}C^{6+}$ + ^{12}C at 116.0 MeV	

0º	2.6×10^{-4}	1.44×10^{-4}	1.81
30º	1.1×10^{-4}	6.87×10^{-5}	1.61
60º	4.4×10^{-5}	2.43×10^{-5}	1.81
90º	3.1×10^{-5}	1.11×10^{-5}	2.79
120º	1.7×10^{-5}	6.51×10^{-6}	2.61

5.4 Experimental errors and uncertainties

The factors that contribute to the errors and uncertainties in the time of flight measurements using the liquid organic scintillators are discussed here. The various sources for uncertainty are like the energy spread in the projectile bunches time resolution which further is a function of many other factors. The major contributing factors to the uncertainties are the intrinsic time resolution of the detector, finite size of the target that may result in energy attenuation and time spread due to production of the neutron over the thickness of the target.

5.4.1 Uncertainty in energy resolution

The relative energy resolution and the uncertainty in the neutron energies due to the measurement system, estimated using the time of flight technique as reported in [129] and is given by

$$\frac{\Delta E}{E} = \gamma(\gamma+1)\left(\frac{\Delta t}{t}\right) \tag{5.12}$$

where,

$$\gamma = 1 + \frac{E}{Mc^2} \tag{5.13}$$

where, E is the neutron kinetic energy, M is the rest mass of the neutron, t is the neutron flight time and Δt is the total resolution in time.The factors contributing to the total resolution in the measurement of time distribution are inherent detector resolution, the spread in time of the incident beam bunch, the dispersion in time due to the variation in the energy of the incident beam bunch, time spread due to production of the neutron over the finite size of the target and the time spread due to detection of neutron in the scintillation material at different positions due to finite size of the detector. The uncertainty due to the target thickness can be neglected since its thickness is very small. The total resolution Δt can be approximated as follows

$$\Delta t = \left[(\Delta\tau)^2 + \left(\frac{\Delta x}{v}\right)^2\right]^{1/2} \tag{5.14}$$

where, $\Delta\tau$ is the total time dispersion in the scintillator detector and the prompt gamma spread. It is proportional to the beam bunch spread. Δx is the finite thickness of the detector and v is the velocity of the incident neutron. $\Delta\tau$ is taken as the FWHM of the prompt gamma peak in the neutron ToF spectra. For the thick target experimental measurement $\Delta\tau$ was obtained to be ~ 1 ns, while, for the thin target measurement the spread of prompt gamma was slightly high ~ 1.7 ns. The energy resolution for the studied system is presented in Fig 5.26. As energy resolution completely depends on the experimental setup and not on the reaction system studied, for the reaction systems $^{12}C^{6+}$+ ^{27}Al at 115.0 MeV and MeV $^{12}C^{6+}$ + ^{12}C at 116.0 is given together. In both the measurements the detectors, path length, beam hall and the beam line were same except few differences in the electronics used.

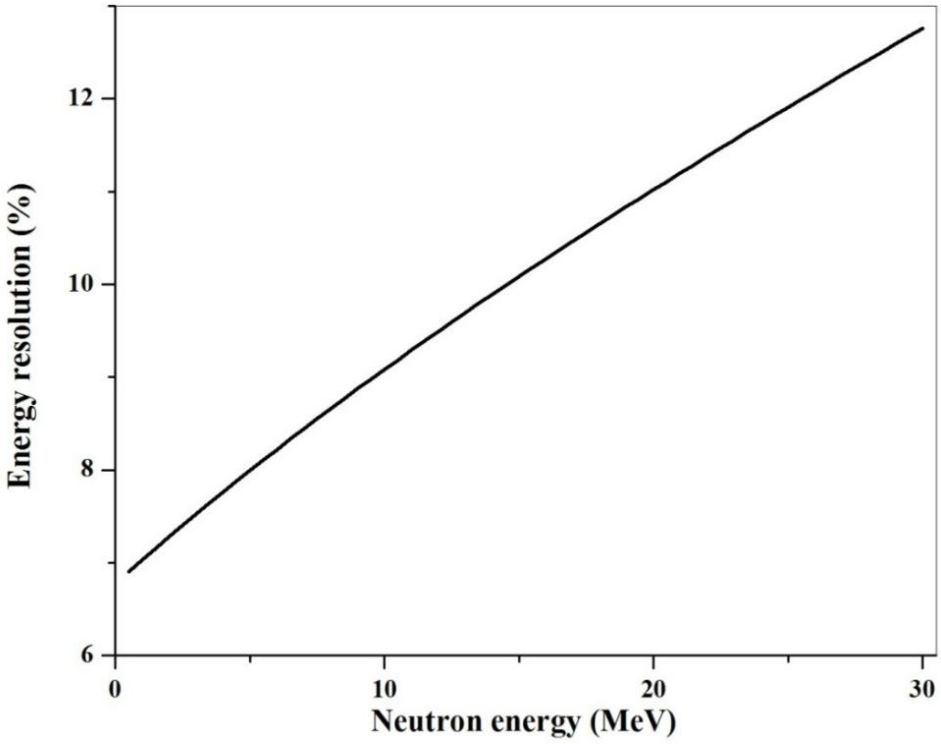

Fig. 5.26 The percentage energy resolution as a function of neutron energy due to time of flight technique, for the present experimental measurements.

5.5 Neutron yield from thin target $^{12}C^{6+}+^{12}C$

Neutron yield from a thin target system $^{12}C + ^{12}C$ over various incident energies were studied and will be discussed here. Since the neutron yield will be low from a thin target, to have better detector efficiency a larger detector 5″ × 2″ set was used in the measurement. Due to the dump which was created at ~ 2.0 m away from the target, to stop the beam; the measurement in 0º was not possible. Four set of detectors were placed at 30º, 60º, 90º and 120º to measure the angular distribution of the neutron yield. Compton edge of the gamma ray spectrum was used for energy calibration of the neutron detectors and to obtain the threshold of the detectors. As seen from the Fig. 5.27 – 5.33, the lower energy cutoff for all the measurements was ~ 1.0 MeV as also determined from the flight time and the TDC settings.

5.5.1 Neutron yield from various projectile energies

The kinetic energy and angular distribution of neutrons from thin carbon target bombarded by ^{12}C in the projectile energy range of 44.0 MeV to 110.0 MeV in steps of 11.0 MeV have been measured. The results obtained from the experimental measurements are plotted and compared to the neutron yield distribution obtained from nuclear reaction codes PACE2 and Fluka in Figs. 5.27 – 5.33. The experimental data are shown with filled black circles, PACE2 calculations with open circles and Fluka results with a histogram.

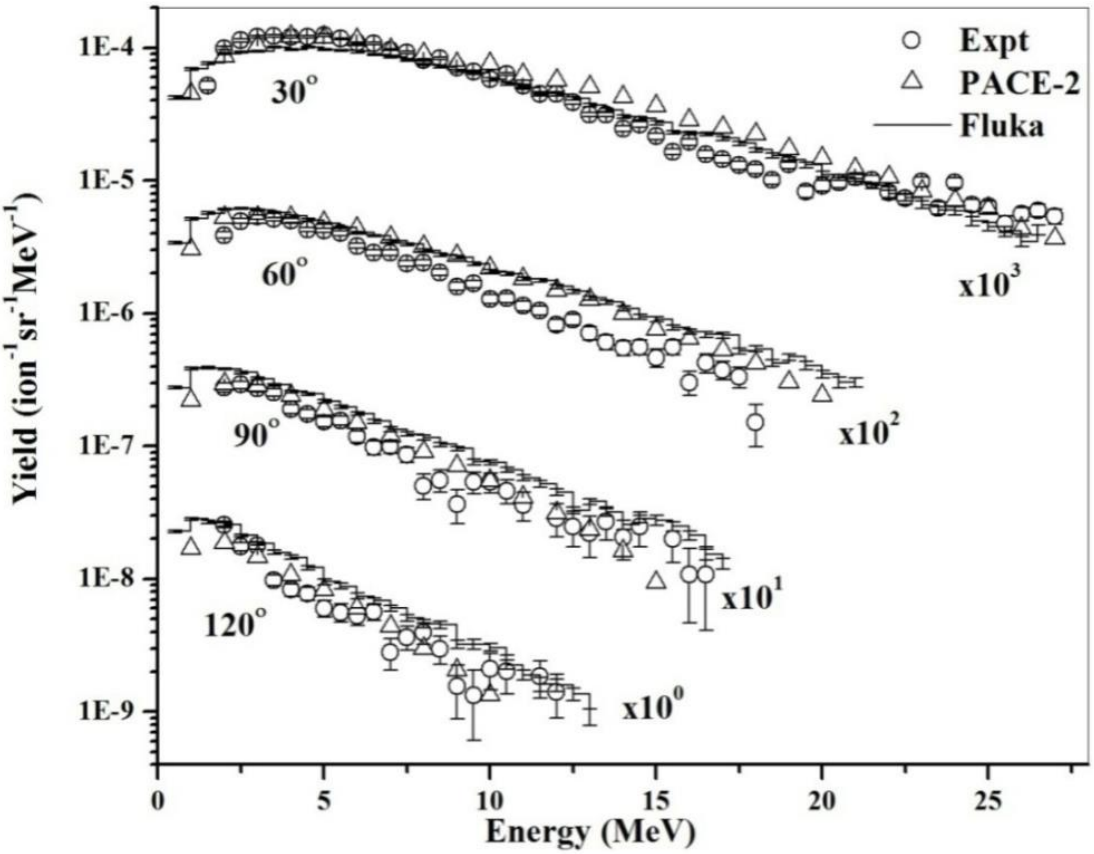

Fig. 5.27 The thin target double differential neutron yield for projectile energy 110.0 MeV, obtained from present experiment (open circles), compared with the reaction model PACE2 (open triangle) and Fluka calculations (histogram).

For the convenience of plotting the data at different angles are scaled up as marked in the plot. The measured neutron yield, as can be seen from Figs. 5.27 – 5.30, extends up to 27.0 MeV in the forward direction for beam energies of 77.0 – 110.0 MeV. The maximum neutron energy at 30^o reduces to around 24.0 MeV for incident energies between 44.0 –66.0 MeV as

seen from Figs. 5.31 – 5.33. In the backward angles this maximum energy of the emitted neutrons decreases and varies between 18.0 – 12.0 MeV in the studied projectile energy range. The shape of the measured neutron yield distribution for all the projectile energies agrees well with that obtained from the PACE2 calculations. The double differential neutron yield distribution data above 5.0 MeV neutron energy show a good match with the PACE2 results for projectile energies of 99.0, 88.0, 77.0, 55.0, 44.0 MeV.

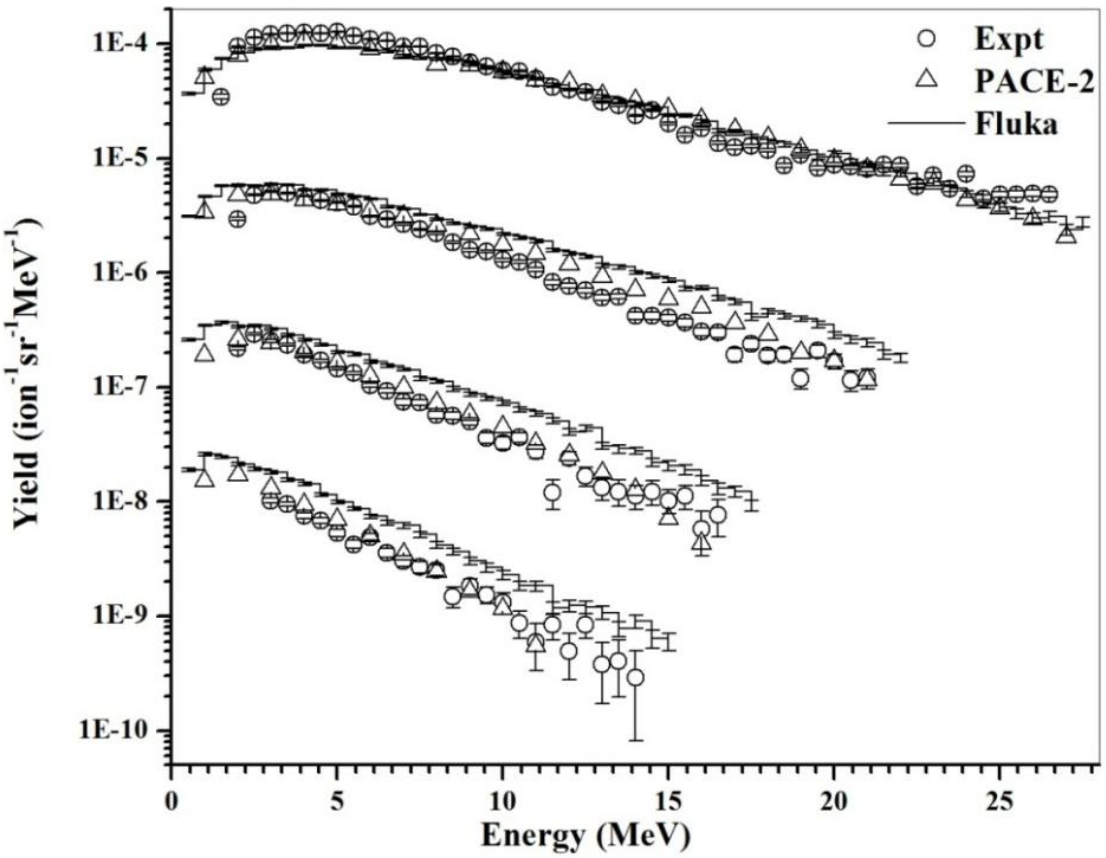

Fig. 5.28 Same as figure 5.27 for 99.0 MeV projectile energy.

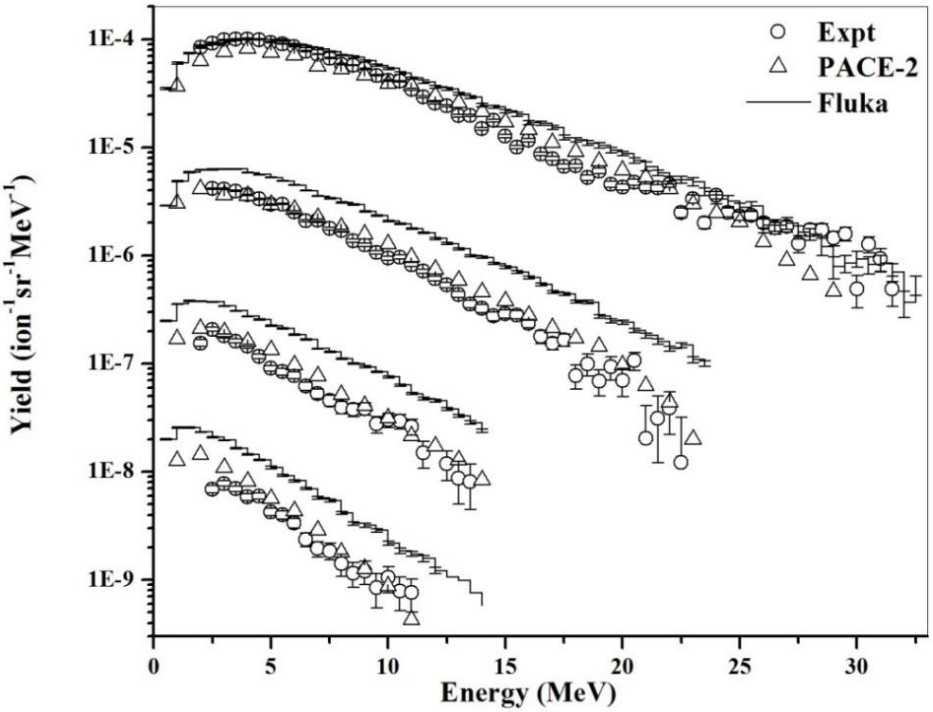

Fig. 5.29 Same as figure 5.27 for 88.0 MeV projectile energy.

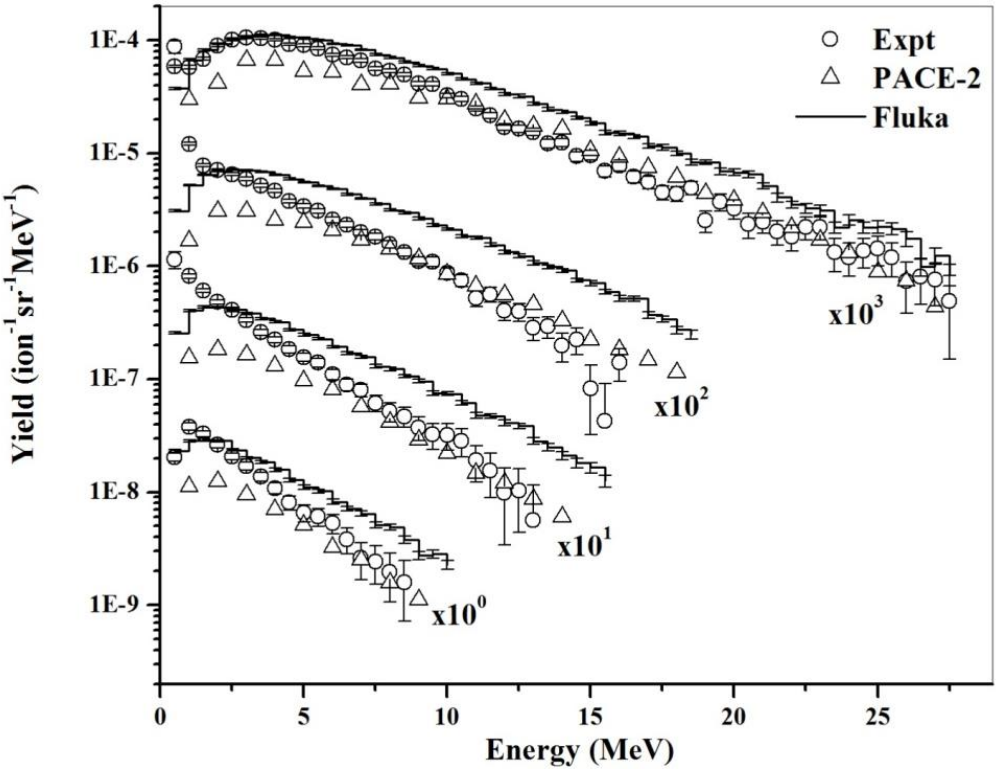

Fig. 5.30 Same as figure 5.27 for 77.0 MeV projectile energy.

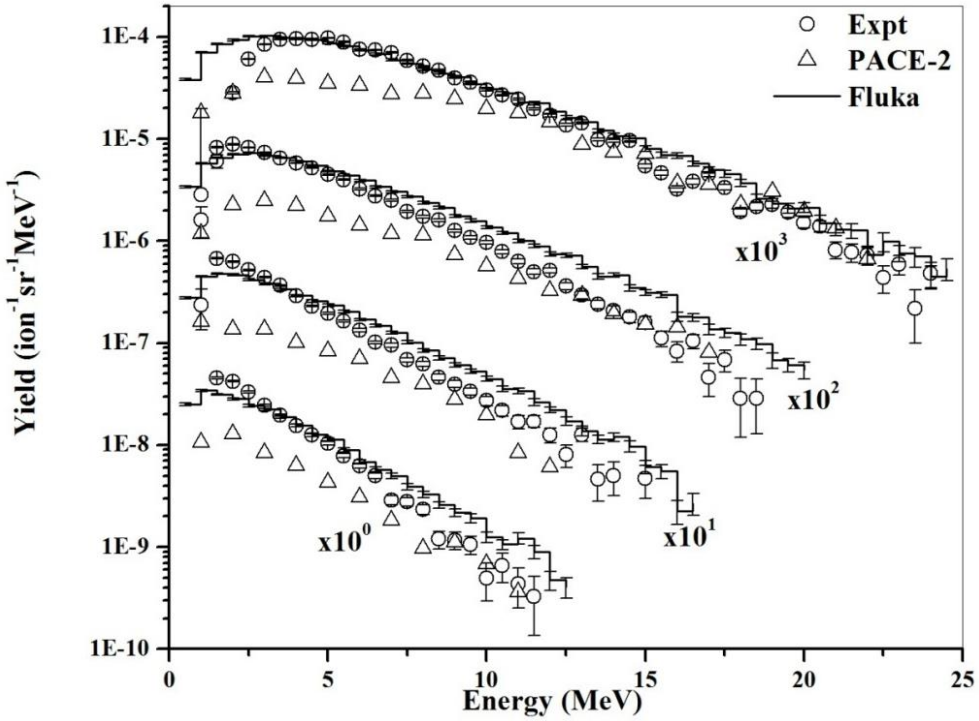

Fig. 5.31 Same as figure 5.27 for 66.0 MeV projectile energy.

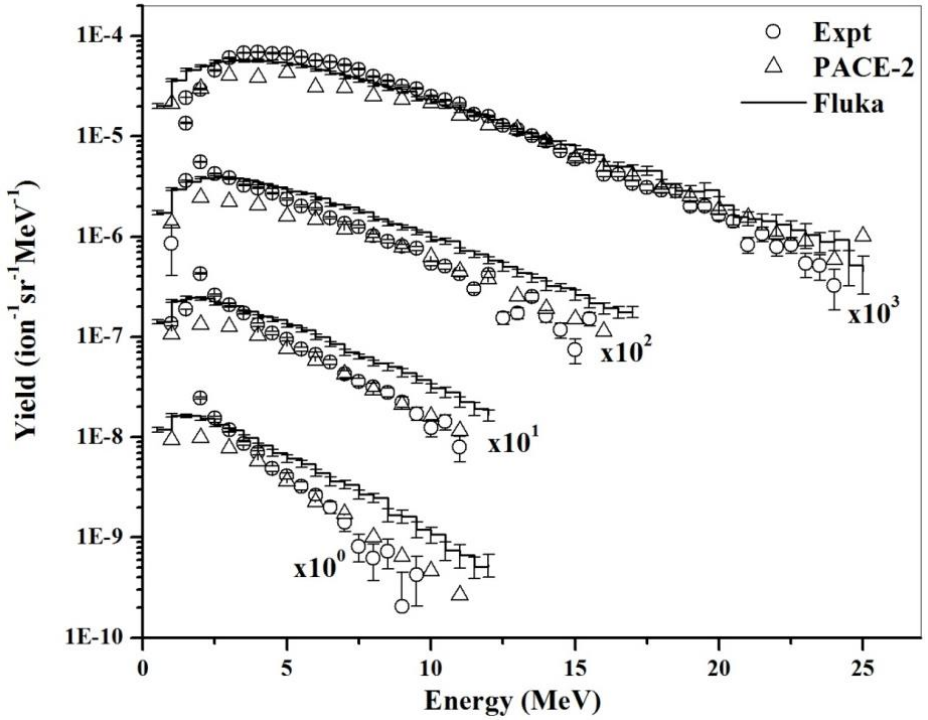

Fig. 5.32 Same as figure 5.27 for 55.0 MeV projectile energy.

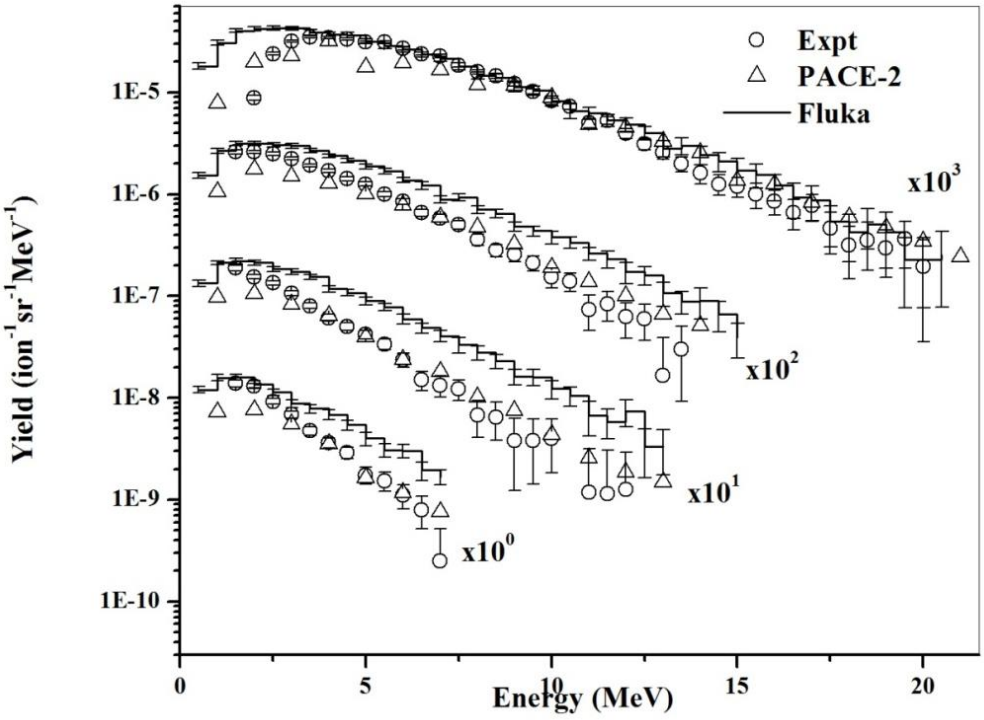

Fig. 5.33 Same as figure 5.27 for 44.0 MeV projectile energy.

In the range of the projectile energy considered in this work, compound nuclear emission dominates the nuclear reaction mechanism and the measured yield fits with Maxwellian distribution. The compound nucleus so formed decays probabilistically through the possible available decay channels. The level density of the compound nucleus and that of the residual nucleus together decide the decay probabilities from different channels. The Gilbert Cameron level density formalism is used in PACE2 calculations and the level density parameter $a = 7$ produces the best agreement. This shows that in the considered projectile energy range the neutrons are contributed mainly through evaporation.

At 110.0 MeV projectile energy the PACE2 calculations over predicts the experimental data at a few emission energies at 30^o and 60^o though the overall trend is reproduced quite well. The Fluka calculations over-estimate the measured neutron distribution, the disagreement being more pronounced at lower beam energies and at backward emission angles. This may be due to the reason that Fluka code is tailored to treat nuclear reactions more accurately at higher

beam energies and the angular distribution of emitted neutrons is not accurately estimated. For all the incident beam energies the peak in the double differential neutron spectra appears between 3.5 - 4 MeV at 30º emission angle, which becomes softer as we start moving towards backward angles. At 60º, the peak appears at 3.0 MeV for incident energies of 88.0 – 110.0 MeV; at lower beam energies the spectrum becomes softer and the peak shifts to ~ 2.0 MeV. As we move further to backward angles of 90º and 120º, the peak of the energy distribution shifts towards the lower energy side at 2.5 - 1.5 MeV over the beam energy range. The peak energies in the neutron distribution as calculated from the nuclear reaction code PACE2 matches very well with the experimental peaks. The one obtained by Fluka calculations appears slightly higher by a difference of 0.5 MeV in all directions except in extreme backward angle where it is lower than the experimental peaks by a value of 1.0 MeV, in almost all incident energies. The fast neutrons mostly have forward direction emission though their probability is relatively small compared to the peak of the distribution.

5.5.2 Integrated thin yield compared with thick target yield

In this part of work we compare the measured total thick target neutron yield (TTNY) distribution with the thin target neutron yield (ThNY) distribution integrated over the full energy range of measurements i.e., 44.0 MeV to 110.0 MeV. This has been done by interpolating the ThNY in steps of 1.0 MeV projectile energy between the two adjacent beam energies, e.g. ThNY at projectile energies of 109.0, 108.0,…., 100.0 MeV are obtained by interpolating the measured ThNY at 110.0 and 99.0 MeV. Linear interpolation was found to work satisfactorily for the purpose. The linear interpolation was first checked for the interpolated data of 99.0 MeV as calculated from the measured yield at 110.0 MeV and 88.0 MeV which was compared with the experimental data at 99.0 MeV and is presented in Fig

5.34. As it can be clearly seen from the Fig 5.34 the interpolated and measured yield distribution agrees quite well with a small under prediction in forward angles.

Similar comparison was carried out over down to 44.0 MeV projectile energy which is the lower bound of thin target measurements. Once the agreement between the interpolated and measured yields was found to be reasonable for all the projectile energies, final interpolation was carried out in step of 1.0 MeV.

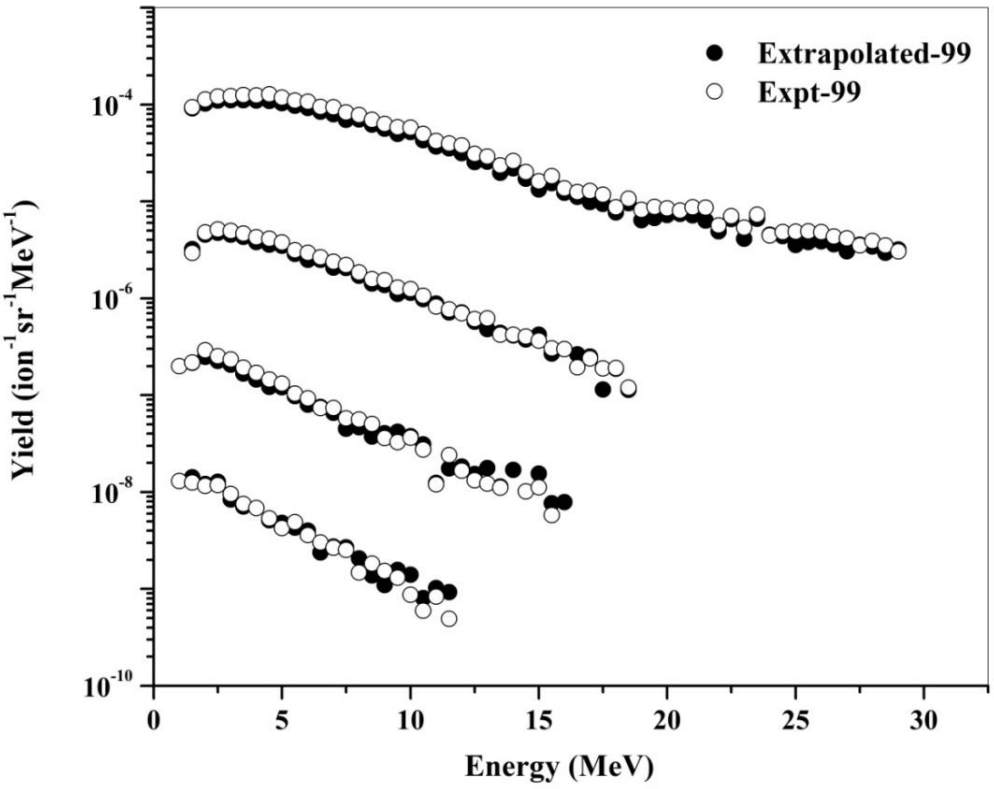

Fig 5.34 Comparison of neutron yield from experimental measurement at projectile energy 99.0 MeV with the extrapolated yield for 99.0 MeV using 110.0 MeV and 88.0 MeV measurements.

The interpolated and measured ThNY were then integrated over the energy range of 44.0 and 110.0 MeV. The total ThNY thus obtained was then compared with the measured TTNY as shown in Fig 5.35. The integrated yield and the thick target yield agree fairly well; the integrated ThNY is slightly lower than the thick target yield at all angles. This is attributed to the fact that the thick target yield is measured at a projectile energy of 116.0 MeV whereas the measured thin target yield was measured from projectile energy of 110.0 MeV down to 44.0

MeV. However, the Coulomb barrier for the reaction is low as 9.4 MeV and neutron yield in the energy 44.0 MeV down to Coulomb barrier was not considered in contrast to the case for the thick target. The under prediction of the interpolated yield distribution at backward angles is also reflected in the total integrated yield distribution, resulting in slightly reduced integrated ThNY distribution when compared to TTNY.

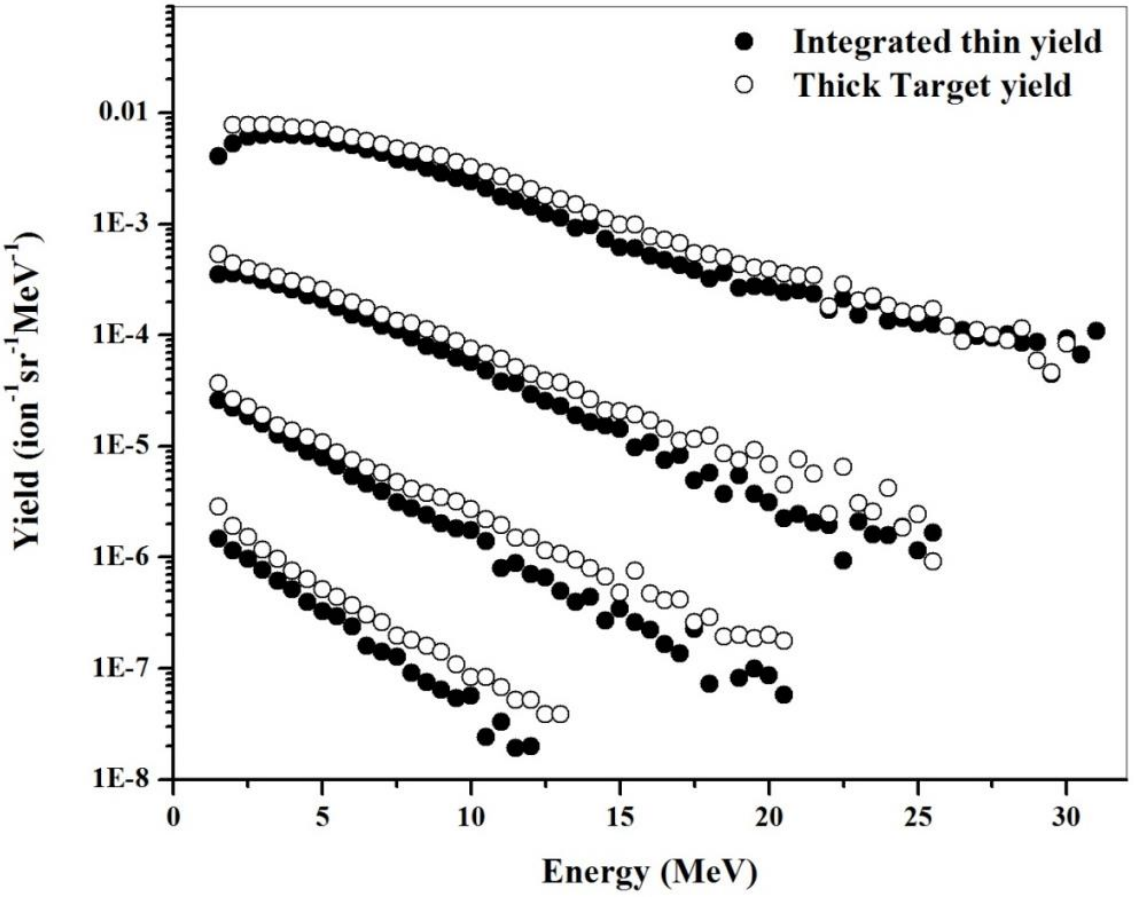

Fig. 5.35 The integrated yield from the thin target compared to the thick target yield. The filled circles represent the integrated yield from thin targets and the open circles represent the thick target yield.

5.5.3 Angular distribution of neutron yield

For the neutron yield from thin target measurements as discussed above four large liquid organic scintillator detectors were used simultaneously and were placed at 30º, 60º, 90º and 120º. The angular distribution of the emitted neutrons from the different projectile energies 44.0 MeV to 110.0 MeV is presented in Fig 5.36 to Fig 5.42. And the data on angular yield is

presented in Table 5.5. For the projectile energies 88.0 – 110.0 MeV as shown in Fig 5.36 – Fig 5.38, the PACE2 data is nearly three times the experimental values. For the lower projectile energies from the yield distribution it can be seen that in the lower neutron emission energies PACE2 is under estimating neutron yield when compared to the experimental results, though at higher energies the match improves. Whereas, for Fluka results in extreme forward angle over all the projectile energies the match is very good.

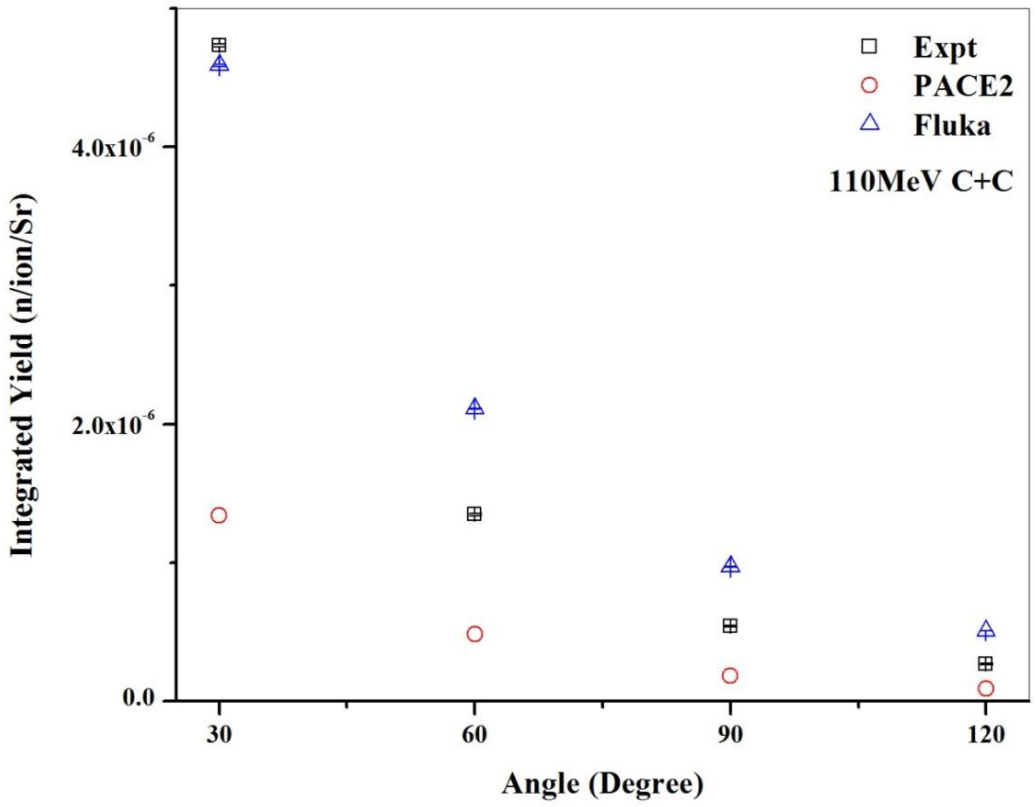

Fig. 5.36 Integrated neutron yield from thin target ^{12}C + ^{12}C system at 110.0 MeV.

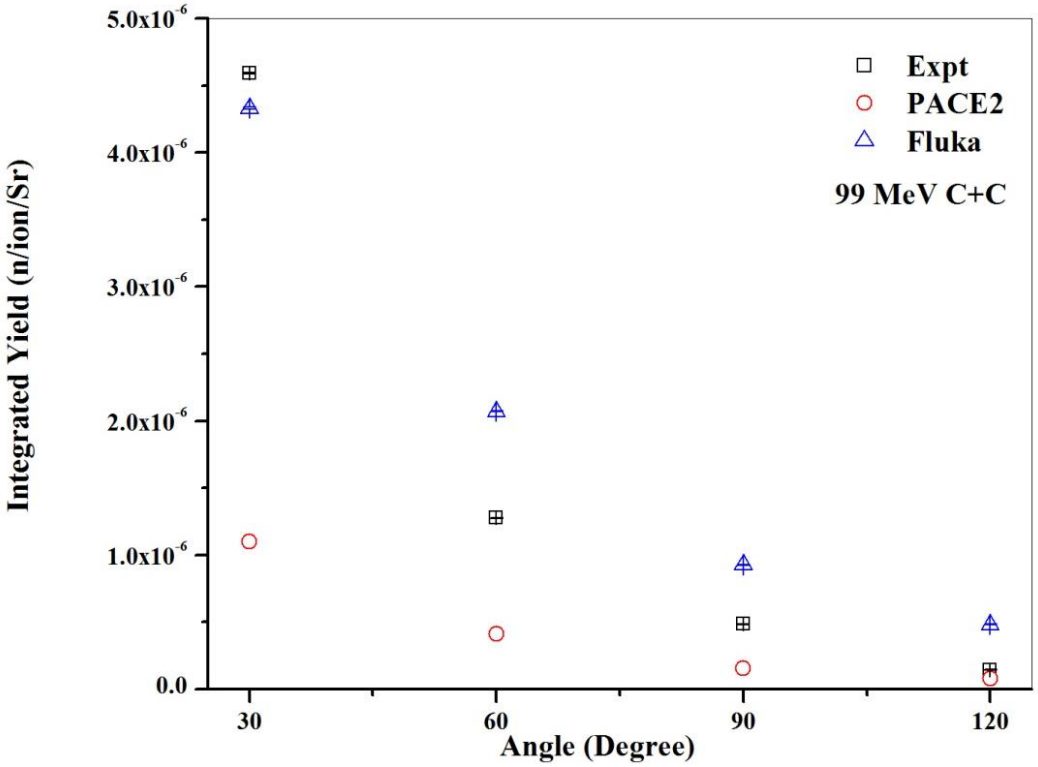

Fig. 5.37 Integrated neutron yield from thin target ^{12}C + ^{12}C system at 99.0 MeV.

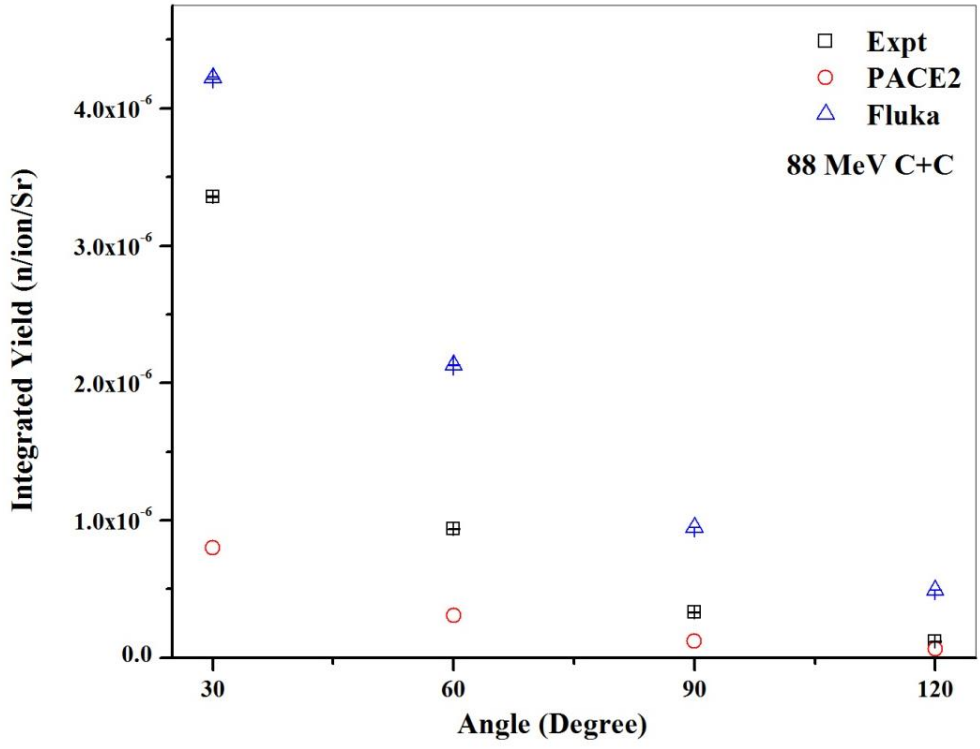

Fig. 5.38 Integrated neutron yield from thin target ^{12}C + ^{12}C system at 88.0 MeV.

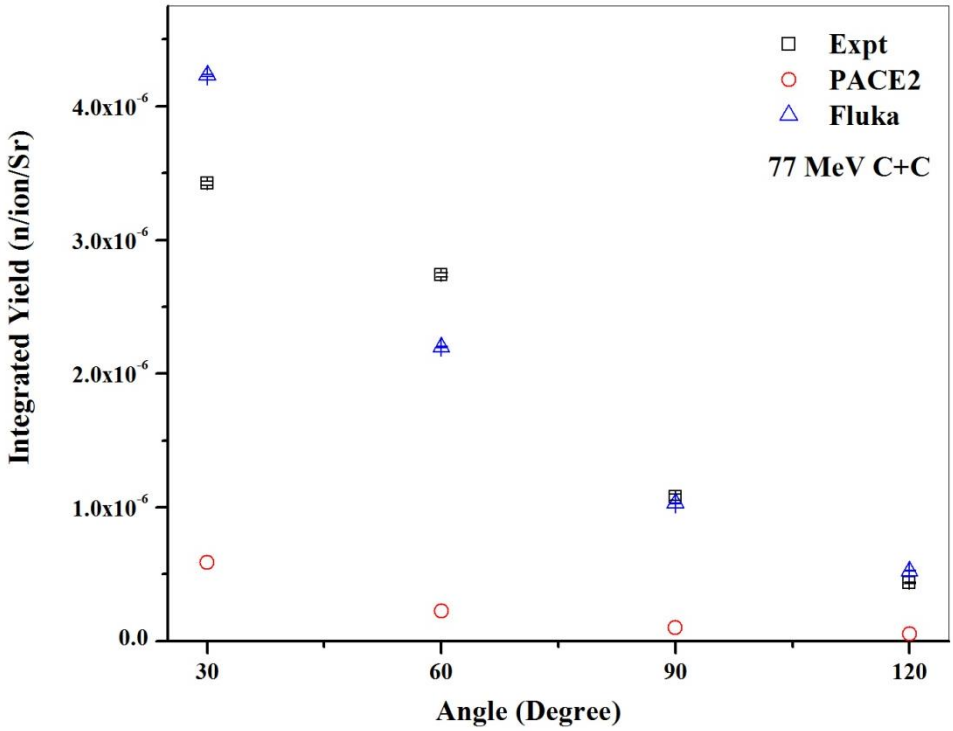

Fig. 5.39 Integrated neutron yield from thin target ^{12}C + ^{12}C system at 77.0 MeV.

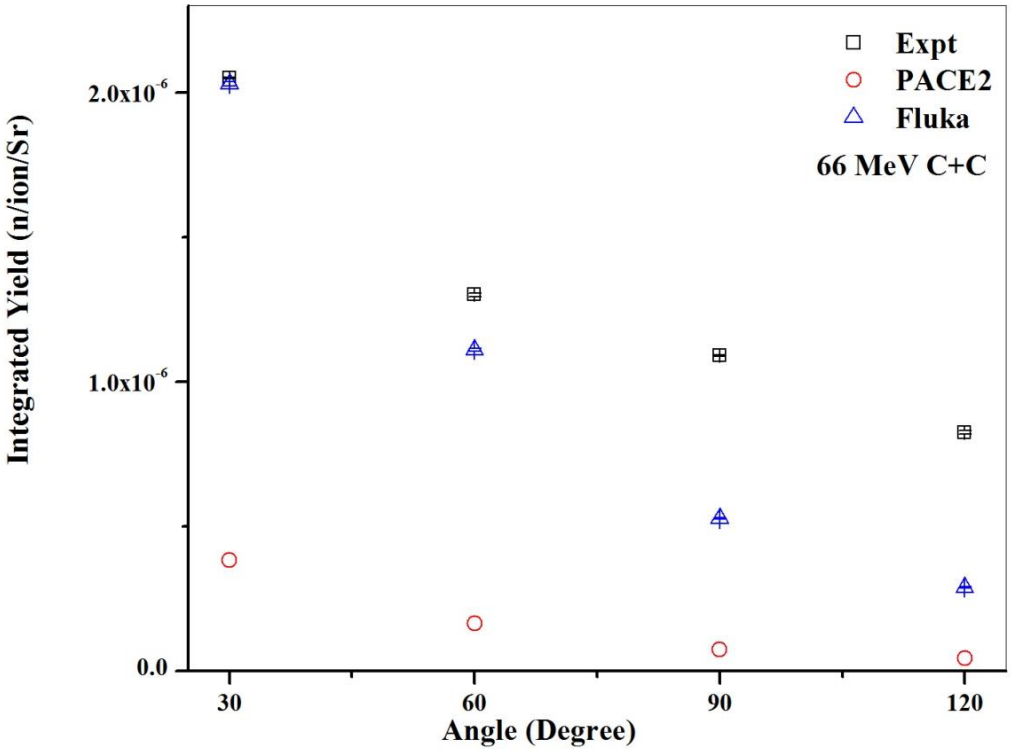

Fig. 5.40 Integrated neutron yield from thin target ^{12}C + ^{12}C system at 66.0 MeV.

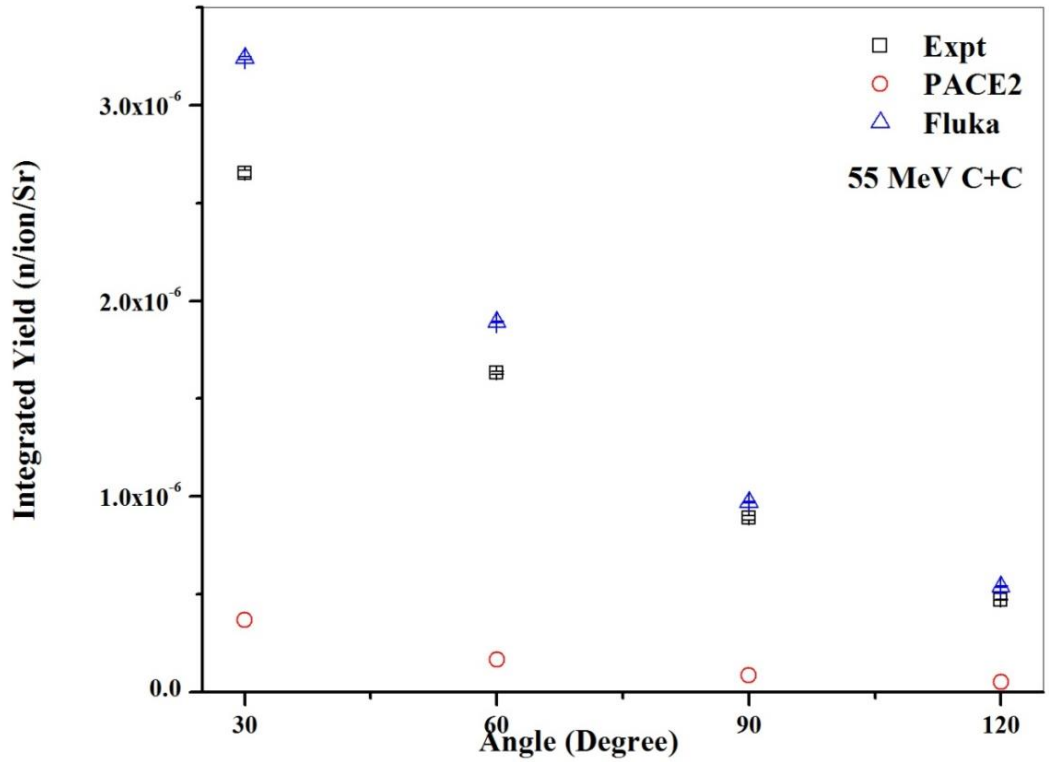

Fig. 5.41 Integrated neutron yield from thin target ^{12}C + ^{12}C system at 55.0 MeV.

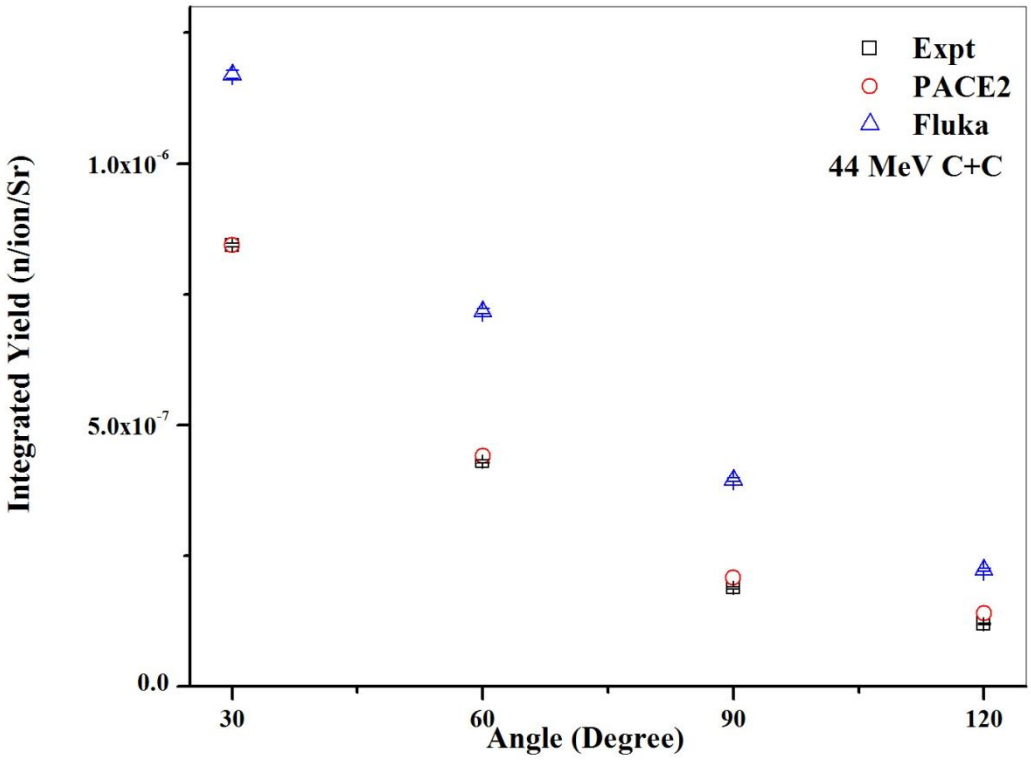

Fig. 5.42 Integrated neutron yield from thin target ^{12}C + ^{12}C system at 44.0 MeV.

Table 5.5 Angular distribution of neutron yield from thin carbon target when impinged

with carbon ions of various energies.

Energy (MeV)	Angle (Degree)	Experimental	PACE2	Fluka
110.0	**30**	4.73×10^{-6}	1.34×10^{-6}	4.59×10^{-6}
	60	1.35×10^{-6}	4.83×10^{-7}	2.11×10^{-6}
	90	5.38×10^{-7}	1.83×10^{-7}	9.69×10^{-7}
	120	2.65×10^{-7}	8.62×10^{-8}	5.07×10^{-7}
99.0	**30**	4.59×10^{-6}	1.10×10^{-6}	4.33×10^{-6}
	60	1.27×10^{-6}	4.09×10^{-7}	2.07×10^{-6}
	90	4.82×10^{-7}	1.56×10^{-7}	9.27×10^{-7}
	120	1.42×10^{-7}	7.62×10^{-8}	4.80×10^{-7}
88.0	**30**	3.3610^{-6}	7.98×10^{-7}	4.22×10^{-6}
	60	9.37×10^{-7}	3.10×10^{-7}	2.13×10^{-6}
	90	3.29×10^{-7}	1.23×10^{-7}	9.49×10^{-7}
	120	1.17×10^{-7}	6.34×10^{-8}	4.90×10^{-7}
77.0	**30**	3.42×10^{-6}	5.87×10^{-7}	4.23×10^{-6}
	60	2.73×10^{-6}	2.25×10^{-7}	2.20×10^{-6}
	90	1.08×10^{-6}	9.86×10^{-8}	1.03×10^{-6}
	120	4.36×10^{-7}	5.26×10^{-8}	5.24×10^{-7}
66.0	**30**	2.05×10^{-6}	3.83×10^{-7}	2.03×10^{-6}
	60	1.30×10^{-6}	1.63×10^{-7}	1.11×10^{-6}
	90	1.09×10^{-6}	7.24×10^{-8}	5.26×10^{-7}
	120	8.24×10^{-7}	4.26×10^{-8}	2.89×10^{-7}
55.0	**30**	2.65×10^{-6}	3.68×10^{-7}	3.24×10^{-6}
	60	1.63×10^{-6}	1.65×10^{-7}	1.89×10^{-6}
	90	8.91×10^{-7}	8.37×10^{-8}	9.70×10^{-7}
	120	4.71×10^{-7}	5.04×10^{-8}	5.38×10^{-7}
44.0	**30**	8.43×10^{-7}	8.43×10^{-7}	1.17×10^{-6}
	60	4.30×10^{-7}	4.40×10^{-7}	7.17×10^{-7}
	90	1.88×10^{-7}	2.07×10^{-7}	3.95×10^{-7}
	120	1.19×10^{-7}	1.85×10^{-7}	2.22×10^{-7}

In the other directions for projectile energies 88.0 – 110.0 MeV, Fig 5.36 – Fig 5.38, the Fluka over predicts the yield and thus the integrated yield. For the lower projectile energies

Fluka results match well with the experimental measurements. It should be noted that the total yield falls by an order in the lateral direction when compared to the forward direction yield. From an order fall can also be predicted that the emission from the reaction is forward directed and not isotropic in the lab frame as expected. The integrated neutron yield is presented in Table 5.5. The spectrum is a soft spectrum with mostly emitted neutron being in lower energy side as the yield falls towards the high energy. The major contribution in the integrated yield is from low energy neutrons almost 75 % till 10.0 MeV and which increases to 90 % till 15.0 MeV. The contribution of neutrons in yield above 15.0 MeV is nearly 10 %, suggesting a soft spectrum.

5.6 Results and Discussions

In this chapter the measurement of neutron yield using time of flight technique and analysis of thick target neutron yield at five emission angles covering forward, lateral and backward angles for $^{12}C^{6+}$ + thick ^{27}Al at projectile energy of 115.0 MeV has been carried out. Results from nuclear reaction model modified PACE2 and Fluka Monte Carlo simulation results were estimated and were compared with the experimental measurements. The slope of the data from codes approximately matches with the slopes of experimental data in forward angles of emission with slight differences in the backward angles. The maximum energy peak also matches closely in backward angles and has slight deviation in forward angle. The double differential neutron distribution obtained from PACE2 and Fluka matches very well in the forward angle but is higher in the backward angles by a factor of 2-3. The maximum energy of neutron emission as seen from the experimental measurement and the model calculations decreases with the increasing emission angle. In addition, the energy and angular distribution of the neutron yield has been measured for 116.0 MeV $^{12}C^{6+}$ beam incident on a thick carbon target, which stops the projectiles completely within the target. The emissions have been

measured from forward 0º to backward 120º in steps of 30º. The neutron yield has been also estimated using standard reaction codes PACE2 and Fluka. The results obtained from the reaction codes were compared to the experimentally obtained yield distribution, which showed a satisfactory agreement. There are a few deviations of the PACE2 calculations that could be assigned to the fact that the PACE2 code is developed to be used for thin target (to calculate multiplicity and cross section) which is tailored, as explained in the text and annexure, to obtain yield from thick target emissions. The Fluka calculations agree better with the measured thick target yield compared to that for thin target.

The thin target neutron yield from natural carbon target at various energies of the ^{12}C projectile has also been studied. The yields were measured at 30º, 60º, 90º and 120º. The experimentally estimated yields were compared with the calculations from the nuclear reaction codes PACE2 and Fluka. The PACE2 calculations are observed to agree well with the measured distribution showing that the neutrons are mostly contributed by compound nuclear emissions. The slope of the yield distributions is better reproduced for the level density parameter $a = 7$. The Fluka calculations over-estimate the double differential yield, more in the backward angle. The energies in between the experimentally measured ones were interpolated using a linear relation which has been first checked on the measured data.

The total neutron yield distribution from the thin target measurements and the interpolated ones were added over energy and were compared with the thick target emission yield. Measured thick target yield was slightly higher than the thin target integrated yield. This is attributed to the fact that the projectile energy considered for thin target was from 110.0 MeV until down to 44.0 MeV as compared to the projectile energy of 116.0 MeV for thick target measurement, which emits neutrons attributable to the projectile ion interacting within target with continuously degrading energy probably until the Coulomb barrier before completely being stopped. Since the slope of the emission yield over energy does not change, it appears

that the yield constitutes mostly of evaporation component and there is no sign for pre-equilibrium emission. This study gives us the confidence to use the modified PACE2 for estimating the double differential neutron yields for thick target nuclear reactions, where the emissions are dominant from the evaporation process.

5.7 Summary

In the present study time of flight technique was used to measure the emitted neutron yield from the thick target projected with heavy ions in the energy range ~ 10 MeV/A. Two sets of thick targets one aluminium and other natural carbon were studied at projectile energies 115.0 MeV and 116.0 MeV respectively. Measurements from five organic scintillator detectors placed at 0°, 30°, 60°, 90° and 120° were carried out to obtain the angular distribution of the emitted neutrons. The contribution in the neutron yield due to scattering from the structural materials and components was corrected using the shadow bar measurements. Shadow bar measurement for the individual detectors were done one at a time to avoid any inter-detector scattering contributions. The experimental results were compared with the estimations from the nuclear reaction codes PACE2 and Fluka, to find a reasonable match.

In addition, a set of thin target measurements were carried out for the reaction $^{12}C^{+6}$ + ^{12}C at projectile energies 44.0 MeV to 110.0 MeV in steps of 11.0 MeV. A beam dump was created at a distance ~ 2 m from the target to completely stop the beam. It was shielded with HDPE and lead blocks to cut off any gammas and neutrons emanating from there to reach any of the neutron detectors. To obtain the angular distribution of the emitted neutrons four liquid organic detectors were used at 30°, 60°, 90° and 120°. The experimental results were compared with the nuclear reaction codes PACE2 and Fluka outputs to find satisfactory match.

Further, the measured thick target neutron yield (TTNY) distribution from the nuclear reaction $^{12}C^{+6}$ + ^{12}C at 116.0 MeV was compared with the integrated thin target neutron yield

(ThNY) distribution over the full energy range of measurements 44.0 MeV to 110.0 MeV. The ThNY was interpolated for the intermediate energies in steps of 1.0 MeV projectile energy between the two adjacent beam energies. Linear interpolation was found to work satisfactorily for the purpose and it was tested on the measured data. The integrated thin target yield ThNY was compared with the thick target yield TTNY and was seen to be slightly lower at all the angles. The reduced neutron yield is due to the reason that the thick target yield is measured at a projectile energy of 116.0 MeV whereas the thin target yield was measured at lower projectile energy of 110.0 MeV down to 44.0 MeV. Since, the Coulomb barrier for the reaction is low at 9.4 MeV the neutron yield in the energy range 44.0 MeV down to Coulomb barrier was not accounted in ThNY contribution in contrast to the case for the thick target.

The neutron yield distribution so measured using the time of technique for the different sets of target and projectile combinations can be folded with the ambient neutron dose to fluence conversion coefficients to obtain the ambient neutron dose. The next chapter discusses the estimation of ambient neutron dose from neutron yield measurements in one of the nuclear reactions discussed here.

CHAPTER 6

Neutron Dose Estimation

High-energy accelerators are increasingly used in medical field for therapy in addition to the basic science research and for development of spallation neutron sources. Neutrons being the major component of the prompt radiation environment of any positive ion accelerator facility, estimation of neutron ambient dose due to its emission from thick targets under normal operations and accidental conditions are important. The doses from neutrons often account for a substantial fraction of the total dose in the accessible areas, behind radiation shielding, in all accelerator facilities. It must be noted that limited dose measurement data is available in literature in the energy range ~ 10.0 MeV/A especially for thick target emissions [40, 41, 64]. The neutron yield measurements from thick target in the said energy range is essential to further improve the present theoretical models which are being used to estimate the neutron yield and dose thereby adding more data points for the completeness of the models. Moreover, unlike gamma doses, the neutron dose is a strong function of energy [28], and the angular distribution depends on various parameters such as types of targets, projectiles and the incident energy of the projectiles.

Since, the conventional dosimeters are used for routine monitoring it becomes important to have its periodic calibration. Most of the neutron dosimeters used are designed in a way to

give count rate per unit incident fluence proportional to the ICRP [28] fluence to dose conversion coefficients. In addition to the measured ambient dose equivalent it is often advantageous to have the neutron yield distribution as a function of the energy and the angular distribution as this complements as well as provide a more detailed procedure for the dose measurements.

The neutron dosimetry has a practical relevance and covers an energy range of at least ten orders of magnitude in which appropriate dosimetric instrumentation is needed, since no single detection system works for the entire energy range. Challenges in neutron dosimetry arises from the energy dependent quality factors and radiation weighting factors that require energy information to have better estimation of the absorbed dose. It is very important to use dosimeters or detector system, which has good neutron gamma separation in a mixed radiation environment.

The previous chapter dealt with the neutron radiation source estimation by experimentally measuring the double differential neutron yield. This chapter deals with the neutron ambient dose calculation from the measured neutron energy distributions and comparing it with the neutron ambient doses measured using standard neutron dosimeters. In the present study, one empirical formulation was also adopted and the doses were estimated for the studied system.

6.1 Health Physics quantities

The dose estimation techniques and the basic health physics quantities to understand the methods for dose assessments will be discussed here. The three principal protection quantities as recommended for the use in radiological protection are explained as follows

1. The mean absorbed dose in an organ or tissue, $\boldsymbol{D_T}$
2. The equivalent dose in an organ or tissue $\boldsymbol{H_T}$; and

3. The effective dose, ***E***

6.1.1 Mean Absorbed Dose

Mean absorbed dose in a specified tissue or organ of the human body, *T*, is mathematically given as

$$D_T = \left(\frac{1}{m_T}\right) \int_{m_T} D dm \tag{6.1}$$

where, m_T is the mass of tissue or organ, and D, is the absorbed dose in the mass element dm. The absorbed dose is the quotient of the mean energy imparted by ionizing radiation to the matter in a specified volume divided by the mass of matter in the volume. The idea behind this quantity is that the physical measure is correlated with the effects of ionizing radiation. Mathematical form of absorbed dose is given below

$$D = \frac{d\bar{\epsilon}}{dm} \tag{6.2}$$

where, *D* is the absorbed dose in the mass element *dm*, and $\bar{\epsilon}$ is average energy imparted by ionizing radiation to matter in the volume. The doses received though is not reported in terms of absorbed doses but taking into consideration the type of radiation and its biological effect on the tissues which gives rise to the need for equivalent dose.

6.1.2 Equivalent Dose

When living matter absorbs any radiation, the radiation can produce some biological effect. Since different types of ionizing radiation vary in how they interact with biological materials, absorbed doses of equal quantities do not necessarily have equal biological effect. A radiation-weighting factor (w_R) is used to equate different types of radiation with different levels of biological effectiveness. The equivalent dose, H_T, is a tissue or organ, *T*, irradiated in

a radiation field consisting of several radiations with different values of w_R the absorbed dose is the sum of average absorbed dose weighted with the radiation quality factor. The relation for equivalent dose is given as below

$$H_T = \sum_R w_R D_{T,R} \tag{6.3}$$

where, $D_{T,R}$ is the average absorbed dose from radiation *R*, in tissue *T*. The equivalent dose provides the doses received by particular tissues, when all such doses over various organs in body are taken together gives the effective dose.

6.1.3 Effective Dose

Different tissues and organs may vary in how they respond biologically to a given type of radiation. For example, a given equivalent dose (per Sievert) has a higher risk of inducing fatal cancer in the lung than in the thyroid gland. Effects can be different both in type and in magnitude and must be considered when assessing radiation exposure's overall detriment to the human health. This is taken into account by multiplying the equivalent dose to an organ or tissue by its respective weighting factor (w_T). The effective dose, *E*, is the sum of the weighted equivalent doses in all the tissues and organs of the body. It is given by the expression below.

$$E = \sum_T w_T H_T \tag{6.4}$$

where, H_T is the equivalent dose in tissue or organ *T* and w_T is the weighting factor for tissue *T*.

The protection quantities are not directly measurable, but may be related to the radiation field in which the body is exposed. To fill this gap a relation was developed as suggested by ICRU that are called the operational quantities for measurement of exposures to external radiations. The operational dose-equivalent quantities defined by the ICRU for physical measurement are following

1. The ambient dose equivalent, ***H*(d)***
2. The directional dose equivalent, ***H'(d, Ω)*** and
3. The personal dose equivalent, $\boldsymbol{H_p(d)}$

To define operational quantities the ICRU has introduced the concepts of aligned and expanded radiation field. An expanded radiation filed is defined as hypothetical field where the fluence and its angular and energy distribution have same value throughout the volume of interest as that in the actual field at the point of measurement. An expanded and aligned represents a field where the fluence and its energy distribution are the same as in an expanded field, but the fluence is unidirectional.

6.1.4 Ambient Dose Equivalent

The ambient dose equivalent, *H*(d)*, at a point in the radiation field is the dose equivalent that would be produced by the corresponding expanded and aligned field in the ICRU sphere at a depth, *d*, on the radius opposing the direction of the aligned field. The recommended value of *d* is 10 mm for penetrating radiation and 0.07 mm for low-penetrating radiation.

6.1.5 Directional Dose Equivalent

The directional dose equivalent, *H'(d, Ω)*, at a point in a radiation field is the dose equivalent that would be produced by the corresponding expanded field in the ICRU sphere at a depth, *d*, on a radius in a specified direction, *Ω*. Here also the recommended value of *d* for penetrating radiation is 10 mm and for low-penetrating radiation it is 0.07 mm.

6.2 Conventional Neutron Dosimeters

Radiation protection is dedicated towards minimizing the radiation dose to the radiation workers, members of public and patients. The commercially available calibrated instruments with optimized neutron response and dose conversion factors (published in ICRP-74) for the

measurement of neutron ambient dose equivalent H*(10), are gaining importance. However, the neutron fluence generated by proton accelerators depends on proton energy and direction of incidence. The sensitivity of the detector is function of both the factors. Consequently, the number of counts recorded will be strongly affected by the size, composition and orientation of the detector and/or phantom. Dosimeters are broadly classified into two general categories, passive and active.

• A passive dosimeter produces a radiation-induced signal, which is stored in the device itself in form of either excited state or some other form. Later on, the dosimeter is processed and the output is analyzed to obtain the dose information.

• An active dosimeter produces a radiation-induced signal and displays a direct reading of the detected dose or dose rate in real time. Active dosimeters are further categorized as personal or area monitors, both give instantaneous doses. However, few conventional detectors are available with an option of the integrated doses over a time span.

Two commercially available neutron survey meters used in the present work is discussed in the following section. Fig 6.1, show the picture of dosimeters used for the ambient neutron dose measurements.

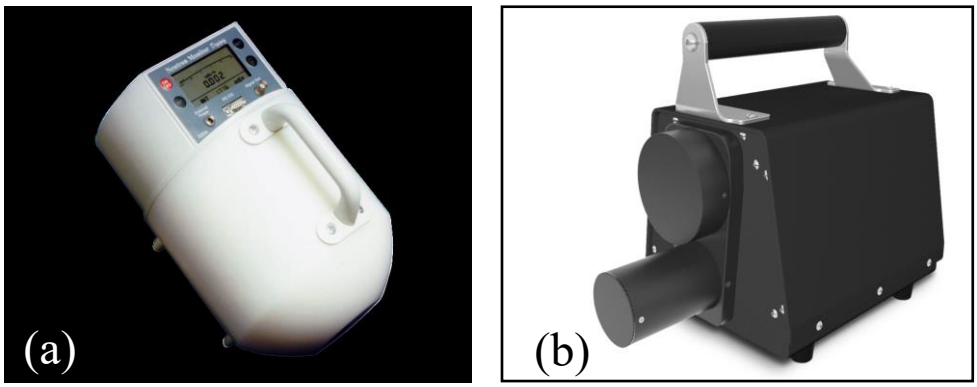

Fig. 6.1 Commercially available neutron survey meters (a) Digipig monitor (2222A, Weldholm medical Studsvik) and (b) Microspec-2 (Bubble Technology Industries), used for dose measurements.

6.2.1 Digipig monitor (2222A, Weldholm)

Portable neutron survey meters are used to monitor neutron doses at working areas. As per the new International Commission on Radiological Protection (ICRP) recommendations on radiation protection quantities (Publication 60) [29], there has been an increased interest in optimization and calibration of the instruments with the neutron ambient dose equivalent H*(10). The neutron monitor 2222A is a portable instrument used in monitoring neutrons in the areas surrounding radiation facilities like reactors, accelerators and other neutron sources. The Digipig monitor (2222A, Weldholm medical Studsvik) has a BF_3 detector surrounded by a cylindrical polyethylene moderator of thickness 21.5 cm in diameter, borated plastic absorber and a digital display. The comparison of the energy response of the neutron monitor [139], with the ICRP 74 neutron sensitivity response curve values show a close agreement above 50 KeV as seen in Fig 6.2.

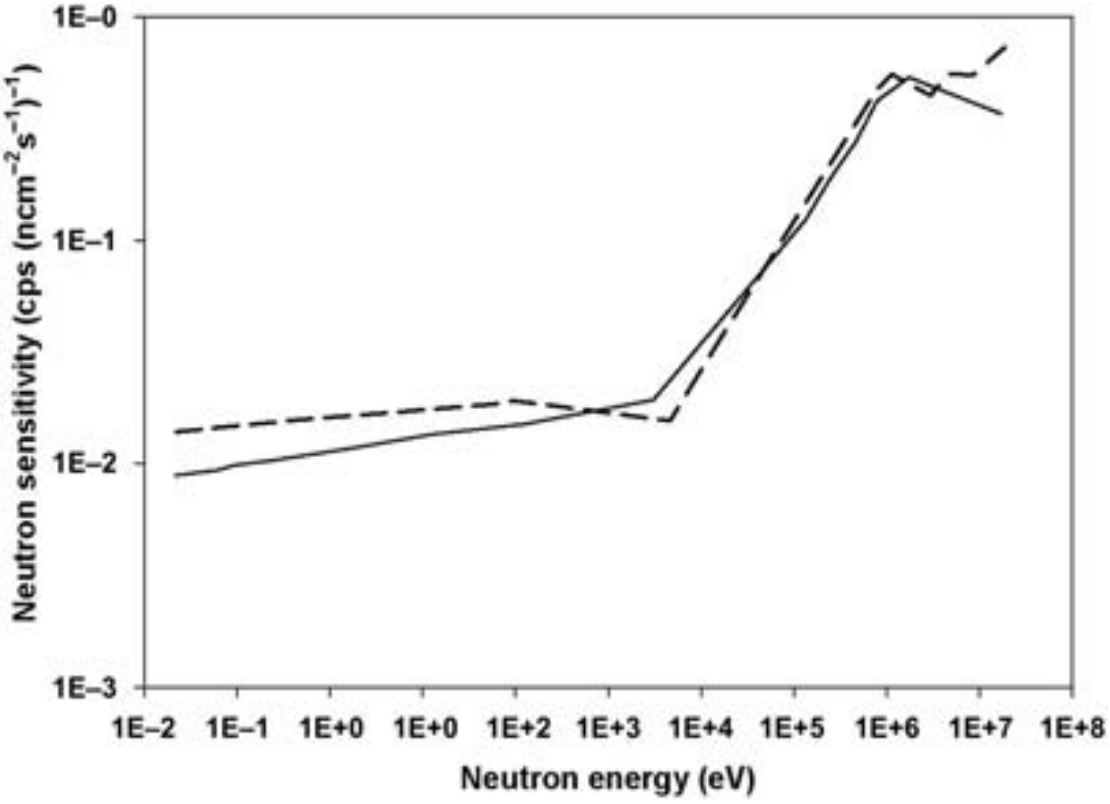

Fig. 6.2 Energy response (thick line) of the 2222A NDE meter (neutron ambient dose equivalent) provided by manufacturer compared with the ICRP response (broken line).

These instruments are designed to provide count rate per unit incident fluence proportional to the ICRP fluence to dose conversion coefficients for neutrons over the energy range of thermal to nearly 17.0 MeV. However, the responses of the conventional rem meters used for neutron ambient dose measurement differ from the actual ICRP-74 responses below 50.0 KeV as can be seen from the Fig 6.2. The monitor has several measurement modes such as dose rate and accumulated dose (updated at 100 second interval). The range for neutron dose rate measurement is from 0.001mSv/h – 999.9 mSv/h. The use of BF_3 detector for neutron detection has the advantage that it can effectively discriminate a background of gamma radiation. The monitor with a proper discriminator level set becomes practically insensitive to gamma doses up to 2 Gy/h.

6.2.2 Microspec Neutron Probe (Bubble Technology Industries)

Microspec probe is used along with the conventional NDE meter for validation of the neutron fields during the experiments. The doses were measured using a neutron dose equivalent meter while the energy spectra were measured using commercially available portable neutron spectrometer with an organic scintillator and ^{3}He detectors. The measurements were done in four directions 0º, 30º, 90º and 120º with respect to the incident beam. The BTI Microspec-2 is a portable spectroscopic survey system. It consists of organic liquid scintillator, which measures neutron spectrum above 0.8 MeV to about 20.0 MeV. It uses pulse shape discrimination to reject gammas. The region from thermal neutrons to 0.8 MeV is measured by a spherical ^{3}He detector. The detector has a cross-section that varies with $1/v$ above thermal energies. To get rid of pulse pile up problem due to high thermal cross-

section, the detector is shielded with a specially designed boron shell to achieve a detector response that is almost flat over the thermal and the epithermal region.

6.2.3 Experimental details and Result

The experiment was carried out at BARC-TIFR Pelletron LINAC facility Mumbai, India. A thick high purity (99.99 %) carbon target was bombarded with completely stripped ($^{12}C^{6+}$) ions of energy 116.0 MeV. Two commercially available conventional dosimeters were used. The conventional dosimeters were Wedholm Medical (Studsvik) model 2222A using the neutron monitor [139] (a moderated BF_3 detector based rem counter) and Bubble Technology Industries (BTI) portable spectroscopic neutron N-probe Microspec [140]. The detectors were placed at varying distances to obtain statistically significant count rates; placing the detectors in lined with the beam line at a height of 172 cm from ground, resulted in reduction of scattered component from the ground. The pictorial representation of experimental setup is shown in Fig 6.3. The measurement time was optimized by placing the detector at a measured distance from the target to get the required count rate. Using the neutron rem monitor the 0º, 30º, 90º and 120º angles with respect to the incident beam were covered one at a time, Microspec N-Probe was used to measure the dose at the 0º, 30º and 90º angles. The various measurements with the two detector setup is tabulated and presented in Table 6.1. The distances at which the rem meter and Microspec dosimeters were kept during neutron ambient dose measurement are presented in Table 6.1. At 0° and 30° both the dosimeters were kept at distance ~ 1m. For the backward angles the dosimeters were brought closer to the target ~ 40 cm, to increase the solid angle to acquire a greater neutron yield. The exact distances for the placement of rem meter and the Microspec dosimeters are given in Table 6.1. The doses were normalized to the total projectile seen by the target, the solid angle which takes care of different distances and the different durations of measurements. The total number of projectile during measurement was extracted

from the current integrator system that measures the total charge deposited on the target by the beam. The charge state of the beam ions were taken in consideration while calculating the number projectile from the total charge deposited.

The angular distribution can be seen in the Fig 6.4. The doses measured by both dosimeters show a good match, also it can be seen that the neutron ambient dose falls by an order in backward angle when compared to the dose measured in forward angle. The ambient neutron dose values for both the dosimeters over the measured angles are presented in Table 6.2. Microspec neutron probe also provides a spectral distribution of the measured neutron field using the programmed spectrum unfolding code.

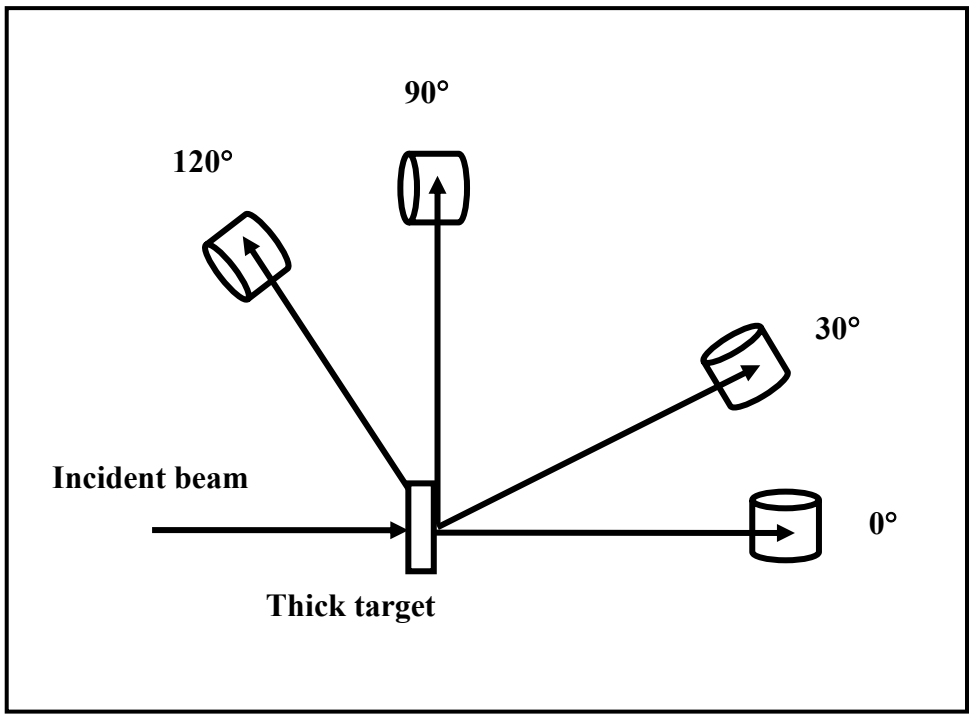

Fig. 6.3 Schematic representation of the experimental set-up showing the positions of rem meter and the Microspec detectors.

Table 6.1 Neutron ambient dose measurement details over direction and distance for rem meter and Microspec dosimeters

REM Meter		Microspec Neutron Probe	
$D_{exp}^{REM}(\theta)$	Distance (m)	$D_{exp}^{BTI}(\theta)$	Distance (m)
0°	1.00	0°	1.02
30°	1.00	30°	0.80
90°	0.40	90°	0.35
120°	0.50	-	-

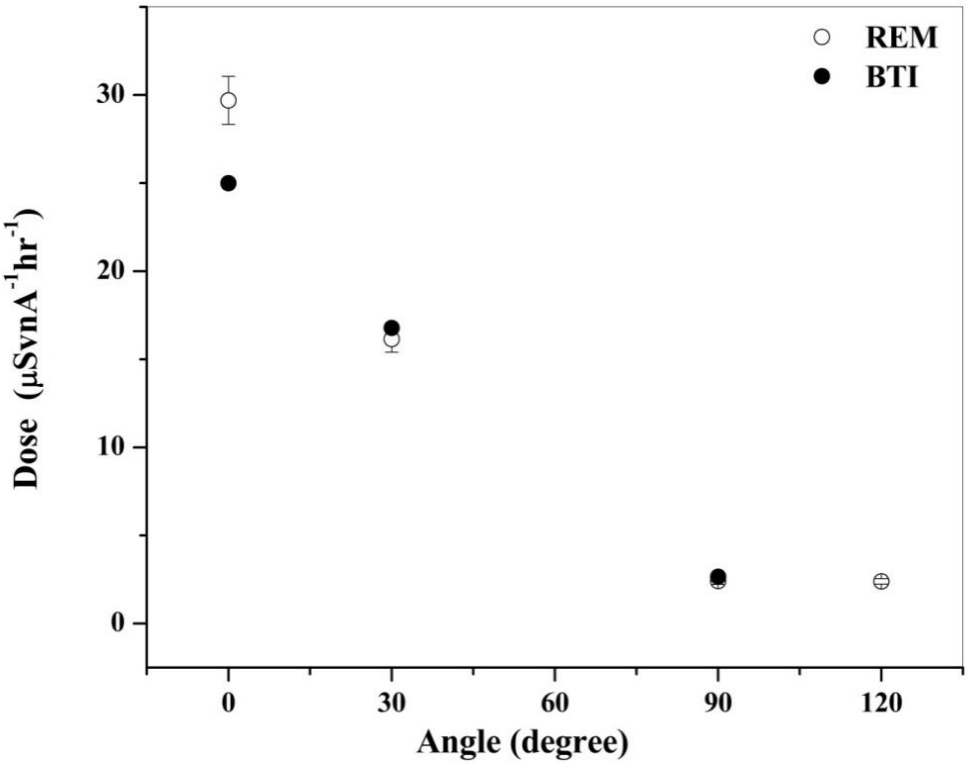

Fig. 6.4 Comparison of angular distribution of the neutron ambient dose equivalent measured using rem and Microspec dosimeters from $^{12}C^{6+}$ at 116.0 MeV incident on thick ^{12}C target. Open circles represent the REM data and the solid circles represent the Microspec data.

Table 6.2 Neutron Ambient Dose Rate measured with Rem meter and Microspec detectors (μSv enA^{-1}h^{-1}) at 1m

Lab angle (degrees)	REM Meter (μSv enA^{-1}h^{-1}) $D_{exp}^{REM}(\theta)$	Microspec Neutron Probe (μSv enA^{-1}h^{-1})
0°	29.69	24.99
30°	16.14	16.7
90°	2.42	2.66
120°	2.39	-

The energy distribution of the measured neutron field for angles 0°, 30° and 90° with respect to the beam direction is presented in Fig 6.5. The decrease in the fluence by an order from forward to backward angle is clearly visible. The gamma sensitivity check of Microspec detector have also been studied in the mixed field conditions of accelerator environment. The detector was shielded with a lead plate of 4 mm thickness to cut off the photons reaching the detector.

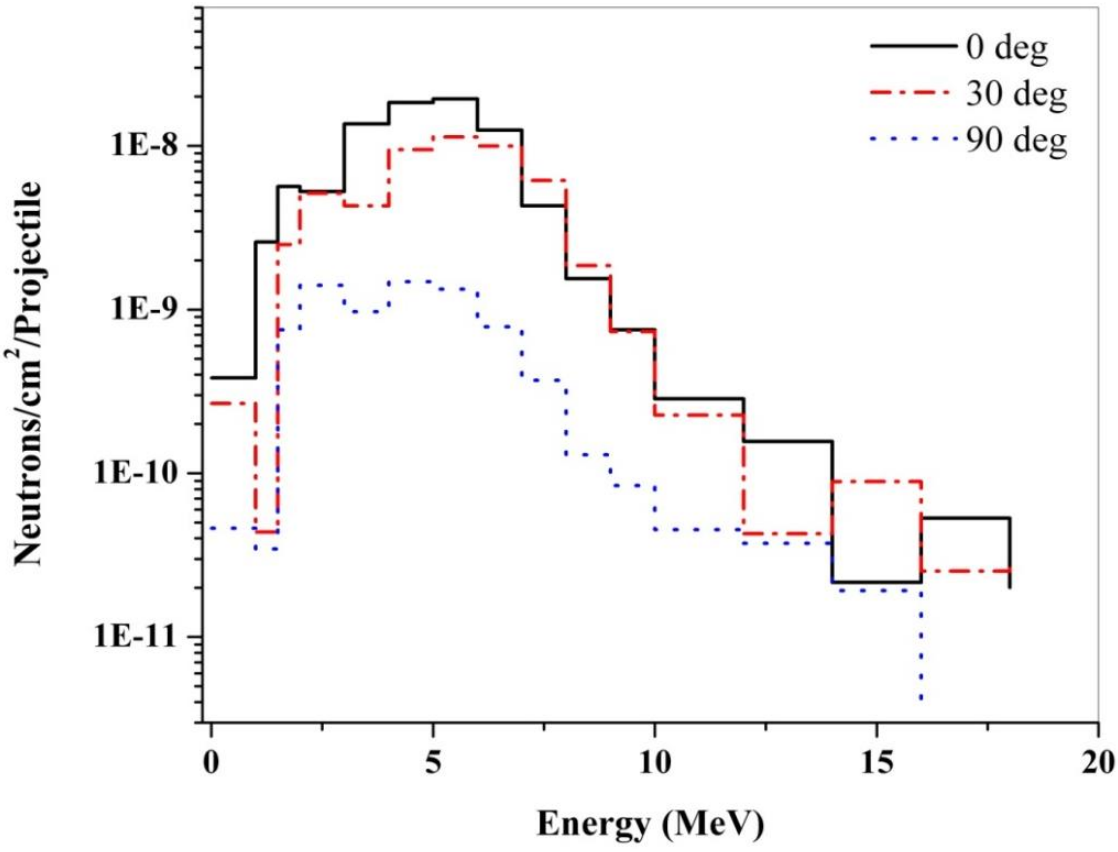

Fig. 6.5 Neutron energy spectra at different angles obtained from Microspec detector from the nuclear reaction $^{12}C^{6+}$ + ^{12}C at 116.0 MeV.

The neutron ambient dose measured with Microspec neutron meter with and without the lead sheet is presented in Fig 6.6. It is evident that the Microspec detectors are typically insensitive to the mixed fields of the gamma. The gamma sensitivity was found to be within 5 % for all the angles. The gamma sensitivity for rem meter Wedholm 2222A is very low, with discriminator level at 2.0 V, the contribution from 1 Sv/h gamma radiation is less than 10 μSv/h

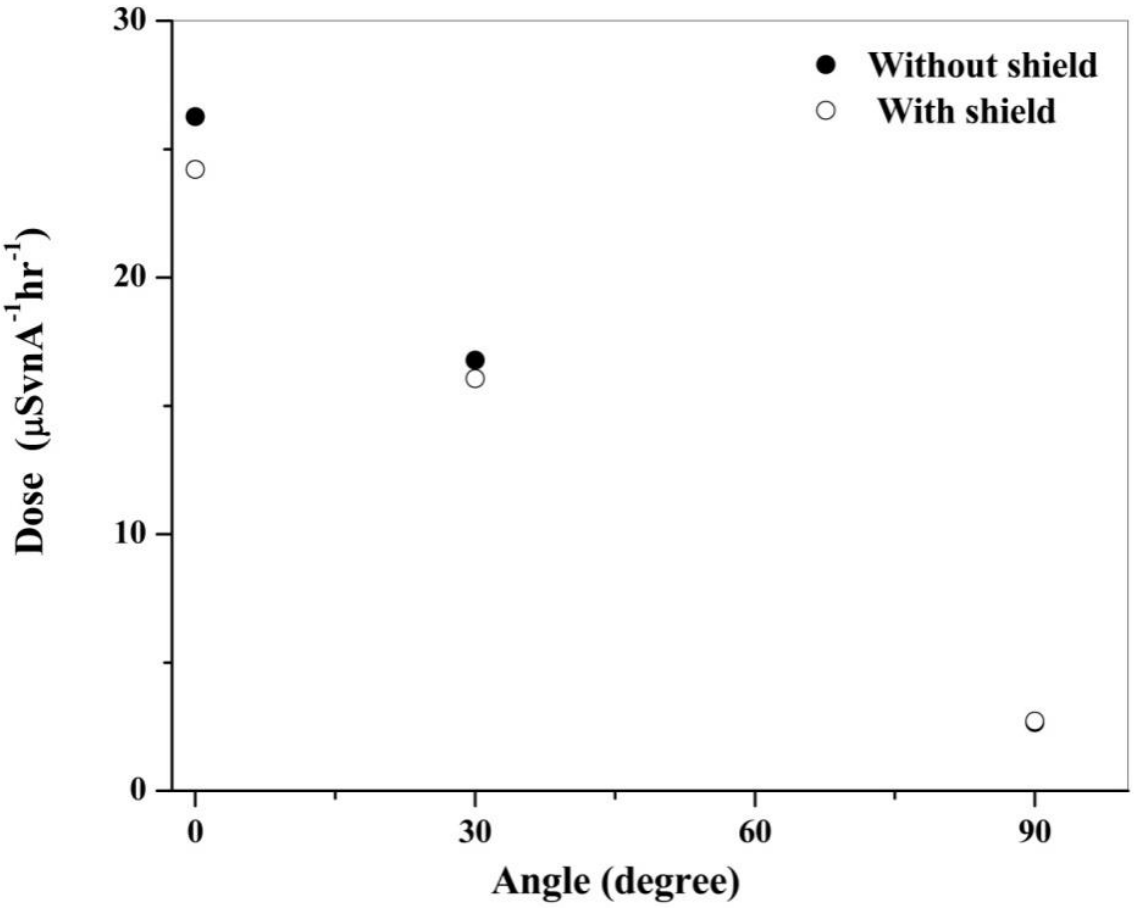

Fig. 6.6 Comparison showing sensitivity of Microspec detector to gammas in mixed radiation field. The neutron ambient dose equivalent measured using Microspec is plotted with (open circle) and without (solid circle) lead shield.

6.3 Neutron dose estimation from spectral distribution

The dosimeters, which are frequently used in accelerator facilities, need to be calibrated at regular intervals as per regulatory recommendations to a keep a check on its proper response. As discussed earlier there are various methods to obtain the neutron energy distribution either directly or by using some mathematical procedures to de-convolute the intertwined spectra with the response function of the detection system. Few of these methods like time of flight; proton recoil and activation foil measurements were also discussed in details in the previous chapters. All these methods provide the information of neutron energy distribution. The neutron doses as discussed earlier being a function of energy and should not be represented by energy averaged flux multiplied by the dose conversion coefficient. The neutron spectra when folded with the energy dependent dose conversion coefficients for neutrons, gives a true representative neutron doses. Also, this way of estimating the neutron ambient dose will facilitate to incorporate any changes in the dose conversion coefficients that may happen in future which will then require doses to be re-estimated as in case of conventional dosimeters. The double differential neutron yield distribution on the other hand is the most basic form and is invariant for any projectile-target system, when folded with energy dependent dose conversion coefficients, the ambient or the personnel neutron dose equivalents can be obtained. The energy differential yield is related to the ambient dose equivalent at an angle by following mathematical expression

$$H(\theta) = \int_E Y(E,\theta) C_H(E) dE \tag{6.5}$$

where, $Y(E,\theta)$ is the measured yield of neutrons having energy E, emitted in direction θ and $C_H(E)$ is the conversion coefficient for fluence to ambient dose equivalent for energy E given by ICRP. This simplifies the estimation of neutron ambient dose equivalents from the measured neutron spectra and its comparison with the one obtained using conventional dosimeters. There

are several active and passive ways to measure the neutron energy spectrum and will be briefly discussed in the following sections.

6.3.1 Experimental details and Results

In addition to the experimental setup given in section 6.2.3, along with the Wedholm neutron monitor and N-probe Microspec, five EJ301 organic liquid scintillator detectors of dimension 2″×2″ were also used and placed as explained in chapter 5. The doses were calculated by folding the ambient neutron dose coefficients to the measured neutron energy distribution over the energy bins of interest. To obtain the angular distribution of the dose, the dose distribution obtained by individual detectors were summed up over the energy. The angular distribution of the integrated doses obtained from time of flight method is compared with the rem meter measurements and are reported in units of μSv/enA/h as shown in Fig 6.7.

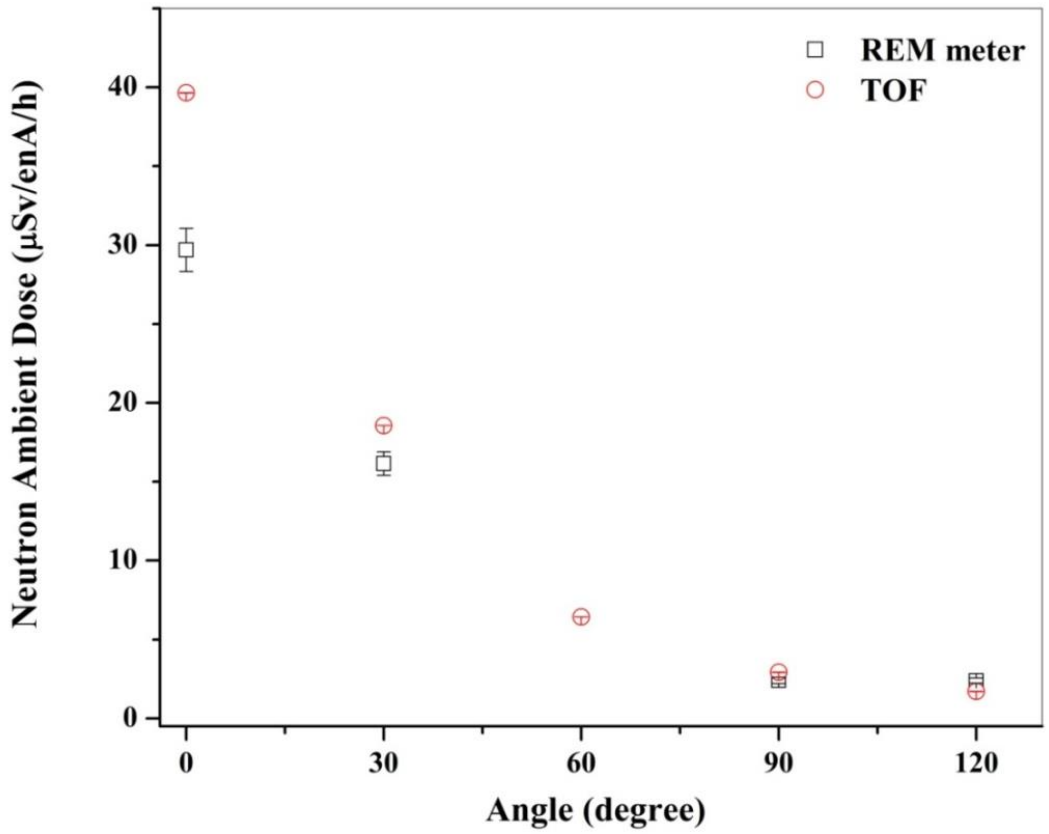

Fig. 6.7 Comparison of angular distribution of the neutron ambient dose equivalent measured using rem meter and time of flight (TOF). Open black squares represent the rem meter data and the open red circles represent TOF values.

From the plot it can be noticed that the rem meter under-estimates the ambient neutron dose in the forward angles but is close to the time of flight values in the backward angles. The under-estimation in dose ranges from 25% to 15%, whereas there is an over-estimation in the 120º measurement by almost 29 %. These variations seem to be big for the fact that the doses are very small numbers and percentage differences blow up. The statistical errors in the measurements are presented by vertical error bars. The doses show an exponential fall.

6.4 Neutron dose estimation using theoretical models

For predictive and quick estimations or evaluation of doses in absence of actual experimental measurements or in cases when measurements are not possible, the theoretical neutron spectrum estimation and eventually dose calculation from it becomes handy. Therefore, in addition to experimental measurements the neutron spectral distribution from frequently used nuclear reaction codes PACE2 and Fluka were also estimated. From the estimated distribution, integrated doses were obtained and the results will be presented in the following sections.

6.4.1 Neutron Dose Estimation – PACE2

The energy distribution of neutron yield obtained from PACE2 in directions 0º, 30º, 90º and 120º for the nuclear reaction $^{12}C + ^{12}C$ at 116.0 MeV as presented and discussed in the previous chapter were used here for estimating the neutron ambient equivalent dose. The neutron energy distribution was convoluted with the ICRP fluence to dose conversion coefficients over energy bins and then integrating the doses over the energy to obtain the integral ambient dose equivalent in the mentioned direction with respect to the incident beam.

The obtained dose values have been compared with the one directly measured with the earlier mentioned conventional dosimeters. The angular distribution of the measured neutron ambient dose is well reproduced by the PACE2 calculations.

6.4.2 Neutron Dose Estimation – Fluka

The details of the simulation tool Fluka can be referred from chapter 2. The simulation was done for a heavy ion carbon pencil beam hitting a thick carbon target and the fluence of the emitted neutrons from the nuclear reaction were scored in five 5.04 cm ϕ × 5.04 cm detectors filled with air. The detectors were placed at the same distances and orientations as were in the actual experimental setup. The fluence in all the directions was later convoluted with the dose to fluence conversion coefficients and will be presented in the results.

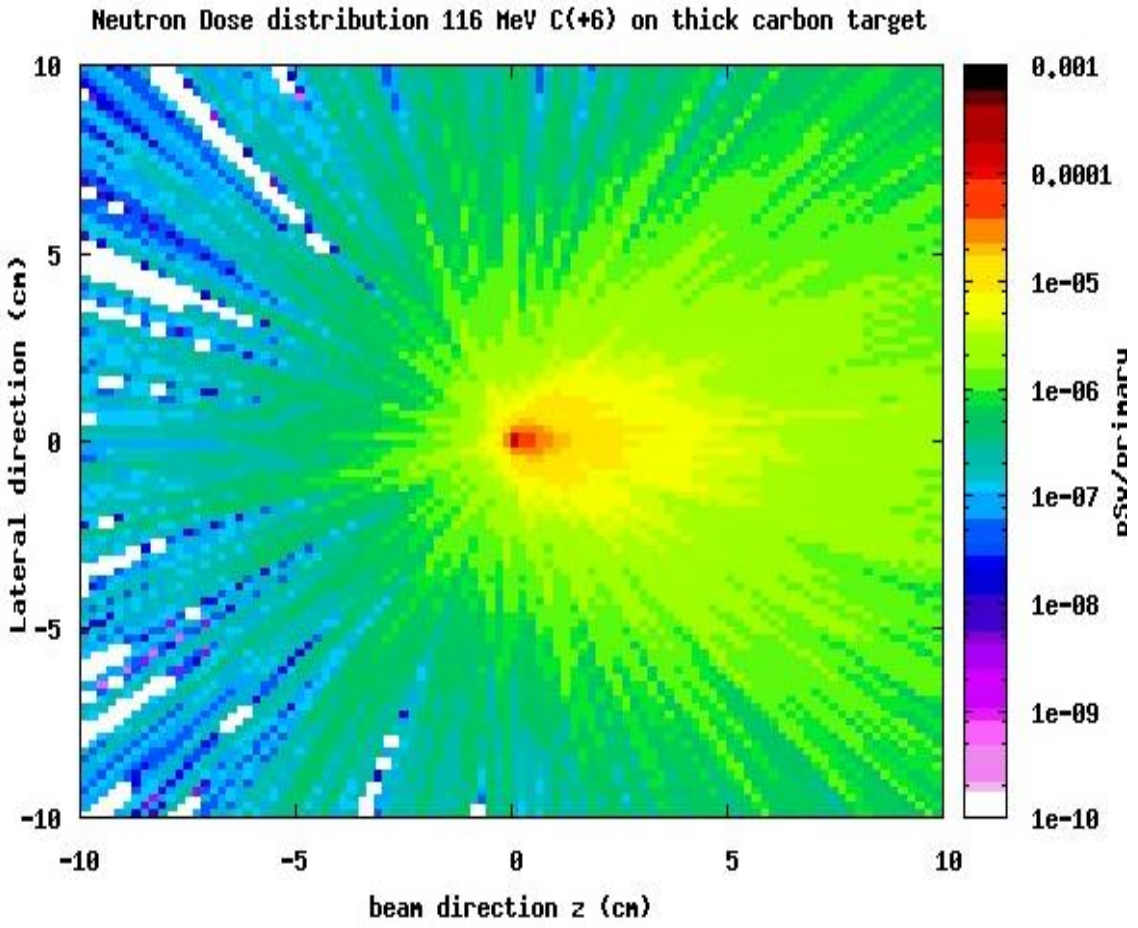

Fig. 6.8 The lateral view for the dose distribution from the nuclear reaction, 116.0 MeV heavy carbon ions on thick carbon target, simulated using Fluka.

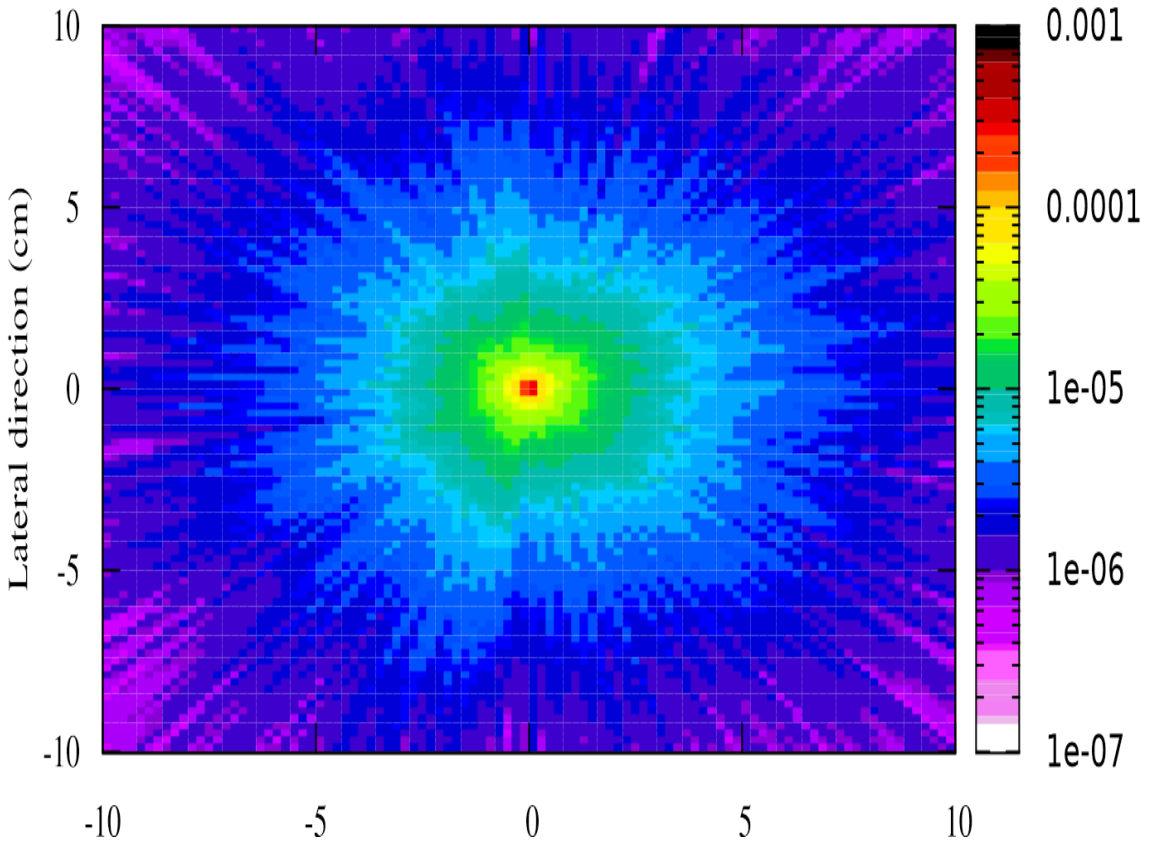

Fig. 6.9 The gamma dose distribution from the nuclear reaction, 116.0 MeV carbon ions on thick carbon target, in the direction of the beam simulated using Fluka.

The simulation was carried out for 1.0E+8 histories to have good statistics. The dose distribution due to emitted neutrons and gammas have also been scored. The dose distribution due to neutron field and gamma field have been plotted and is as shown in Fig 6.8 and Fig 6.9 respectively. The doses seen here are in units of pSv/primary. The neutron ambient dose distribution is forward peaked as it can be seen clearly in Fig 6.8. From the figure it is clear that the dose projection perpendicular to beam direction, is symmetric around the direction of beam. In addition, it is also visible that the dose reduces by an order from forward direction to lateral direction. Fig 6.9 presents the gamma dose distribution and is almost symmetric across the direction of beam.

6.4.3 Results and Discussion

The neutron integrated doses over different angles were calculated from the spectral distributions obtained from the PACE2 and Fluka. The comparison of the angular distribution in the integrated doses from rem meter and the time of flight measurements is plotted and presented in Fig 6.10. The code Fluka over-estimates the doses in almost all the directions by a factor less than two. The reaction code PACE2 also over-estimates the doses in all directions except 0º, also by a factor of less than one. In the extreme forward direction the PACE2 under estimates ambient dose by almost 4%. The differences if seen closely are not very much, the doses from all the methods match closely within a factor of 1.5.

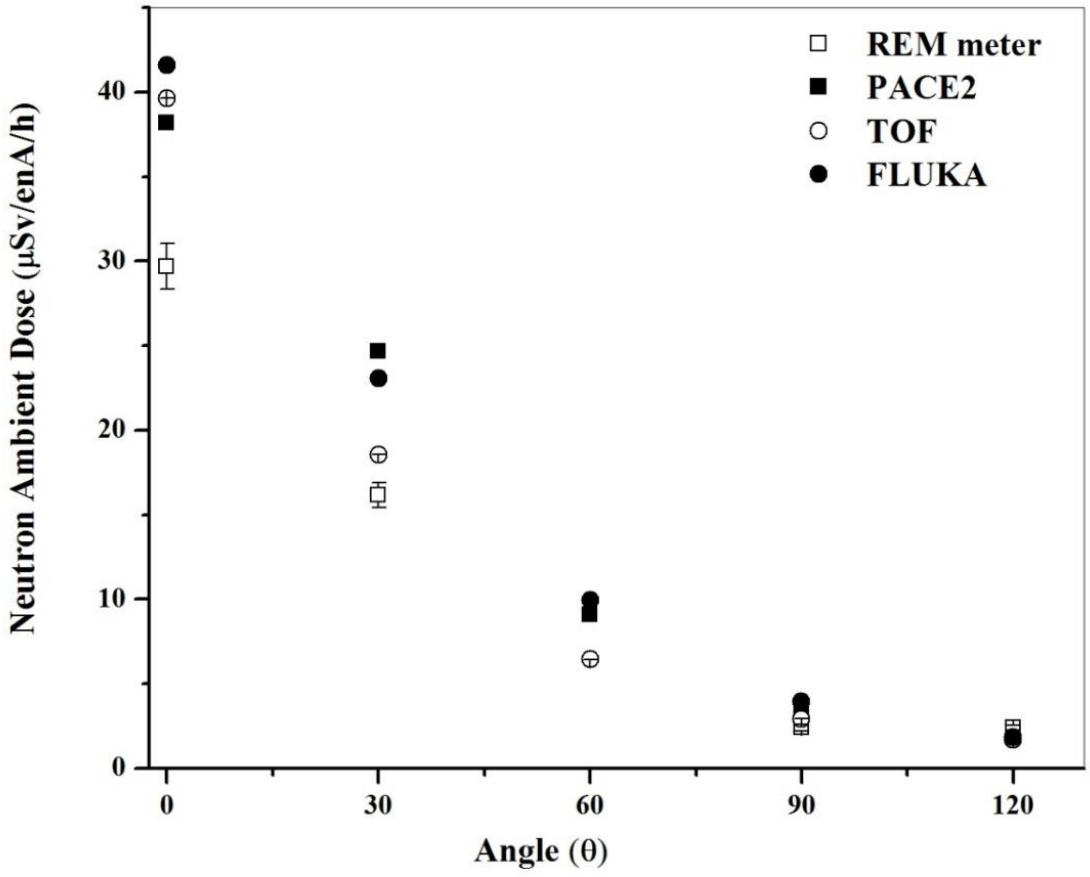

Fig. 6.10 Comparison of angular distribution of the neutron ambient dose equivalent measured using rem meter, time of flight (TOF) and estimated from PACE2 and Fluka reaction codes for 116.0 MeV ^{12}C ions incident on thick ^{12}C target.

6.4.4 Empirical Formulations - Dose Calculations

Many researchers in past have presented empirical formalism for estimation of neutron yield, total dose and angular distribution of the dose due to emitted neutrons from heavy ion reaction on thick targets. The formalism given by Guo *et al* [39] is used in this study and here, it was applied for estimation of neutron dose for the 116.0 MeV $^{12}C^{6+}$ projectile ions on thick ^{12}C target system. A brief description and mathematical formulation of Guo *et al* is given below.

6.4.4.1 Formulations by Guo et al.

Guo *et al* have given a mathematical formulation for estimation of angular distribution of neutron dose as a function of various parameters viz., projectile energy, atomic number of the projectile, beam current, angle of measurement, distance between target and detector etc. The mathematical form is given as below

$$D(\theta_L) = \overline{D} K_m exp(S\theta_L)$$

(6.6)

where, S is the slope of the $D(\theta_L)$ vs θ_L curve and K_m is a normalization factor and is given as

$$K_m = \frac{2(1+S)^2}{1+exp(S_n)} \quad (6.7)$$

the parameter S is proportional to the center-of-mass velocity and is approximated as

$$S = 0.5 \frac{A_p}{A_p + A_t} \sqrt{\frac{E_p}{A_p}} \quad (6.8)$$

where, A_p and A_t are the mass numbers of projectile and target respectively; and E_p is the projectile energy. The author has not mentioned the parameter S_n in their paper, thus here in present work we have adopted $S = S_n$.

The spatially averaged mean dose rate ($\mu Sv h^{-1} p\mu A^{-1}$ at 1 meter) is given as

$$\overline{D} = \left(33.4\overline{R_p R_t}\right)^2 (P + 0.35)^2 \text{ for } P > 0$$

(6.9)

where, values of the parameters R_p and R_t is given in Guo *et al* [39]; and P is given as

$$P = \frac{E_p - CB}{A_p} \tag{6.10}$$

and CB is given in terms of MeV

$$CB = 1.44 \frac{A_p + A_t}{A_t} \frac{Z_p Z_t}{1.9 + 1.209\left({A_p}^{1/3} + {A_t}^{1/3}\right)}$$

(6.11)

where, Z_p and Z_t are the atomic numbers of the projectile and the target respectively. Guo *et al* have also given the conversion factor to estimate total neutron yield from the spatially averaged dose $\overline{D}$ and the expression is as given

$$Y = 1.41 \times 10^{-8} \overline{D} \text{ n/proj} \tag{6.12}$$

6.4.4.2 Results and Discussion

The neutron ambient doses acquired by all the methods will be discussed here. The doses were obtained by directly measuring it using commercially available rem meter and Microspec neutron probe, and by estimating it from the spectral distribution. The energy distribution of the neutron field obtained using time of flight technique was used for calculating the neutron ambient doses. In addition, the theoretical methods of estimation of spectral distribution using reaction codes PACE2 and Fluka were used and the doses were calculated thereafter. In addition, a theoretical empirical formulation given by Guo *et al* was used for the dose estimation. A comparison of the doses obtained from all these methods are collectively given

in Fig 6.11. As discussed earlier the doses from rem meter, Microspec, PACE2 and Fluka the factor is less than one when compared to the TOF doses. It is clearly seen that dose calculated from Guo *et al* underestimates the doses and it is almost 3.5 and 2.5 times lower in the forward direction 0º and 30º.

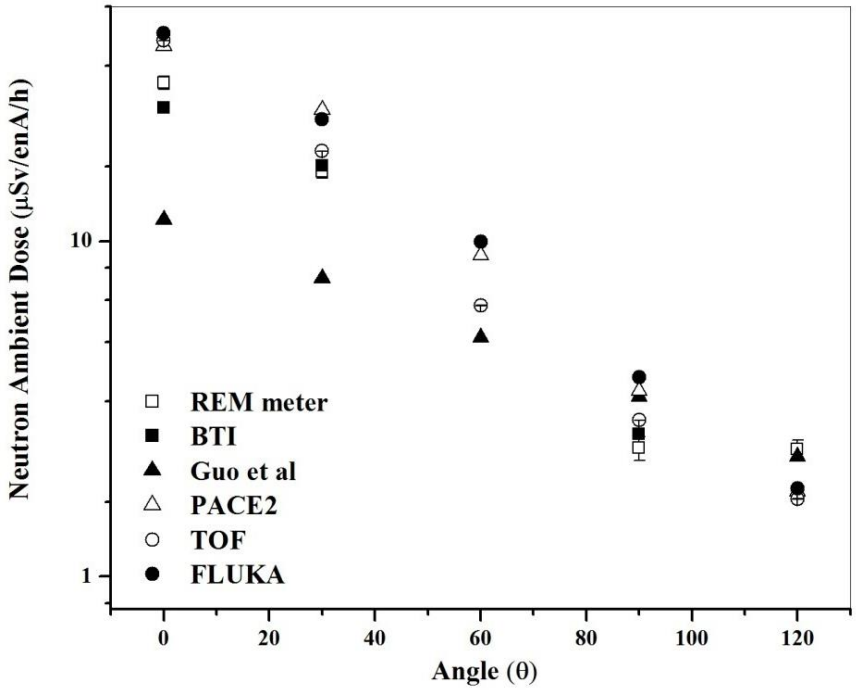

Fig. 6.11 Comparison of the neutron ambient doses obtained using different methods.

The agreement improves in the 60º to 120º directions as the ratio to TOF comes closer to one. The ratios of the obtained doses from different approaches to TOF are presented in Fig 6.12. The neutron ambient dose for the nuclear reaction 116.0 MeV carbon ion on thick carbon target is presented in Table 6.3, obtained from all the experimental measurements as well as the theoretical estimations.

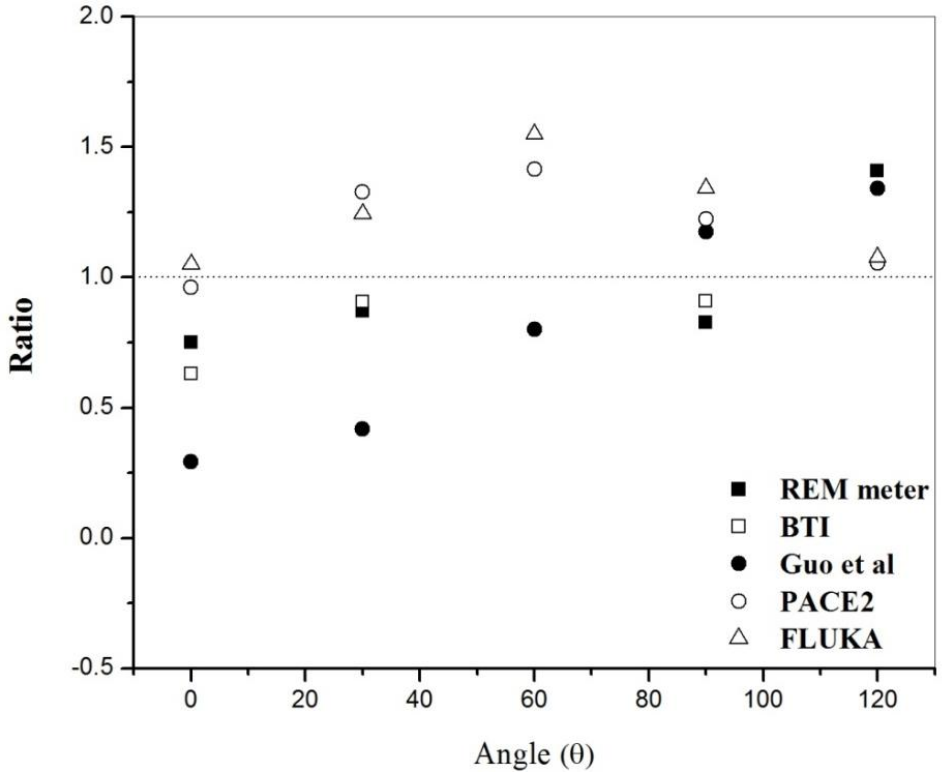

Fig. 6.12 Comparison of the ratio from the neutron ambient doses obtained using different methods with respect to TOF measurements.

Table 6.3 Ambient neutron dose obtained using various techniques, from nuclear reaction carbon ions at 116.0 MeV on thick carbon target.

Direction (Degree)	Ambient neutron dose (μSv/enA/h)					
	REM meter	BTI	TOF	PACE2	FLUKA	GUO
0º	29.69	24.99	39.65	38.17	41.62	11.6
30º	16.14	16.78	18.56	24.64	23.07	7.74
60º			6.43	9.10	9.96	5.15
90º	2.42	2.66	2.92	3.57	3.92	3.43
120º	2.39		1.70	1.80	1.83	2.28

The ratio of the doses from all methods with respect to the dose obtained from time of flight method is presented in Table 6.4. The ratio provides information on the variation with respect to the time of flight measurements.

Table 6.4 Ratio of the ambient neutron dose presented in Table 6.3, above.

Direction (Degree)	Ratio $(D_{REM,BTI,PACE2,FLUKA,GUO}/D_{TOF})$				
	REM meter	**BTI**	**PACE2**	**FLUKA**	**GUO**
0º	0.75	0.63	0.96	1.05	0.29
30º	0.87	0.90	1.33	1.24	0.42
60º	-	-	1.41	1.55	0.80
90º	0.83	0.91	1.22	1.34	1.17
120º	1.41	-	1.05	1.08	1.34

6.5 Uncertainties in Measurements

Uncertainties in the results arise mainly due to propagation of the statistical and systematic uncertainties. The systematic uncertainties are associated with the total charge obtained from the current integrator, the detector positions and due to the scattered component from the surrounding surfaces of the experimental hall. The statistical uncertainties arise from the integral counts in the detectors which was estimated to be less than 5% in forward direction (0º and 30º) and about 10% in backward angles (90º and 120º). The scattered contribution was not measured during this measurement. However, a Fluka [63, 141] Monte Carlo radiation transport simulation carried out to estimate this, yielded approximately 5% in the forward

direction and 10% in the backward (90° and 120°) directions with respect to the beam direction. The larger value at the backward angles is due to the enhanced scattering from the concrete walls. Similar results were also obtained experimentally [142] in the same experimental hall in a previous experiment conducted by the authors with similar neutron emission characteristics and are therefore assumed to hold true in this experiment. The results are however not corrected for this contribution since it was not measured but is mentioned here to give an expected estimate. The uncertainty in the position and in the precision current integrator readings were both less than 1%. Due to extended size of the rem-meter (21.5 cm diameter) compared to the beam spot on the target there will be an uncertainty in horizontal alignment of the detector which was also estimated to be within 1%. The overall uncertainty in the measurements is estimated to be less than 11%.

6.6 Summary

The directional distribution of neutron ambient dose equivalent was measured for the neutrons originating from a thick carbon target bombarded by 116.0 MeV carbon ions. The ambient doses were measured using the conventional neutron dosimeters. The neutron ambient dose is not seen to be isotropic and appears to be forward peaked. The angular distribution of the neutron ambient dose also shows a forward peaked characteristic and an order of magnitude reduction at the backward angle. The energy distribution measured by a commercially available neutron spectrometer also shows the fluence reduction by an order of magnitude at the backward angle. The various approaches using two commercially available dosimeters, the time of flight technique, spectral distribution estimation from nuclear reaction codes PACE2 and Fluka and using empirical formulation of Guo *et al*, were used to compare the doses. The theoretical estimation of doses obtained from codes PACE2 and Fluka were slightly over-estimating as compared to the doses obtained from time of flight measurements. The doses

obtained using the empirical formulation were under-estimated in the forward direction while were over-estimated in the backward angles. The neutron ambient dose measurements obtained from rem meter and the BTI detectors also showed some under-estimation in the forward direction which improved in the backward angles. The uniformity in the neutron ambient dose measurements of the discussed dosimeters needs to be further explored with different projectile target and energy sets of measurements. Similar comparisons between different approaches give a basis to improve the nuclear reaction codes for dose predictions.

CHAPTER 7

Summary and Conclusions

7.1 Summary and Conclusions

Neutron is a major ionizing radiation which constituents the prompt radiation field in any heavy ion accelerator facility. The probability of neutron interaction with matter strongly depends on the neutron kinetic energy and the target composition. The radiation protection quantities like, absorbed dose, ambient neutron dose and neutron dose coefficients are a strong function of kinetic energy distribution of the emitted neutrons. The present study has been mainly motivated by the scarcity of neutron emission data from both thin and thick target in the heavy ion bombarding energy ~ 10 MeV/A and to improve in neutron dosimetric estimations by including use of neutron yield and energy distribution for dose estimation.

In the present work, a neutron spectrum unfolding code "Genetic Algorithm based Monte Carlo De-convolution (GAMCD)" has been developed for extracting the neutron energy distribution from the active proton recoil and threshold foil measurement data. The method is population driven which makes use of basic operation of selection and crossover to generate new solution points in search space. The initial solution set is generated randomly from a uniform distribution requiring no *a priori* information about the shape of the solution spectrum. A new mutation operator based on iterative method was adopted in addition to point wise

mutation and the former was found to speed up the search. Mutation in general helps the solution to escape the local minimum if got stuck midway of the convergence. The average of all the scores from each history is taken as the final solution.

The significant features of the present method are as follows:

i. Considers the uncertainties present in the measured data as well as in the response matrix.
ii. Does not yield any negative values in the solution.
iii. Does not require any *a priori* information about the shape of the final solution, although there is provision for accepting any *a priori* information if available
iv. Confidence interval of the final solution after considering all uncertainties (measured data and response matrix) can be estimated easily.
v. The method is well suited for solving the under-determined problems and obtains meaningful solutions.
vi. The method can equally be extended to other optimization problems.

The proposed neutron spectrum unfolding method GAMCD has been validated with unfolding a simulated spectrum in addition to proton recoil and activation foil measurements. The proton recoil measurement for the nuclear reaction $^{12}C+ {}^{nat}Ag$ at 144.0 MeV have been unfolded using GAMCD and is compared with the FERDOR unfolding code predictions.

The code has also been used to extract neutron energy spectra for the $^{1}H + {}^{9}Be$ reaction at 20.0 MeV, where multiple threshold foils were irradiated by the emitted neutrons and their activities were later measured. Two sets of multiple activation foils with different thresholds were mounted at extreme forward (0°) and lateral direction (90°) with respect to projectile direction. The signature of the emitted neutrons from the interaction of 20.0 MeV protons on thick ^{9}Be target, are measured as activities of the irradiated foils using an HPGe spectrometer. The measured activities and the reaction cross-section data were used in MAXED and GRAVEL codes for unfolding the spectra at the mentioned angles and the unfolded spectra

was found to be comparing well with the unfolded spectra from GAMCD code. The neutron spectra was characterized by a large peak at about 3 MeV contributed by the three body break up process, a possible high energy peak was seen around 15 MeV giving a signature of direct reaction; amplitude of which reduces in backward direction. The unfolded spectra when folded back with the response function to calculate the activity matched well with the actual measured activities, GAMCD results being the closest. The performance of the present GAMCD code on artificially prepared under-determined problem from the actual measured data was also found to be highly satisfactory when compared with the results from some validated standard unfolding codes.

While response function is an essential input parameter to perform unfolding, a study has been carried out to prepare a response function for one of the detectors used in proton recoil and time of flight experiments. The response function have been generated using the GEANT-4 simulation tool for a 12.7 cm ϕ x 5.08 cm liquid scintillator detector. The pulse height distributions of the two mono-energetic neutron energies from DD and DT reactions have been measured. The data is fitted to parametric equations to estimate light output coefficients. To account for the smeared Compton edge a smearing function is included in the simulated response to match with the actual response. The response matrix for the liquid scintillator detector is prepared using the fitted relation. With the prepared response function and the measured pulse height distribution the actual neutron energy distribution from DD and DT reactions is obtained using GAMCD. The spectral distribution obtained from unfolding is satisfactory, except the scattered components.

The neutron energy spectra have been measured from the bombardment of $^{12}C^{6+}$ ions on thick ^{27}Al target at 115.0 MeV and on thick ^{12}C target at 116.0 MeV. The double differential neutron yield from heavy ions is measured using five EJ-301 liquid scintillator detectors at 0°, 30°, 60°, 90° and 120° for the thick targets. Time of flight technique is used for neutron energy

distribution measurement by placing the detectors at known location from the target. The measured neutron yields are compared with the PACE2 and Fluka nuclear reaction codes at all the measured angles. The comparison is reasonable and the most probable emission energies match well. For the range of projectile energies considered in this work, compound nuclear emissions dominate and the measured neutron yield fits with Maxwellian distribution. Furthermore, no change in slope is observed suggesting that the neutron contribution is mainly through evaporation and there is no pre-equilibrium contribution at this projectile energy range. The yield falls by an order of magnitude when compared from forward to the lateral direction.

The neutron yield from bombardment of natural thin carbon target at various energies of the ^{12}C projectile has been studied. The yields have been measured at 30º, 60º, 90º and 120º with respect to the beam direction. The experimentally estimated yields are compared with the calculations from the nuclear reaction codes PACE2 and Fluka. The PACE2 calculations are observed to agree well with the measured distribution showing that the neutrons are mostly contributed by compound nuclear emissions. With the level density parameter $a = A/7$, the slope of the yield distribution curve is better reproduced. In the backward angles Fluka calculations over-estimated the double differential yield. A linear interpolation has been carried out for the energies in between the experimentally measured ones using relation which was first checked for the measured data. The total neutron yield distribution from the thin target measurements and the interpolated ones is added over energy and are compared with the thick target emission yield. The measured thick target yield is slightly higher than the thin target integrated yield. This is attributed to the fact that the projectile energy considered for thin target is from 110.0 MeV till 44.0 MeV as compared to the projectile energy of 116.0 MeV for the thick target measurement which probably goes down till the Coulomb barrier within the target before completely being stopped. Since, the slope of the emission yield over energy does not

change, it appears that the yield constitutes mostly of evaporation component and there is no sign for pre-equilibrium emission.

Finally, with the active techniques mentioned above the neutron energy distribution is convoluted with the ambient neutron dose coefficients and is integrated over the energy to obtain the ambient neutron doses. For the emitted neutrons from nuclear reaction $^{12}C^{6+}$ + ^{12}C at 116.0 MeV in addition to the double differential neutron yield, the ambient neutron doses using two conventional neutron dosimeters were also measured. The neutron ambient dose similar to the neutron yield is forward peaked and not isotropic. The angular distribution of the ambient dose was also studied by measuring doses at different angles. The neutron ambient dose is seen to fall towards the backward angle by almost an order of magnitude of the forward angle dose. The Neutron ambient doses obtained by the two commercially available dosimeters, the time of flight technique, spectral distribution estimation from nuclear reaction codes PACE2 and Fluka and using empirical formulation of Guo *et al*, are compared. The experimental measurements and the theoretical estimations compare reasonably well except there is a noticeable under estimation by the dosimeters and the empirical formulation.

7.2 Scope for future work

The present work deals with measurement and analysis of the neutron yield from heavy ion and proton induced reactions. Comparison of the results with the nuclear reaction codes have been carried out. Improvements can be achieved by comparing experimental results with different target projectile combinations and bombarding energy range. The angular distribution predicted by the nuclear reaction codes need to be analyzed with more similar experimental data to further establish its correctness. The GAMCD code can be further validated for unfolding the energy spectrum from bonner sphere measurements using different passive

detectors. More proton recoil measurements can be carried out for GAMCD validation with time of flight measurements.

Further studies on ambient neutron dose measurements and angular yield distributions can be carried out using different techniques. Studies can also be performed with different target - projectile combinations at various energies to verify the neutron ambient dose responses with these techniques.

CONTENTS

Summary

One of the major research goals on radiation safety in the accelerator facilities is to accurately measure the radiation sources and understand its radiological characteristics. The positive ion accelerator environment consists of mixed radiation field including neutrons, which are of main concern. Accurate estimation of neutron dose to occupational workers is important from the radiological safety point of view. Neutron dosimetry is a complex field and fluence to dose conversion factor is normally used for estimating the neutron ambient dose. The measurement of neutron fluence and dose is also a complicated task due to highly anisotropic nature of the emission, wide range of energy and fluence and in some cases pulsed nature of the emissions. The neutron yields are usually reported in terms of energy and angular distributions and is a function of nuclear reaction parameters like, target - projectile configuration, incident projectile energy and charge state.

Double differential neutron yield, with respect to neutron energy and angular distributions, will provide the source term which is a critical input for the shielding calculation of the facility. Moreover, it is the input for estimations of air and structural activations in the high energy and high current accelerators. Also, the data generated from measurements of neutron energy distribution and neutron ambient dose will help in benchmarking the reaction codes for predictive estimations in absence of measurements. This brings out the need for carrying out the neutron spectrometry and dosimetry study using various active techniques in positive ion accelerators.

The work presented in this thesis has been divided into three parts. The first part focusses on development of a genetic algorithm based neutron spectrum unfolding code (GAMCD). This code can be applied when direct techniques like time of flight cannot be used for neutron energy spectrum measurements. Using the GAMCD code an activation foil measurement for $^{1}H + ^{9}Be$ at 20 MeV and a proton recoil measurement for $^{12}C + ^{nat}Ag$ system at 144 MeV, were

unfolded to obtain the underlying neutron energy distributions. This method overcomes the requirement of any guess spectra, in absence of which few available codes like MAXED and GRAVEL fail to work satisfactorily. In addition to the code, the neutron response function of the organic liquid scintillator detector that goes as input in unfolding is prepared. For one of the liquid scintillator detector used in this study the pulse height of mono-energetic neutron sources DD and DT are measured experimentally. Pulse height distribution for various incident energies has been simulated using GEANT-4 and the fitted parameters and smearing has been added to match the detector resolution.

In the second part of the work, measurement of double differential neutron yield and angular distribution by time of flight method for the thick targets $^{12}C + ^{27}Al$ at 115.0 MeV and $^{12}C + ^{12}C$ at 116.0 MeV has been carried out. The measured yields were compared with the reaction codes Fluka and modified PACE2 estimations. A measurement of neutron yield and its angular distribution using time of flight method for thin target $^{12}C + ^{12}C$ system at various projectile energies 44 MeV – 110 MeV have also been carried out. The measured neutron energy distributions are compared with predictions of statistical code PACE2.

In the final part neutron ambient dose is estimated from neutron energy distribution obtained from time of flight measurements and the reaction codes, using ICRP 74 fluence to dose conversion coefficients. The estimated doses are compared to the experimentally measured neutron ambient doses and its angular distribution, using commercial dosimeters for thick target $^{12}C + ^{12}C$ system at 116.0 MeV.

The present study brings out the importance of neutron ambient dose estimation from measured and estimated neutron energy distributions compared to experimental rem meter measurements. The theoretical estimations and experimental measurements compare reasonably well except there is a noticeable under estimation by the dosimeters and the empirical formulation.

The present study further emphasizes that the dose measurements carried out with commercial rem meters should be periodically compared with the neutron ambient doses estimated using neutron energy distribution data, either obtained experimentally from time of flight technique or neutron spectrum unfolding and obtained from nuclear reaction codes. The present study will also help in understanding radiation environment both qualitatively and quantitatively in low energy positive ion accelerator facilities and plan for radiation protection activities. The measured data will also help to benchmark the reaction codes for neutron yield and dose predictions when experimental data are not available for quick references.

LIST OF FIGURES

Figure **Page**

LIST OF TABLES

Tables **Page**